TECHNISCHE UNIVERSITÄT MÜNCHEN

TUM School of Engineering and Design

Snow and glacier melt runoff forecasting under current and climate change scenarios and improved degree-day factor estimation

Muhammad Fraz Ismail

Vollständiger Abdruck der von der TUM School of Engineering and Design der Technischen Universität München zur Erlangung des akademischen Grades eines

Doktors der Ingenieurwissenschaften (Dr.-Ing.)

genehmigten Dissertation.

Vorsitzender:	Prof. Dr. Gabriele Chiogna
Prüfer der Dissertation:	
	1. Prof. Dr.-Ing. Markus Disse
	2. Prof. Dr. Lucas Menzel

Die Dissertation wurde am 16.05.2022 bei der Technischen Universität München eingereicht und durch die TUM School of Engineering and Design am 09.09.2022 angenommen.

Abstract

Fresh water in the form of snow and ice melt from the mountainous regions is of critical importance for sustaining human subsistence in both mountains and adjacent lowlands. Due to heterogeneous hydrologic processes and spatio-temporal changes in hydro-meteorological variables, understanding of mountain hydrosphere is a complex subject as timing and amount of generated melt is highly variable and subject to change. In addition, changing climate poses a difficult challenge in the form of changing future cryosphere, which will ultimately affect the future water availability by altering the flow regimes from snow and ice melt driven mountainous regions. The transboundary Upper Indus Basin (UIB) in the High Mountain Asia (HMA), which is characterized by high altitudinal ranges, is one such example of a complex mountainous catchment. This mountainous region is not only crucial in terms of providing fresh water supply to millions of people but also vulnerable after becoming a climate change hotspot. Besides, food security of Lower Indus Basin (LIB) (which includes the Indus Basin Irrigation System) is critically dependent on timing and volumes of seasonal and long-term snow and ice melt in the UIB. Hence, understanding and adequate modelling of UIB's hydrology is of utmost importance for sustainable water and food security within UIB and downstream in LIB. However, understanding and modelling the hydrology as well as climatology of the UIB is a huge challenge, since there are only few data measuring stations in the region, whereas its physical spread is substantial.

This dissertation aims to contribute to the challenges faced by the UIB regarding understanding and quantifying future water availability as well as water resource forecasting (i.e. seasonal and long-term) under present and projected climate. This thesis is divided into three major topics i.e. (i) *Snow and ice melt runoff modelling and forecasting,* (ii) *future water availability using enhanced hydrological modelling and uncertainty quantification under changing climate* and (iii) *improved estimation of degree-day factor based on energy flux components*.

A reliable forecast of seasonal water availability for the Kharif cropping season (i.e. 1st April – 30th September) from the UIB can pave the way towards better water management which subsequently enhance the agro-economy of Pakistan. In order to fulfil this objective, a temperature-index model (i.e. Snowmelt Runoff Model + Glaciers) in conjunction with satellite-based remote sensing data has been employed for modelling the snow and ice melt runoff from the UIB. The main reason for using the temperature-index model is that it has proved to be a suitable tool for modelling the snow and ice melt processes especially in data scarce mountainous regions. A seasonal scenario-based approach is used

for forecasting the seasonal (i.e. 6 months) snowmelt. This approach is similar to Ensemble Streamflow Prediction (ESP) method and uses historic meteorology as model forcing. This seasonal scenario approach is a step towards probabilistic forecasting of seasonal flows in the UIB. This approach may be further enhanced by selecting a subset of ensemble members according to forecasted seasonal anomalies in temperature and precipitation.

In the UIB, seasonal snow and ice melt contributes more than 70% of water. However, due to the impact of climate change, hydrological regimes are bound to change. In this context, it is critically important to understand how the climate change will influence the future water availability from the UIB. For this purpose, first of all an enhanced model calibration/validation approach has been applied to calibrate and validate the hydrological models for the UIB. This enhanced model calibration/validation approach is adopted because it takes into account the quality of observational data, utilizes contrasting climate data for calibration, includes comparison of discharge for multiple sub-catchments (i.e. intermediate gauges), includes multi-variable calibration for variables like evapotranspiration, glacier mass balance or snow cover area and evaluate observed and simulated trends in the observational period. Based on the parameterisation from the enhanced model calibration approach future water availability under changing climate was assessed, which shows that the future flow regime will alter. The combined long-term projected changes in discharge from both hydrological models show contrasting trends for two Representative Concentration Pathways (RCPs: 2.6 and 8.5). The largest increases in discharge are projected for RCP8.5. The analysis of variance (ANOVA) method is used in order to quantify hydrological model uncertainty and it can be concluded from this study that the uncertainty contribution from the hydrological models is getting smaller for projections simulated using the enhanced method.

The temperature-index models are commonly used for assessing present and future water availability in data limited snow and glacier fed catchments. These models use degree-day factors (*DDF*) as key parameter to estimate melt merely from air temperature. The *DDF* is commonly treated as a model calibration parameter. However, in the present research, a methodology was adopted to estimate the *DDF* from energy flux components based on an assumption that the snowpack is isothermal at 0 °C and in fully ripe state. The melt obtained from the energy flux components is converted into *DDF* by dividing it with respective degree-days. The objective of this study is to better understand the *DDF* and its dependencies (e.g. cloud cover, snow albedo and season). Estimation of the *DDF* through these energy flux components is providing a physical background, which will help to find more realistic values of the *DDFs*. In this study, a brief analysis of the *DDF* under the influence of climate change shows that the *DDFs* are expected to decrease when comparing periods of similar degree-days, as melt will occur earlier in the year and snow albedo is then likely to be higher. Thus, the *DDF* cannot be treated as a constant parameter especially when using temperature-index models for forecasting present or predicting future water availability.

Zusammenfassung

Süßwasser aus saisonaler Schnee- und Gletscherschmelze in Gebirgsregionen ist von entscheidender Bedeutung für die Aufrechterhaltung des menschlichen Lebensstandards sowohl in den Bergen als auch im angrenzenden Flachland. Aufgrund der heterogenen hydrologischen Prozesse und der starken räumlichen und zeitlichen Variabilität der hydro-meteorologischen Einflussgrößen ist die Gebirgshydrologie ein komplexes Thema, da Zeitpunkt und Menge der Schneeschmelze sehr variablen Veränderungen unterworfen sind. Darüber hinaus stellt der Klimawandel eine große Herausforderung in Folge der sich verändernden Kryosphäre dar, die sich auf die künftige Wasserverfügbarkeit auswirken wird, indem sie das Abflussregime von schnee- und gletscherbedeckten Bergregionen verändert. Das grenzüberschreitende Obere Indusbecken (UIB) im asiatischen Hochgebirge (HMA), das durch große Höhenunterschiede gekennzeichnet ist, ist ein besonderes Beispiel für ein komplexes Gebirgseinzugsgebiet. Diese Gebirgsregion ist nicht nur für die Trinkwasserversorgung von Millionen von Menschen von entscheidender Bedeutung, sondern auch äußerst vulnerabel, da sie ein Hotspot des Klimawandels ist. Darüber hinaus hängt die Ernährungssicherheit des Unteren Indusbeckens (LIB), zu dem auch das Bewässerungssystem des Indusbeckens gehört, entscheidend vom Zeitpunkt und den Mengen der saisonalen und langfristigen Schnee- und Gletscherschmelze im UIB ab. Daher ist das Verständnis und die adäquate Modellierung der Hydrologie des UIB von größter Bedeutung für eine nachhaltige Wasser- und Ernährungssicherheit im gesamten Indusbecken. Die Hydrologie und Klimatologie des UIB zu verstehen und zu modellieren ist jedoch eine große Herausforderung, da es nur wenige Messstationen in der Region gibt, während die räumliche Ausdehnung beträchtlich ist.

Diese Dissertation zielt darauf ab, einen Beitrag zumVerständnis und zur Quantifizierung der zukünftigen Wasserverfügbarkeit sowie zur Vorhersage von Wasserressourcen (d.h. saisonal und langfristig) unter dem gegenwärtigen und dem prognostizierten Klima im UIB zu leisten. Diese Arbeit gliedert sich in drei Hauptthemen: *(i) saisonale Vorhersage des Abflusses aus der Schneeschmelze, (ii) Abschätzung der zukünftigen Wasserverfügbarkeit durch verbesserte hydrologische Modellierung und Quantifizierung von Unsicherheiten unter veränderten klimatischen Bedingungen und (iii) verbesserte Schätzung von Gradtagfaktoren auf der Grundlage von Energieflusskomponenten*. Eine zuverlässige Vorhersage der saisonalen Wasserverfügbarkeit für die Kharif-Anbausaison (d.h. 1. April - 30. September) im UIB kann den Weg für ein besseres Wassermanagement ebnen, welches in der Folge der Agrarwirtschaft Pakistans zugutekommt. Um dieses Ziel zu erreichen, wurde ein

Temperaturindexmodell (Snowmelt Runoff Model + Glaciers) in Verbindung mit satellitengestützten Fernerkundungsdaten zur Modellierung des Schnee- und Eisschmelzabflusses aus dem UIB eingesetzt. Der Hauptgrund für die Verwendung des Temperaturindexmodells ist, dass es sich als adäquates Werkzeug zur Modellierung von Schnee- und Eisschmelzprozessen insbesondere in datenarmen Gebirgsregionen erwiesen hat. Für die Vorhersage der saisonalen (d.h. 6-monatigen) Schneeschmelze wird ein auf saisonalen Szenarien basierender Ansatz verwendet. Dieser Ansatz ähnelt der ESP-Methode (Ensemble Streamflow Prediction) und verwendet die historische Meteorologie als Modelleingangsgröße. Dieser Ansatz für saisonale Szenarien ist ein Schritt in Richtung auf eine probabilistische Vorhersage der saisonalen Abflüsse im UIB. Die Methodik könnte noch weiter verbessert werden, indem eine Auswahl von Ensemble-Mitgliedern entsprechend den vorhergesagten saisonalen Anomalien bei Temperatur und Niederschlag ausgewählt wird.

Im UIB stammen mehr als 70 % des Abflusses aus der saisonalen Schnee- und Eisschmelze. Aufgrund der Auswirkungen des Klimawandels werden sich die hydrologischen Verhältnisse jedoch ändern. In diesem Zusammenhang ist es von entscheidender Bedeutung zu verstehen, wie der Klimawandel die zukünftige Wasserverfügbarkeit des UIB beeinflussen wird. Zu diesem Zweck wurde zunächst ein erweiterter Modellkalibrierungs- und -validierungsansatz angewandt, um zwei hydrologische Modelle für das UIB zu kalibrieren und zu validieren. Dieser erweiterte Modellkalibrierungs-/Validierungsansatz wurde gewählt, weil er die Qualität der Beobachtungsdaten berücksichtigt, kontrastierende Klimadaten für die Kalibrierung verwendet, den Vergleich der Abflüsse für mehrere Teileinzugsgebiete (d.h. Zwischenpegel) einschließt, eine multivariable Kalibrierung anhand von Variablen wie Evapotranspiration, Gletschermassenbilanz oder Schneedeckenfläche beinhaltet sowie beobachtete und simulierte Trends im Beobachtungszeitraum bewertet. Die kombinierten, langfristigen prognostizierten Änderungen des Abflusses aus beiden hydrologischen Modellen zeigen gegensätzliche Trends für zwei repräsentative Konzentrationspfade (RCPs: 2.6 und 8.5). Die größten Abflusserhöhungen werden für RCP8.5 projiziert. Die Methode der Varianzanalyse (ANOVA) wurde zur Quantifizierung der Unsicherheit der hydrologischen Modelle verwendet. Aus dieser Studie kann geschlossen werden, dass der Beitrag zur Unsicherheit durch die hydrologischen Modelle für Vorhersagen, die mit der erweiterten Kalibrierungsmethode simuliert wurden, geringer wird.

Temperaturindexmodelle werden häufig zur Bewertung der gegenwärtigen und zukünftigen Wasserverfügbarkeit aus der Schnee- und Gletscherschmelze in Einzugsgebieten mit begrenzter Datenverfügbarkeit verwendet. Diese Modelle verwenden Gradtagfaktoren (*DDF*) als Schlüsselparameter, um die Schmelzhöhe anhand der Lufttemperatur abzuschätzen. Der *DDF* wird im Allgemeinen als Parameter für die Modellkalibrierung behandelt. In der vorliegenden Untersuchung wurde jedoch eine Methode zur Schätzung des *DDF* aus den Komponenten der Energiebilanz der Schneedecke angewandt, die auf der Annahme beruht, dass das Schneepacket isotherm bei einer

Schneetemperatur von 0°C und im sogenannten "reifen" Zustand ist. Die aus den Energieflusskomponenten gewonnene Schmelzhöhe wird in *DDF* umgerechnet, indem sie durch die entsprechenden Gradtage geteilt wird. Ziel dieser Studie ist es, den *DDF* und seine Abhängigkeiten z.B. von Bewölkung, Schneealbedo und Jahreszeit besser zu verstehen. Die Abschätzung des *DDF* anhand von Energieflusskomponenten liefert einen physikalischen Hintergrund, der helfen kann, realistischere Werte für den *DDF* zu finden. In dieser Studie zeigt eine kurze Analyse über den Einfluss des Klimawandels auf den *DDF*, dass der *DDF* beim Vergleich von Perioden mit ähnlichen Gradtagen voraussichtlich abnehmen wird, da die Schneeschmelze früher im Jahr stattfindet und die Schneealbedo dann wahrscheinlich höher ist. Daher kann der *DDF* nicht als konstanter Parameter behandelt werden, insbesondere wenn Temperaturindexmodelle zur Vorhersage der gegenwärtigen oder zukünftigen Wasserverfügbarkeit verwendet werden.

Acknowledgements

First of all, I would like to thank my supervisor Prof. Dr.-Ing. Markus Disse for giving me this great opportunity and research environment to prepare and present my dissertation under his guidance at the Chair of Hydrology and River Basin Management at the Technical University of Munich. I would like to pay my special gratitude to my mentor Prof. Dr.-Ing. Wolfgang Bogacki who is always there to guide and encourage me throughout this time in my research. I would like to particularly mention that without his support and guidance, it would not have been possible to conduct this research.

Special thanks belongs to Prof. Dr. Lucas Menzel, for his support and becoming my third supervisor. I would like to thank Prof. Dr.-Ing Lothar Kirschbauer for providing his technical support for our snow and meteorological parameters measurement station. Furthermore, I want to thank Prof. Dr. Gabriele Chiogna for taking over the role as chairman for my Ph.D. defence.

I am deeply thankful to all the colleague's form the Department of Civil Engineering at the Hochschule Koblenz University of Applied Science for their help and support as well as sharing thought provoking ideas during my time here working as a research assistant. In particular, I owe my colleagues Oliver, Michael, William, Paul, Florian, Marcel, Gina, Martina, Kay, Johannes, Isabelle, Elisabeth, Claudia Reime, Claudia Meseck and Elke.

I want to gratefully acknowledge the Forschungszentrum der Hochschule Koblenz for financing the snow and meteorological parameters measurement station. I would like to thank Graduate Center of Hochschule Koblenz for providing the funding for my international research stays and for offering a versatile educational program during my Ph.D. I would like to further acknowledge the TUM Graduate School for offering great educational programs. I would to thank and appreciate all my co-authors including Bibi Naz, Michel Wortmann and Laura C. Bowling for their support and advice for climate impact assessment study. I am committed to thank Valentina Krysanova from Potsdam Institute for Climate Impact Research. She continuously supported me throughout the climate impact assessment study.

A special thanks belongs to all the friends who supported my research and project activities over the years. In particular, I want to thank Dr. Taimoor, Umar Farooq and Haris Mushtaq who helped me in the development of the snow and glacier situation monitoring tool. I would like to thank and acknowledge different data providers from Pakistan including Water and Power Development Authority, Indus River System Authority and Pakistan Meteorological Department. Furthermore, I

would like to say special thanks to National Engineering Services Pakistan for the study leave in order to complete my Ph.D.

Finally, I would like to thank my friends and family for all their encouragement and support. I am greatly indebted to my best friend Asif who supported me throughout my Ph.D. research.

My sincere thanks goes to my (late) mother and my father who are always supportive of my life long struggle. Without their advices and encouragement, I would never have reached the point where I am now. The same accounts for my brother Shakaib who is always there for me.

This Ph.D. thesis is the product of countless sleepless nights of work and a lot of stress, I owe my wife Yasmeen my deepest respect for all her moral support and encouragement. Even sacrificing her career and job for my Ph.D. You have always been there for me through every thick and thin and I am the luckiest person to have you and my sons Rouhaan and Affan in my life.

Research articles and author contributions

Presented research articles

The presented cumulative dissertation is based on three research articles. All of them are peer-reviewed and published in relevant international journals. The works of Ismail et al., (2018), Ismail et al., (2020) and Ismail et al., (2022) are the first author publications, which are required for this cumulative dissertation. Chapter 01, 02 and 06 are added to complete the storyline of this dissertation. All the articles are presented in Chapters 03 to 05.

Article 1

Ismail, M. F. and Bogacki, W.: Scenario approach for the seasonal forecast of Kharif flows from the Upper Indus Basin, Hydrol. Earth Syst. Sci., 22, 1391-1409, https://doi.org/10.5194/hess-22-1391-2018, 2018.

- 1 of 3 required first author publications (core publication)
- Chapter 03
- Author contributions: Muhammad Fraz Ismail and Wolfgang Bogacki conceived the research idea. Muhammad Fraz Ismail incorporated the glacier component in the snowmelt runoff model. Muhammad Fraz Ismail and Wolfgang Bogacki analysed the modelling results. Both authors reviewed the article. Muhammad Fraz Ismail prepared all the graphics presented in the article. Muhammad Fraz Ismail and Wolfgang Bogacki wrote the final version of the article.

Article 2

Ismail, M.F., Naz, B.S., Wortmann, M., Disse, M., Bowling, L.C., Bogacki, W.: Comparison of two model calibration approaches and their influence on future projections under climate change in the Upper Indus Basin. Climatic Change 163, 1227–1246 (2020). https://doi.org/10.1007/s10584-020-02902-3.

- 2 of 3 required first author publications (core publication)
- Chapter 04

- Author contributions: Muhammad Fraz Ismail and Bibi S. Naz conceived the research idea from Valentina Krysanova. Muhammad Fraz Ismail, Bibi S. Naz analysed the modelling results. Muhammad Fraz Ismail prepared and bias corrected the climate data. Bibi S. Naz, Michel Wortmann helped in glacier mass balance estimations. All authors reviewed the article. Muhammad Fraz Ismail prepared all the graphics presented in the article. Muhammad Fraz Ismail and Bibi. S. Naz wrote the final version of the article. Laura C. Bowlings, Markus Disse, Wolfgang Bogacki and Valentina Krysanova supervised this study.

Article 3

Ismail, M.F., Bogacki, W., Disse, M., Schaefer, M., Kirschbauer, L.: Estimating degree-day factors based on energy flux components, The Cryosphere Discuss. [preprint], https://doi.org/10.5194/tc-2022-64, in review, 2022.

- 3 of 3 required first author publications (core publication)
- Chapter 05
- Author contributions: Muhammad Fraz Ismail and Wolfgang Bogacki conceived the research idea. Muhammad Fraz Ismail and Wolfgang Bogacki analysed the modelling results. Lothar Kirschbauer and Michael Schaefer helped in collecting the field data. All authors reviewed the article. Muhammad Fraz Ismail prepared all the graphics presented in the article. Muhammad Fraz Ismail and Wolfgang Bogacki wrote the final version of the article. Markus Disse and Wolfgang Bogacki supervised this study.

Further scientific contributions

Oral presentations

- **Ismail, M. F.** and Bogacki, W. 2017: Schneemessstation Brunnenkopfhütte – Tag der forschung Hochschule Koblenz (Germany).
- **Ismail, M. F.** and Bogacki, W. 2018: Catchment delineation and snow/ice hydrology of Kabul River Basin (KRB) – Tag der ESRI Trier (Germany).
- **Ismail, M. F.,** Disse, M. and Bogacki, W. 2018: Trend of degree-day factors in response to the hydro-climatological and physiographic parameters – Ph.D. Seminar WS2017/2018 – Munich (Germany).
- **Ismail, M. F.,** Disse, M. and Bogacki, W. 2018: Trends of degree-day factors – A case study in the German Alps – Symposium on Management of Land and Water Resources – Tsuruoka (Japan).
- Bogacki, W. and **Ismail, M. F.** 2018: Verbesserung der Qualität saisonaler Schneeschmelze-Abflussvorhersagen durch eine auf Langzeitvorhersagen klimatischer Anomalien basierte Auswahl des Scenario Ensembles – Tag der forschung Hochschule Koblenz (Germany).
- Bogacki, W., **Ismail, M. F.** and Disse, M. 2018: Upper Chenab Snow- and Glacier Melt Runoff Modelling for Forecasting Seasonal Water Availability – SnowHydro Heidelberg (Germany).
- **Ismail, M. F.,** Disse, M. and Bogacki, W. 2019: Trends of degree-day factors and snowmelt runoff modelling for the Dreisäulerbach catchment – Ph.D. Seminar WS2018/2019 – Munich (Germany).
- Bogacki, W. and **Ismail, M. F.** 2020: Influence of input data sources on SRM seasonal snowmelt runoff prediction – SnowHydro conference Bolzano (Italy).
- **Ismail, M. F.,** Disse, M., Bogacki, W., Brandt, A. and Lopez, L. M. 2020: Trends of the degree-day factors in the mountainous regions – EGU General Assembly conference – online – Vienna (Austria).
- **Ismail, M. F.,** Naz. B.S., Wortmann, M., Bowlings L.C., Disse, M., and Bogacki, W. 2020: Comparison of two model calibration approaches and their influence on future projections under climate change in the Upper Indus Basin – Ph.D. Seminar SS2020 – Munich (Germany).

- **Ismail, M. F.,** Bogacki, W., Disse, M., Schäfer M., Kirschbauer, L., 2022: Estimating degree-day factors based on energy flux components (Grenoble (France) – Online – 3rd International Snowhydro conference 2022).

Posters

- **Ismail, M. F.,** Disse, M. and Bogacki, W. 2017: Diversified patterns of degree-day factors in response to the hydro-climatological and physiographic heterogeneity – Tag der Hydrologie Trier (Germany).
- **Ismail, M. F.,** Disse, M. and Bogacki, W. 2018: Trend of degree-day factors in response to the hydro-climatological and physiographic parameters – SnowHydro conference Heidelberg (Germany).
- **Ismail, M. F.,** Disse, M. and Bogacki, W. 2018: Trend of degree-day factors in response to the hydro-climatological and physiographic parameters – Doctoral candidate day – Munich (Germany).
- **Ismail, M. F.,** Disse, M., Bogacki, W. and Kopp, M. 2019: Snowmelt measurements and trends of Degree Day Factors (DDFs) in an Alpine catchment– Tag der Hydrologie Karlsruhe (Germany).
- **Ismail, M. F.,** Disse, M. and Bogacki, W. 2019: Snowmelt measurements and trend of degree-day factors (DDFs) in an alpine – Doctoral candidate day – Munich (Germany).
- **Ismail, M. F.,** Disse, M., Bogacki, W., Brandt, A. and Lopez, L. M. 2020: Evaluating the trends of degree-day factors in high-altitude regions – SnowHydro conference Bolzano (Italy).
- **Ismail, M. F.,** Bogacki and W. Disse, M. 2020: Methods for Bias correction to EWEMBI temperature for the Upper Indus Basin – ISIMIP workshop Paris (France).

Contents

List of Figures

List of Tables

Chapter 1

Introduction

Melt water from snow and ice dominated catchments is a unique and vital source of fresh water in many mountainous regions. Freshwater is stored during the snow accumulation season and later on as the snowmelt season progresses; this water becomes available for critical consumption in the summer season. Hence, accurate hydrological modelling of the physically based snow and ice melt runoff phenomenon is crucial for numerous basins across the globe and is an important topic in hydrological modelling research.

Numerous river basins of the South Asian region (e.g. Indus Basin) also rely heavily on snow and ice storage for consumptive water use, especially for use in agriculture and food production. The Himalayas-Karakoram-Hindukush (HKH) region for instance, also known as *the third-pole*, is amongst a very few regions outside of the two poles, that stores a huge bulk of fresh water in the form of snow and ice and thus, has become a climatic change hot spot as well (De Souza et al., 2015). This water is in-turn critical for water resources availability, water and food security for many countries within the region, including China, Pakistan, India, Bangladesh etc. Pakistan's water resources in particular are intricately linked to snow and ice storage in HKH region. Almost 90% of food production in Pakistan is being contributed by the waters come from the Indus Basin (Qureshi, 2011). The Indus River and its major tributaries originate from the HKH region feed on snow and ice melt accounting for 76% runoff within the Indus basin (Armstrong et al., 2019). Consequently, water economy of Pakistan is at risk due to recent and impending changes in climate within HKH region (Hasson, 2016).

The climate related challenges of Pakistan, especially linked to snow and ice storage in the HKH region, are complicated further by the transboundary nature of the Upper Indus Basin region (see Figure 1.1), which is a part of the HKH region. All major rivers of Pakistan (which are also part of Indus basin) are transboundary rivers and water sharing rights between Pakistan and India for these rivers is ascertained by the World Bank brokered Indus Water Treaty (IWT) of 1960. IWT gave Pakistan full consumptive use rights to the waters of Indus, Jhelum and Chenab rivers (i.e. western rivers), whereas full rights of Ravi, Sutlej and Beas rivers (i.e. eastern rivers) were given to India. This decision of IWT created critical water management challenges for Pakistan post 1960.

Freshwater originating from the Upper Indus region and routed via the eastern and western rivers are the primary water source for the Indus Basin Irrigation System (IBIS) (see Figure 1.2). Enaction of IWT post 1960 meant that significant portion of IBIS agriculture land in the Punjab province suddenly deprived of waters from the eastern rivers. This led to the construction of one of the major reservoirs in Pakistan i.e. Tarbela reservoir on the Indus River in which stored inflows are mostly derived from snow and ice melt (see Figure 1.1). Moreover, construction of a series of link canals were carried out, which helped in diverting waters from western rivers to eastern rivers (i.e. Ravi, Sutlej and Beas rivers) agricultural command areas. The main portion of water in western rivers is predominantly contributed by melting of seasonal snow and glacier cover (Lutz et al., 2014, 2016; Hasson et al., 2019). Hence, a complete understanding of snow storage and prediction of snowmelt-dominated runoff in the western river basins is critical for effective water management in Pakistan.

The Indus River System Authority (IRSA) of Pakistan not only regulates reservoir storages but also monitors snow storage of the western rivers. In order to adequately forecast seasonal stream flows to these rivers. Every year by the end of month of March different statistical as well as hydrological models are run by the authority in order to forecast the seasonal water availability for the forthcoming Kharif cropping season (i.e. 1st April – 30th September). IRSA then distributes the water among the provinces as per the Water Apportionment Accord (WAA) of 1991 (IUCAN, 2010). This water availability forecast is relevant because the provinces then use it for running their irrigated agriculture infrastructure and coping with the provincial water demand and supplies. Since, Pakistan is an agrarian economy, which is mainly dependent on irrigated agriculture, accurate seasonal water availability forecasts are critical for optimizing operational water supply within the Indus Basin Irrigation System (IBIS). This irrigation system is one of the largest contiguous irrigation network in the world (Bhatti et al., 2009) and since it has very limited reservoir storage, seasonal planning of IBIS operations is dependent on accurate prediction of snow storage and related runoff. The vast Indus River and its two western tributaries (i.e. Jhelum and Chenab) which mainly feed on the water contributed by the seasonal snow and ice melt, contribute a major share of water supply within IBIS.

Given IBIS's dependence on snow and glacial dominant runoff, it is imperative that research linked to Pakistan's water resources should focus on understanding and modelling snow and ice melt. The importance of this understanding has been emphasised in recent years due to numerous factors including (i) uncertainties linked with climate change (ii) declining per capita water availability in Pakistan and (iii) increasing inclination towards high delta crop production.

The sustainability of Pakistan's agro-economy and regional food security depends upon proper agriculture and water resources management (with snow and glacier being critical components of water resource availability). In addition, any change in these available fresh water resources through climate

variability, socio-economic factors or international policies will ultimately have a serious impact on food security and the environment in Pakistan (Tahir et al., 2011).

The impact of climate change on future water availability is also a key concern for water management in Pakistan. This discussion is not only limited to what will happen to these huge water towers (Viviroli et al., 2007) by the end of current century due to the influence of climate change but also it is focused on the short-term (i.e. 10-daily) as well as seasonal (e.g. Kharif cropping season) water availability. One major concern is seasonal shift in water availability due to changing climate. Because changing climate puts pressure on the available water resources as it alters the time and magnitude of water availability. It will also have significant impact on the state of the cryosphere in the mountainous regions (Vaughan et al., 2013). Because in these rugged complex mountainous regions minor changes in temperature highly effect the precipitation regime (e.g. snow or rain) and these changes will ultimately alter the future flow regimes from these mountainous areas (Viviroli et al., 2007; Beniston, 2003). A shorter duration of the seasonal snow cover and shrinking glacier area will change the runoff characteristics in the mountainous catchments as well as downstream of these mountainous regions (Hock, 2005; Huss et al., 2008; Huss, 2011). Hence, mountainous catchments are among the places where it is expected to observe the strongest climate-induced changes and the harshest effect on the fresh water resources.

Improvements in the water availability forecasts by utilizing latest innovative techniques and remote sensing data for this complex mountainous region will prove to be helpful for a better planning and management of water resources. One of the purpose of this research is to add value in the existing forecasting system of IRSA, because a reliable forecast of seasonal water availability will help in paving the way for better decision making.

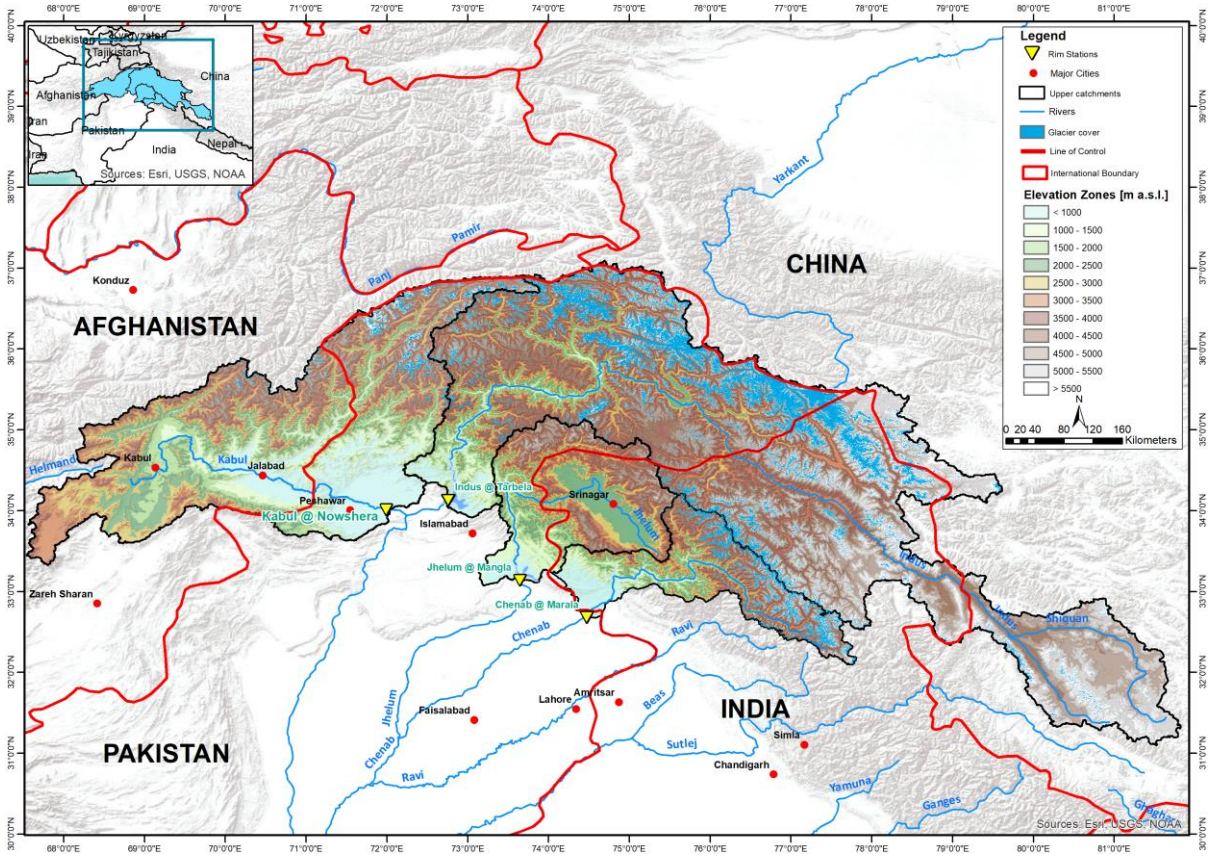

Figure 1.1 Upper Indus region covering all the four-rim stations (i.e. Tarbela, Mangla, Marala and Nowshera)

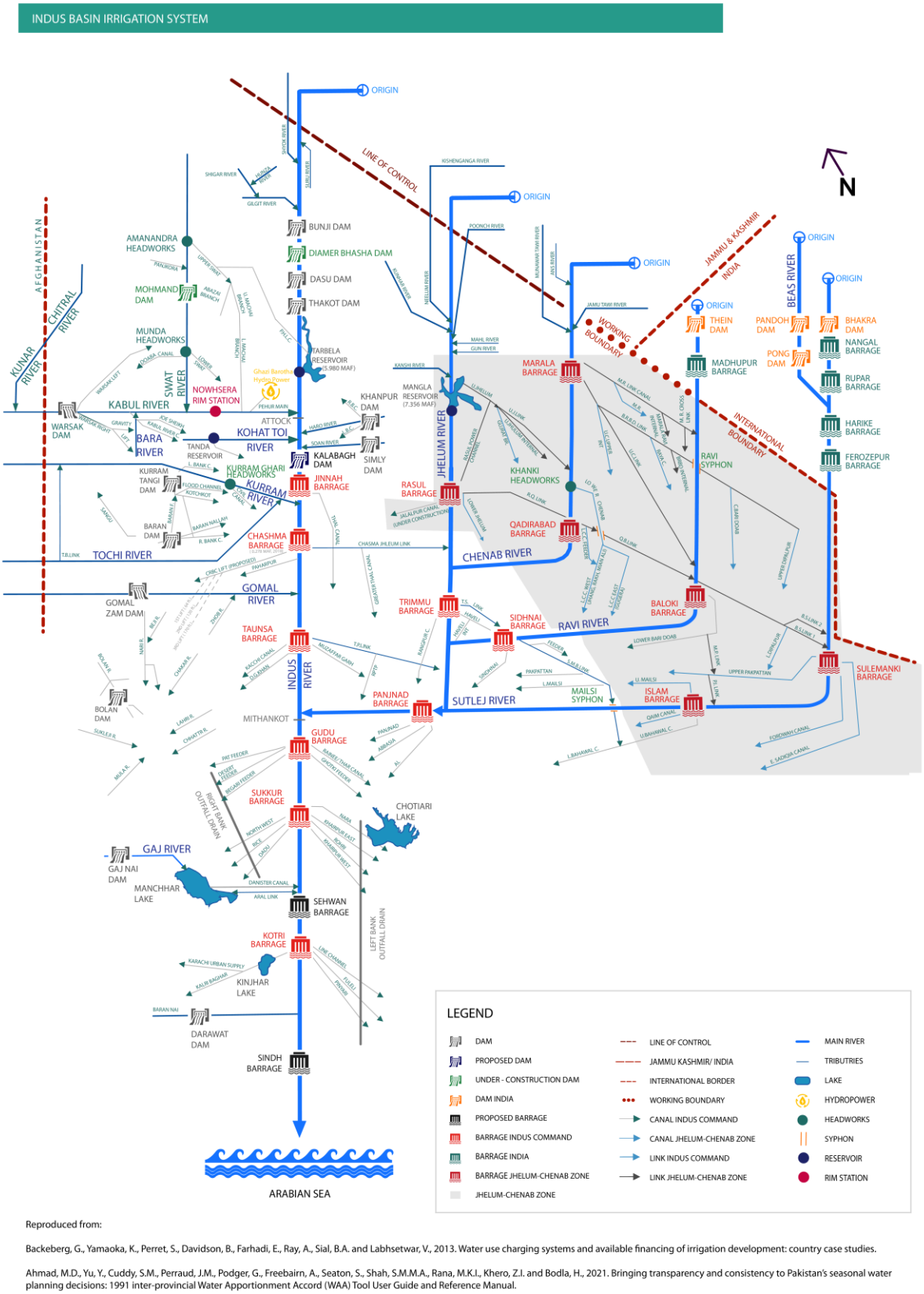

Reproduced from:

Backeberg, G., Yamaoka, K., Perret, S., Davidson, B., Farhadi, E., Ray, A., Sial, B.A. and Labhsetwar, V., 2013. Water use charging systems and available financing of irrigation development: country case studies.

Ahmad, M.D., Yu, Y., Cuddy, S.M., Perraud, J.M., Podger, G., Freebairn, A., Seaton, S., Shah, S.M.M.A., Rana, M.K.I., Khero, Z.I. and Bodla, H., 2021. Bringing transparency and consistency to Pakistan's seasonal water planning decisions: 1991 inter-provincial Water Apportionment Accord (WAA) Tool User Guide and Reference Manual.

Figure 1.2 Schematic diagram of the Indus Basin Irrigation System (IBIS) – prepared by Haris Mushtaq

1.1 Problem statement

Snow and ice are the significant components of the hydrological cycle. Water availability due to seasonal melting of snow and ice is a blessing for some regions but it can also have devastating effect in the form of sudden floods when snow rapidly melts in combination with rainfall. The downstream regions, which are depending upon seasonal snow and ice melt, are highly vulnerable with regard to the presence or absence of snow or ice in the upstream regions. Moreover, global climate change is a major cause that will modify seasonality of the runoff from mountainous catchments and thus lead to changing water availability. The consequences of reduced snowfall period and an increasing share of rainfall on precipitation may completely change the hydrology of a region and it may lead to water crisis. In this context, a reliable modelling and forecasting of snow and ice melt governed processes remains a challenge because of spatio-temporal heterogeneity of snow accumulation and melt in a complex rugged mountainous terrain.

Two types of modelling techniques are used in snow and ice melt runoff modelling. One is the energy balance and other is the temperature-index approach. The energy balance approach is very sophisticated when it comes to modelling the melt processes. Hydrological models using the energy balance approach have shown good accuracy in simulating the process-based phenomenon. However, at the same time this approach is more data intensive, which limits its use only for the data abundant catchments. On the other hand, temperature-index models are less data intensive but with good accuracy on catchment scale. Even though temperature-index models work well over longer time period but their accuracy decreases with increasing temporal resolution as well as there exist shortcomings in modelling spatial variability of melt rates, which may vary considerably in mountainous regions (Hock, 2003). Both approaches have their pros and cons. However, it is critical to keep in mind the limitations when applying these approaches for simulating snow or ice melt. For example, it could either be the data scarcity or heterogeneous topography of the mountainous region, which makes it difficult to use an approach that is unable to cope with these limitations. Though, this research is primarily carried out with hydrological models that uses the temperature-index approach for modelling snow and ice melt runoffs. As stated earlier, temperature-index approach is widely popular because of its only dependence on air temperature, which is commonly available and also a good indicator of melt depths.

The key parameter in the temperature-index models controlling the snowmelt, is the Degree-Day Factor (*DDF*). It transforms one degree-day T_{DD} (°C d) into the melt depths M (mm). The *DDF* is not a constant factor but it changes as the snowmelt season progresses (Rango and Martinec, 1995; Hock, 2003). In snowmelt runoff models, the *DDF* is generally obtained by treating it as a hydrological model parameter and calibrating it on observed hydrograph (Luo et al., 2013). However, because of the shortage of data measuring points in the mountainous catchments it is always a challenge to estimate the appropriate values of the *DDF* (He et al., 2014). This challenge gets more demanding when it comes to forecasting

the snow or glacial melt runoffs using these temperature-index models. Because in the forecasting stage, the variation of the *DDF* should be known in advance. Thus, it is critical to know all influencing factors including physical catchment characteristics (Bormann et al., 2014) affecting the *DDF* values so that related uncertainties can be minimized.

Another challenging aspect in the snow and ice melt modelling is the adoption of appropriate model parameterization (i.e. calibration and validation) especially when it comes to assessing the future water availability under climate change scenarios. It is challenging, because capturing the melt processes in a hydrological model is itself a complex task and if the model parameterization is incorrect then it will raise questions on the reliability of the outcome (i.e. simulated water availability). Hence, it is of utmost importance to use realistic model parameterization especially those parameters, which are associated to melt generation (i.e. snow or ice melt). Here in this research the parameter controlling the melt is the *DDF*. Consequently, if the *DDF* values either used in a hydrological model for assessing the future water availability under climate change scenarios or for forecasting the snow and glacier melt runoff are not realistic then it will result in a flawed outcome. Therefore, this dissertation is an effort to address these research challenges.

1.2 Main objectives

The main objective of this research work is to develop a framework for assessing the short and long-term water availability for snow and ice fed catchments. In order to achieve the objective this research work has been divided into three topics listed as follows.

1. Snow and ice melt runoff forecasting based on seasonal scenario approach
2. Future water availability under changing climate with improved hydrological modelling
3. Improved estimation of the degree-day factor for snowmelt prediction

The objective of the first topic is to propose a snow and ice melt runoff-forecasting approach for assessing the seasonal water availability for a cold region. This approach is like the well-established Ensemble Streamflow Prediction (ESP) (Day, 1985) approach and also take into account for the limitations in the absence of skilful meteorological predictions. The second topic focuses on assessing the impact of climate change scenarios on future water availability but following an enhanced hydrological model evaluation procedure so that the results obtained are more credible. The intention of the third topic is to propose a new and improved method for degree-day factor estimation based on energy flux components.

The main hypotheses, specific research questions as well as the expected outcome is presented in the following section.

1.3 Main hypotheses and research questions

The main hypothesis for each research topic as well as related research questions are given as follows.

Hypothesis 1

The forecast of seasonal snow and ice melt water availability from mountainous regions can be improved by implementing a scenario-based approach

Research questions

1.3.1 Seasonal snow and ice melt runoff modelling and forecasting

1. How to perform a simplified snow and ice melt runoff modelling and forecasting for an improved seasonal water availability information?
2. How to incorporate the ice melt component in the existing Snowmelt Runoff Model (SRM)?
3. How to tackle the degree-day factor variation using time dependency approach?

Expected outcome

- Snow and ice melt runoff modelling for the Upper Indus Basin
- Scenario based seasonal (i.e. 6-months) forecast approach
- Time dependent degree-day factor application

Hypothesis 2

A good calibration and validation procedure for a hydrological model will increase confidence of projected impacts under climate change

Research questions

1.3.2 Future water availability under climate change

1. How an enhanced calibration and validation approach works for a snow and ice melt dominated catchment?
2. What are the climate change impacts on future water availability in the Upper Indus Basin?
3. What are the contributions of different sources of uncertainty while accessing the impacts of climate change?

Expected outcome

- Credible results by using enhanced multi-model calibration and validation approach
- Future water availability under climate change scenarios for the snow and ice fed Upper Indus Basin
- Uncertainty quantification for the different sources of uncertainty

Hypothesis 3

Estimation of the degree-day factors can be improved by assessing the melt generated through different energy flux components

Research questions

1.3.3 Degree-day factor estimation

1. How degree-day factor can be estimated using the minimum available information for a data scare region?
2. How degree-day factor can be separated into different energy flux components and what are the dependencies?
3. How degree-day factors will change under the influence of climate change scenarios?

Expected outcome

- Development of a degree-day factor estimation approach using minimum available information
- Validation of the degree-day factors estimated through energy flux components with field observations (i.e. using data from snow measurement station)
- Estimation of the degree-day factors for the future climate changes

An overview of the three research topics including specific research questions is presented in Figure 1.3. These research questions are addressed in a series of publications (i.e. Chapters 3 – 5).

Figure 1.3 Framework of this cumulative dissertation

1.4 Dissertation outline

This dissertation comprises of three research articles with relevant literature reviews and structured into six chapters. To summarise, this section gives an overview of the conducted research.

- *Chapter 1* provides an introduction of this dissertation
- *Chapter 2* provides an overview of the study area, models and methods
- *Chapter 3* presents scenario based seasonal snowmelt runoff modelling and forecasting
- *Chapter 4* sheds light on different multi-model calibration/validation techniques and future water availability under the influence of climate change
- *Chapter 5* explains the degree-day factors estimation based on energy flux components
- *Chapter 6* draws the overall conclusions and outlook for the future work

More specifically,

Chapters 1: provides an introduction including problem statement, research objectives, and thesis framework/outline.

Chapters 2: provides an overview of the selected study areas, introduction of snowmelt runoff modelling techniques, snow and glacier melt runoff model and generalized methodology of this dissertation.

Chapter 3: presents the first work package, which focuses the scenario based approach for forecasting the snow and glacier melt runoff on seasonal basis for the Upper Indus Basin. It presents the available data in the study area, hydrological model used, calibration and validation methods as well as evaluation of model forecasting skills.

Chapter 4: presents the second work package, which focuses on the Comparison of two model calibration approaches and their influence on future projections under climate change in the Upper Indus Basin. It presents two different calibration/validation techniques for the hydrological models, applies climate change scenario for assessing future water availability from the snow and glacier fed catchment and assess the uncertainty contributions from different sources of uncertainty.

Chapter 5: presents the final work package, which focuses on the estimation of the degree-day factors based on energy flux components. It discusses the dependencies as well as future course of degree-day factor development under the influence of climate change. It also presents the field measurements carried out for acquiring snow data in the German Alps.

Chapter 6: presents the overall summarized conclusions, addressing the research questions and presenting outlook for further research.

Chapter 2

Study areas, models and methods

2.1 Study Areas

This research focuses on two study areas. One is in the Hindukush-Himalaya-Karakoram (HKH) region namely the Upper Indus Basin (UIB). In the UIB, hydrological modelling, seasonal forecasting as well as the future water availability assessment has been done. Another research site is in the Ammergau Alps (i.e. Dreisäulerbach catchment). In this catchment, a snow measurement station in conjunction with standard meteorological station has been installed for studying the snowmelt dynamics.

2.1.1 Upper Indus Basin

The upper catchments of the Indus river basin (see Figure 2.1) primarily feed Tarbela reservoir of Pakistan. The Upper Indus Basin (UIB) has an area of ≈173,345 km^2 out of which approximately 11.5% is covered by perennial glacial ice (Tahir et al., 2011). At the end of most winters, nearly the entire UIB above 2200 m a.s.l. is covered with snow, resulting in that more than 60% snowmelt contribution in annual flows in the Upper Indus River (Bookhagen and Burbank, 2010). Seasonal melting of snow contributes to the bulk of the flow of the Upper Indus streams from the month of May – July. Indus River starts rising gradually in the month of March and reaching its maximum in July, while peak flood events usually occur during monsoon season in July – September. By the end of July, when the flows reduce due to diminished snow cover in the lower catchment, the high altitude glaciered basins become important contributors to the flows due to first melting of seasonal snow cover and then melting of the glacier ice. Glacial melt dominates the flows of the largest tributaries of Indus River, i.e. Gilgit, Hunza, Shigar and Shyok rivers (Tahir et al., 2011, 2016).

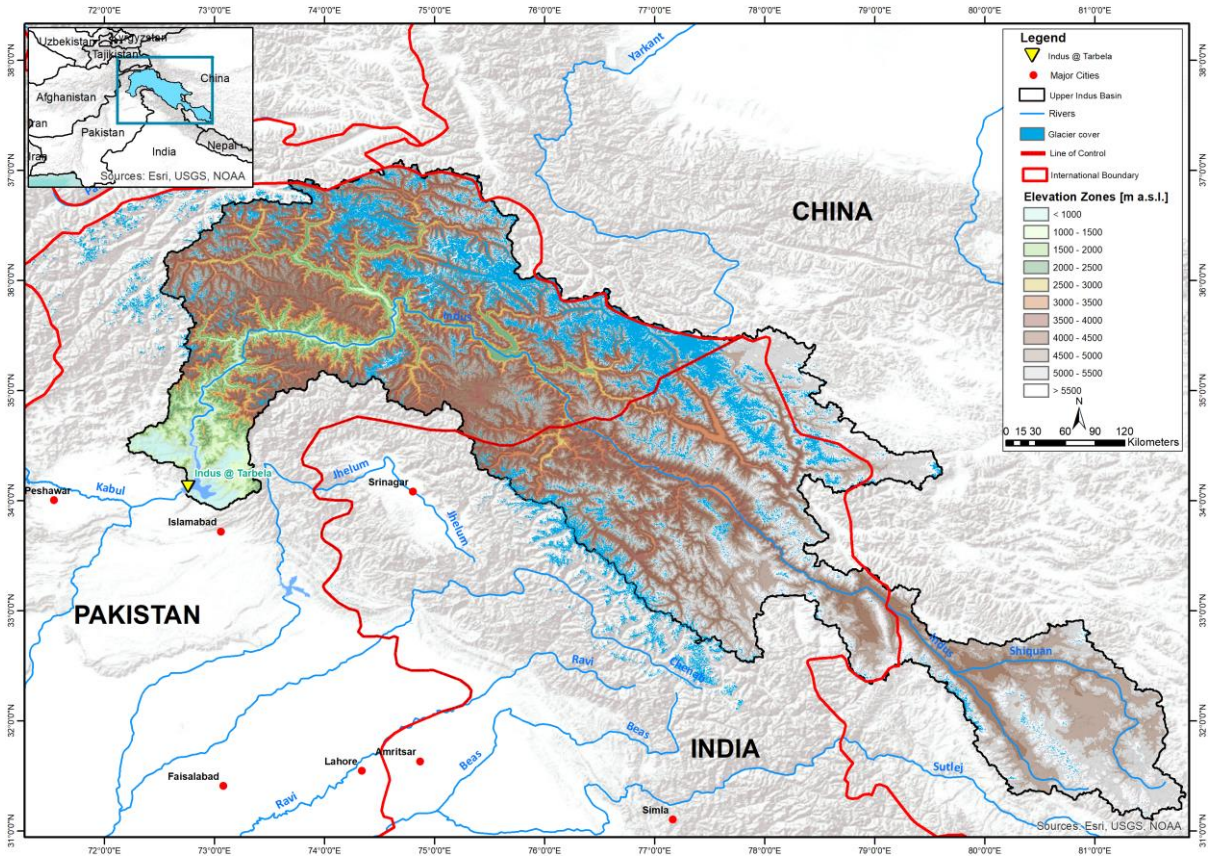

Figure 2.1 Upper Indus Basin at Tarbela spread over three countries (i.e. Pakistan, India and China)

2.1.2 Dreisäulerbach catchment

The Dreisäulerbach catchment is a part of Isar river system lies in the sub-alpine region of Bavaria in the Ammergauer Alps and it is approximately located between latitudes 47°34'55"– 47°35'05" North and longitudes 10°56'40"–10°57'07" East. It covers an area of ~2.3 km^2 and has a mean hypsometric elevation of just over 1200 m a.s.l. The elevation ranges from 950 m a.s.l. at Linderhof gauging station up to 1768 m a.s.l. The snow measurement station at Brunnenkopfhütte is located at an elevation of 1602 m a.s.l. (Figure 2.2).

The area in the Dreisäulerbach catchment mostly consists of south facing slopes, but also contains northern slopes in southern parts of the catchment (Kopp et al., 2019). The catchment is densely forested which during the winter season is fully covered with snow. The mean annual temperature in the observation period (i.e. November 2016 – May 2021) is about 5.8 °C and the long-term annual precipitation at the Ettal-Linderhof station of the Water Science Service Bavaria is reported to be 1676 mm (Kopp et al., 2019).

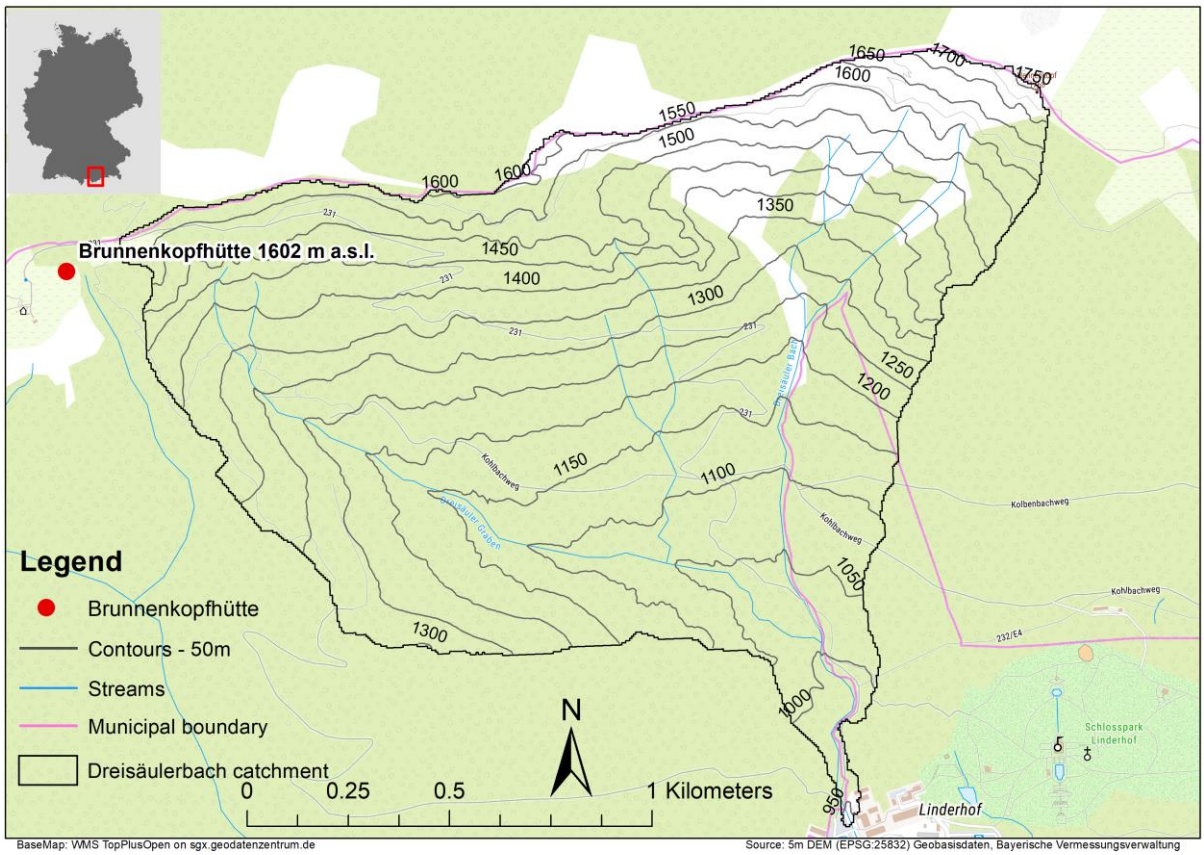

Figure 2.2 Dreisäulerbach catchment and location of Brunnenkopfhütte station in the German Alps

2.2 Snowmelt modelling approach

This section provides an overview of the snowmelt modelling approaches as well as an introduction to the Snowmelt Runoff Model (SRM). There are two basic approaches to model the snowmelt runoff process. These approaches are mentioned as follows.

1. Energy balance approach
2. Temperature-Index approach

2.2.1 Energy balance approach

Energy balance models attempt to quantify melt as residual of energy balance equation (Hock, 2003). Since the conversion from ice to water requires the input of energy, the process of snowmelt is intricately linked to the flow and storage of energy into and through the snowpack. The governing energy budget equation (USACE, 1998) that describes the energy available for snowmelt can be written as follows. These energy fluxes are usually measured as energy per time per unit area of snow.

$$Q_m = Q_{sn} + Q_{ln} + Q_c + Q_e + Q_g + Q_p - \Delta Q_i \quad (2.1)$$

where

Q_m = total energy available for snowmelt per area unit
Q_{sn} = net shortwave radiation
Q_{ln} = net longwave radiation
Q_c = convective heat flux
Q_e = latent heat flux
Q_g = conduction of heat from the ground
Q_p = heat content of precipitation
ΔQ_i = rate of change internal energy content of the snowpack

In general, the minimum data requirements for the application of energy budget equation are air temperature, incoming solar radiations, vapour pressure and wind speed. However, there is usually a limited availability of these datasets in high altitude areas. Moreover, it is also difficult to spatially extrapolate this data from point measurements to mean areal values in a topologically complex and rugged terrain. Hence, most of the applications based on this modelling approach are restricted to only a point or a small catchment (Leavesley, 1989). However, there also exist another point of view in literature regarding the process-based snowmelt modelling especially in context of input data requirements. In the absence of ground observations, the process-based snowmelt modelling input data requirements can be reduced to only air temperatures as required by the temperature-index models (Walter et al., 2005).

2.2.2 Temperature-Index or degree-day approach

The temperature-index or degree-day approach utilizes air temperature as an index to snowmelt. Air temperature is assumed as a predominant variable in the energy budget equations and it is physically connected with many of the energy exchanges involved in the snowmelt process (Chinarro, 2014). Degree-day models are used due to several reasons like wide availability of air temperature data, easy interpolation, forecasting possibilities, good model performance and computational simplicity (Hock, 2003). Although, the degree-day model does not include all fluxes contributing to snowmelt, it is almost as efficient like the energy balance model (Debele et al., 2010). The general equation of classical degree-day approach is given as under:

$$M = DDF_{snow,ice}\,(T) \tag{2.2}$$

Where $T > T_T$

Where, M is the snow or ice melt (mm), T is the mean daily air temperature for a day (˚C d) and T_T is a threshold temperature above which melt is assumed to occur (e.g. = 0 ˚C) (Rango and Martinec, 1995).

The outcome of the degree-day approach (i.e. snowmelt) can be improved by including net radiation, vapour pressure and wind speed rather than using only air temperatures (Zuzel and Cox, 1975). However, increasing input variables in the degree-day equation will lead to gradual transition from classical degree-day approach to physically based expression. One widely known example is a combination method (Anderson, 1973), where a simple degree-day approach is used for the dry periods and simplified energy balance formulations for the rainy period (Hock, 2003). In order to improve the classical degree-day approach radiation term is introduced in the general melt equation of the degree-day model (Martinec and de Quervain, 1975; Hock, 1999) The modified formulation is expressed as follows.

$$M = \left(f_m + R_f I_{pot}\right) T \tag{2.3}$$

Where, M is the melt rate (mm h^{-1}), T is hourly mean air temperature (°C) and I_{pot} is potential clear-sky direct solar radiation (Wm^{-2}). f_m and R_f are two empirical coefficients, respectively the melt factor and radiation factor, which are expressed in mm h^{-1} °C^{-1} and m^2 mm W^{-1} h^{-1} °C^{-1}.

Furthermore, there also exist an enhanced temperature-index approach where the melt relationship is updated by incorporating not only the modelled shortwave radiation data but also snow albedo properties (Pellicciotti et al., 2005) . The proposed equation for the enhanced temperature-index model is given as under:

$$M = \mathrm{TF}\ (\mathrm{T}) + \mathrm{SRF}(1 - \alpha)\mathrm{G} \tag{2.4}$$

Where, α is albedo and G is incoming shortwave radiation (W m^{-2}). TF and SRF are two empirical coefficients, respectively the degree-day factor (*DDF*) and shortwave radiation factor, expressed in mm h^{-1} $^{\circ}C^{-1}$ and mm h^{-1} W^{-1} m^2. T_T is threshold temperature and assumed to be equal to 0 $^{\circ}$C. There is one other assumption that when the temperature is below T_T no melt occurs. Incorporating albedo and shortwave radiation in the enhanced temperature-index approach can calculate the changes in melt rate associated with snow metamorphism and with the transition from snow to ice.

Although above mentioned enhancements in the original degree-day approach are important but the classical degree-day approach due to its only dependence on air temperature is still widely applicable in the large basins even for operational purposes (Schaper et al., 1999; Hock, 1999, 2003; Pellicciotti et al., 2005; Martinec et al., 2008; Schaper and Seidel, 2000).

2.2.3 Snowmelt Runoff Model (SRM)

One of the most commonly used temperature-index model is the Snowmelt Runoff Model (SRM) which was developed in 1973 at the Federal Institute for Snow and Avalanche Research in Davos, Switzerland

(Martinec, 1975). SRM was designed for remotely sensed Snow Cover Area (SCA) input and is used in number of countries around the globe. SRM has been applied to more than 100 watersheds ranging from 0.3 to 917444 km^2 and an elevation range from 0 to 8840 m a.s.l. (Martinec et al., 2008). SRM uses percentage areal snow cover, air temperature, and precipitation as daily input variables. The watershed is divided into elevation zones and accounts for the degree-days in each elevation zone to drive the amount of snowmelt. Specific basin characteristics include runoff coefficients, degree-day factors, and recession coefficients. The main strength of SRM is its reliance on the snow cover area, which can be derived today from readily available remote sensing snow products, e.g. MODIS Snow Products. Another advantage of using SRM is that there are quite large number of river catchments in the Himalayas where it has already been applied. Experiences from these catchments provide a good basis for the comparison of model parameters and results.

The governing equation of SRM is given below:

$$Q_{n+1} = \sum_{i=1}^{m} \left\{ \left[M_{n,i} + R_{n,i} \right] . \frac{10000}{86400} A_i \right\} . (1 - k_{n+1}) + Q_n k_{n+1} \tag{2.5}$$

where Q is the average daily discharge (m^3 s^{-1}), M and R are the daily runoff depths originating from snowmelt and rainfall (cm d^{-1}), A is the total area of the elevation zone (km^2), k is the recession coefficient (–), n is the index of the simulation day, and i and m are the indices and total number of elevation zones, respectively. Daily runoff from snowmelt and rainfall is calculated by eq. (2.6) and eq. (2.7):

$$M_{n,i} = c_{Sn,i} . a_{Sn,i} . T_{n,i} . S_{n,i} \tag{2.6}$$

$$R_{n,i} = c_{Rn,i} . P_{n,i} \tag{2.7}$$

where c_S and c_R are the runoff coefficients (–) for snowmelt and rain, respectively, a_S is the degree-day factor for snow (cm °C^{-1} d^{-1}), T the degree-days (°C d) for each elevation zone, S the ratio of the snow covered area to the total area (–), and P is the daily precipitation (cm d^{-1}).

2.2.4 Snowmelt Runoff Model (SRM) + Glaciers (G)

The original SRM approach has been enhanced by considering a separate glacier melt contribution (Schaper et al., 1999). This enhancement in the model considers in addition to the variables used by SRM, the area covered by exposed glaciers (i.e. not snow covered). An additional melt component is added to eq. (2.5) that takes into account the specific degree-day factors for glaciers according to eq. (2.8):

$$G_{n,i} = c_{Gn,i}.a_{Gn,i}.T_{n,i}.S_{Gn,i} \quad (2.8)$$

where G is the daily melt (cm d^{-1}) from exposed glaciers in each elevation zone, c_G is the runoff coefficient (–), a_G is the degree-day factor (cm $°C^{-1}$ d^{-1}) for glaciers, and S_G is the ratio of the exposed glacier area to the total area (–). This model was found to be highly accurate even in basins with 67% glacier area. The three alpine basins where this model was initially tested were Rhine-Felsberg, Rhône-Sion, and Ticino-Bellinzona in Switzerland (Schaper and Seidel, 2000). Apart from the improvement in the runoff modelling, the independent computation of glacier melt is an important step towards evaluations of glacier behaviour with regard to climate change.

2.3 Methodology

The primary focus of this research is water availability in a data limited mountainous region. A prime example of such a region is the Himalayas-Karakoram-Hindukush (HKH). This complex mountainous region has also become a climate change hotspot and with such drastic climatic changes, the flow regime is bound to alter which would ultimately cause a seasonal shift in the water availability and thus effect the irrigated agriculture and agro-economy of this region. The research topic has been further divided into three major sub-topics, in order to understand what will be the water availability from these data scarce region under future climate change projections.

In order to evaluate the current situation regarding the water availability in near future, snow and ice melt runoff forecasting will be carried out. Then the assessment of future water availability under climate change scenarios will be performed after following an enhanced hydrological model evaluation criterion specifically designed for climate change impact assessment studies so that the outcome (i.e. future water availability) would be more credible and less uncertain. Finally, in order to address the data scarcity problem in context of snowmelt modelling, analysis of the most critical parameter of a degree-day model i.e. degree-day factor will carried out with the intention that using realistic values of this critical parameter would ultimately enhance confidence in the simulated runoff.

The proposed research methodology and the research workflow is given in Figure 2.3. As stated earlier, the research work is planned in three different phases (i.e. three major topics) as shown in the following work flow diagram.

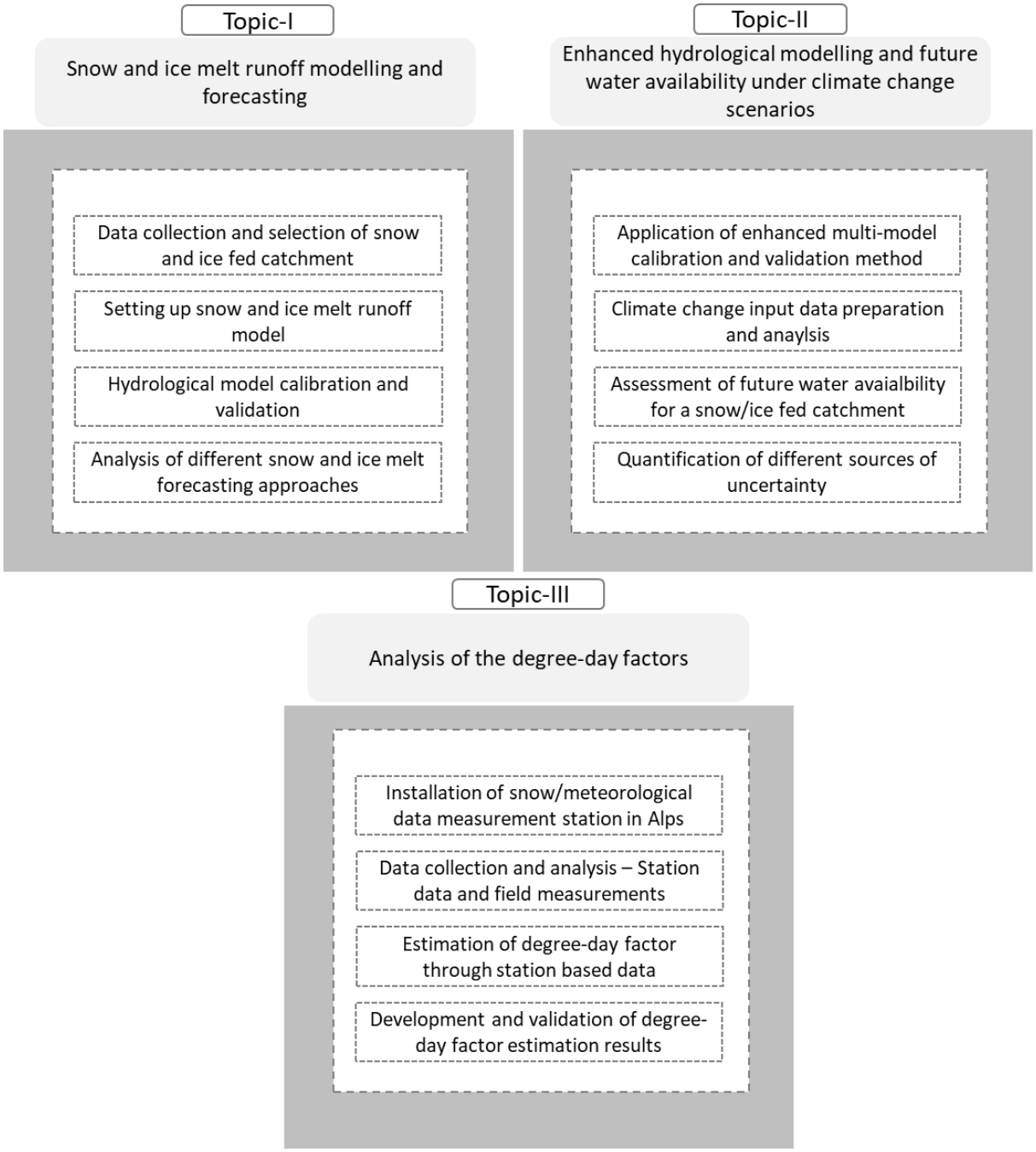

Figure 2.3 Proposed research topics and related work flow

Following section gives a brief overview of the overall methodology adopted in this research project.

2.3.1 Snow and glacier melt runoff modelling and forecasting

Flow forecasting is challenging, when it comes to complex rugged mountainous catchments where observed data availability is limited that leads to uncertainties in predicting input variables for the forecasting period. Although some limitations can be handled by applying state of the art remote sensing techniques (e.g. application of satellite based remote sensing datasets). In context of this specific

research project, which aims to forecast seasonal water availability, a simplified scenario approach is adopted. This scenario approach considers the weather situation of different years and results in an ensemble of possible flows that can be statistically evaluated to arrive at different levels of prediction. For example, “most likely” (median) flows as well as the probability levels of “dry” and “wet” years can be defined. The scenario based approach is adopted because of unavailability of reliable meteorological forecasts of temperature and precipitation for a lead-time of 6-months. For seasonal weather prediction, today’s climate models can provide a rough indication of “warmer” or “cooler” respectively “drier” or “wetter” compared to the average conditions, but no sufficient forecasts for detailed flow modelling. The main working steps are summarized as follows.

1. Data collection and evaluation for the selected mountainous catchment
2. Setting up a degree-day snow and ice melt runoff model
3. Calibration and validation of simulated snow and ice melt runoffs
4. Application and analysis of seasonal scenario based forecasting approach
5. Analysis of time-dependent degree-day factor approach

2.3.2 Enhanced hydrological modelling and future water availability under climate change scenarios

This topic aims at assessing the future water availability in a snow and glacier dominated catchment under changing climate. The pre-requisite is a good calibration/evaluation procedure for the hydrological model especially judging model applicability for climate impact studies. The main hypothesis is that a good performance of a hydrological model in the historical period increases confidence of projected impacts under climate change and decreases the portion of uncertainty in projections related to hydrological models.

In order to complete this work package, a five-step model evaluation criterion (Krysanova et al., 2018) has been applied. This five-step model evaluation is a helpful tool in order to have more credible model outcome. These five steps are listed as follows.

1. Evaluate the quality of observational data and take into account the related uncertainty.
2. Apply contrasting climate data for model calibration.
3. Validate the model performance for multiple sub-catchments (i.e. intermediate gauges).
4. Perform multi-variable calibration for variables like evapotranspiration, glacier mass balance or snow cover area in order to ensure internal consistency of the simulated processes.
5. Evaluate observed and simulated trends in the observational period.

2.3.3 Analysis of the degree-day factors

The main objective of this work package is to develop better understanding about the degree-day factor (*DDF*) and its dependencies.

There are two ways by which the *DDF* can be obtained.

i. By measuring the daily snowmelt and degree-days, which required field observations (i.e. snow and meteorological variables measurement station).
ii. By treating it as a calibration parameter and calibrating it on flows in a degree-day model

In order to estimate the *DDF* through field observations a snow measurement station in conjunction with a standard meteorological station has been installed in the Dreisäulerbach catchment at an elevation of 1602 m a.s.l. near Brunnenkopfhütte (see Figure 2.4, Appendix-A). This station is functioning since November 2016, and data is available with a temporal resolution of 10-minutes.

The objective of installing a snow measurement station is to provide necessary information for estimating the *DDF*. As mentioned earlier, knowing the variation of the *DDF* in advance is crucial in seasonal flow forecasting as well as assessing the future water availability. The goal of this part of the research project is to develop a simple *DDF* estimation method based on energy flux components while assuming that the snowpack is in fully ripe state (i.e. isothermal at 0 °C).

The major working steps for this research topic are summarized as follows.

1. Installation of snow and meteorological station in the German Alps for data collection
2. Estimation of degree-day factors based on observed data and energy flux formulations
3. Comparison of observed vs estimated degree-day factors
4. Analysis of degree-day factors dependencies
5. Estimation of degree-day factor for changing climate

Figure 2.4 Location of automatic weather and snow measurement station at Brunnenkopfhütte [1602 m a.s.l.] in German Alps

Chapter 3

Scenario approach for the seasonal forecast of Kharif flows from the Upper Indus Basin

Muhammad Fraz Ismail and Wolfgang Bogacki (2018)[1]

Abstract

Snow and glacial melt runoff are the major sources of water contribution from the high mountainous terrain of the Indus River upstream of the Tarbela reservoir. A reliable forecast of seasonal water availability for the Kharif cropping season (April – September) can pave the way towards better water management and a subsequent boost in the agro-economy of Pakistan. The use of degree-day models in conjunction with satellite-based remote-sensing data for the forecasting of seasonal snow and ice melt runoff has proved to be a suitable approach for data-scarce regions. In the present research, the Snowmelt Runoff Model (SRM) has not only been enhanced by incorporating the "glacier (G)" component but also applied for the forecast of seasonal water availability from the Upper Indus Basin (UIB). Excel based SRM+G takes account of separate degree-day factors for snow and glacier melt processes. All-year simulation runs with SRM+G for the period 2003 – 2014 result in an average flow component distribution of 53, 21, and 26% for snow, glacier, and rain, respectively. The UIB has been divided into Upper and Lower parts because of the different climatic conditions in the Tibetan Plateau. The scenario approach for seasonal forecasting, which like the Ensemble Streamflow Prediction method uses historic meteorology as model forcings, has proven to be adequate for long-term water availability forecasts. The accuracy of the forecast with a mean absolute percentage error (MAPE) of 9.5% could be slightly improved compared to two existing operational forecasts for the UIB, and the bias could be reduced to -2.0 %. However, the association between forecasts and observations as well as the skill in

[1] **Ismail, M. F.** and Bogacki, W.: Scenario approach for the seasonal forecast of Kharif flows from the Upper Indus Basin, Hydrol. Earth Syst. Sci., 22, 1391-1409, https://doi.org/10.5194/hess-22-1391-2018, 2018.

predicting extreme conditions is rather weak for all three models, which motivates further research on the selection of a subset of ensemble members according to forecasted seasonal anomalies.

3.1 Introduction

Mountains are the water towers of the world. They are the biggest resource of freshwater to half of the world's population fulfilling their needs for irrigation, industry, domestic and hydropower applications (Viviroli et al., 2007). The Indus River on which Pakistan's socio-economic development depends, can be termed as the bread basket of Pakistan (Clarke, 2015). Due to an agrarian economy, Pakistan's agriculture share in water usage is about 97%, which is well above the global average of about 70% (Akram, 2009). In Pakistan, the Indus River System Authority (IRSA) decides the provincial water shares according to the Water Apportionment Accord (WAA) of 1991 and provincial irrigation departments subsequently determine the seasonal water allocation to the different canal command areas depending upon the water availability forecast carried out at the end of March for the forthcoming Kharif cropping season (April–September). A reliable seasonal forecast of the water availability from snow and glacial melt is therefore of utmost importance for agricultural production and efficient water management.

On the other hand, snowmelt runoff modelling in mountainous regions faces the challenge of data scarcity as well as the uncertainty in parameter calibration (Pellicciotti et al., 2012). The need of the hour is to not only develop such a hydrological model which has the capability to cater for both snow and glacial melt components but also a reliable forecast technique which could help water managers and policy makers to enhance water resources management in the future.

The present paper focuses on the implementation of the Snowmelt Runoff Model (SRM) including the glacier melt component (+G) based on the methodology proposed by (Schaper et al., 1999), which is an important value addition to the existing ExcelSRM version (Bogacki and Hashmi, 2013) of the WinSRM (Martinec et al., 2008) model. In the earlier studies on the Upper Indus Basin (UIB) and its sub-catchments, e.g. (Immerzeel et al., 2010a), (Tahir et al., 2011), (Butt and Bilal, 2011), and (Adnan et al., 2017), they have only used the SRM standard version, while glaciers are dealt with by taking them as a part of the snow covered area. The underestimation of flows in periods associated with the glacier melt contribution, as pointed out by (Tahir et al., 2011), has now been dealt with by incorporation of a glacier melt component. A unique methodology has been adopted to deal with the early fading of snow cover area from the Tibetan Plateau by separating the whole UIB into two sub-catchments, which is not implemented in the original WinSRM model.

Ensemble Streamflow Prediction (ESP), developed at the U.S. National Weather Service (Day, 1985), is widely used to generate probabilistic long-term stream-flow forecasts. As already successfully

applied in the Upper Jhelum basin (Bogacki and Ismail, 2016), a scenario approach is used for seasonal flow forecasting in the UIB, which has much similarity to ESP. It also uses historical meteorology as model forcings; however, like the other operational forecast models for UIB, it is mainly focussed on a deterministic forecast of total Kharif inflow to the Tarbela reservoir.

3.2 Materials and methods

3.2.1 Study area

The upper catchments of the Indus River basin (Figure 3.1) primarily feed the Tarbela reservoir, which is the larger of the only two major reservoirs in Pakistan. The UIB has an area of about 173345 km^2, of which approx. 11.5% is covered by perennial glacial ice (Tahir et al., 2011). At the end of most winters, nearly the entire UIB above 2200m a.s.l. is covered with snow, resulting in more than 60% of annual flow in the Upper Indus River to originate from snowmelt (Bookhagen and Burbank, 2010). The distribution of monthly inflows into the Tarbela reservoir (see Figure 3.2) shows that these flows tend to rise progressively as melting temperatures advance into areas of higher snowpack at the higher elevations. The Indus River starts rising gradually in March reaching its maximum in July, while peak flood events usually occur during the monsoon season during July–September. By the end of July, the flows reduce due to the diminished snow cover in the lower catchment and glacier melt becomes an important flow component in the late summer months. This is due to the first melting of their seasonal snow cover and, when the snow has vanished, melting of the glacier ice. According to (Tahir et al., 2011), glacial melt dominates the flows of the largest tributaries of the Indus River, i.e. the Chitral, Gilgit, Hunza, Braldu, and Shyok rivers.

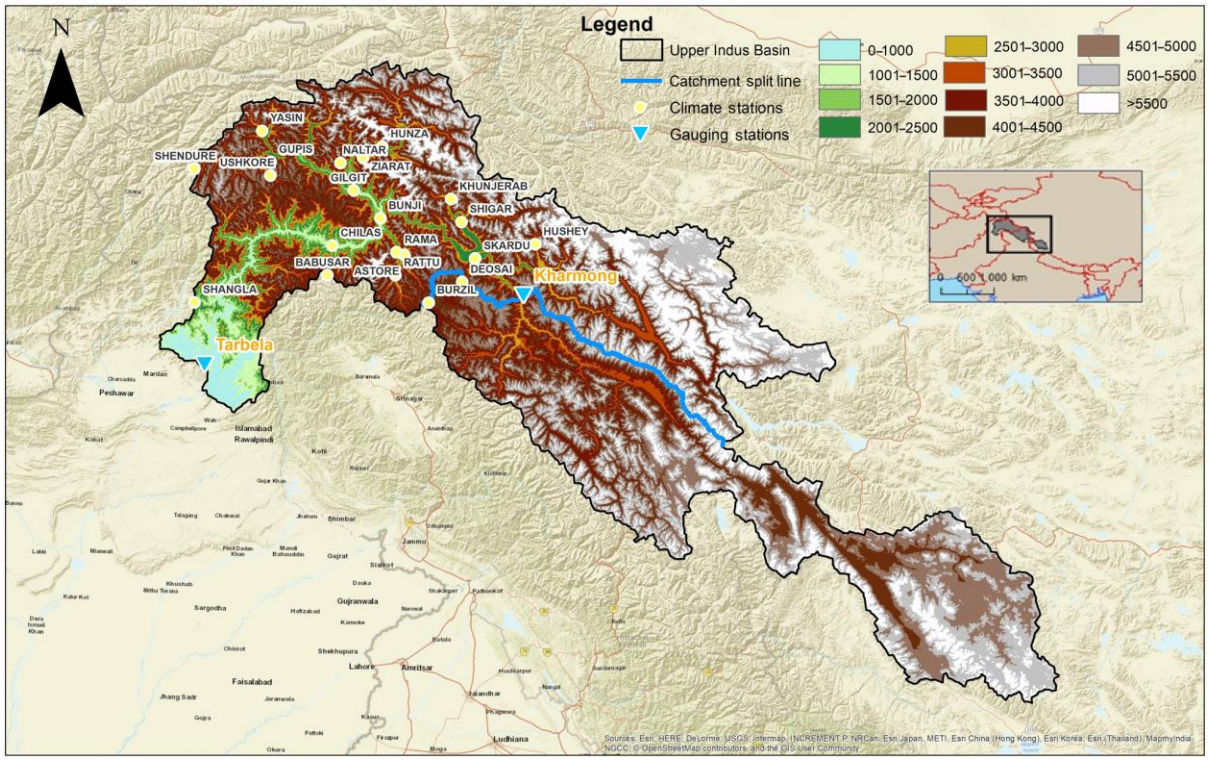

Figure 3.1 Map of the Upper Indus Basin (UIB) showing different elevations and splitting of the UIB at the Kharmong gauging station into Upper and Lower UIB.

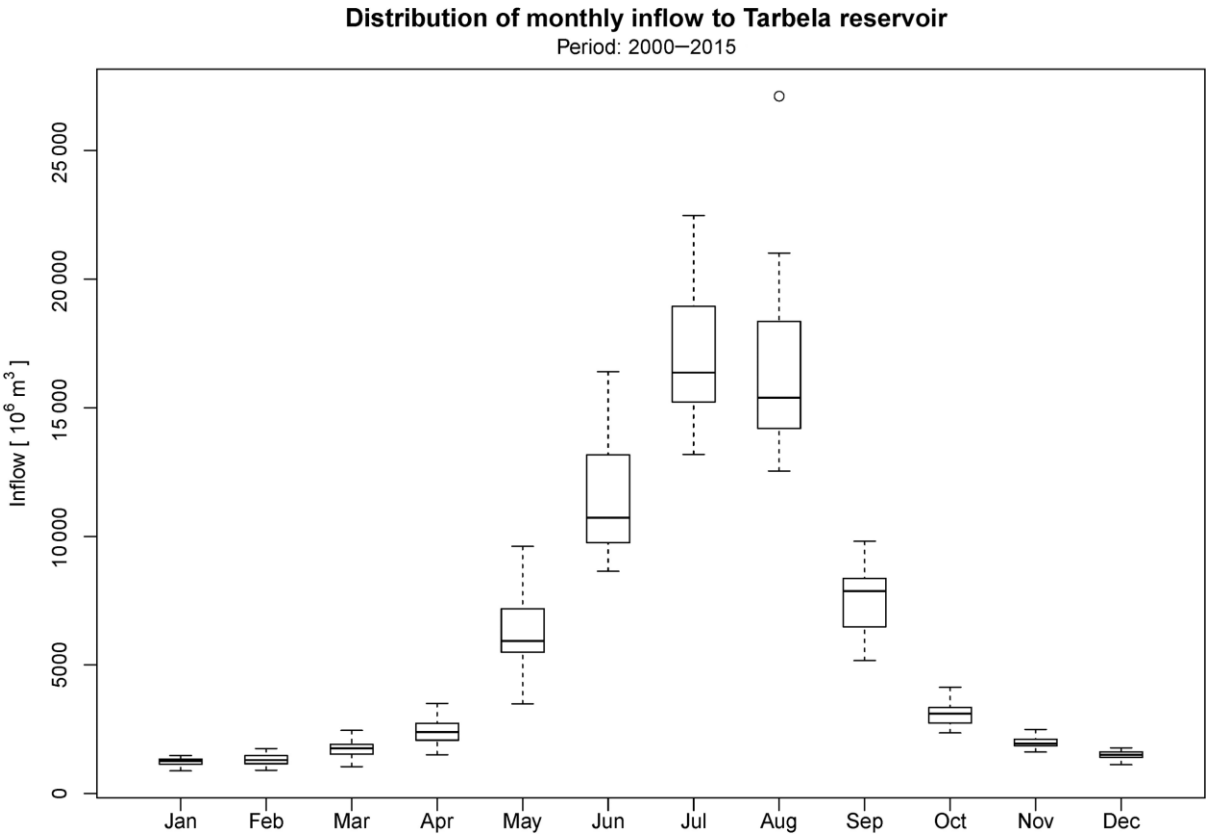

Figure 3.2 Monthly distribution of inflows to the Tarbela Reservoir from 2000–2015.

3.2.2 Model structure

The Snowmelt Runoff Model (SRM; (Martinec, 1975)) is a semi-distributed, lumped temperature-index model which is specifically designed to simulate the runoff in snow dominated catchments that has been successfully applied in more than one hundred snow-driven basins around the globe (Martinec et al., 2008). Input variables of the SRM are daily values of air temperature, precipitation, and snow covered area. The catchment is usually subdivided into elevation zones of about 500m each and the input variables are distributed accordingly. The total daily amount of water produced from snowmelt and rainfall in the catchment is superimposed on the calculated recession flow according to Eq. (3.1):

$$Q_{n+1} = \sum_{i=1}^{m} \left\{ \left[M_{n,i} + R_{n,i} \right] . \frac{10000}{86400} A_i \right\} . (1 - k_{n+1}) + Q_n k_{n+1} \tag{3.1}$$

where Q is the average daily discharge ($m^3 s^{-1}$), M and R are the daily runoff depths originating from snowmelt and rainfall (cm d^{-1}), A is the total area of the elevation zone (km^2), k is the recession coefficient (–), n is the index of the simulation day, and i and m are the indices and total number of elevation zones, respectively. Daily runoff from snowmelt and rainfall is calculated by Eqs. (3.2) and (3.3):

$$M_{n,i} = c_{Sn,i} . a_{Sn,i} . T_{n,i} . S_{n,i} \tag{3.2}$$

$$R_{n,i} = c_{Rn,i} . P_{n,i} \tag{3.3}$$

where c_S and c_R are the runoff coefficients (–) for snowmelt and rain, respectively, a_S is the degree-day factor for snow (cm °C^{-1} d^{-1}), T the degree-days (°C d) for each elevation zone, S the ratio of the snow covered area to the total area (–), and P is the daily precipitation (cm d^{-1}). (Schaper et al., 1999) introduced an enhancement in the original SRM approach by incorporating the separate glacial melt component in the model. In addition to the variables used by SRM, it also considers the area covered by exposed glaciers, i.e. not snow covered. An additional melt component is added to Eq. (3.1) that takes into account the specific degree-day factors for glaciers according to Eq. (3.4):

$$G_{n,i} = c_{Gn,i} . a_{Gn,i} . T_{n,i} . S_{Gn,i} \tag{3.4}$$

where G is the daily melt (cm d-1) from exposed glaciers in each elevation zone, c_G is the runoff coefficient (–), a_G is the degree-day factor (cm °C^{-1} d^{-1}) for glaciers, and S_G is the ratio of the exposed glacier area to the total area (–). This model was tested in several basins and was found to be highly accurate even in basins with 67% glacier area. The three alpine basins were Rhine-Felsberg, Rhône-Sion, and Ticino-Bellinzona in Switzerland (Schaper and Seidel, 2000). Apart from the improvement

in the runoff modelling, the independent computation of glacier melt is an important step towards evaluations of glacier behaviour with regard to climate change. The glacier melt component according to Eq. (3.4) was incorporated into the existing ExcelSRM (further referred to as SRM+G). This extension requires the glacier exposed area as an additional daily input variable and respective model parameters as given in Eq. (3.4). An additional enhancement is the possibility to split the watershed into different sub-catchments. This feature is realised by adding the pre-calculated outflow of a sub-catchment obtained by a separate simulation to the discharge of the downstream sub-catchment. The travel time can be considered by applying a time lag to the daily discharge time series.

3.2.3 Splitting the UIB into two sub-catchments

In the Karakorum–Western-Himalayas region, snow accumulates during winter and reaches its maximum extent in February or March. Higher altitudes typically have a 90 – 100% snow cover that stays more or less constant until melting starts in spring. There is, however, a characteristic bias between the north-western part of the UIB, where at altitudes above 4000 m a.s.l. the snow covered area usually starts gradually decreasing in March, and the south-eastern part, namely the Tibetan Plateau, where at the same altitudes snow cover is fading away rapidly. This bias leads to an inevitable underestimation in forecasting the snowmelt-dominated early Kharif flows (see Sect. 3.3.1), which motivates the splitting of the UIB into two sub-catchments.

Ideally, the catchment should be split directly downstream of the Tibetan Plateau. However, because the first gauging station where daily flow data were available is the Kharmong gauging station (when the Upper Indus River has entered into Pakistan), this location was chosen to split the UIB into upstream and downstream sub-catchments (namely the Upper and Lower UIB; Figure 3.1). The hypsometric characteristics including the number of elevation zones and their corresponding areas of both sub-catchments are shown in Figure 3.3.

According to the two sub-catchments, two separate SRM+G models were created. For each simulation, first the Upper UIB model is run in order to simulate flows at Kharmong. These flows are then superimposed onto the flows calculated by the Lower UIB model using a time lag between Kharmong and Tarbela that was estimated by Kirpich (Eq. (3.5); (Kirpich, 1940; USDA, 2010)).

$$t = 0.00195\, L^{0.77}\, S^{-0.385} \tag{3.5}$$

In this empirical equation, the time of concentration t (min) is only related to the length of the main channel L (m) and the slope of the longest hydraulic length S (–). Given the altitudes of Kharmong and

Darband (upstream Tarbela reservoir) gauging stations as 2542 and 436 m a.s.l., respectively, and a channel length[2] of about 617 km, the approximated time lag of 5000 min was finally rounded to 3 days.

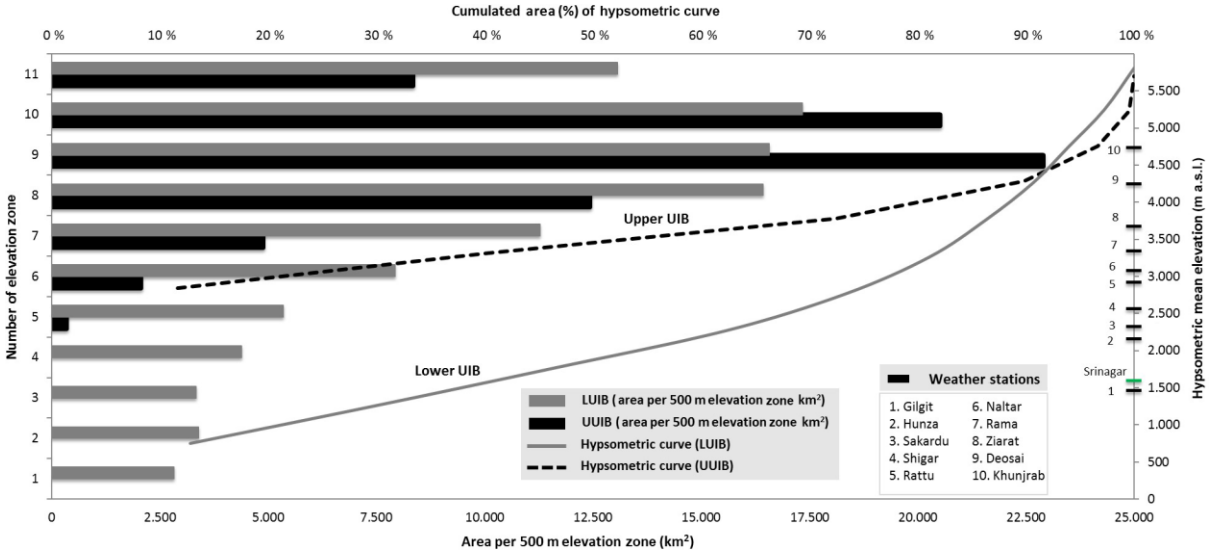

Figure 3.3 Hypsometric curves and the distribution of area under 500m elevation bands for the Upper and Lower UIB. Eleven and seven elevation zones were made for the Lower and Upper UIB, respectively, and the elevation of the weather stations in the western portion of the UIB are presented on the right hand side y-axis.

3.2.4 Data sources

There are a number of high-elevation climate stations in the Pakistani part of the UIB operated by WAPDA's[3] Glacier Monitoring and Research Centre (GMRC) and the Pakistan Meteorological Department (PMD). However, they are concentrated on the western part of the UIB and data is not available online. In order to have the most recent data for operational flow forecasting, the World Meteorological Organization (WMO) climate station at Srinagar airport located at an altitude of 1587m a.s.l. was chosen as temperature base station, which already had proven to give representative temperatures for that region in the SRM model of the Upper Jhelum catchment (Bogacki and Ismail, 2016) and a full set of climatic data can be obtained online from the GSOD[4] database with a time lag of about 2 days only. Based on the daily air temperature data, degree-days in each elevation zone were calculated using a constant temperature lapse rate of -6 °C km^{-1}.

[2] Digitised from Esri's World Imagery. Sources: Esri, Digital-Globe, GeoEye, i-cubed, USDA, USGS, AEX, Getmapping, Aerogrid, IGN, IGP, swisstopo, and the GIS user community

[3] Pakistan Water and Power Development Authority

[4] Global Summary Of the Day. Download at ftp://ftp.ncdc.noaa.gov/pub/data/gsod/

The MODIS/Terra Snow Cover Daily L3 Global 500m Grid (MOD10A1) product[5] has been used to determine the daily snow covered area in the elevation zones. The compatibility of using MODIS data in conjunction with SRM in the Himalayas and its surroundings has already been investigated by (Immerzeel et al., 2009, 2010a). As the MODIS sensor cannot detect snow below clouds, a cloud elimination algorithm is applied using temporal interpolation between two cloud-free days for each pixel. Afterwards the daily percentage of snow cover area in each elevation zone is calculated and smoothed by moving average.

At the beginning of the melting season, glaciers are usually completely covered by fresh snow. As the melting season progresses, the snow cover will fade away and glacier exposed area will increase. The actual glacier extent was derived from two data sources. As a major source on global glacier distribution, the Global Land Ice Measurements from Space (GLIMS) data archive was used (Raup et al., 2007). This data was complemented by interpretation of Landsat 8 scenes (30m spatial resolution) from late summer to early fall 2013, in order to identify the maximum of the glacier exposed area. The merged data were mapped on the 500m MODIS grid. On a daily basis, the glacier exposed area is determined by all pixels that are classified as glacier but not identified as snow by the MODIS sensor.

A spatial interpolation of in situ (station) precipitation data in mountainous regions is particularly difficult and often biased towards lower values (Archer and Fowler, 2004) as the rain gauge network is usually sparse and mainly located at the valley floors, while maximum precipitation occurs on mountain slopes and increases with altitude in general. A promising alternative to station data are gridded, remote sensing-based precipitation products. However, regional and temporal patterns as well as multiannual means of these products differ significantly in the Himalayas (Palazzi et al., 2013). In particular, the widely used TRMM dataset is known to underestimate the precipitation at high altitudes, as found in the UIB (Forsythe et al., 2012) or the Andes (Ward et al., 2011).

Based on our own precipitation product comparisons for the Upper Chenab catchment, the gridded RFE 2.0 central Asia[6] daily rainfall product (Xie et al., 2002) is used in the present model. According to SRM's elevation band approach, the gridded data, having a spatial resolution of 0.1° latitude and longitude, is mapped to the respective elevation zones. For the period 2003–2015, the product yields a mean annual precipitation of 854 and 482 mm year^{-1} for the Lower and the Upper UIB, respectively, which reflects the significantly lower annual precipitation on the Tibetan Plateau compared to the western Himalayas (e.g. (Ménégoz et al., 2013; Bookhagen and Burbank, 2010)). The RFE basin-wide annual mean of 701 mm year^{-1} lies well in the range of 675±100 mm year^{-1} derived for the whole UIB by (Reggiani and Rientjes, 2015).

[5] Hall et al. (2006), updated daily. MODIS/Terra Snow Cover Daily L3 Global 500m Grid V005, (February 2000–September 2016, tiles h23v05 & h24v05). NSIDC Boulder, Colorado, USA. Download at https://n5eil01u.ecs.nsidc.org/MOST/MOD10A1.005.

[6] RainFall Estimates version 2.0 created by the NOAA Climate Prediction Center's FEWS-NET group sponsored by USAID. Download at ftp://ftp.cpc.ncep.noaa.gov/fews/afghan

3.2.5 Model parameters

The most important parameter of a temperature-index model that is controlling daily snow and glacial melt is the degree-day factor (cm $°C^{-1}$ d^{-1}), which transforms the index variable degree-day (°C d) into actual melt (cm d^{-1}). In the case of glaciers, a constant degree-day factor of 0.70 cm $°C^{-1}$ d^{-1}, as proposed by (Schaper et al., 2000), was chosen, which also corresponds to degree-day factors reported from glaciers in the Himalayas at a comparable latitude (Hock, 2003). The approach for degree-day factors for snow is more elaborate. In the first step, optimal degree-day factors were obtained for each elevation zone and year by diagnostic calibration, i.e. by achieving the best possible fit between simulated and observed hydrographs for each year. From this calibration exercise, it appears that degree-day factors are increasing by the time melting has started in a particular elevation zone (Figure 3.4 and Figure 3.5). Because a generalised rule is needed in the forecasting procedure, zone-wise degree-day factor functions, as suggested by (Ismail et al., 2015), were developed by linear regression between the calibrated degree-day factors and time.

The increase in the degree-day factors with the passage of time is because the snow absorbs energy due to physical conditions such as increasing temperatures and solar radiation intensities. This process of energy storage plays a pivotal role in the ripening of the snowpack, which melts rapidly as the snow melting season progresses. The extent to which degree-day factors increase is related to the calibration procedure because it was observed during the model calibration that in a certain elevation zone when the degree-day factors attain a certain value, e.g (0.80 cm $°C^{-1}$ d^{-1}), the snow cover area in that very elevation zone has almost completely faded away so there is no advantage in further increasing the values of degree-day factors. The limit of the degree-day factors increase at a certain spatio-temporal region depends upon various physiographic and climatic parameters and research is on-going to evaluate the trend of degree-day factors in response to the aforementioned parameters.

The start of snowmelt and the corresponding application of the developed degree-day factor generalised rule is correlated with a certain threshold temperature (T_{th}) for each elevation zone (see Table 3.1 and Table 3.2). The other model parameters required by SRM like temperature lapse rate, recession coefficient, runoff coefficient for snow, lag time, etc., were applied basin-wide and kept constant for all years (see Table 3.3). The values of these parameters were determined according to the methods described by (Martinec et al., 2008) and slightly adjusted to achieve a good fit over the whole calibration period. It has to be noted that these parameter values will differ for other catchments.

Table 3.1 Zone-wise melting start threshold temperatures and time-dependent degree-day factors for the Lower UIB.

	Elevation Zone (m a.s.l)							
	≤2500	2500–3000	3000–3500	3500–4000	4000–4500	4500–5000	5000–5500	>5500
T_{th}*	9.0	7.0	5.0	4.0	2.0	1.0	1.0	1.0
Days after melting start								
10	0.20	0.21	0.22	0.22	0.19	0.18	0.18	0.20
20	0.30	0.32	0.32	0.32	0.30	0.31	0.31	0.33
30	0.39	0.43	0.41	0.43	0.41	0.43	0.44	0.46
40	0.48	0.53	0.51	0.54	0.52	0.56	0.57	0.59
50	0.57	0.64	0.61	0.65	0.63	0.68	0.70	0.72
60	0.67	0.75	0.70	0.80	0.74	0.80	0.80	0.80
70	0.80	0.80	0.80	0.80	0.80			

*10-day average temperature in °C in each elevation zone.

Table 3.2 Zone-wise melting start threshold temperatures and time-dependent degree-day factors for the Lower UIB

	Elevation Zone (m a.s.l)						
	≤3000	3000–3500	3500–4000	4000–4500	4500–5000	5000–5500	>5500
T_{th}*	2.0	2.0	2.0	2.0	0.5	0.5	0.5
Days after melting start							
10	0.37	0.35	0.35	0.52	0.56	0.48	0.60
20	0.43	0.40	0.40	0.59	0.64	0.54	0.70
30	0.49	0.45	0.46	0.66	0.73	0.80	0.80
40	0.54	0.51	0.51	0.73	0.80		
50	0.60	0.56	0.56	0.80			
60	0.66	0.61	0.62				
70	0.71	0.66	0.67				

*10-day average temperature in °C in each elevation zone.

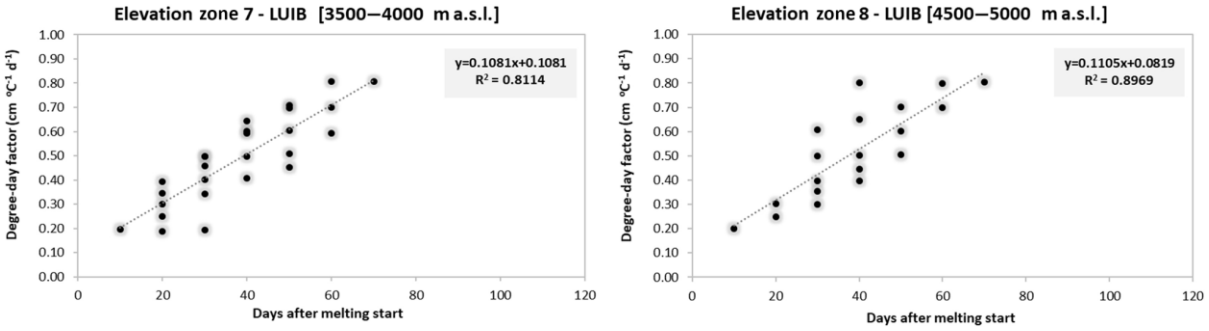

Figure 3.4 Increase in degree-day factors with time after start of melting for elevation zones 7 and 8 for the Lower UIB. Degree-day factors are obtained by diagnostic calibration.

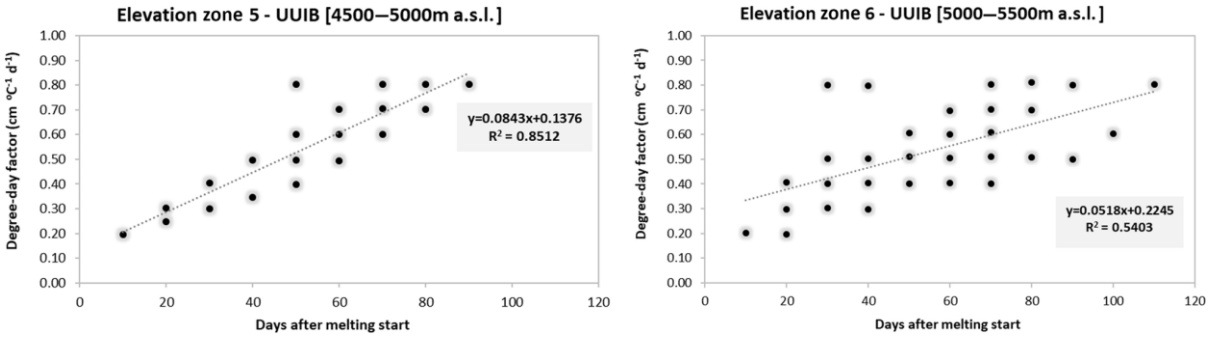

Figure 3.5 Increase in degree-day factors with time after start of melting for elevation zones 5 and 6 for the Upper UIB. Degree-day factors are obtained by diagnostic calibration.

3.2.6 Scenario approach for forecasting

In the forecasting period which starts from 1 April, the four model variables temperature, precipitation, snow covered area, and glacier exposed area have to be predicted for the forthcoming 6 months of the Kharif cropping season (April–September). As the level of skill of seasonal climate forecasts for the Hindukush–Karakoram–Western-Himalaya region for such a lead time is still not sufficient, a scenario approach already successfully applied in the Upper Jhelum catchment (Bogacki and Ismail, 2016) is used.

This scenario approach has a lot in common with traditional ESP methods (developed at the U.S. National Weather Service as a method for generating long-term probabilistic streamflow outlooks; (Day, 1985)). Based on the assumption that past meteorology is representative of possible future events, ESP uses historical temperature and precipitation time series as forcings for the hydrological model to produce an ensemble of streamflow traces. A probabilistic forecast is created by statistical analysis of the multiple streamflow scenarios produced (Franz et al., 2008). Initial basin conditions are usually estimated by forcing the hydrological model with observed meteorology in a "warm-up" phase up to the time of forecast (Wood and Lettenmaier, 2008).

The seasonal scenario approach also uses historical temperature and precipitation as forcings for the SRM+G model. In contrast to ESP, however, this approach is, like the other operational forecast models

for the UIB, primarily focussed on a deterministic forecast of total Kharif flow volume. Besides the "most likely" (median) flow, SRM+G forecasts only give an indication of the bandwidth of expected flows by the dry (20 %) and wet (80 %) quantiles as limits of the "likely" range.

The other notable differences are the initial basin conditions. SRM and SRM+G do not use any initial conditions, like soil moisture state of snow-water equivalent as used in other hydrological models. Instead, however, the snow cover area and the glacier-exposed area are input variables to the model. For reasons of simplicity, the glacier-exposed area is treated like the meteorological variables, i.e. the historical time series are used. However, the depletion of the snow covered area during the forecast period, which is the decisive factor for each forecast, is predicted by so-called "modified depletion curves". These modified depletion curves are derived from the conventional depletion curves of each elevation zone by replacing the timescale with the cumulative daily snowmelt depth (Martinec et al., 2008). The decline of the modified depletion curves depends on the initial accumulation of snow and represents the actual snow-water equivalent.

When initial snow depth is low, the modified depletion curve declines faster than in years when a lot of snow has accumulated. At the end of March, when the seasonal forecast is carried out, an elevation zone already showing some decline in snow covered area, and hence having also some cumulated degree-days, is chosen as a "key zone". Comparing the relationship of decline in snow covered area versus cumulated degree-days with a statistical analysis of the modified depletion curves of previous years, the actual amount of snow is estimated and the future depletion anticipated accordingly, while assuming similar snow conditions for all elevation zones.

The ESP approach usually has the advantage that errors in the initial conditions are progressively superseded by the meteorological forcings. In SRM+G, however, if an erroneous depletion estimate is in effect, then it will persist during the whole forecast period. As all ensemble traces are based on the chosen depletion curves, the initial estimate is crucially influencing each trace of the ensemble in the same direction.

Table 3.3 SRM+G model parameters for both the upper and Lower UIB.

Parameters	Symbol	Value	Units	Remarks
Temperature lapse rate	γ	6.0	°C km^{-1}	
Recession coefficient	k_x	1.193	–	October-February
	k_y	1.060		March – September
		0.029		October-February
		0.020		March – September
Critical precipitation	P_{crit}	1	cm	constant
Lag time	L	54	h	2.5 days delay between melt and runoff at Tarbela
Critical temperature	T_{crit}	0.5 – 3.0	°C	variable
Rainfall contributing area	RCA	0	–	November – March

Parameters	Symbol	Value	Units	Remarks
		1		April – October
Runoff coefficient - snow	c_S	0.80	–	constant
Runoff coefficient - glacier	c_G	0.70	–	constant
Runoff coefficient - rain	c_R	0.25 – 0.75	–	
Degree-day factor - snow	α	0.15 – 0.80	cm °C^{-1}d^{-1}	
Degree-day factor - glacier	a_G	0.70	cm °C^{-1}d^{-1}	constant

3.2.7 Verification methods

Model verification comprises the simulation model as well as the forecasting model. The accuracy of the simulation model was evaluated by the two standard criteria used in the SRM (Martinec et al., 2008), namely the relative volume difference Eq. (3.6)

$$D_v = \frac{V - V^*}{V} \times 100\ [\%] \tag{3.6}$$

and the coefficient of determination R^2 Eq. (3.7)

$$R^2 = 1 - \frac{\sum_{i=1}^{n}(Q_i - Q_i^*)^2}{\sum_{i=1}^{n}(Q_i - \bar{Q})^2} \tag{3.7}$$

where V and V^* are the observed and the simulated annual flow volumes, Q_i and Q_i^* are the observed and the simulated daily discharge values, and $\bar{Q}$ is the average observed daily discharge.

The skill of the forecasting model was assessed in comparison with IRSA's forecasts that are based on a statistical model and with forecasts from the UBC[7] watershed model (Quick and Pipes, 1977) that is used by WAPDA's Glacier Monitoring Research Centre. The set of verification metrics was chosen taking into account that the existing operational forecasts for Kharif flows are traditionally issued in the form of deterministic forecasts, thus only the 'most likely' values forecasted by these models are available.

The accuracy of a forecast is a measure of the error between predicted and observed values. The root mean squared error (RMSE; Eq. (3.8)), mean percentage error (MPE; Eq. (3.9)), and mean absolute

[7] University of British Columbia Watershed Model.

percentage error (MAPE; Eq. (3.10)) were used as deterministic metrics to assess the accuracy of the predicted mean Kharif flow volumes.

$$RMSE = \sqrt{\frac{1}{n}\sum_{i=1}^{n}(f_i - o_i)^2} \tag{3.8}$$

$$MPE = \frac{1}{n}\sum_{i=1}^{n}\frac{(f_i - o_i)}{o_i} \tag{3.9}$$

$$MAPE = \frac{1}{n}\sum_{i=1}^{n}\frac{|f_i - o_i|}{o_i} \tag{3.10}$$

In the above equations, f_i is the forecasted and o_i the observed flow volume and n the total number of considered forecasts. Both, RMSE and MAPE measure the average magnitude of the forecast errors, where RMSE penalises larger errors more than MAPE. The mean percentage error measures the deviation between average forecasted and average observed flows, i.e. a positive MPE indicates over-forecasting and a negative under-forecasting.

As a commonly used deterministic measure of association, the correlation coefficient, Eq. (3.11), was applied to assess the correspondence between forecasted and observed values.

$$R = \frac{\sum_{i=1}^{n}(f_i - \bar{f})(o_i - \bar{o})}{\sqrt{\sum_{i=1}^{n}(f_i - \bar{f})^2}\sqrt{\sum_{i=1}^{n}(o_i - \bar{o})^2}} \tag{3.11}$$

In addition, the uncentered anomaly correlation AC_u (Eq. (3.12); (Wilks, 2006)) was used as another measure of association.

$$AC_u = \frac{\sum_{i=1}^{n}(f_i - \bar{c})(o_i - \bar{c})}{\sqrt{\sum_{i=1}^{n}(f_i - \bar{c})^2}\sqrt{\sum_{i=1}^{n}(o_i - \bar{c})^2}} \tag{3.12}$$

where $\bar{c}$ is the climatological average value. The anomaly correlation is designed to measure similarities in the patterns of anomalies from the climatological average between forecasted and observed values. An AC ≥ 0.6 is usually regarded as an indication of some forecasting skill (Wilks, 2006). In the present context, the climatology average $\bar{c}$ is equivalent to the average observed flows $\bar{o}$.

The ability of a non-probabilistic forecast to predict extreme conditions is usually assessed by defining discrete categories like below normal, normal, and above normal. The Heidke and Peirce skill scores for multi-categorical forecasts measure the fraction of correct forecasts in each category in relation to those forecasts, which would be correct due purely to random chance. The Peirce skill score, Eq. (3.13),

$$PSS = \frac{\sum_{j=1}^{m} p(f_j, o_j) - \sum_{j=1}^{m} p(f_j)\, p(o_j)}{1 - \sum_{i=j}^{m} p(o_j)^2} \tag{3.13}$$

is unbiased in the sense that it assigns a marginal distribution to the reference random forecast which is equal to the (sample) climatology (Wilks, 2006). In the above equation, *m* is the number of categories, $p(f_j, o_j)$ the joint distribution of forecasts and observations, where $p(f_j)$ and $p(o_j)$ are the respective marginal distributions.

As the existing operational forecasts are primarily designed as point estimates of the mean flow volume and hence a comparison of probabilistic metrics between these models is not possible, only a basic probabilistic evaluation of the SRM+G scenario ensembles was carried out. The ranked probability score RPS was used, which is essentially an extension of the Brier score to the many-event situation (Wilks, 2006). It reflects the overall performance of a multi-category probabilistic forecast (Franz et al., 2003). In order to calculate the RPS, first the quantiles of *m* categories have to be determined based on given non-exceedance probabilities of the observed values. Then, for each forecast, the ensemble members as well as the observed flow are assigned to these categories and the respective cumulative distributions, Eq. (3.14), are calculated

$$F_i = \sum_{j=1}^{m} p_j(f_i) \qquad O_i = \sum_{j=1}^{m} p_j(o_i) \tag{3.14}$$

where *Fi* is the cumulative ensemble distribution of forecast *i* and $p_j(f_i)$ is the relative frequency of an ensemble member falling into category j . For each forecast *i*, there is only one observation o_i, hence the category *j* the observation falling in is given a relative frequency of $p_j(o_i) = 1$ while all others are set to 0. Finally, the RPS (Eq. (3.15)) for *n* forecasts is the average of the sum of the squared differences in the cumulative distributions.

$$RPS = \sum_{i=1}^{n} \left\{ \sum_{k=1}^{m} \left[\sum_{j=1}^{k} p_j(f_i) - \sum_{j=1}^{k} p_j(o_i) \right]^2 \right\} \tag{3.15}$$

The RPS penalises forecasts more severely when their probabilities are further from the actual observations. The relative improvement or skill of a probability forecast over climatology as a reference forecast is assessed by the ranked probability skill score (RPSS; Eq. (3.16))

$$RPSS = 1 - \frac{RPS}{RPS_{ref}} \tag{3.16}$$

where RPS_{ref} is the RPS calculated with a constant forecast, e.g. the average of the observed series.
Besides the RPSS as a single-number score for the forecast performance, the reliability diagram (Wilks, 2006) is used to show the full joint distribution $p(f_i, o_j)$ of forecasts and observations of a binary predictand in terms of its calibration – refinement factorisation (Murphy and Winkler, 1987)

$$p(f_i, o_j) = p(o_j|f_i) \cdot p(f_i) \qquad i = 1, \dots, m \quad j = 1, \dots, n \tag{3.17}$$

where the *m* conditional distributions $p(o_j|f_i)$ specify how often each possible observation o_j occurred when the particular forecast f_i was issued, or in other words how well each forecast f_i is calibrated. Forecasts f_i that fall near to the 1:1 line in the reliability diagram result in a small (good) reliability term of the algebraic decomposition of the Brier score (Murphy, 1973), which is the weighted average of the squared vertical distances.
The other part of the above factorisation is the unconditional (marginal) distribution $p(f_i)$ that specifies how often each of the *m* possible forecast values occurred. This so-called refinement distribution is visualised by a probability histogram that is also referred to as a sharpness diagram. A distribution with a large spread indicates that different forecasts are issued relatively frequently, and so have the potential to discern a broad range of conditions. Conversely, a narrow distribution, i.e. if most of the forecasts *fi* are the same or in a similar range, indicates a lack of sharpness (Wilks, 2006).
While the calibration–refinement factorisation relates to a binary predictand, the SRM+G scenario forecasts are grouped into three categories: less than normal, near normal (most likely), and higher than normal. According to (Murphy, 1972), this N-state situation is handled as a collection of $N \times m$ scalar forecasts, thus treating each category as a separate binary forecast *fi* that either meets or does not meet the observation o_j.

3.3 Results and discussion

The development of the SRM+G forecasting model for the UIB has been an iterative process with the focus on creating an operational forecasting tool for Kharif flow volumes to the Tarbela reservoir. Thus, not all improvements have been tested individually while not changing the other components, which

would allow an independent assessment of the individual effects. Nevertheless, the results are discussed below separately for each component.

3.3.1 Splitting of the UIB catchment

While the simulation results using a sole model for the whole UIB showed an acceptable agreement between simulated and observed flows in terms of R^2 and D_v, initial hindcast results proved to be unsatisfactory, especially for the early Kharif (1 April–10 June) season, which is the major snowmelt contribution period. The mean percentage error MPE between hindcasts and observations of -21.0% for the years 2003–2014 indicated a severe bias towards underestimating the actual flows and the respective MAPE of 25.9% was also unexpectedly large.

An analysis of MODIS snow cover data indicates that in the south-eastern part of the UIB, namely the Tibetan Plateau, already in March the snow cover is fading away rapidly. On the other hand, in the north-western part of the catchment, the same elevation zone is still widely covered with snow (Figure 3.6). In Table 3.4 the snow cover area of the relevant elevation zones for the south-eastern (Upper) and north-western (Lower) part of the UIB is given on 1 March and 1 April as an example for the year 2003. While at an elevation of 4000m a.s.l. the snow cover area reduces from 82 to 71% in the Lower UIB, in the Upper UIB the snow cover area shrinks sharply from 79 to 50 %. A similar behaviour can be observed for most of the other years as well. As in forecasting mode, the depletion of the snow cover area during the whole forecasting period is predicted depending on the reduction in the "key zone" in March (see Sect. 3.2.6). The relatively larger depletion in the Upper UIB

leads to an underestimation of the available snow-water equivalent for the whole catchment, which explains the subsequent underestimation of early Kharif flows by the initial hindcasts and in turn motivates the splitting of the UIB into two sub-catchments and separate models (see Sect. 3.2.3). As a result of this splitting, the MPE of the hindcasts for early Kharif changed to a modest overestimation of 4.2%, while the MAPE could be reduced to 15.8%.

Table 3.4 Percentage depletion of snow cover area for the Upper and Lower UIB during March 2003.

Elevation (m a.s.l.)	3500	4000	4500	5000	5500	>5500
1 March 2003						
Lower UIB	66%	82%	88%	87%	83%	94%
Upper UIB	58%	79%	58%	51%	58%	71%
1 April 2003						
Lower UIB	42%	71%	84%	84%	78%	92%
Upper UIB	24%	50%	48%	43%	51%	73%

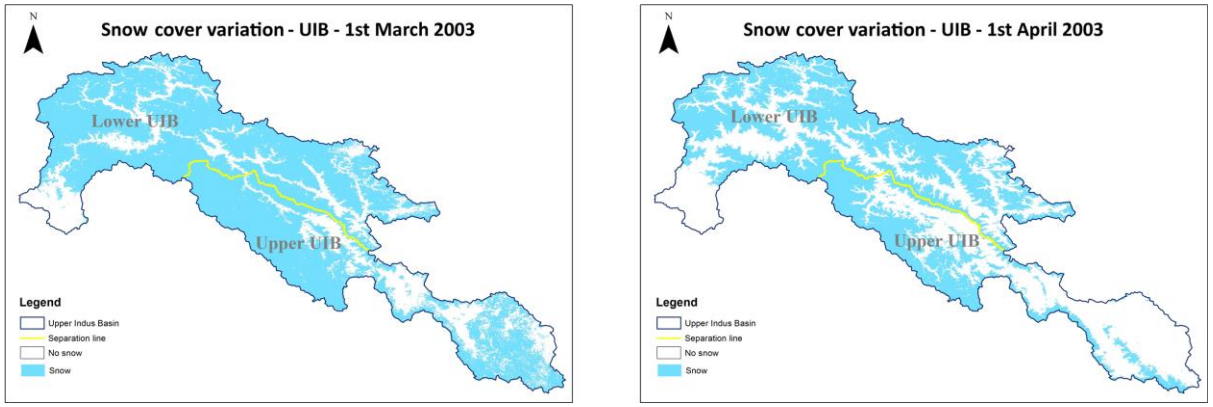

Figure 3.6 Snow cover variation in the months of March (Left) and April (Right) 2003 in UIB.

3.3.2 Glacier melt component

During the first diagnostic calibration of the degree-day factors, it became obvious that in late summer, even with extreme high degree-day factors, it was usually not possible to reproduce the observed hydrograph. The analysis of the snow cover depletion showed that in most of the years, snow has vanished from areas below 4000m a.s.l. already in June and elevation zones below 5000m a.s.l. usually become snow free in July. Thus, the snowmelt contribution to the flow is rapidly diminishing in August and September (see Figure 3.7).

Although the monsoon season usually starts in July, bringing the highest monthly precipitation depth to the UIB in July and August, the resulting flow component from rain is not sufficient to create the necessary discharge. Therefore, many studies postulate a substantial contribution from glacier melt to the annual flow in the UIB. For example, (Immerzeel et al., 2010b) estimate a contribution of 40% from snow and 32% from glacier melt with the remaining 28% from rain, (Charles, 2016) mentioned that the contribution is 50% from snow and 20% from glacial melt.

Figure 3.7 shows the monthly distribution of the three flow components as calculated by SRM+G before subjecting to the recession flow calculation according to Eq. (3.1). SRM's simple recession flow approach is not mass conservative and does also not allow a direct attribution, at what day these flow components actually occur in the daily discharge Q_{n+1}.

However, an overall water balance shows that the difference between water going into the (virtual) storage and water taken out by the recession flow term Q_n is about 7%, which seems acceptable in relation to the uncertainty associated with the input data. Having in mind the above limitation, the average (2003–2014) flow component distribution as simulated by SRM+G is 53, 21, and 26% for snow, glacier, and rain, respectively, which is well within the magnitude of the values found in other studies.

Figure 3.8 and Figure 3.9 compare the hydrographs of simulation runs with and without the glacier component for the Upper and Lower UIB. The effect is more visible in the Lower UIB as about 10.5% of the catchment is glaciated, while for the Upper UIB the glaciated area is merely 1.7 %.

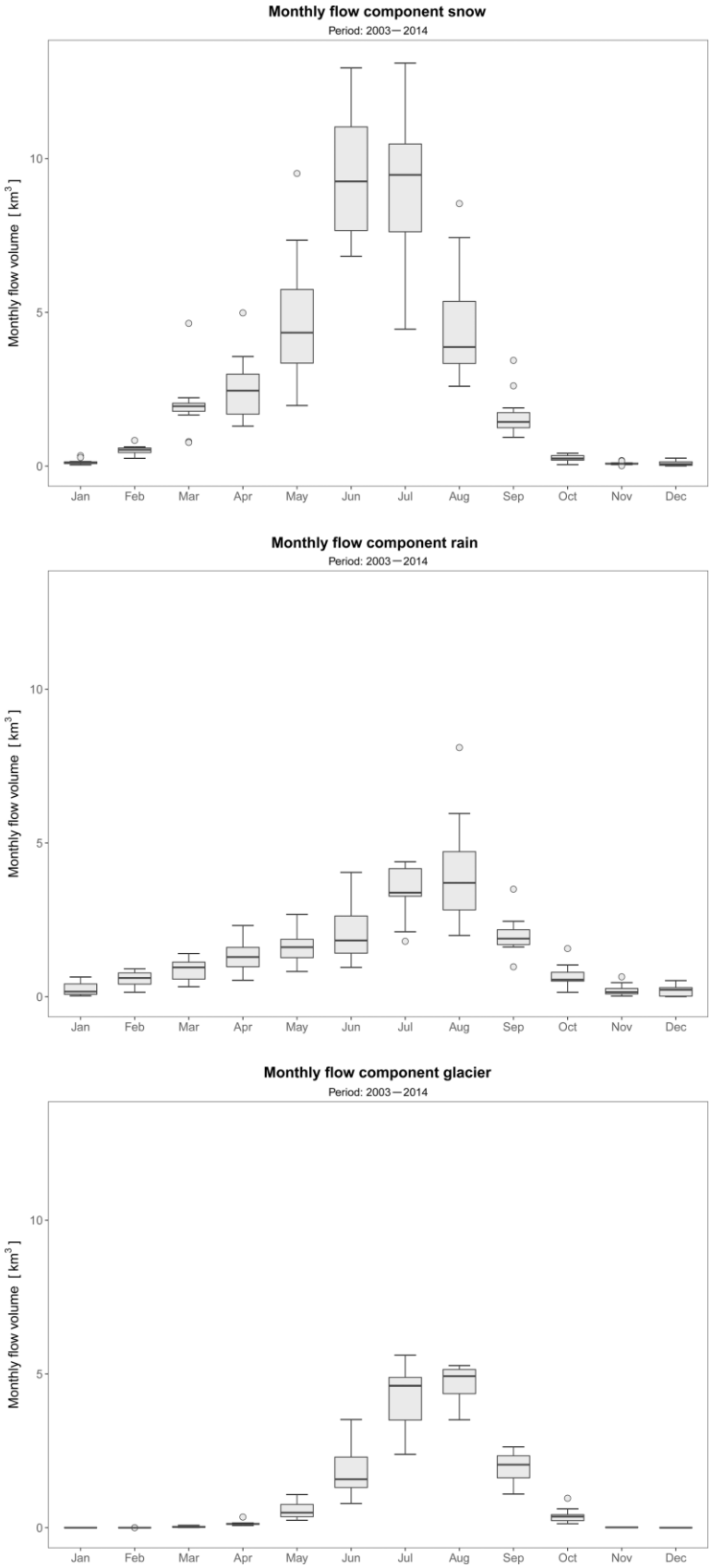

Figure 3.7 Monthly distributions of flow components (snow, rain, and glacier) in the UIB.

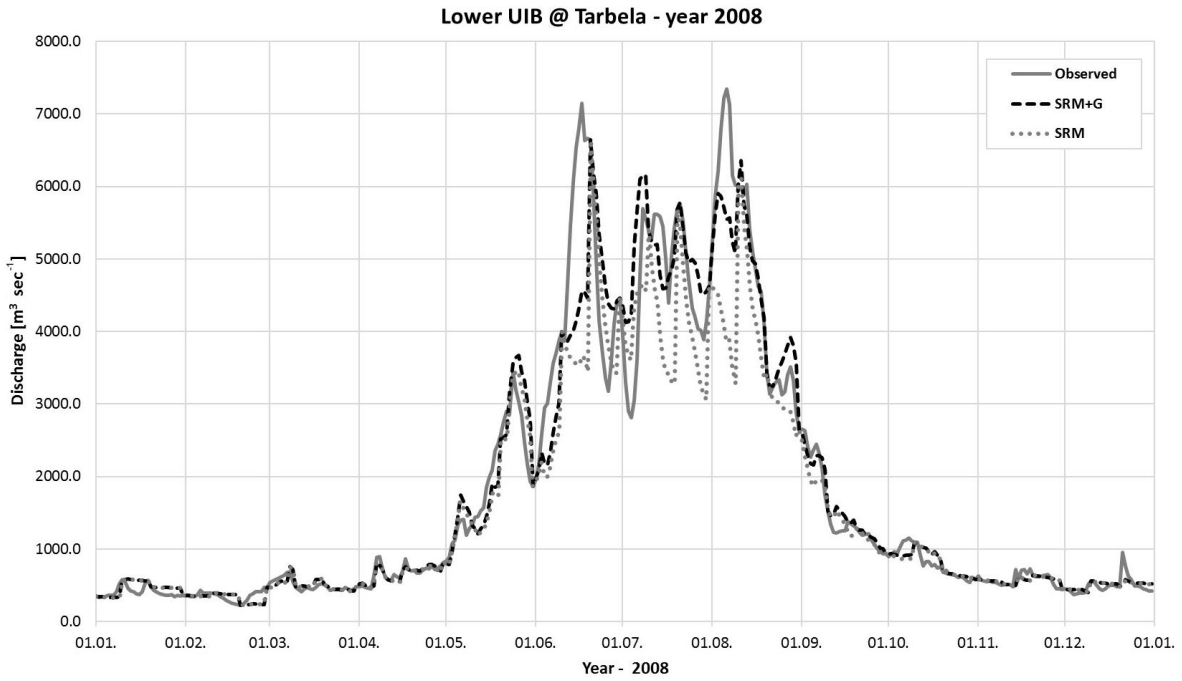

Figure 3.8 Comparison of SRM+G (with glaciers) and SRM (without glaciers) for the Lower UIB in 2008.

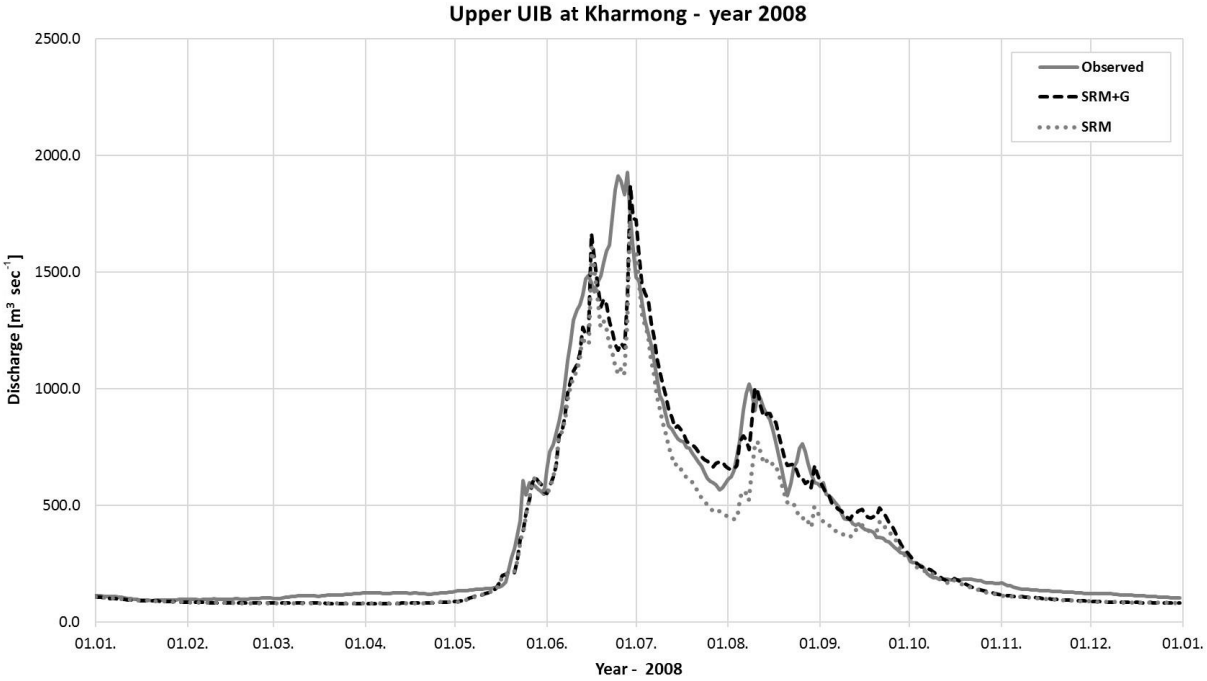

Figure 3.9 Comparison of SRM+G (with glaciers) and SRM (without glaciers) for the Upper UIB in 2008.

3.3.3 Simulation model verification

The simulation model was verified by comparing full year (1st January – 31st December) simulation runs using the actual temperature, precipitation, and snow cover data versus observed daily flows. Examples of respective hydrographs for the Upper and Lower UIB are given in Figure 3.10 and Figure 3.11. The resulting coefficients of determination R^2 and relative volume differences D_v for each year and both the Upper and Lower UIB model are given in Table 3.5. Although the years 2003 – 2012 were used to calibrate certain model parameters (see Sect. 3.2.5), they are also used to validate the model in "forecasting mode", as in particular the degree-day factor functions (Table 3.1 and Table 3.2) were applied as during a real forecasting procedure, i.e. the starting point was chosen according to the melting start threshold temperatures as given in Table 3.1 and Table 3.2. The years 2013 and 2014, on the other hand, were not used at the time of model calibration; thus, they represent a fully independent verification of the simulation model.

The average R^2 of 0.86 and 0.88 for the Upper and Lower UIB, respectively, indicate that in general the two models simulate the variations in the observed hydrographs quite acceptably. Values for the years 2013 and 2014 are even above the average for Lower UIB, which is finally essential for Tarbela inflows, but extreme floods, like 2010 during monsoon season, are not reproduced that well. The average relative volume differences D_v of -1.89 and 0.03% for the Upper and Lower UIB, respectively, show that the simulation models, although not mass-conservative due to the recession approach (Sect. 3.2.2) and volume differences vary from year to year, are in terms of total flow volume not biased over the long run.

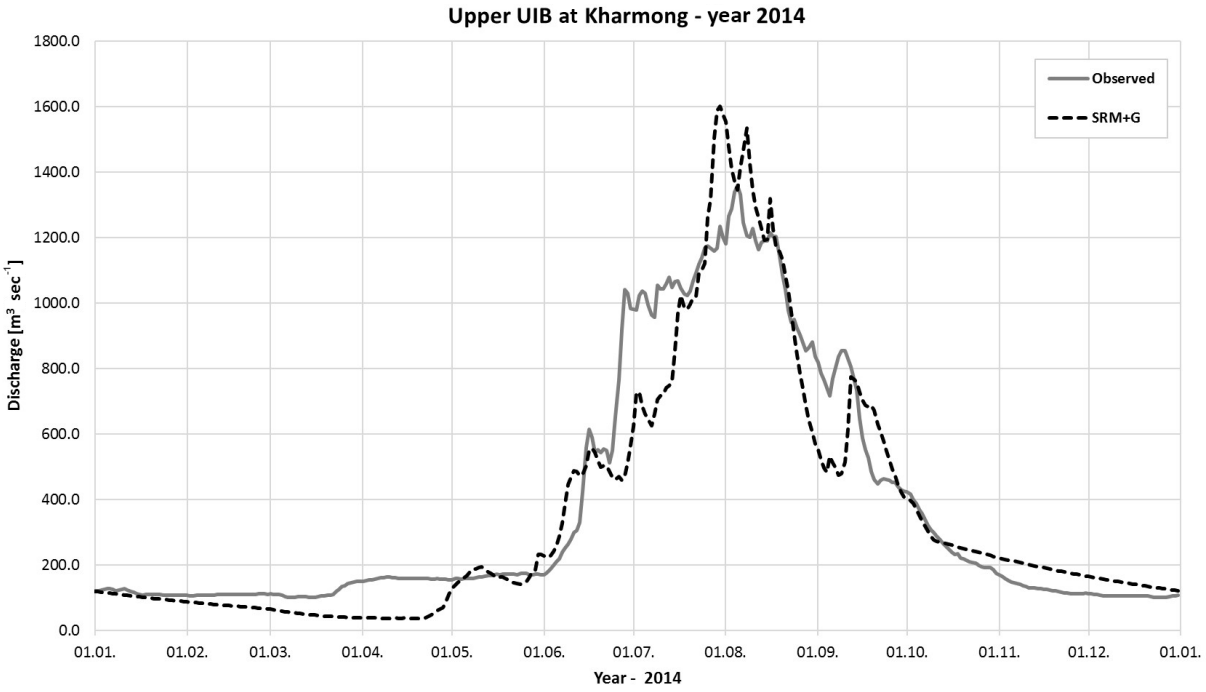

Figure 3.10 Results of the validation of the final Upper UIB flow forecast model (dashed line) compared to observed flows at Kharmong (solid line) for the year 2014.

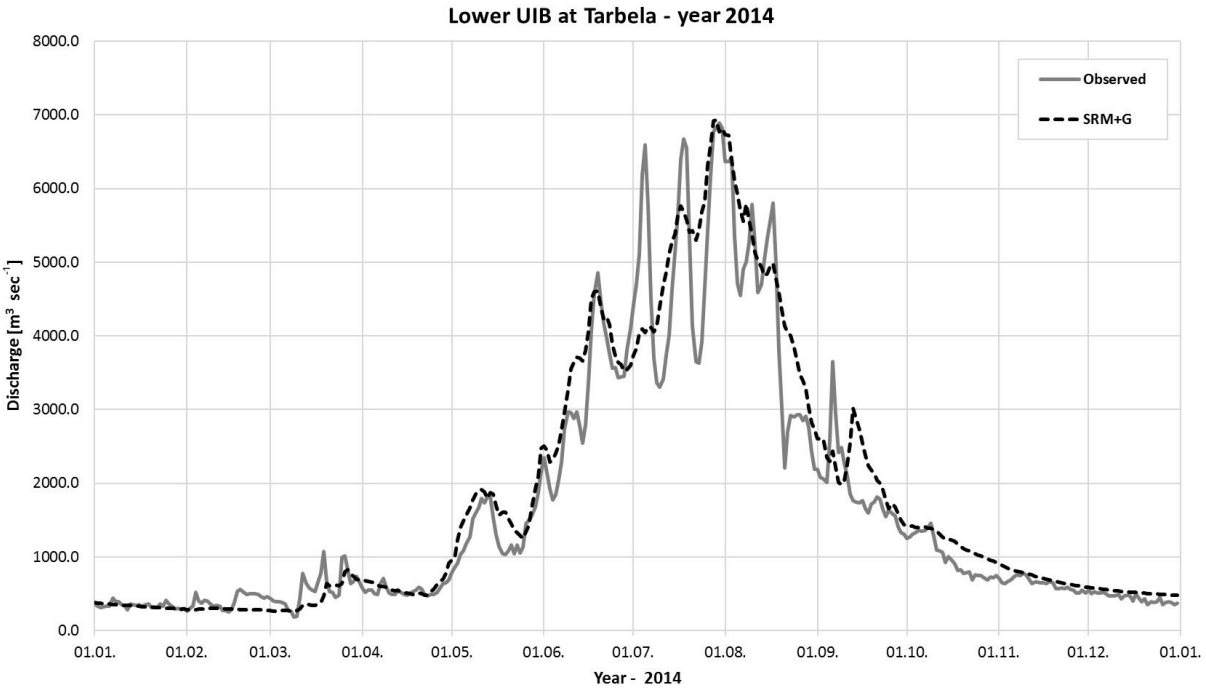

Figure 3.11 Results of the validation of the final Lower UIB flow forecast model (dashed line) compared to observed inflows at Tarbela (solid line) for the year 2014.

Table 3.5 Coefficient of determination R^2 and relative volume difference D_v for the Upper and Lower UIB.

	Upper UIB		Lower UIB	
Year	R^2	D_v [%]	R^2	D_v [%]
2003	0.86	-17.3	0.92	4.6
2004	0.84	2.2	0.90	0.1
2005	0.89	15.3	0.83	-17.4
2006	0.85	8.4	0.91	-3.5
2007	0.80	4.0	0.88	-4.1
2008	0.94	-6.7	0.92	-1.4
2009	0.79	14.2	0.86	16.4
2010	0.90	-1.9	0.77	-16.3
2011	0.88	-9.1	0.88	4.5
2012	0.87	-16.0	0.89	11.9
2013	0.77	-9.3	0.93	-2.5
2014	0.88	-6.5	0.92	8.0
Average	0.86	-1.89	0.88	0.03

3.3.4 Evaluation of forecasting skills

In order to evaluate the skills of the forecasting model, hindcasts were carried out for the years 2003 – 2014 always using all years, i.e. also the hindcasted year, as scenario members.

For the years 2015 and 2016, real forecasts have been determined before 1 April of these years, thus without using the particular year as a scenario. In all cases, the expected depletion of snow cover area was predicted for each scenario member based on the respective situation in March of the specific year.

In Table 3.6, the ensemble medians of hind- and forecasts by SRM+G are compared with observed flows, with IRSA's forecasts that are based on a statistical model, and with forecasts from the UBC watershed model (Quick and Pipes, 1977) that is used by WAPDA's Glacier Monitoring Research Centre. All values are total Kharif (1 April–30 September) flow volumes in 10^9 m^3. Figure 3.12 presents all model results and observed flows and shows also the 20 and 80% quantiles of the SRM+G scenario ensemble. Table 3.7 summarises the metrics that are used to compare the forecast skills of the three models. The RMSE, MAE, and MAPE show an improvement in accuracy by SRM+G and the MPE shows a reduction of bias where SRM+G tends to slightly underestimate, while the two other forecasts moderately overestimate the total Kharif flows. However, both the correlation coefficients *R* and the anomaly coefficients AC_u indicate however, that the association between forecasts and observations is weak for all three models. Here, the UBC forecasts show the best correlation followed by SRM+G and IRSA. The above aspects of model performance are synoptically visualised in the Taylor diagram (Taylor, 2001) in Figure 3.13 that was plotted using the R-package Plotrix (Lemon, 2006). All models are comparable far away from the point of observations given on the x-axis, with SRM+G having the smallest centred root mean square difference and UBC the best correlation coefficient.

In order to evaluate the model skills in forecasting extreme conditions, i.e. dry or wet, the Peirce skill score was applied.

Table 3.6 Comparison of Kharif flow volumes (km^3) during 2003–2016.

Year	Observed	IRSA	UBC	SRM+G
2003	67.8	64.0	63.5	63.1
2004	51.8	60.5	63.6	60.8
2005	68.9	69.0	73.3	60.9
2006	67.8	68.4	73.3	61.6
2007	60.5	74.9	70.1	61.0
2008	57.7	68.5	59.2	53.9
2009	57.6	63.7	67.2	62.4
2010	76.6	63.3	68.4	61.4
2011	60.0	67.2	70.8	59.9
2012	55.4	61.3	61.7	60.4
2013	65.6	64.9	58.8	59.8
2014	52.9	64.6	64.2	61.4
2015	67.2	63.3	61.3	58.9
2016	66.4	62.4	66.5	63.1

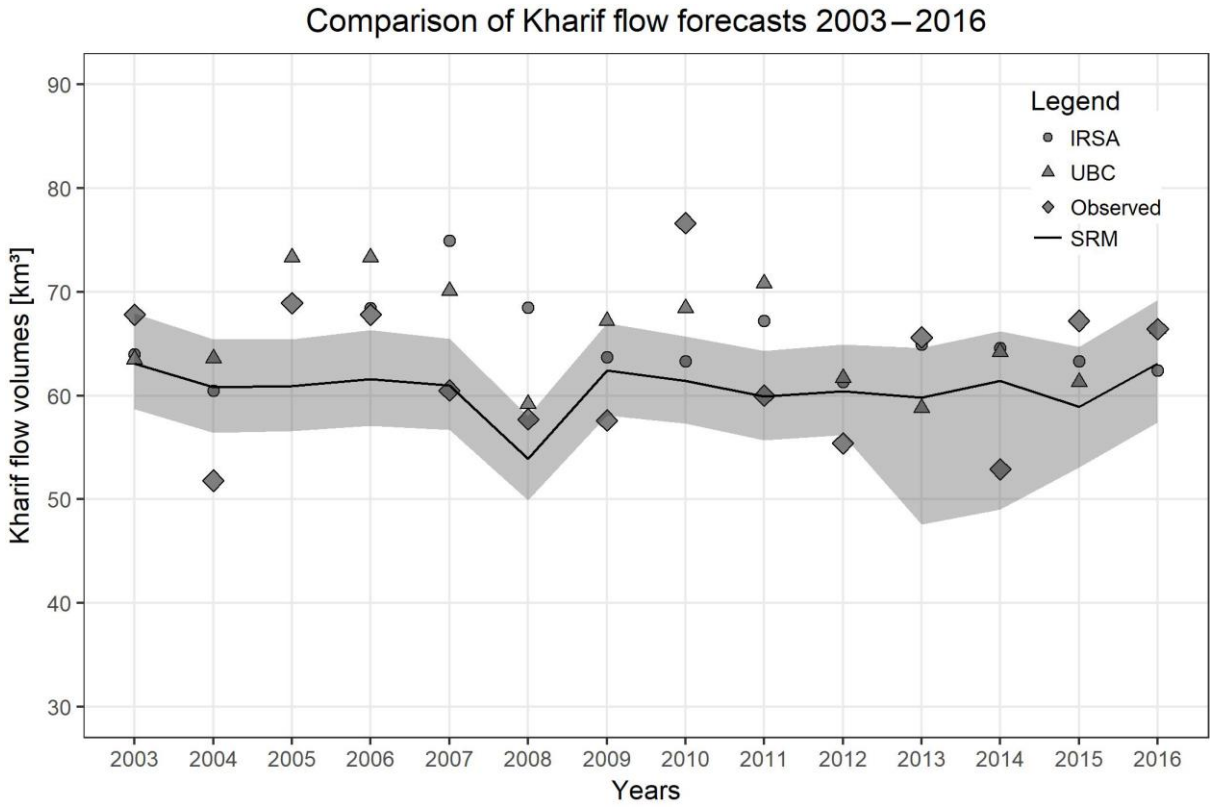

Figure 3.12 Comparison of Kharif flow forecasts with 20 and 80% quantiles of the SRM+G scenario ensembles for the years 2003–2016.

Table 3.7 Comparison of forecast skills between IRSA, UBC, and SRM+G.

Model	MAE	RMSE	MPE	MAPE	R	AC_u	PSS
	km^3	km^3	%	%	–	–	–
IRSA	6.5	8.0	5.8	10.9	0.107	0.085	-0.070
UBC	6.9	7.7	6.3	11.4	0.318	0.260	0.096
SRM+G	6.0	7.0	-2.0	9.5	0.223	0.168	-0.079

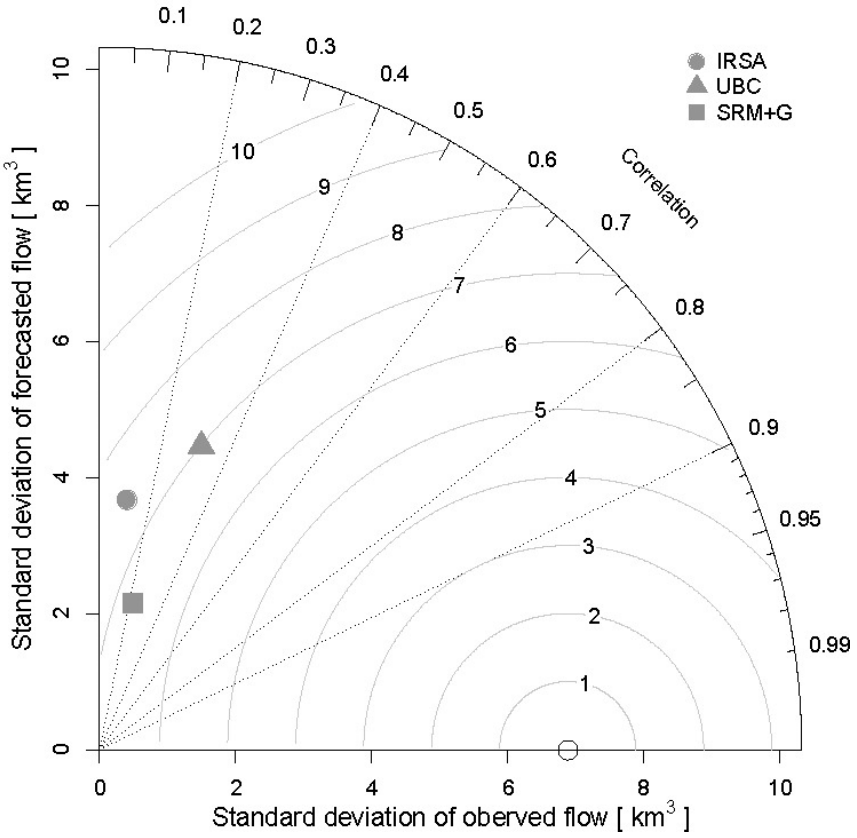

Figure 3.13 Taylor diagram of IRSA, UBC, and SRM+G model performance.

The limits between the categories dry, normal, and wet conditions were defined as 20 and 80% non-exceedance of the observed historic Kharif flow series 2003 – 2016, which corresponds to quantiles of 56.8 and 67.9 km^3, respectively. Obviously IRSA and SRM+G forecasts have no skill in this respect, while UBC shows some, although limited, skill compared to purely random chance.

As only point estimates of IRSA and UBC forecasts were available, the assessment of probabilistic skill only applies to the SRM+G scenario ensembles. Figure 3.14 and Figure 3.15 show typical traces of ensemble members as well as the observed, mean, and historic trace. In most years, the ensemble mean is closer to the observed value than the historic trace.

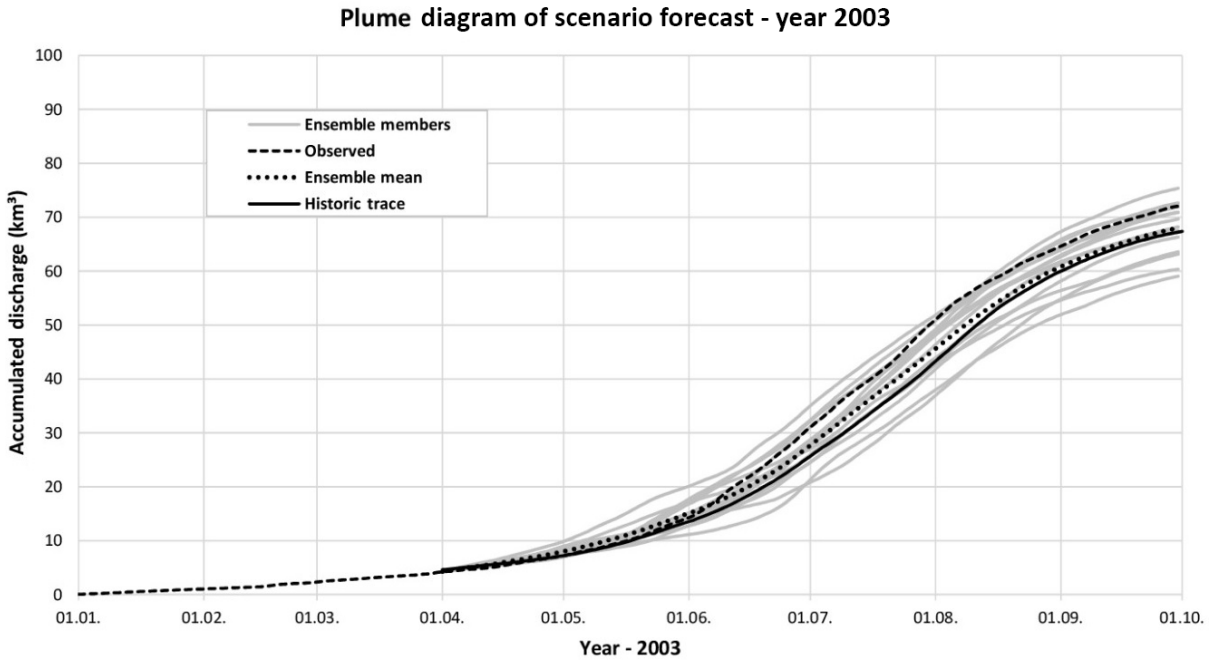

Figure 3.14 Plume diagram of ensemble member traces in 2003.

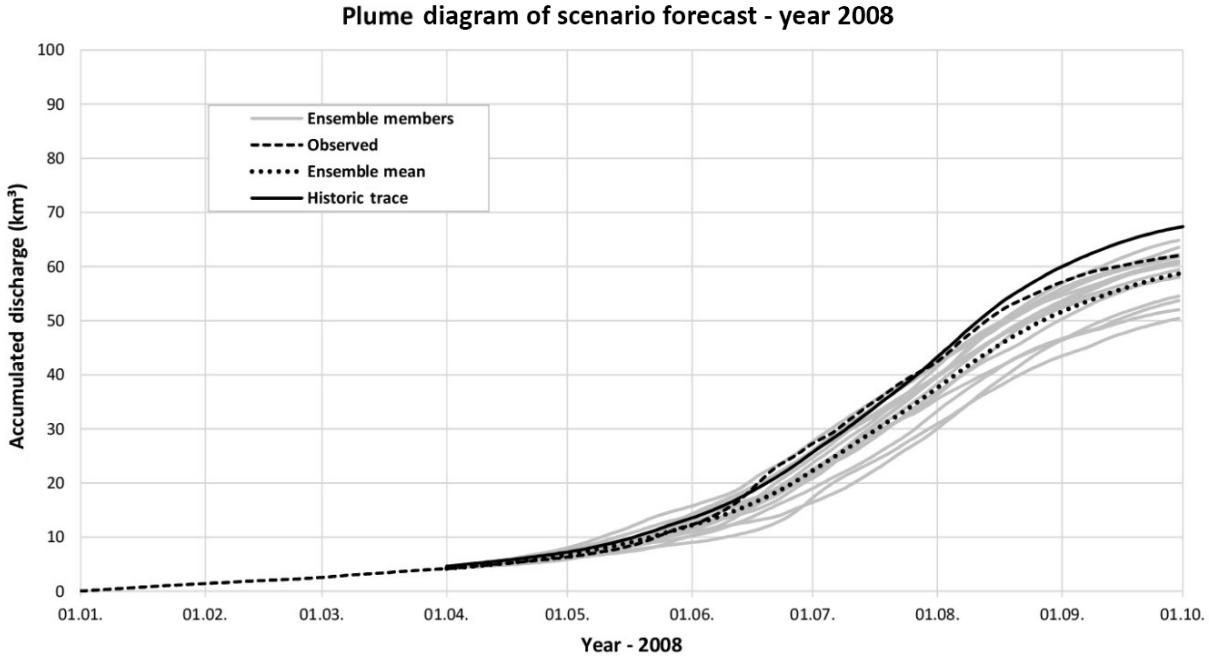

Figure 3.15 Plume diagram of ensemble member traces in 2008.

The RPSS was used to assess the overall performance of the probabilistic forecast. The same category limits as for the Peirce skill score were chosen, i.e. the 20 and 80% quantiles of the observed flow series. As no other probabilistic forecasts were available as reference forecast, the ranked probability score RPS of the scenario forecast ensembles was compared to the climatology, i.e. the average Kharif flow of the observed series of 62.7 km^3. The RPS of scenario forecast ensembles and climatology were 0.370

and 0.462, respectively. The resulting RPSS of 0.20 indicates that the scenario ensemble shows some, however limited, skill and improvement over a constant forecast of the historic average.

The reliability diagram (Figure 3.16) was constructed with the aforementioned three forecast categories: dry (≤56.8 km^3), near normal, and wet (> 67.9 km^3) conditions based on the historic observations and using for each forecast the frequency of ensemble members falling into the respective category. The resulting reliability diagram is relatively rugged and has gaps in several classes, although each forecast category was treated as an individual forecast resulting in 42 scalar forecasts. However, in total there are only 14 observations, which causes the outlier at the forecast probability class 0.6. There were 3 forecasts that fell into this very class but none of the 14 observations. As can be seen from the sharpness diagram, there are also empty forecast classes (0.4 and 0.5), meaning these probabilities have never occurred in any forecast category. Besides the shortcoming of the limited sample size and in particular the outlier, most points are located around the 1 : 1 line indicating that there is no dry or wet bias and that they fall within an acceptable distance. Resolution, although difficult to assess taking the limited number of points, seems to be a bit weak, i.e. with a tendency to over-confidence, which may be caused by the fact that the available scenario years comprise mostly near normal conditions.

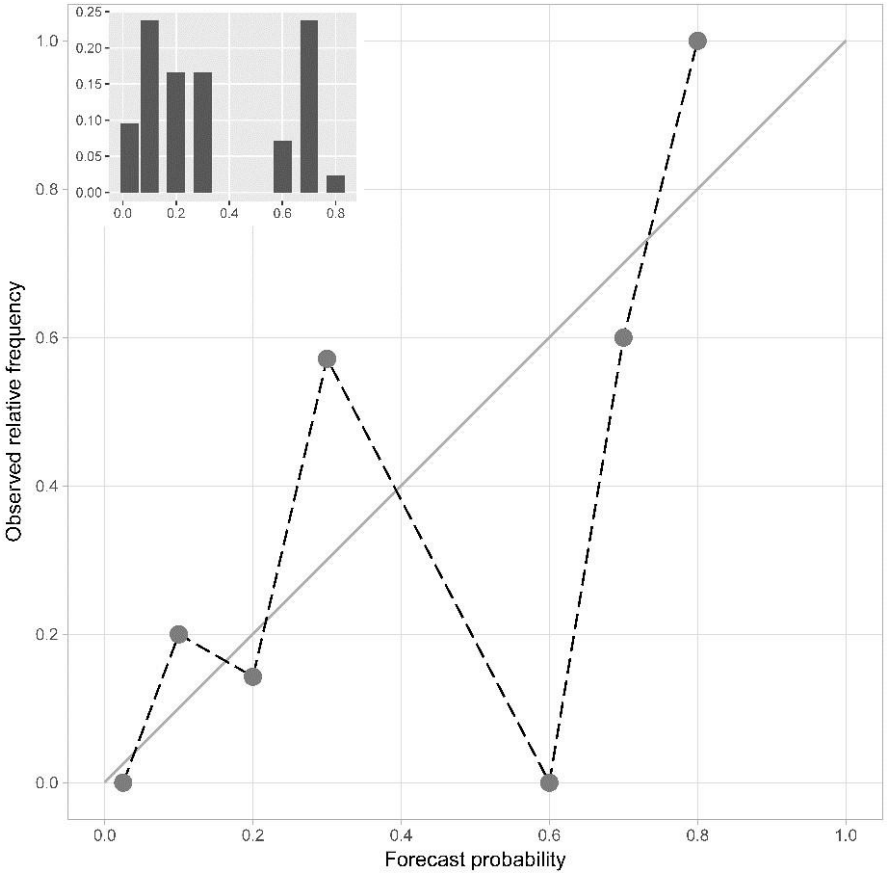

Figure 3.16 Reliability diagram of probability forecasts in the categories dry (≤ 20 %), near normal, and wet (> 80 %) of 2003–2014 flows.

3.4 Conclusions

The SRM was applied to the UIB in order to forecast the total Kharif inflow to the Tarbela reservoir. Several improvements had to be introduced to SRM in order to meet the specific requirements of the UIB.

Not surprisingly, a separate component had to be added to SRM in order to consider the flow component originating from glacier melt. Without this component, especially in the late summer months, there is a lack of water to meet the observed hydrograph. All-year simulation runs with SRM+G for the period 2003–2014 result in an average flow component distribution of 53, 21, or 26% for snow, glacier, or rain, respectively, which fits well to the values found in a number of other studies.

It is well known, that the Tibetan Plateau receives significantly lesser precipitation than the western parts of the UIB. In addition, MODIS data shows that the snow cover is fading away in early spring much faster than in the other parts. In the present study, SRM's modified depletion curve approach for predicting the snow cover depletion during the forecast period has proven to be very sensitive to errors in the estimation of the actual snow-water equivalent. In such cases, it is inevitable to split the catchment into more homogeneous units. Therefore, the superposition of flows from sub-catchments by using a time lag was introduced to SRM+G, which leads to a significant improvement in the forecasts of snowmelt dominated early Kharif flows in particular.

The scenario approach is a step towards probabilistic forecasting of seasonal flows in the UIB. As the accuracy of existing forecasts with a mean volume error of 10.9 and 11.4% is already quite high, the improvement by SRM+G having a MAPE of 9.5% is only limited. The bias, however, could be reduced to -2.0 %. Association between forecasts and observations is rather weak for all three models, just as none of the models has significant skill in predicting extreme dry or wet conditions.

Regarding the scenario approach, it is obvious that as far as the variables precipitation and temperature are concerned, these tend towards the climatology, i.e. the long-term averages. A variance in the forecasts is only introduced by the different estimates of the snow-cover depletion curves for each forecast. Thus, a promising way to improve the association and sharpness of the scenario approach would be a selection of a subset of ensemble members according to forecasted seasonal anomalies in temperature and precipitation. A quick test using only the five lowest, middle, or highest ensemble members selected according to the (known) relative flow frequency of the forecasted year gives promising results, e.g. not only a MAPE of 4.9% but also an AC_u of 0.78 and a PSS of 0.41. The challenge of course is to forecast the seasonal anomaly in temperature and precipitation. In this respect, further research is needed on how today's global forecast systems may allow a more specific selection of ensemble members particularly in the UIB, where the correlation to common teleconnections like the ENSO[8] status is known to be weak.

[8] El Niño Southern Oscillation.

Chapter 4

Comparison of two model calibration approaches and their influence on future projections under climate change in the Upper Indus Basin

Muhammad Fraz Ismail, Bibi S. Naz, Michel Wortmann, Markus Disse, Laura C. Bowling and Wolfgang Bogacki (2020)[1]

Abstract

This study performs a comparison of two model calibration/validation approaches and their influence on future hydrological projections under climate change by employing two climate scenarios (RCP2.6 and 8.5) projected by four global climate models. Two hydrological models (HMs), snowmelt runoff model + glaciers and variable infiltration capacity model coupled with a glacier model, were used to simulate streamflow in the highly snow and glacier melt–driven Upper Indus Basin. In the first (conventional) calibration approach, the models were calibrated only at the basin outlet, while in the second (enhanced) approach intermediate gauges, different climate conditions and glacier mass balance were considered. Using the conventional and enhanced calibration approaches, the monthly Nash-Sutcliffe Efficiency (NSE) for both HMs ranged from 0.71 to 0.93 and 0.79 to 0.90 in the calibration, while 0.57 – 0.92 and 0.54 – 0.83 in the validation periods, respectively. For the future impact assessment, comparison of differences based on the two calibration/validation methods at the annual scale (i.e. 2011 – 2099) shows small to moderate differences of up to 10%, whereas differences at the

[1] **Ismail, M.F.**, Naz, B.S., Wortmann, M., Disse, M., Bowling, L.C., Bogacki, W.: Comparison of two model calibration approaches and their influence on future projections under climate change in the Upper Indus Basin. Climatic Change 163, 1227–1246 (2020). https://doi.org/10.1007/s10584-020-02902-3.

monthly scale reached up to 19% in the cold months (i.e. October – March) for the far future period. Comparison of sources of uncertainty using analysis of variance showed that the contribution of HM parameter uncertainty to the overall uncertainty is becoming very small by the end of the century using the enhanced approach. This indicates that enhanced approach could potentially help to reduce uncertainties in the hydrological projections when compared to the conventional calibration approach.

4.1 Introduction

River basins in high Asia with mountainous headwaters having seasonal storage in the form of snow and ice are vital because they contribute substantially to the water supply in the densely populated lowlands by forming a natural buffer against drought (Pritchard, 2019; Vanham et al., 2008). The Upper Indus Basin (UIB) is one such example that supplies water to the vast Indus plain, often termed the bread basket of Pakistan (Clarke, 2015). It plays an important role in feeding the population of 197 million of Pakistan. But this South Asian region is also a hotspot of climate change which will affect the future water availability (De Souza et al., 2015). The snow and glacier melt–dominated hydrological cycle of the UIB is likely to undergo drastic changes due to the adverse effects of climate change (Hasson, 2016) and it is expected that the flow regime could be radically altered for the UIB (Mukhopadhyay, 2012).

In the last decade, a number of studies have assessed the future water availability from the UIB. For example, (Hasson et al., 2019) showed that when there is no change in glacier area, the annual water availability will increase by 34% and 43% on average in the Himalayan watersheds based on the global warming scenarios of 1.5 °C and 2.0 °C, respectively. But if glacier area is reduced then the overall water availability in the UIB will be reduced under the prevailing climatic conditions (Hasson, 2016). Moreover, (Lutz et al., 2014, 2016) concluded that the future water availability for the UIB is highly uncertain but the basin-wide trends and patterns of seasonal shifts in water availability are consistent across climate change scenarios based on the glacio-hydrological model's simulations. (Lutz et al., 2016) also projected an initial increase in water availability for the UIB in summer months in the early decades of the twenty-first century and a sharp decline at the end of the century due to diminishing glacier coverage. Similarly, (Laghari et al., 2012) concluded that climate change will result in increased water availability in the short term (e.g. < 10 years); however, long term water availability will decrease. Most of these studies suggested that the reduced water availability in the future will be intensified during the spring and summer months, while snowmelt will occur earlier than the main monsoon flows.

Despite these big modelling efforts in recent years, glacio-hydrological projections are still associated with large uncertainties due to insufficient observations and process understanding in snow- and glacier-dominated basins (Pellicciotti et al., 2012), as well as the coarse resolution of global climate models (GCMs) (Vetter et al., 2015). For example, (Krysanova and Hattermann, 2017) investigated the climate

change impacts on river discharge for 12 large-scale river basins and showed that larger uncertainties were associated with global climate projections than hydrological models; however, (Vetter et al., 2015) showed that in melt dominated basins, hydrological models (HMs) also have relatively high contribution to uncertainties in hydrological projections. These uncertainties in the HMs can be attributed to model parameterization (Ragettli et al., 2013), implementation of hydrological processes (Orth et al., 2015) or model calibration and validation approach (Troin et al., 2016). The quantification of different sources of uncertainties is an important factor when it comes to interpreting the results of climate impact studies, because different uncertainty sources could influence projected water availability differently.

Judging the model performance before applying it to impact assessments can be one way to minimize the overall uncertainties but it is still questionable if good model performance in the historical time period should increase confidence in projected impacts and decrease the model related uncertainties. For example, (Coron et al., 2012) argue that good model performance in the historical time period might show lack of robustness when models are used under a changing climate, if the model parameterization is unable to tackle the non-stationarity of future climate data. However, some studies have shown that when the models are calibrated for longer records that include different hydro-climatic periods, they can reasonably simulate the hydrological processes under different climatic conditions (Guo et al., 2018). Some studies have used a variety of approaches to enhance prediction for non-stationary conditions (Vaze et al., 2010). These approaches, for example, include better representation of vegetation processes (Murray et al., 2011), more complex hydrological models (Barnard et al., 2019) or use of different approaches for parameterization and calibration (Merz et al., 2011; Smith et al., 2008). The choice of calibration method has a major impact on a model's ability to represent different processes, especially in glacierized basins, because the compensation effect between runoff generation processes can impact the overall results. Therefore, constraining the snow and glacier melt in hydrological modelling is essential for preventing internal process compensation (Tarasova et al., 2016; He et al., 2018).

In the past, most of the climate change impact assessment studies carried out specifically for the UIB only used a conventional calibration method in which model parameters were adjusted based only on comparison of simulated and observed discharges at the downstream outlet of the catchment (Lutz et al., 2016; Hasson et al., 2019) for one continuous time period. A common assumption implicit in most of these studies is that hydrological models calibrated over the historical period are valid for use in the future under the changed climate conditions. However, to our knowledge, there are no studies for the UIB investigating whether a model calibrated for different climatic conditions (dry/wet periods) will simulate different hydrologic response in future than the model parameterized using the conventional method.

In the present study, we have applied a five-step enhanced calibration/validation method (Krysanova et al. 2018) which (1) takes into account the quality of observational data, (2) utilizes contrasting climate data for calibration, (3) includes comparison of discharge for multiple sub-catchments (i.e. intermediate gauges), (4) includes multi-variable calibration for variables like evapotranspiration, glacier mass balance (GMB) or snow cover area (SCA) and (5) evaluates observed and simulated trends in the observational period.

The aim of this study is to compare two calibration/validation approaches applied to two HMs, and analyse their influence on future climate change impact projections and the HM related uncertainty. The specific objectives are (a) to apply and analyse two model calibration/validation methods (i.e. conventional and an enhanced approach); (b) to compare climate change impacts on discharge using the two model parameterisations; and (c) to assess and compare the contribution of representative concentration pathways (RCPs)', GCMs' and HMs' (based on two calibration/validation methods) uncertainties to the overall uncertainty. To achieve these objectives, two HMs with different model complexities were used. The lumped conceptual snowmelt runoff model + glaciers (SRM + G) (Schaper et al., 1999), which is a glacier-integrated enhanced version of SRM (Martinec, 1975), and the semi distributed process-based variable infiltration capacity (VIC) model (Liang et al., 1994) coupled with a glacier model (VIC-Glacier). Both HMs were applied to the UIB, which has dominant snow and glacier melt regime. For climate change impact assessment the bias-corrected climate scenarios from four GCMs (GFDL-ESM2M, HadGEM2-ES, IPSL-CM5A-LR, MIROC5) driven by two representative concentration pathways (RCPs), which were provided by the ISIMIP project (Hempel et al., 2013; Frieler et al., 2017) were used.

4.2 Materials and methods

4.2.1 Study area

The Indus River is one of the longest flowing rivers in Asia originating from the Tibetan Plateau and ending in the Arabian Sea. During its course, it runs through the Karakoram and Himalayan ranges. The UIB primarily feeds the largest reservoir Tarbela (Supplementary Figure B.1[2]) in Pakistan (Figure 4.1). The UIB upstream of Tarbela has an approximate drainage area of 173345 km^2 spread over three countries, namely China, India and Pakistan (Ismail and Bogacki, 2018). It has a very rugged mountainous terrain with more than 65% of the area above 4000 m.a.s.l. (Supplementary Figure B.2). The glacier area in the UIB is approximately 21000 km^2 (~ 12% of the total UIB area) based on the estimates from the Global Land Ice Measurements from Space (GLIMS) database (Raup et al., 2007).

[2] B in numbering of Figures and Tables means that they are in Supplementary materials – B.

In addition, two sub-basins (Hunza and Astore) were selected for enhanced calibration. More detailed information about the hydro-climatic characteristics of the UIB is given in Supplementary section B1.

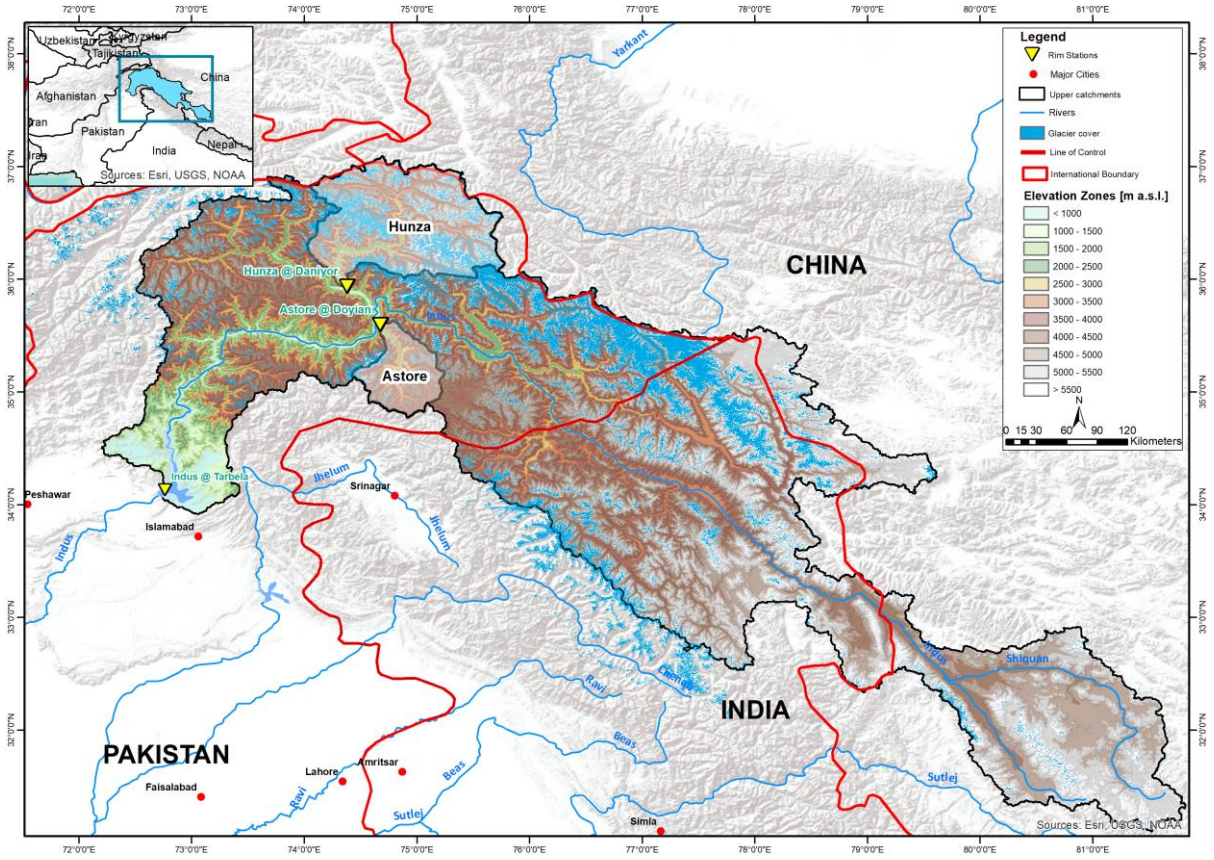

Figure 4.1 Map of the Upper Indus Basin with sub-catchments Hunza and Astore showing different elevation zones and glacier coverage of the whole basin

4.2.2 Hydrological models

Two HMs, SRM + G and VIC-Glacier with different levels of complexity in the implementation of modelled processes, were applied in this study. The overall general comparison between the two models has been summarized in Supplementary Table B.1.

4.2.2.1 SRM+G

The Snowmelt Runoff Model (SRM) (Martinec, 1975) is a lumped, temperature index (TI) model which was designed to simulate the runoff in snowmelt-dominated regions. It has been successfully applied in more than hundred snowmelt-driven basins around the globe (Martinec et al., 2008). In this study, the catchment is sub-divided into elevation zones with 500m intervals (with the exception of the lowest zone, which extends from 432 to 1000 m.a.s.l.). The input data for the SRM consist of daily air temperature, precipitation and SCA, assigned to each elevation zone. SRM calculates snowmelt using the degree-day method. An enhancement of the original SRM approach called SRM+ G has been

introduced by incorporating a separate glacier melt component that considers the area covered by exposed (i.e. not snow-covered) glaciers (Schaper et al., 1999). This extension requires the zonal exposed glacier area for each elevation zone as an additional daily input variable and respective model parameters.

4.2.2.2 VIC-Glacier

The variable infiltration capacity (VIC) model is a macroscale hydrologic model (Liang et al., 1994) which has been successfully applied to many basins in regional and global scale applications e.g. (Huang et al., 2018; Naz et al., 2016) with a spatial resolution ranging from 0.04° to 2°. The VIC model solves full water and energy balances independently for each grid cell within a watershed. A routing algorithm is used to simulate streamflow at a specified location by routing runoff and base flow from each grid cell (Lohmann et al., 1998; Cherkauer et al., 2003). The VIC snow algorithm uses a two-layer energy and mass balance approach to simulate snow accumulation and ablation, including explicit tracking of the energy used for snowmelt and refreezing, and changes to the snowpack heat content (Andreadis et al., 2009). Each VIC model grid cell can be sub-divided into snow elevation bands to represent the effect of sub-grid topography on snow accumulation and melt. As implemented here, the VIC model represents the areal extent of the snow cover based on the assumption that snow fully covers the fractional area of each snow elevation band. To explicitly simulate glacier melt in each grid cell, a novel approach as a third bottom ice layer is introduced to the two-layer VIC snow model (Supplementary Figure B.3). During the model run, the ice thickness is updated at each model time step for each elevation band as a function of net mass balance changes using a similar approach to (Naz et al., 2014) (Supplementary section B3). It is the first time that an energy balance–based glacier model has been incorporated in the original VIC model, hereafter referred to as VIC-Glacier. The glacier movement and short-term storages of meltwater through englacial and sub-glacial drainage system as well as within a firn layer were not directly considered in the model.

4.2.3 Input weather data and climatic change scenarios

The input data required by both HMs include the altitudinal characteristics, temperature and precipitation while the VIC-Glacier model also requires humidity, wind speed and radiation. Ground observations from the Pakistan Meteorological Department (PMD) and the Water and Power Development Authority (WAPDA) were used to check the quality of the gridded EWEMBI[3] climate dataset (Lange, 2018) in the historical period. For the climate impact assessment, the HMs were driven with outputs of four bias-corrected earth system models i.e. GFDL-ESM2M, HadGEM2-ES, IPSL-CM5A-LR and MIROC5 for two representative concentration pathways (RCPs) (i.e. RCP2.6 and

[3] EWEMBI = EartH2Observe, WFDEI and ERA-Interim data Merged and Bias-corrected for ISIMIP

RCP8.5). For the VIC-Glacier model setup, all the above climatic input data were resampled to 0.25° resolution from 0.5° using bilinear interpolation and disaggregated to a 3-hourly temporal resolution. The 3-hourly temperature and downward short- and long-wave radiation data were derived from the daily temperature range and daily total precipitation using methods described in (Nijssen et al., 2001) and daily precipitation data were temporally disaggregated by equally apportioning precipitation to 3-hourly intervals for each grid cell at 0.25° resolution.

4.2.4 Spatial model setup

In SRM + G, the whole basin was sub-divided into 11 elevation zones with an interval of 500 m using NASA's 1-arcsecond Shuttle Radar Topography Missions (SRTM) Digital Elevation Model (DEM) (Supplementary Figure B.2). The MODIS/Terra Snow Cover Daily L3 Global 500 m Grid (MOD10A1) product (Hall et al., 2006) was used to determine the daily SCA after 2000 (Figure B.4). But the historical reference period used for climate change impact was 1976–2005. Therefore, the percentage of SCA before year 2000 and for future time periods was estimated using a new empirical temperature similarity approach based on the assumption that snow cover conditions in an elevation zone are best defined by temperature as described in Supplementary section B5. Mean monthly historical and future temperature for each zone was first compared and then based on the best fit criteria using the optimum Kling-Gupta efficiency (KGE) (Kling et al., 2012) (Supplementary section B6) the relevant zonal SCA was selected from the historical MODIS snow cover data (i.e. 2000 – 2016).

Historical glacier extent was derived from the GLIMS data. The evolution of the exposed glacier area ratio which is required for the SRM + G model is presented in Supplementary Table B.2 and Figure B.5. For future changes in the glacier area, a glacier area reduction scenario was assumed. In this scenario, the glacier area is reduced to 75%in the near future (2011 – 2040), 50% in the mid future (2041 – 2070) and 25% in the far future (2071 – 2099) periods under both RCPs. While in the historical time period, 100% glacier area was used (i.e. no area reduction). Similar assumptions of glacier area reduction for the UIB can be found in (Hasson et al., 2019) and (Hasson, 2016). The assumption that the glacier area will be reduced to 25% at the end of the century is within the range of the results presented in (Lutz et al., 2016), where the simulated mean remaining glacier area under two RCPs (i.e. 4.5 and 8.5) using 4 GCMs for the Hindukush-Himalayan-Karakoram (HKH) region by 2100 was 32% and 15%, respectively. Glacier area is reduced from lower to higher zones successively. SRM + G uses runoff coefficients for snow, glacier and rain in order to account for the losses, which are the differences between the available water volume and the outflow from the basin.

For the VIC-Glacier model, each grid cell is divided into a maximum of 25 elevation bands to represent the effect of topography on precipitation and temperature to account for variability within grid. Within each band, the fractional area, average elevation and fractional precipitation were calculated. The

average elevation of the band was calculated based on the maximum and minimum elevation within each band using the 30m SRTM DEM. To account for the effects of sub-grid topography on precipitation distribution within a grid cell, the precipitation fraction within each band was calculated using precipitation climatology data available at 30 arc second resolution from WorldClim (version 1.4, (Hijmans et al., 2005)) averaged over 1950– 1990. Using the glacier cover extent, average ice thickness values were calculated using the surface slope information derived from the 30 m SRTM DEM for each band (Supplementary section B3, Eq. 1). This information was then used as an input to the VIC-Glacier model in addition to fractional area, average elevation and fractional precipitation for the 25 elevation bands. The areal extent of glaciers in the VIC-Glacier model was based on the estimated extent of snow-covered glacier, clean ice and debris-covered areas of the glaciers from cloud-free Landsat scenes at the end of the melting season available between 1998 and 2002 based on (Khan et al., 2015), which showed a good agreement (i.e. 91% accuracy) with the GLIMS inventory for the central Karakoram region.

4.2.5 Model calibration and validation

Two model calibration/validation methods (i.e. hereafter referred to as conventional and enhanced methods) were applied. Both the HMs were calibrated and validated using the observed inflows at Tarbela using a manual calibration method. For SRM + G, there were 11 parameters to calibrate including the three-runoff coefficients and the separate degree-day factors (DDF_s) for snow and glaciers (Supplementary Table B.3). For the VIC-Glacier model, 5 parameters including the variable infiltration parameter, bi, the three base flow parameters (W_s, D_s, and $D_{s\,max}$), and the snow roughness length were used to calibrate the model. After identification of the sensitive and key parameters for both models, the HMs were first calibrated using the conventional method, i.e. only against discharge at the final outlet gauge as adopted in many previous climate impact studies (Krysanova et al., 2017; Reed et al., 2004). The models were calibrated for 9 years (i.e. 2003–2011) and validated for 8 years over two periods (2000–2002 and 2012–2016). Model performance was judged only on the basis of the model's ability to simulate the discharge at the basin outlet. Secondly, for the enhanced calibration/validation method, the five calibration and validation steps suggested by (Krysanova et al., 2018) were followed, as explained in the following sub-sections.

4.2.5.1 Checking the data quality

Station data was utilized to check the data quality by comparing the observed monthly temperature and precipitation time series with EWEMBI data for the calibration/validation period (i.e. 2000–2016). Both EWEMBI temperature (Supplementary section B7–9) and precipitation (Supplementary section B10) were bias-corrected. In case of temperature, quantile-mapping method (Piani et al., 2010a) was used for bias correction, while for the precipitation; altitude correction approach adopted by (Immerzeel et al., 2015) was used to calculate the bias correction factor. After the bias correction, EWEMBI-based annual

precipitation for the whole UIB averaged for the period 2000–2016 is about 604 mm/year. This value is in the range of previously reported e.g. 675 ± 100 mm/year (Reggiani and Rientjes, 2015) and 608 mm/year (Khan and Koch, 2018).

4.2.5.2 Calibration and validation for contrasting climatic periods

Two different climatic conditions (i.e. cold/dry and warm/wet) within the given time period were identified to calibrate and validate the HMs for these conditions. Calibration and validation of the model in contrasting climates will give more credibility to the fact that the model can perform well in a changing climate (i.e. considering climatic non-stationarity). The available time period was sub-divided into 'dry/cold' and 'wet/warm' periods based on the basin-averaged bias-corrected annual precipitation and air temperature. The periods 2000–2004 and 2008–2010 were then selected as 'dry/cold' and 'wet/warm' respectively (Supplementary Figure B.7).

4.2.5.3 Multi-site calibration and validation

The third step involved the calibration and validation for intermediate gauges. The Daniyor (Hunza) and Doyian (Astore) gauges were selected as intermediate gauges (Figure 4.1).

For multi-site calibration and for different climate periods, an optimal parameter set was identified through an objective function θ formulated as Eq. (4.1):

$$\theta = \left(1 - KGE_{wet\ and\ warm\ period}\right) + \left(1 - KGE_{dry\ and\ cold\ period}\right) \tag{4.1}$$

Where, KGE is calculated from the monthly discharge time series. The KGE for the two distinct climates is a weighted sum of KGEs of all selected gauges (Eq. (4.2) and (4.3)).

$$KGE_{wet\ and\ warm\ period} = \sum_{i=1}^{n} \left(\frac{Area_i}{\sum_{i=1}^{n} Area_i} \times KGE_{i,\ wet\ and\ warm\ period} \right) \tag{4.2}$$

$$KGE_{dry\ and\ cold\ period} = \sum_{i=1}^{n} \left(\frac{Area_i}{\sum_{i=1}^{n} Area_i} \times KGE_{i,dry\ and\ cold\ period} \right) \tag{4.3}$$

Where, n=3 is the number of gauges selected in catchment.

4.2.5.4 Calibration for additional variables

The calibration/validation of an additional variable means that the model shall not only be restricted to observe discharge but also consider other observations such as snow cover area (SCA), glacier mass balance (GMB) or actual evapotranspiration (ET_a) so that internal consistency of the simulated processes can be ensured. In the UIB, the most important discharge component is meltwater generation through snow and glacier melt. Hence, it is essential to take into account the GMB while simulating discharge in order to prevent internal process compensation (Hagg et al., 2006; Finger et al., 2015; He et al., 2018). In case of SRM + G, degree-day factors for the glaciers (a_g) (Table B.3) were manually adjusted to consider the GMB. These calibrated a_g values are well within range compared to earlier studies (Lutz et al., 2016). For SRM + G, GMB is calculated annually by subtracting the glacier melt component from snowfall on to the glaciers. For VIC-Glacier, the net annual GMB is determined from the change in storage states of snow and ice water equivalent at the end of each hydrological year (Supplementary section B11). The model parameters related to snow accumulation/ablation, snow roughness length and temperature lapse rate were manually calibrated to adjust GMB. Literature-based GMB values available for this region (Supplementary Table B.4) were considered for comparing the mean annual mass balance values over the UIB (period: 2000–2016) in the model calibration/validation in order to avoid the compensation effect between glacier and non-glacier runoff.

Secondly, basin-averaged ET_a based on the Global Land Evaporation Amsterdam Model (GLEAM) (Martens et al., 2017; Miralles et al., 2011) was compared with the simulated ET_a of VIC-Glacier and with the losses generated through the runoff coefficients in the SRM + G model.

4.2.5.5 Validation for trends

The Mann–Kendall Trend Test (Mann, 1945; Kendall, 1975) was applied to check for consistently increasing or decreasing monotonic trends in simulated and observed discharges. It should be noted that the hydrological trend analysis should be done with long-term data (e.g. 40 years) but here the trend analysis was performed with only 17 years of available data.

4.2.6 Analysis of uncertainties under climate scenarios

In this study, we have applied the analysis of variance (ANOVA) (Gottschalk, 2005) approach to decompose the sources of uncertainties (Kaufmann and Schering, 2014). Here, we have three different sources of uncertainties including two HMs, four GCMs and two RCPs, so we have applied a three-way ANOVA. It gives the share of uncertainties related to a specific source as well as their interaction terms. A more detailed description of the ANOVA method can be found in (Vetter et al., 2015).

4.3 Results

4.3.1 Calibration and validation of hydrological models

The results for the conventional and enhanced calibration/validation methods based on KGE, NSE and Percent bias (Pbias) criteria are presented in Table 4.1. Overall for the UIB, the monthly KGE values in the calibration/validation period are around 0.86 for the SRM + G model, while for the VIC-Glacier model the KGE values ranged from 0.57 to 0.64 using the conventional method. SRM + G underestimates discharge in the first half of the year when snowmelt is dominating while it overestimates discharge in July–September when the glacier melt comes into effect. VIC-Glacier overestimates peak flows, with under-prediction of winter base flow in many of the calibration years (Supplementary Figure B.8).

Using the enhanced method, the model calibration/validation was performed against discharge of the UIB and intermediate gauges of Astore and Hunza for different climate conditions. Additionally, GMB and ET_a were also considered. The calibration periods of 2000 – 2004 and 2008 – 2010 were selected for the dry and wet climate conditions, respectively.

For the model validation, the remaining years (2005 – 2007 and 2011 – 2016) were selected. In general, for the UIB, both HMs perform well for dry and wet periods with KGE $\geq$ 0.65. For the validation years, the monthly KGE values are 0.91 and 0.65 for the SRM + G and VIC-Glacier HMs, respectively. However, both HMs show relatively weaker performance for the Hunza and Astore basins compared to the whole UIB. The monthly KGE values for both dry and wet periods from both HMs are greater than 0.38 and 0.49 for Hunza and Astore river basins, respectively. For the validation period, the monthly KGE value for SRM + G model is 0.52 in the Hunza basin, while VIC-Glacier model shows weaker performance with KGE value of 0.25. For the Astore basin, SRM+ G shows satisfactory performance with KGE value of 0.64 while VIC-Glacier shows very good performance with KGE value of 0.79 in the validation time period. Some unsatisfactory results for the Hunza and Astore basins show the diversified hydrological regimes of the sub-catchments with Hunza being more glacier dominated and Astore as a snowmelt-driven catchment. In case of SRM + G, the DDFs controlling the snow and glacier melt were shifted and adjusted to achieve adequate results in both the Hunza and Astore basins as well as the whole UIB. Consequently, the results for the sub-catchments are not as good as obtained in previous studies (Tahir et al., 2011, 2016) since they calibrated and validated each catchment separately, while in the present study a single set of parameters was applied to all sub-basins which explains some differences in results.

The unsatisfactory performance of the VIC-Glacier model in the wet and validation periods in the Hunza catchment might be related to the biases in the forcing datasets. While the air temperature in the present study was bias-corrected with station data, for precipitation a single basin-wide multiplication factor

was used. This can lead to degraded model performance (Islam and Déry, 2017), especially in the sub-catchments with complex spatial and temporal variability in precipitation (Archer and Fowler, 2004). Hydrological responses in the UIB can be improved with better quality data particularly for the models that resolve the full energy and water balances such as VIC-Glacier.

In order to constrain melt parameters and achieve higher internal model consistency (Mayr et al., 2013), a comparison of simulated GMB with the literature-based GMB was performed. Simulation for calibration/validation period (i.e. 2000 – 2016) yields GMB values of about -98 mm/year and -83 mm/year for SRM + G and VIC-Glacier, respectively, which is in the range of many previous studies for the Karakoram ranges summarized in Supplementary Table B.4.

The validation for ET_a for the SRM + G model was not a one-to-one comparison as explained earlier (Sect. 3.2.5.4). However, the average annual ET_a modelled by GLEAM (220 mm/year) vs SRM + G losses (258 mm/year) for the calibration/validation period are relatively close (Supplementary Figure B.9). For the VIC-Glacier model, the simulated long-term average annual ET_a is underestimated (125 mm/year) in comparison to GLEAM's ET_a, but these results are well in range compared to the values 200 ± 100 mm/year found in the literature (Reggiani and Rientjes, 2015). Seasonally, the GLEAM-estimated ET_a is generally higher than the VIC-Glacier-simulated ET_a (Supplementary Figure B.10). The differences in the ET_a might be related to different estimation methods used by VIC-Glacier and GLEAM. VIC-Glacier uses an energy balance approach to account for sublimation, and GLEAM calculates sublimation over snow and ice-covered areas using a specific parameterization of the Priestley and Taylor equation (Martens et al., 2017), which highly relied on the quality of the data from satellites products.

The last step was to validate the model for the observed or lack of trend. The trend was calculated for the annual median flows for the outlet. The calculated Mann–Kendall Tau coefficient (τ) for the observed flows (i.e. 2000–2016) was 0.015 while it was 0.38 and 0.45 for SRM + G and VIC-Glacier, respectively. Similarly, the Sen's slope (S) (Sen, 1968) was 1.9, 25.1 and 58.0 [$m^3\ s^{-1}\ year^{-1}$] for the observed, SRM + G and VIC-Glacier respectively. The positive values of τ and S for the simulated and observed discharges show that there are increasing trends. These trends are statistically significant for the simulated discharges ($p < 0.05$ significance level).

After the performance evaluation, a possibility of model weighting for the impact assessment was analysed. Model weighting has been recommended in some studies as a feasible approach in reducing uncertainties in climate impact studies (Greene et al., 2006; Zhu et al., 2013). This technique gives more weights to the more skilful models and lesser weights to the models that do not match the observed dynamics (Vetter et al., 2015). In this study, there are only two HMs so both HMs have been assigned equal weights instead of specific weights. If there were more than two HMs, then it would make more

sense to apply specific weights based on model performance. The calibration/validation results have been summarized as Taylor diagrams (Taylor, 2001) (Supplementary Figure B.11) showing extended performance metrics in addition to Table 4.1.

Table 4.1 Goodness of fit statistics' comparison in the calibration/validation as well as overall time period (conventional and enhanced methods)

Conventional				
	Calibration		Validation	
	SRM+G	VIC-Glacier	SRM+G	VIC-Glacier
Period	2003 – 2011		2000 – 2002 & 2012 – 2016	
NSE	**0.93**	**0.71**	**0.92**	0.57
Pbias	**2.2**	**2.7**	**1.2**	**6.3**
KGE	**0.86**	0.64	**0.86**	0.57

Enhanced						
	Calibration				Validation	
	SRM+G	VIC-Glacier	SRM+G	VIC-Glacier	SRM+G	VIC-Glacier
Period	2000 – 2004 [Dry]		2008 - 2010 [Wet]		2005 – 2007 & 2011-2016	
	UIB					
NSE	**0.90**	**0.82**	**0.87**	**0.79**	**0.83**	0.54
Pbias	**-4.3**	**-7.7**	**4.4**	**-0.9**	**1.7**	**11.3**
KGE	**0.93**	0.73	**0.92**	0.65	**0.91**	0.65
	Hunza					
NSE	**0.77**	0.55	0.65	*-0.23*	0.60	*-1.2*
Pbias	**6.9**	14.2	*18.4*	15.9	*18.0*	*34.8*
KGE	**0.85**	0.67	0.61	*0.38*	0.52	*0.25*
	Astore					
NSE	**0.77**	*-0.25*	0.61	*0.49*	**0.71**	**0.72**
Pbias	*-24.9*	*45.0*	**4.1**	-16.1	*-23.6*	**-3.2**
KGE	0.64	0.49	**0.80**	0.54	0.64	**0.79**

Period [2000 – 2016] - UIB	Conventional		Enhanced	
	SRM+G	VIC-Glacier	SRM+G	VIC-Glacier
NSE	**0.88**	0.65	**0.86**	0.66
Pbias	**1.9**	**4.6**	**0.5**	**3.9**
KGE	**0.88**	0.61	**0.93**	0.62

Note: Very good; good (bold); Satisfactory (normal); Unsatisfactory (italic)

4.3.2 Evaluation of climate change scenarios

To assess the climate change scenarios, three periods 2011 – 2040 (near), 2041 – 2070 (mid) and 2071 – 2099 (far) were compared to the historical period 1976 – 2005. The changes in bias corrected precipitation and temperature were evaluated and compared between the historical and future periods for the UIB (Supplementary Figure B.12). The long-term annual median precipitation based on 4 GCMs in the historical period is about 620 mm. In the RCP2.6 scenario, the change in the average annual precipitation is in the range of 2 to 6% for all 3 future periods while it ranges between 6 and 15% for RCP8.5 with the highest increase at the end of the century.

Long-term changes in air temperature range from 1.4 to 2.0 °C and 1.7 to 6.2 °C for RCP2.6 and RCP8.5, respectively (historical median is close to 0 °C). The highest projected increase in the median temperature is more than 6 °C compared to the historical period for RCP8.5 by the end of the current century.

4.3.3 Impacts on the long-term mean annual and seasonal dynamics

Both HMs were run for the period 1976 – 2099 forced by four GCMs and two RCPs. In total, 24 time series were obtained for each HM (i.e. based on four GCMs, two RCPs, two calibration/validation methods, plus 8 historical runs for two calibration/validation methods), which were then analysed for the long-term mean annual and seasonal dynamics as shown in Figure 4.2a and Figure 4.2b.

The combined long-term projected changes in discharge from both HMs show contrasting trends for two RCPs and between two calibration/validation methods (Figure 4.2a). The largest increases in discharge are projected for RCP8.5 in the mid-century (median: 15%) and far future (median: 19%) based on the enhanced method, and the median changes based on two methods differ in sign for RCP2.6 in all periods and for RCP8.5 in the near future.

The comparison of differences between the mean impacts based on two methods at the annual scale (Figure 4.2a) shows minor to moderate differences in impacts based on these two methods for both RCPs and for all three future periods, with a maximum difference of about 9% for RCP2.6 and 10% under RCP8.5 in the far future scenario (Supplementary Table B.5).

However, at the monthly time scale, there are moderate to large differences in impacts between simulations based on the two calibration/validation methods, especially in the cold months (Supplementary Table B.5). The largest differences were found in October–November (6 – 9%) in all periods under RCP2.6, and in March (-8%, -17%) and October–November (8 – 9%, 18 – 19%) in the mid and far future periods, respectively, under RCP8.5. The simulated seasonal impacts are different based on these two calibration/validation methods especially for RCP8.5.

The projected monthly changes in discharge (Figure 4.2b, comparison of the long-term mean monthly flows for historical and future periods are also shown in Supplementary Figure B.13) indicate an increase in discharge in the low flow season (October – March) for all three future periods and both RCPs. An increase in flows is projected in the early spring months where most of the water is contributed by snowmelt. In the high flow season (July – September), there is a projected decrease in discharge for all three future periods. The projected decrease in late summer flows is mainly because of the decrease in glacier melt which is indicated by both the HMs (Table 4.2). This change in water availability for the high flow season will ultimately impact the overall water availability which is also

evident in Figure 4.2b. Figure B.14 in Supplementary shows a comparison of projected changes in total discharge simulated by both HMs. There are rather small median changes (maximum: 7%) simulated by SRM + G for both RCPs in all periods and by VIC-Glacier for RCP2.6 in all periods and RCP8.5 in near future. However, quite significant increases (31 – 43%) are projected by VIC-Glacier under RCP8.5 in the mid and far future periods (Table 4.2). These differences reflect the differences in glacier parameterization in the two models. The future SCA percentages within SRM + G as estimated by the temperature similarity approach were 35% and 45% lower for RCP2.6 and RCP8.5, respectively, when compared to the historic time period (Supplementary section B5), whereas, VIC-Glacier explicitly models the changes in snow/glacier area as a result of snow and glacier melt within a given elevation zone of a grid cell.

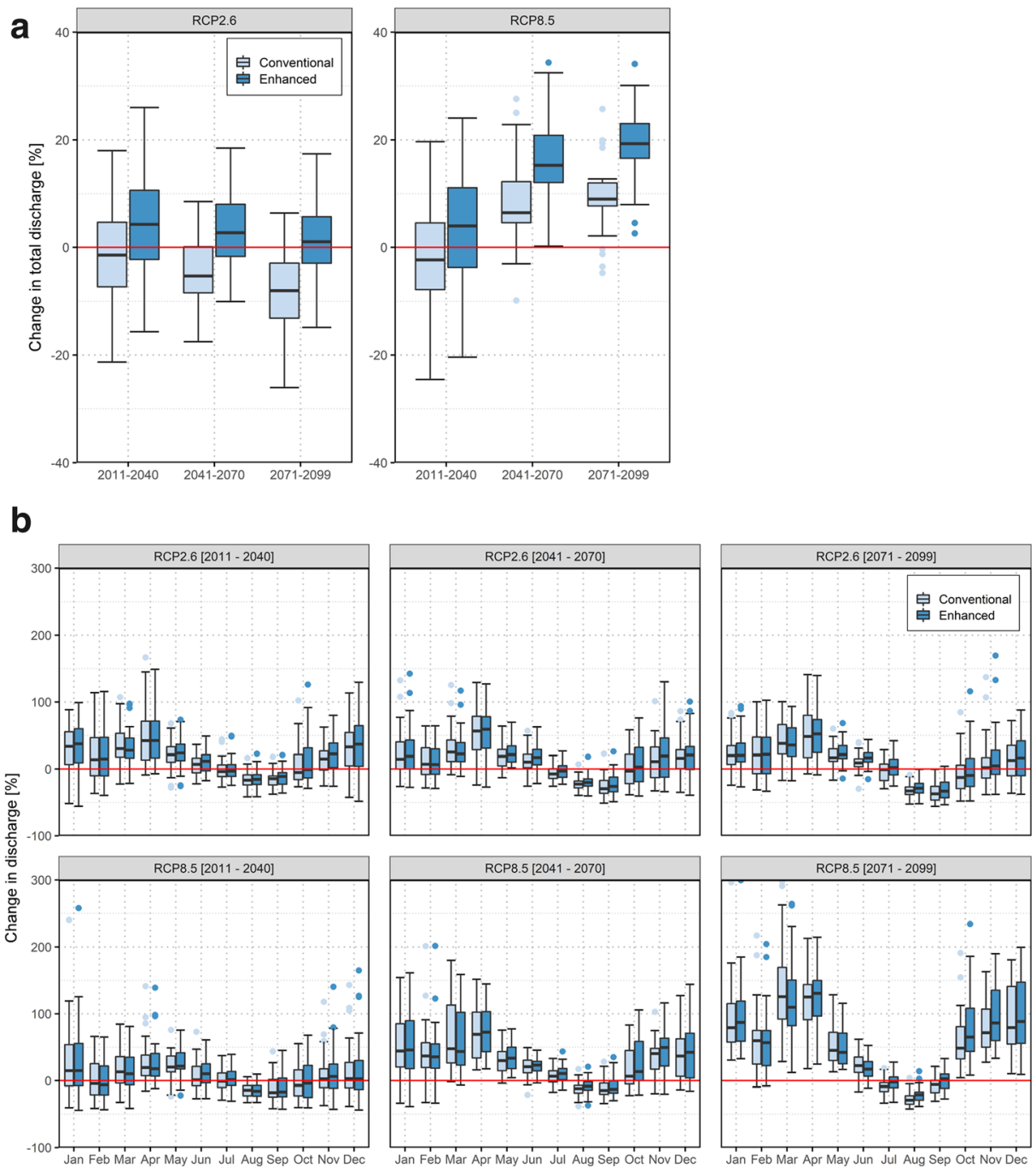

Figure 4.2 (a) Projected changes in the long-term mean annual discharge under RCP2.6 and 8.5 for future periods based on both calibration/validation methods using two HMs and four GCMs. (b) Projected changes in the mean monthly discharge for the near, mid and far future periods compared to the historical period based on both calibration/validation methods under both RCPs for two HMs using four GCMs

4.3.4 Discharge components for the UIB

In order to assess the hydrological regime changes for different flow components (i.e. snowmelt, glacier melt and rainfall) under the climate change scenarios, analysis of meltwater contribution to annual

discharge has been performed separately for the two HMs (Supplementary Figure B.15 and Table 4.2). For the SRM + G model, the snowmelt, glacier melt and rain contributions to river discharge at Tarbela for the historical time period (1976 – 2005) are about 48%, 25% and 27%, respectively. These contributions are similar to the earlier studies (Mukhopadhyay and Khan, 2015). For RCP2.6, there is a projected increase in snowmelt ranging from 5 to 6% compared to the historical period (Table 4.2). The rainfall contribution increased by 36 – 40%. In case of glacier melt, large decreases ranging between -28 and -79% are projected. Moreover, for RCP8.5, snowmelt contribution initially increased a little in the near future and then decreased by -12 to -36% in the mid and far future periods. The rainfall contribution is projected to increase by 20 – 67%, while the contribution due to glaciers decreases by -19 to -45%.

For the VIC-Glacier model, the snowmelt, glacier melt and rain contributions to total discharge are estimated to be about 29%, 31% and 40%, respectively, in the historical period. There is a projected increase in snowmelt contribution ranging from 35 to 42% under RCP2.6 and 35 – 68% under RCP8.5, whereas the contribution from the rainfall increases by 15 – 17% under RCP2.6 and 16 – 58% under RCP8.5. Glacier melt contributions in the future decrease by -77 to -93% under RCP2.6 and -73 to -77% under RCP8.5. These changes are consistent with the previous projections of changes in glacier and snowmelt in the UIB (Lutz et al., 2016).

Although two HMs apply different modelling approaches (Sect. 3.2.4), both show a similar behaviour towards the changes in the glacier melt contribution. It should be noted that SRM+ G assumed a glacier area reduction to 25% till the far future period, whereas VIC-Glacier explicitly modelled the glacier area as a result of glacier ablation within a given elevation zone.

An important contrast to highlight, in SRM+ G, these decreases in glacier melt are mandated by the imposed decrease in glacier area, while in the VIC-Glacier model this reflects simulated change in storage. However, the contradictory trends in projected changes in snowmelt between the two HMs could be due to the fact that SRM+ G uses temperature index while VIC-Glacier is employing the two snow layer energy balance approach and explicitly simulates the snow sublimation, as well as differences in the lapsing of temperature which controls the partitioning of precipitation into snow and rain components.

Table 4.2 Change in different flow components with reference to the historical period for both the models under RCP2.6 and 8.5 scenarios using enhanced method

Scenario	RCP2.6 [Δ]							
Models	SRM+G [%]				VIC-Glacier [%]			
Periods	ΔQ_T	Glacier	Snow	Rain	ΔQ_T	Glacier	Snow	Rain
2011 - 2040	7.2	-28.5	5.7	36.6	0.6	-77.2	35.4	15.6
2041 - 2070	1.5	-52.8	5.6	40.5	5.1	-85.4	41.4	17.1
2071 - 2099	-0.8	-79.5	6.0	39.4	3.5	-93.1	41.7	16.6
	RCP8.5 [Δ]							

2011 - 2040	3.5	-19.1	0.1	20.3	5.5	-73.1	35.5	15.8
2041 - 2070	-0.5	-25.6	-11.9	42.9	31.1	-74.5	68.0	36.6
2071 - 2099	-5.1	-44.7	-35.6	67.4	43.2	-77.1	67.1	57.5

4.3.5 Contribution of sources of uncertainty

The sources of simulation uncertainty were analysed by the ANOVA method as applied by (Vetter et al., 2015). The sum of squares for different sources of uncertainty for each 30-year period for the mean discharge has been summarized (Figure 4.3). The uncertainty contributions from different sources (i.e. HMs, RCPs, GCMs and interactions) vary but the overall result shows that the uncertainty increases from near to far future. For the enhanced method, the uncertainty contribution from the HMs becomes very small towards the end of the century, compared to the conventional method (Figure 4.3). But in the near future, HM uncertainty contribution is larger for the enhanced method which is most likely related to the differences in timings of peak flow in two HMs for two calibration methods. For example, VIC-Glacier simulates the peak discharge in July–August under both calibration methods, while SRM+ G simulates the peak in July–August in the conventional and June–August in the enhanced method. This could explain the larger HM uncertainty based on the enhanced method in the first period.

Regarding the RCPs, initially, the uncertainty contribution in the near future period is close to zero but it increases for the far future time period as the scenarios diverge. The GCMs uncertainty contribution is higher for the mid future period than the near and far future periods. The 1st and 2nd order interactions between the HMs, RCPs and GCMs also show an increased uncertainty contribution from near future to far future scenarios, whereas, the residual sum of squares which is the portion of total variability that is not explained by the model decreases from near to far future.

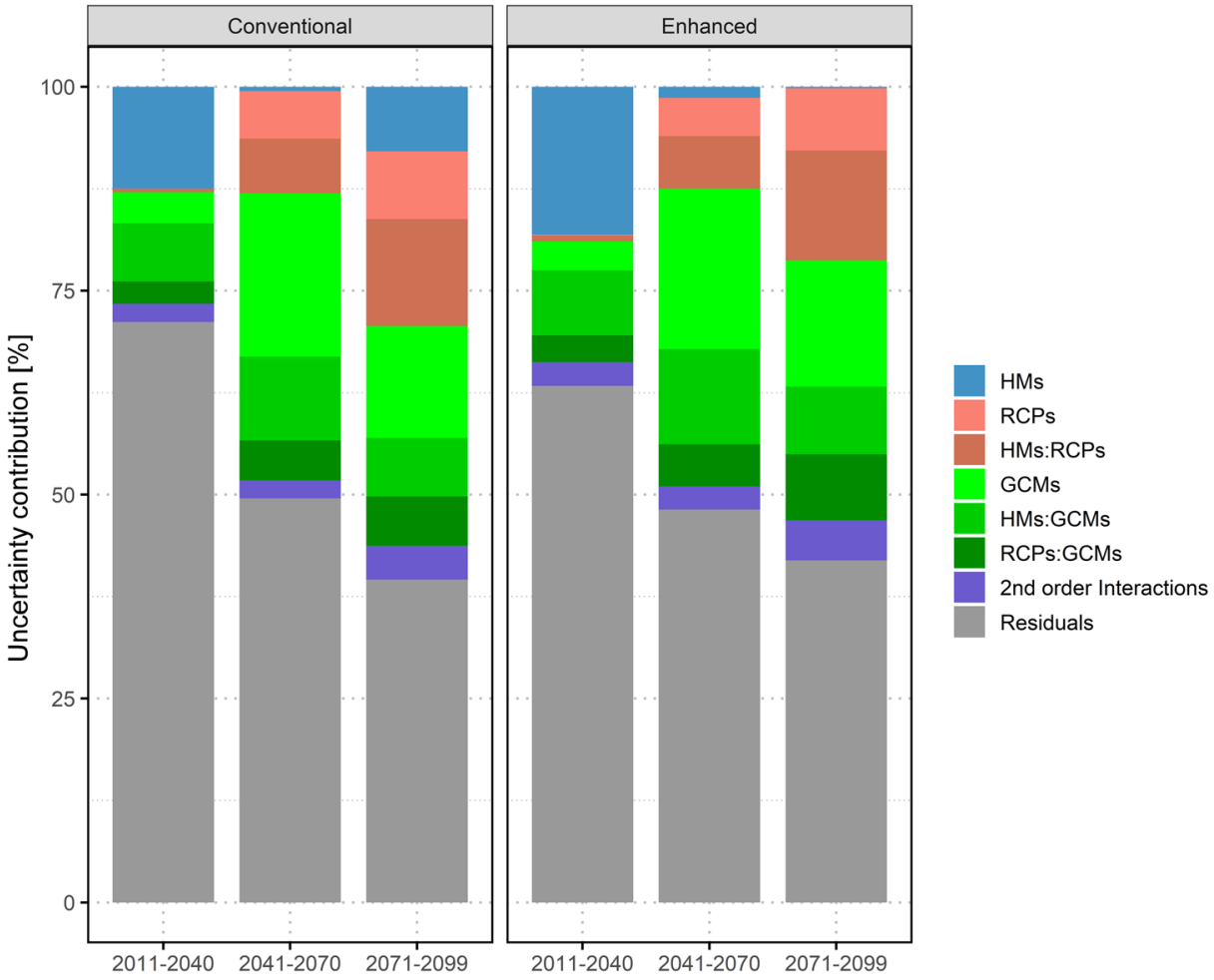

Figure 4.3 Comparison of contribution of different sources of uncertainties in future periods for model projections based on both calibration/validation methods: conventional and enhanced

4.4 Discussion and conclusions

This paper analyses and quantifies the influence of two calibration/validation strategies on future projections for the UIB. By comparing the two approaches for the same catchment, the main outcome is increased confidence in the projections generated using the enhanced calibration/ validation method. The impact results based on the enhanced method are more credible because in this method, (i) calibration parameters were tested for intermediate gauges as well as for the contrasting climatic conditions, (ii) GMB was considered in model calibration/ validation and (iii) model parameters remained homogenous throughout the catchment. It is true that discharge for the intermediate gauges was better reproduced in previous studies (Hayat et al., 2019) but our weaker results can be attributed to the fact that in previous studies the intermediate gauges were separately calibrated and validated. Calibrating for the contrasting climate in the enhanced method can help to address climate non-stationarity (Vaze et al., 2010) by giving more assurance that the model with these parameters is more

suitable to variable climate conditions. The enhanced method also addressed to some extent problems related to equifinality by validating for additional variables (e.g. ET_a and GMB).

It can also be concluded that the uncertainty contribution from the HMs is getting smaller for projections simulated using the enhanced method compared to the conventional method, except for the near future (Sect. 3.3.5). The two different parameterizations for the HMs provided quite different impact assessment results under RCP8.5. As the enhanced method is considered more reliable, impacts based on this method are more trustworthy. Different HMs might give different signals for projected hydrological change, especially for the different flow components as shown here, where one model showed increased snowmelt and the other decreased. It is recommended to use a multi-model ensemble for impact assessment in order to minimize the model-related uncertainties.

The assessment of the hydrological regime changes in the UIB is a complex subject because it involves snow and glacier melt dominated processes and uncertainties related to these methods. There exist different estimates on the contributions from glacier and snowmelt for the UIB in the literature. Recently, some studies for the UIB showed that there is an increase in overall discharge. For example, (Hasson et al., 2019) suggested that in the UIB, future flow will increase from 34 to 43%, while assuming that glacier areas remain unchanged. But if it is assumed that glacier area will decline in the future then ultimately flows will show a negative trend (i.e. UIB discharge will reduce to roughly 8% under RCP4.5) (Hasson, 2016). Moreover, (Lutz et al., 2016) also concluded that there could be both rising as well as falling trends for the water availability in the UIB ranging from -15 to 60% by the end of the twenty-first century under RCP4.5 and 8.5, based on a different GCM ensemble and for different areal extent of the UIB.

Bearing in mind that the focus of this study is the comparison of different calibration strategies in a mountainous catchment, we have to admit that some assumptions in the modelling had certain shortcomings (due to data scarcity and data quality problems in this region) for an accurate estimation of future contributions of snow and glacier to river discharge. For example, in the VIC-Glacier model, the change in glacier area is explicitly modelled as a result of glacier ablation within a given elevation zone of a grid cell, although no glacier movement to lower elevations is simulated. As a result, the decrease in glacier area is likely overestimated which may also contribute to the strong decrease in glacier melt contribution by end of the century (more than 70%). In SRM + G, this is overcome by forcing future glacier area reduction based on results of previous studies on glaciological modelling. We acknowledge that if different glacier area reduction scenarios had been considered for each RCP, then the outcome would have been different. Thus, a precise assessment of existing glaciers tipping point is critical for assessing the future water availability.

Long-term mean annual GMB as simulated by SRM + G in the historical period (1976 – 2005) is about -86 mm/year, with similar trends in future periods ranging between -52 and -15 mm/year, and -85 and -74 mm/year for RCP2.6 and RCP8.5, respectively (Supplementary Figure B.16). For VIC-Glacier, the long-term historical mean annual GMB is about 0.62 mm/year. While for the future period, it ranges between 22 and 44 mm/year and -125 and 3 mm/year for RCP2.6 and RCP8.5, respectively (Supplementary Fig. S16). Simulated GMB for the calibration/validation period (2000 – 2016) is comparable to earlier studies (Bolch et al., 2017; Muhammad et al., 2019) for the Karakoram ranges (Supplementary Table B.4). The use of different datasets and time periods as well as different size of study areas is among the potential reasons for differences between the modelled GMB results compared to previous studies. Although our knowledge of snow/glacier changes and their responses to climate forcing is still incomplete, consideration of GMB in the enhanced method makes the simulated glacier melt contribution more credible. However, it is important to note that presently the glacier evolution is not explicitly modelled in both HMs. A dynamic representation of glaciers in a HM would be better suited to simulate future glacio-hydrological changes in such a catchment (Wortmann et al., 2019).
Moreover, the procedural gap like the unavailability of simulated actual evapotranspiration (ET_a) data from SRM + G model was handled by using model losses as a proxy for ET_a. Besides, a new temperature similarity approach was used to estimate the future depletion of snow cover in the catchment, which can be improved by taking into account seasonal snow accumulation. This is to say that the models used here can be further improved for a more accurate assessment of future water availability but are used here to demonstrate the influence of different calibration strategies on projection of discharge.

The main conclusions from this study can be summarized as follows:

- The model parameterization achieved in the enhanced calibration/validation method is better suited for climate change impact assessment because these parameters were tested at three gauges under different climate conditions and GMB was also given due consideration.
- Calibration/validation for multiple variables (i.e. discharge, GMB, ET_a) leads to more accurate simulation of hydrological processes with little sacrifice of model performance in terms of goodness of fit statistics.
- Two different parameterizations of the HMs lead to different impact assessment results at the mean monthly and annual scales reaching up to 19% and 10%, respectively. We consider the impacts based on the enhanced method more credible.
- According to the analysis of variance, the contribution of HM parameter uncertainty to the overall uncertainty becomes very small by the end of the century based on the enhanced calibration/validation approach.

Chapter 5

Estimating degree-day factors based on energy flux components

Muhammad Fraz Ismail, Wolfgang Bogacki, Markus Disse, Michael Schäfer and Lothar Kirschbauer (2022)[1]

Abstract

Melt water from snow and ice dominated mountainous catchments is a valuable source of fresh water in many regions. Seasonal snow cover and glaciers act like a natural reservoir by storing precipitation during winter and releasing it in spring and summer. Snowmelt runoff is usually modelled either by energy balance or by temperature-index approaches. The energy balance approach is process-based and more sophisticated but requires extensive input data, while the temperature-index approach uses the degree-day factor (*DDF*) as key parameter to estimate melt merely from air temperature. Despite its simplicity, the temperature-index approach has proved to be a powerful tool for simulating the melt process especially in large and data scarce catchments.

The present study attempts to quantify the effects of spatial, temporal, and climatic conditions on the *DDF*, in order to gain a better understanding which influencing factors are decisive under which conditions. The analysis is physically based on the individual energy flux components, however approximate formulas for estimating the *DDF* are presented to account for situations where observed data is limited. A detailed comparison between observed and estimated *DDF* values yielded a fair agreement with BIAS= 0.2 mm $°C^{-1}$ d^{-1} and RMSE=1.1 mm $°C^{-1}$ d^{-1}.

[1] **Ismail, M. F.**, Bogacki, W., Disse, M., Schäfer, M., and Kirschbauer, L.: Estimating degree-day factors based on energy flux components, The Cryosphere Discuss. [preprint], https://doi.org/10.5194/tc-2022-64, in review, 2022.

The analysis of the energy balance processes controlling snowmelt indicates that cloud cover and under clear sky snow albedo are the most decisive factors for estimating the *DDF*. The results of this study further underline that the *DDF* changes as the melt season progresses and thus also with altitude, since melting conditions arrive later at higher elevations. A brief analysis of the *DDF* under the influence of climate change shows that the *DDFs* are expected to decrease when comparing periods of similar degree-days, as melt will occur earlier in the year and albedo is then likely to be higher. Therefore, the *DDF* cannot be treated as a constant parameter especially when using temperature-index models for forecasting present or predicting future water availability.

5.1 Introduction

Melt water from snow and ice dominated mountainous basins is a unique source of fresh water in many regions. Seasonal snow cover and glaciers act as natural reservoirs which significantly affect catchment hydrology by temporarily storing and releasing water on various time scales (Jansson et al., 2003). In such river basins, snow and glacier melt runoff modelling is a valuable tool when predicting downstream river flow regimes, as well as when assessing the changes in the cryosphere associated with climate change (Hock, 2003). Therefore, a most accurate quantification of the melt processes and related parameters is the key to a successful runoff modelling for the prediction of present and future water availability.

Two different approaches are common in snowmelt runoff modelling. The energy balance approach is process-based however data-intensive, since melt is deduced from the balance of in- and outgoing energy components (Braithwaite, 1995; Arendt and Sharp, 1999). On the contrary, temperature-index or also-called degree-day models merely use the air temperature as an index to assess melt rates (Martinec, 1975; Bergström, 1976; Quick and Pipes, 1977; DeWalle and Rango, 2008). The relationship between temperature and melt is defined by the degree-day factor (*DDF*) (Braithwaite, 2008), which is the amount of melt that occurs per unit positive degree-day (Braithwaite, 1995; Kayastha et al., 2003; Martinec et al., 2008). There are different methods by which the *DDF* can be determined, e.g. by measurements using ablation stakes (Zhang et al., 2006), using snow lysimetric outflows (Kustas et al., 1994), by estimating daily changes in the snow water equivalent (Martinec, 1960; Rango and Martinec, 1979, 1995; Kane et al., 1997), or using satellite based snow cover data (Asaoka and Kominami, 2013; He et al., 2014).

Because sufficient direct observations are typically lacking in large catchments, the *DDF* is usually treated as a decisive parameter subject to model calibrations. Most commonly, for calibrating the *DDF*, runoff is used (Hinzman and Kane, 1991; Klok et al., 2001; Luo et al., 2013; Bogacki and Ismail, 2016). However, it is also important to note that the calibration of the *DDF* can be significantly affected by other model parameters due to their interdependency (Gafurov, 2010; He et al., 2014).

Snowmelt runoff modelling using the degree-day approach is very common (Hock, 2003) and popular since air temperature is an excellent surrogate variable for the energy available in near-surface atmosphere that governs the snowmelt process (Lang and Braun, 1990). Despite its simplicity, this approach has proved to be a powerful tool for simulating the complex melt processes especially in large and data scarce catchments (Zhang et al., 2006; Immerzeel et al., 2009; Tahir et al., 2011; Lutz et al., 2016).

Extensive research has been devoted to the enhancement of the original degree-day approach. Braun, (1984) introduced the Temperature-Wind-Index method by inclusion of a wind-dependent scaling factor. A hybrid approach, which combines both, temperature-index and energy balance methods was introduced by Anderson, (1973). Hock, (1999) attempted to improve the simple temperature-index model by adding a term to consider potential incoming direct solar radiation for clear sky conditions. The potential clear sky solar radiation is calculated as a function of position of the sun, geographic location and a constant atmospheric transmissivity (Hock and Noetzli, 1997; Hock, 1999). This model is comparable with the data requirements of a simple degree-day model. Pellicciotti et al., (2005), considered the net shortwave radiation instead of just incoming shortwave radiation by including snow albedo in their proposed degree-day model. Although all these enhancements focus on adding more physical foundation to the original degree-day method, the classical approach is still more popular because of its simplicity and merely dependence on air temperatures.

A weakness of the degree-day approach is the fact that it works well over longer time periods but with increasing temporal resolution, in particular for sub-daily time-steps, the accuracy decreases (Lang, 1986; Hock, 1999). In addition, the spatial variability of melt rates is not modelled accurately as usually the *DDFs* are considered invariant in space. However, melt rates can be subject to substantial small-scale variations, particularly in high mountain regions due to topography (Hock, 1999). For example, topographic features (e.g. topographic shading, aspect and slope angles) including altitude of a basin can influence the spatial energy conditions for snowmelt and lead to significant variations of the *DDF* (Hock, 2003; Marsh et al., 2012; Bormann et al., 2014). Under otherwise similar conditions, *DDFs* are expected to increase with increasing elevation, with increasing direct solar radiation input and with decreasing albedo (Hock, 2003).

Obviously, the *DDF* cannot be treated as a constant parameter as it varies due to the changes in the physical properties of the snowpack over the snowmelt season (Rango and Martinec, 1995; Prasad and Roy, 2005; Shea et al., 2009; Martinec et al., 2008; Ismail et al., 2015). The spatio-temporal variation in the *DDF* (Zhang et al., 2006; Asaoka and Kominami, 2013) not only affects the accuracy of snow and ice melt modelling (Quick and Pipes, 1977; Braun et al., 1993; Schreider et al., 1997) but also is a key to estimate heterogeneity of the snowmelt regime (Hock, 1999, 2003; DeWalle and Rango, 2008; Braithwaite, 2008; Schmid et al., 2012). Since the melt depends on energy balance processes, changes in *DDFs* are a result of energy components that vary with different climatic conditions (Ambach, 1985;

Braithwaite, 1995). Another topic that needs attention is the stationarity of the *DDF* under climate change (Matthews and Hodgkins, 2016). Future water availability under climate change scenarios is typically modelled with *DDFs* calibrated for the present climate, which increases the parametric uncertainty introduced by the hydrological models (Lutz et al., 2016; Ismail and Bogacki, 2018; Hasson et al., 2019; Ismail et al., 2020).

In order to allow for a more process-based estimate of the *DDF*, the present study attempts to quantify the contribution of each energy balance component to melt and subsequently to the overall *DDF*. Considering that degree-day models are typically utilised in large catchments with data scarce conditions, energy balance components are approximated by formulas with minimum data requirement following the approach by Walter et al., (2005). Based on these formulas, the *DDF* contribution corresponding to the respective energy components is quantified in tables and graphs for common snowmelt conditions, which can be used for a rapid appraisal. The presented approach is open in the sense that if for any of the energy balance components observed data is available or more sophisticated models are desired, these can easily replace each of the presented approximations.
It shall be emphasised, that the objective of this study is not to incorporate an energy balance based *DDF* approach into temperature index models. The aim is rather to gain a quantitative idea how different factors affect the *DDF* in order to obtain a good estimate and realistic limits for calibration of this model parameter as well as to predict changes during the melt season in case of forecasting or due to the effects of climate change.

5.2 Study area

The study area covers the Dreisäulerbach catchment, which is a part of Isar River system lies in the sub-alpine region of Bavaria in the Ammergauer Alps. It is approximately located between latitudes 47°34’55”– 47°35’05” North and longitudes 10°56’40”–10°57’07” East. It covers an area of about ~2.3 km^2 and has a mean hypsometric elevation of just over 1200 m a.s.l. (Figure 5.1). The elevation ranges from about 950 m a.s.l at Linderhof gauging station up to 1768 m a.s.l at the Hennenkopf.

The area is mostly made up by south facing slopes, but also contains northern slopes in southern parts of the catchment (Kopp et al., 2019). The catchment is densely forested which during the winter season is fully snow-covered. The mean annual temperature in the observation period (i.e. November 2016 – May 2021) is about 5.8 °C and the long-term mean annual precipitation at the Ettal-Linderhof station of the Water Science Service Bavaria is reported to be 1676 mm (Kopp et al., 2019).

In order to observe the seasonal snow dynamics, snow measurement instruments in addition to standard meteorological station has been installed at the Brunnenkopfhütte at an elevation of 1602 m a.s.l. (see Figure 5.2). The installed station has various sensors including temperature, pressure, wind, solar

radiation (incoming, outgoing), snow depth, snow scale, snowpack analyzer and pluviometer. Table 5.1 summarize the observed monthly meteorological data at Brunnenkopfhütte station.

Table 5.1 Observed monthly average meteorological data – (Brunnenkopfhütte: November 2016 – May 2021)

Variables	Jan	Feb	Mar	Apr	May	Jun	Jul	Aug	Sep	Oct	Nov	Dec
T_a (°C)	-2.48	-0.41	0.52	4.14	6.76	12.40	13.62	14.22	9.69	7.72	3.06	0.08
P [mm]	230.2	147.3	138.8	115.1	188.0	185.4	216.5	241.5	183.7	162.4	107.2	195.9
u (ms^{-1})	1.08	1.01	1.10	0.97	0.71	0.60	0.59	0.59	0.60	0.79	1.02	1.00
RH (%)	74.2	69.3	73.4	72.2	82.1	78.2	76.7	78.1	82.8	71.7	70.5	69.4
*A (-)	0.80	0.74	0.69	0.51	0.42	-	-	-	-	-	0.45	0.72
K_T (-)	0.51	0.52	0.53	0.53	0.40	0.43	0.43	0.45	0.48	0.55	0.50	0.49
SR_{in} (KJ $m^{-2}d^{-1}$)	5310	8367	12814	17270	15628	17922	17320	15997	12989	10282	5899	4408

** Albedo (A): only considered when ground is snow covered.*

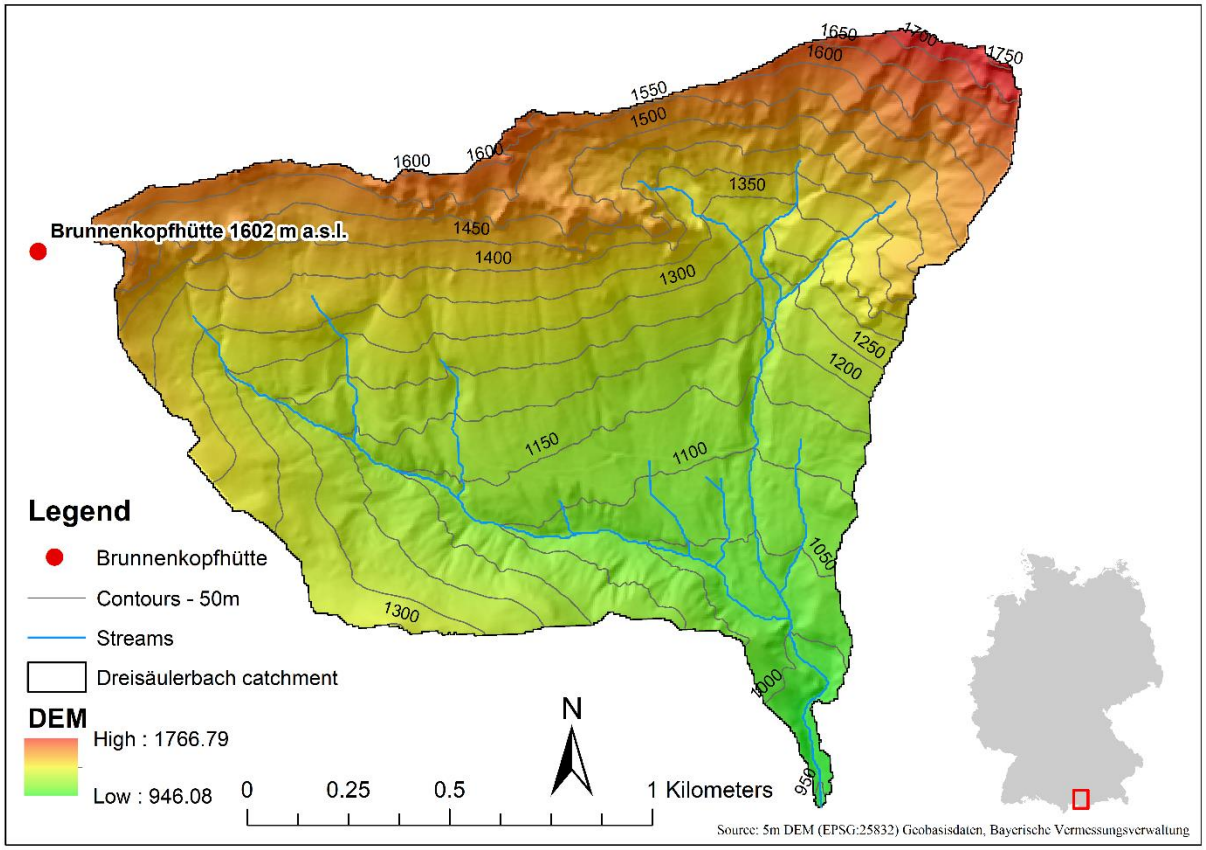

Figure 5.1 Location of Brunnenkopfhütte snow station in the Dreisäulerbach catchment – German Alps

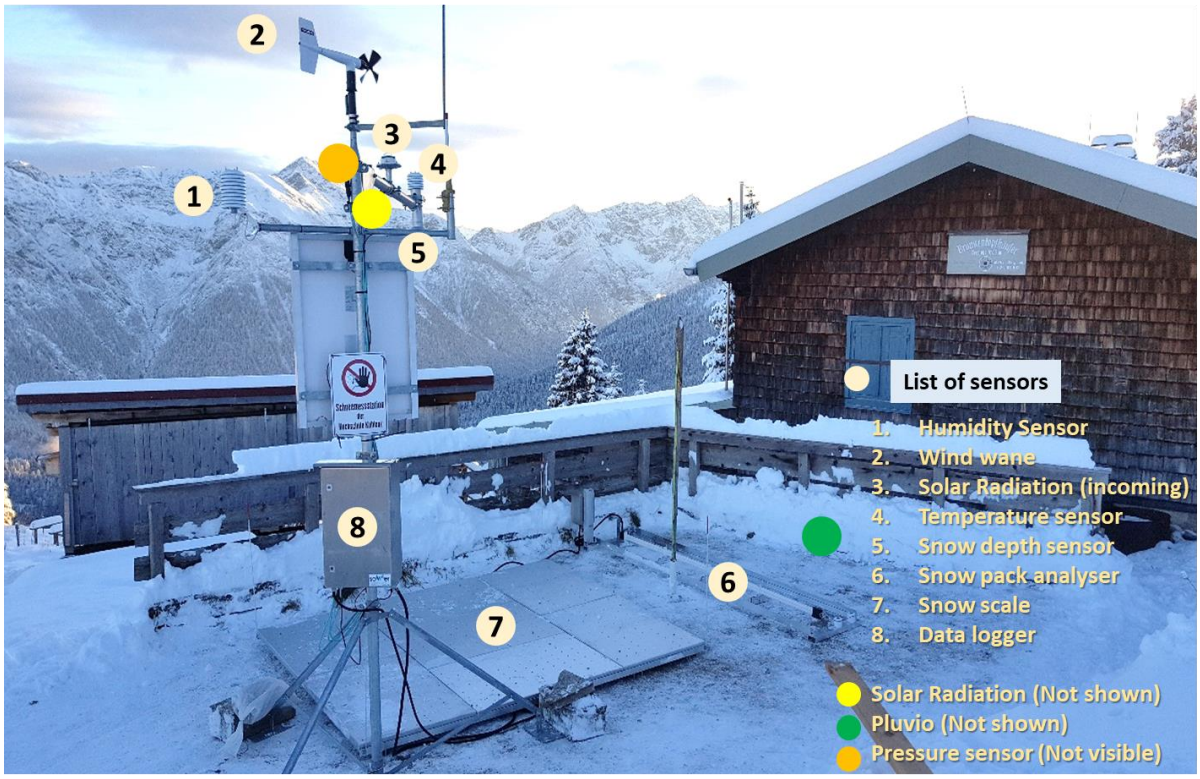

Figure 5.2 Automatic weather and snow measurement station at Brunnenkopfhütte in Ammergauer Alps [1602 m a.s.l.] – (image credit: Wolfgang Bogacki)

5.3 Materials and methods

The primary objective of this paper is to analyze the contribution of individual energy balance components to snowmelt, in order to better understand and probably to predict, how the lumped degree-day factor will vary with the season, latitude, altitude, and the concrete meteorological conditions. In addition, we want to demonstrate along the approach of Walter et al., (2005), how these energy balance components can be estimated with minimal data requirements, as limited data availability is the major reason to apply temperature-index respectively degree-day factor models.

5.3.1 Degree-Day Factor

The basic formulation of the degree-day method to calculate daily snowmelt depth M (mm) multiplies the number of degree-days T_{DD} (°C d) with the degree-day factor DDF (mm °C^{-1} d^{-1}) (Rango and Martinec, 1995).

$$M = DDF \times T_{DD} \tag{5.1}$$

Degree-days T_{DD} are only defined if a characteristic air temperature lies above a reference temperature; otherwise, T is set to 0°C. Typically, the freezing point 0°C is chosen as reference temperature. The characteristic air temperature is usually calculated by the average of daily minimum and maximum

temperature, but other approaches like the mean of hourly temperature observations, daily maximum temperature (Bagchi, 1983), or integrating only the positive temperatures of a day (Rango and Martinec, 1995; Ismail et al., 2015) are also common. By a simple re-arrangement of eq. (5.1) to

$$DDF = \frac{M}{T_{DD}} \tag{5.2}$$

the *DDF* can be back-calculated for given degree-days T_{DD}, if the daily melt depth M is known either by observation or by calculation. Likewise, the portion of the degree-day factor DDF_i associated to the melt depth M_i related to any of the individual energy balance components (see eq. (5.4)) can be determined.

The energy needed to melt ice at 0°C into liquid water at 0°C is defined by the latent heat of fusion of ice (333.55 kJ kg^{-1}). Thus the melt depth M_i caused by an energy flux Q_i (W m^{-2}) over a certain time-period Δt (s) can be calculated from the relation (USACE, 1998; Hock, 2005)

$$M_i = \frac{Q_i}{\lambda\, \rho_w} \Delta t \cong 3.00 \times 10^{-6}\, Q_i \Delta t \tag{5.3}$$

where ρ_w is the density of water at 0°C (999.84 kg m^{-3}). In the context of degree-day factor models, the time-period Δt is usually taken as 1 day = 86400 s, though some authors (Hock, 1999; McGinn, 2012) have calculated degree-day factors also for sub-daily, e.g. hourly periods. According to the relation given in eq. (3), an energy flux of 1 W m^{-2} for 1 day will result in a melt depth of 0.26 mm.

5.3.2 Energy Balance

The energy flux available for snowmelt Q_M can be calculated from the balance of energy fluxes over the surface of the snowpack and the change in the internal energy stored in the snowpack ΔQ (e.g. USACE, 1998)

$$Q_M = Q_S + Q_L + Q_H + Q_E + Q_G + Q_P - \Delta Q \tag{5.4}$$

where Q_S and Q_L are the net short- and longwave radiation, Q_H is the sensible heat, Q_E the latent energy of condensation or vaporization, Q_G the heat conduction from the ground, and Q_P the energy contained in precipitation (all terms in W m^{-2}).

In the following sections, the individual components of the energy balance will be discussed in more detail.

5.3.2.1 Shortwave Radiation

Shortwave radiation emitted from the sun is usually the most important source of energy input to the snowpack. The net energy flux Q_S (W m^{-2}) entering the snowpack by absorption of shortwave radiation is (USACE, 1998)

$$Q_s = (1 - A)S_i \tag{5.5}$$

where A is the snow albedo (–) and S_i the incident solar radiation (W m^{-2}) on the snow surface. A widely used approach to determine the incident solar radiation on earth's surface is the introduction of a clearness index K_T (–)

$$S_i = K_T S_0 \tag{5.6}$$

where S_0 is the mean daily potential extra-terrestrial solar radiation (W m^{-2}) that would insolate a horizontal surface on the earth's ground if no atmosphere would be present. The potential insolation, which is only dependent on the changing position of the sun during the year in relation to the geographic location of the incident point on the earth's surface, can be calculated from the equation (Masters, 2004)

$$S_0 = G_S \frac{1}{{d_r}^2} \frac{1}{\pi} (\cos(\emptyset) \cos(\delta) \cos(\omega_s) + \omega_s \sin(\emptyset) \sin(\delta)) \tag{5.7}$$

where G_S is the solar constant (W m^{-2}), d_r the relative distance earth to sun (–), ϕ the geographic latitude (rad) of the incident point, δ the solar declination (rad), and ω_s the sunrise hour angle (rad). The solar constant G_S is slightly varying with the occurrence of so-called sunspots, however a constant value of 1367 W m^{-2} has been used for the last decades. New measurements indicate a somewhat lower value of 1361 W m^{-2} (Kopp and Lean, 2011).

Both sun position variables, the relative distance earth to sun and the solar declination, can be calculated quite exactly by rigid astronomical algorithms (Meeus, 1991; Reda and Andreas, 2004) however for non-astronomical purposes, more simple formulas are sufficiently accurate. The relative distance earth to sun, which is varying over the year due to the elliptical orbit of the earth, can be approximated by (Masters, 2004)

$$\frac{1}{{d_r}^2} \approx 1 + 0.034 \cos\left(\frac{2\pi . J}{365}\right) \tag{5.8}$$

where J is the day of the year, while the solar declination can be obtained from the sinusoidal relationship

$$\delta \approx 0.409 \sin\left(\frac{2\pi}{365}(J - 81)\right) \tag{5.9}$$

that puts the spring equinox on day J = 81. Knowing the solar declination δ, the sunrise hour angle ω_s can be calculated from

$$\cos \omega_s = -\tan(\emptyset)\tan(\delta) \tag{5.10}$$

On the northern hemisphere the maximum extra-terrestrial radiation occurs at the summer solstice with a fairly identical mean daily energy flux of about 480 W m^{-2} over latitudes 30° – 60° North, as the sun's lower altitude angle at higher latitudes is compensated by longer daylight hours. On the contrary, minimum extra-terrestrial radiation at the winter solstice varies strongly with latitude, e.g. 227 W m^{-2} at 30° and only 24 W m^{-2} at 60° North.

When the solar radiation passes through the atmosphere, it is partly scattered and absorbed. While even on a clear day only about 75% of the incoming radiation reaches the ground, by far the largest attenuation is caused by clouds. A vast number of solar radiation models exist that parameterize this effect, which is denoted as clearness index K_T or atmospheric transmissivity τ, as a function of meteorological variables. For a review see e.g. Evrendilek and Ertekin (2008), Ahmad and Tiwari (2011), or Ekici (2019).

A fundamental and widely used solar radiation model which is proposed in the context of evapotranspiration calculations (Allen et al., 1998) is the Ångström-Prescott model, that relates the clearness index to the relative sunshine duration

$$K_T = \frac{S_i}{S_0} = a + b\frac{n}{N} \tag{5.11}$$

with n is the actual and N the maximal possible duration of sunshine (hr) where the latter can be calculated from the sunrise hour angle ω_s by

$$N = \frac{24}{\pi}\omega_s \tag{5.12}$$

The parameters a and b in eq. (5.11) are regression parameters, that usually have to be fitted to observed global radiation. In case no actual solar radiation data is available, the values $a = 0.25$ and $b = 0.50$ are recommended (Allen et al., 1998). Though the Ångström-Prescott model has the disadvantage, that the parameters have to be fitted and the actual duration of sunshine has to be observed, it has the benefit, that both parameters allow for a direct physical interpretation and a straight demonstration of the effects of cloud cover. The parameter a represents the clearness index K_T on overcast days ($n = 0$), while their sum $a + b$ gives the clearness index on clear days ($n = N$).

In the common situation in remote mountainous regions, that only temperature data is available, another group of solar radiation models can be utilised, which uses the difference between daily maximum and minimum air temperature ΔT (°C) as a proxy for cloud cover, because clear sky conditions result in a higher temperature amplitude between day and night than under overcast conditions. Typical models are the exponential approach proposed by Bristow and Campbell (1984) and its later modifications or the simple empirical equation by Hargreaves and Samani (1982)

$$K_T = k.\sqrt{\Delta T} \tag{5.13}$$

with the empirical coefficient k = 0.16 for inland and k = 0.19 for coastal locations.

It is obvious, that the attenuation of extra-terrestrial solar radiation is a function of the distance the rays have to travel through the atmosphere, as absorption and scattering occurs all along the way. Several solar radiation models consider altitude as a variable, from which the models below are of Ångström-Prescott type, thus the altitude effects can be directly compared.

Jin et al. (2005):

(a) $$K_T = (0.0855 + 0.0020\emptyset + 0.030z) + 0.5654\frac{n}{N} \tag{5.14}$$

(b) $$K_T = (0.1094 + 0.0014\emptyset + 0.0212z) + (0.5176 + 0.0012\emptyset + 0.0150z)\frac{n}{N} \tag{5.15}$$

Rensheng et al. (2006):

$$K_T = (0.122 + 0.001\emptyset + 0.0257z) + 0.543\frac{n}{N} \tag{5.16}$$

Liu et al. (2019):

$$K_T = (0.1755 + 0.0136z) + (0.5414 + 0.0117z)\frac{n}{N} \tag{5.17}$$

For all models, z is the altitude (km) and ϕ the latitude (deg). In order to separate the altitude effect from other parameters, a clearness altitude factor K_Z (–) with

$$K_z = \frac{K_T}{K_{T_0}} \tag{5.18}$$

is introduced, where K_{T_0} is the clearness factor at z = 0 m a.s.l. which results in K_Z = 1 at sea level for all models and all values of relative sunshine duration n/N. Though the individual clearness altitude factors obtained from the above models are different, they all exhibit a constant increase per unit altitude for a given n/N and highest values for overcast conditions (n/N = 0) while the altitude effect under clear sky conditions (n/N = 1) is significantly smaller.

While the albedo of fresh snow is well above 0.9 (Hock, 2005), indicating that most of the shortwave radiation is reflected, it may drop significantly within a few days due to snow metamorphism. Well aged snow generally has an albedo in the range of 0.4 – 0.5 (Anderson, 2006). Snow albedo is primarily dependent on the grain size of the snow crystals near the surface but also on aerosols in the snow and dust deposits. Respective snow albedo models are proposed e.g. by Wiscombe and Warren (1980) and Warren and Wiscombe (1980) however, due to the data requirements, commonly surrogate exponential decay models as formulated by (USACE, 1956) are used, which assume the decrease of albedo as a

function of time after the last significant snowfall. For example Walter et al., (2005) use the empirical relationship

$$A_n = 0.35 - (0.35 - A_{max}).\,exp\left[-\left(0.177 + \ln\left(\frac{A_{max} - 0.35}{A_{n-1} - 0.35}\right)^{2.16}\right)\right]^{0.46} \quad (5.19)$$

where, A_{n-1} is the albedo of the previous day and A_{max} is the maximum albedo (~0.95) of fresh snow. Following eq. (5.19), the snow albedo will decrease from 0.95 to 0.52 after 10 days and to 0.43 after 30 days if no new snowfall occurs.

5.3.2.2 Longwave Radiation

The longwave radiation net energy flux over the snow surface Q_L (W m^{-2}) is the balance

$$Q_L = Q_{L,in} - Q_{L,out} \quad (5.20)$$

between incoming longwave radiation that is emitted by the atmosphere $Q_{L,in}$ (W m^{-2}) and outgoing radiation from the snowpack $Q_{L,out}$ (W m^{-2}).

Longwave radiation is a function of the temperature of the emitting body and can be calculated with the Stefan-Boltzmann law

$$L = \varepsilon\, \sigma\, T^4 \quad (5.21)$$

where L is the radiative flux (W m^{-2}), ε and T are the emissivity (–) and the absolute temperature (K) of the emitting body, and σ is the Stefan-Boltzmann constant (5.67×10^{-8} W m^{-2} K^{-4}).

In particular fresh snow is nearly a perfect blackbody with respect to longwave radiation, thus it has a high emissivity of 0.99 (Warren, 1982; USACE, 1998; Anderson, 2006). For old snow, Brutsaert (1982) gives an emissivity value of 0.97. Given a melting snowpack having a surface temperature of 0°C, the outgoing energy flux can be taken as constant with $Q_{L,\mathbf{out}}$ ~310 W m^{-2}.

For the atmospheric longwave radiation, usually the air temperature T_a (K) is used in eq. (5.21). However, while the snowpack longwave emissivity is virtually a constant, the emissivity of the atmosphere is highly variable. Typical values under clear sky conditions range from 0.6 – 0.8, primarily depending on air temperature and humidity (Anderson, 2006) whereas for overcast conditions it can be close to 1.0.

A number of empirical and more physically based approaches exist to estimate atmospheric longwave emissivity from standard meteorological data (see Hock, 2005 for a discussion). For clear sky conditions, Brutsaert (1975) developed a theoretically based formula depending on air temperature and vapour pressure

$$\varepsilon_{ac} = 1.24\left(\frac{p_v}{T_a}\right)^{\frac{1}{7}} \quad (5.22)$$

where ε_{ac} is the clear sky longwave emissivity (–), p_v the actual vapour pressure (hPa), and T_a the air temperature (K). Later, Brutsaert reconciled eq. (5.22) with an empirical approach proposed by Swinbank (cited in Brutsaert, 1982)

$$\varepsilon_{ac} = 9.2 \times 10^{-6}\, T_a^2 \tag{5.23}$$

that considers the strong correlation between vapour pressure and air temperature, thus only air temperature is needed as input variable. Using above relation, at an air temperature of 10 °C the atmospheric longwave radiation flux into the snowpack will amount to $Q_{L,in}$ = 281 W m^{-2} under clear sky conditions, which is less than the outgoing flux of 310 W m^{-2}, i.e. the snowpack will lose energy in this situation.

The variability of atmospheric emissivity due to cloud cover, which increases the longwave emissivity, is significantly higher than variations under clear sky conditions. Monteith and Unsworth (2013) give the simple linear relationship.

$$\varepsilon_a = (1 - 0.84c)\varepsilon_{ac} + 0.84c \tag{5.24}$$

where ε_a is the atmospheric longwave emissivity, c the fraction of cloud cover (–), and ε_{ac} is calculated by eq. (5.22) or eq. (5.23). For overcast conditions and an air temperature of 10 °C, eq. (5.24) yields an atmospheric emissivity of 0.96, which results in an atmospheric longwave radiation flux of $Q_{L,in}$ = 351 W m^{-2} and thus a positive flux of Q_L = 41 W m^{-2} into the snowpack.

Although cloud cover is difficult to parameterise as clouds can be highly variable in space and time and effects on radiation dependent on the different cloud genera, a strong correlation between cloud cover and sunshine duration is obvious. Doorenbos and Pruitt, (1977) give a tabulated relation between cloudiness c and relative sunshine hours n/N (see eq. 11), that can be fitted by the quadratic regression

$$c = 1 - 0.5544\,\frac{n}{N} - 0.5483\left(\frac{n}{N}\right)^2 \tag{5.25}$$

Nevertheless, in simple sky models usually a linear relation between cloudiness and relative sunshine hours is applied as a first approximation (e.g. Brutsaert, 1982; Annandale et al., 2002; Pelkowski, 2009), for which Badescu and Paulescu, (2011) give a probabilistic reasoning.

5.3.2.3 Sensible Heat Exchange

Sensible heat exchange describes the energy flux due to temperature differences between the air and the snow surface while air is permanently exchanged by wind turbulences. A frequent approach to parameterise turbulent heat transfer is the aerodynamic method, that explicitly includes wind speed as a variable (Braithwaite et al., 1998; Lehning et al., 2002; Hock, 2005).

$$Q_H = \rho_a c_p C_H u(T_a - T_s) \tag{5.26}$$

where ρ_a is the air density (~1.29 kg m^{-3}), c_p the specific (isobaric) heat capacity of air (= 1006 J kg^{-1} °C^{-1}), C_H the exchange coefficient for sensible heat (–), u the mean wind speed (m s^{-1}), T_a the air temperature (°C), and T_s the temperature at the snow surface (°C).

The exchange coefficient C_H can be approximated with (Campbell and Norman, 1998)

$$C_H = \frac{k^2}{ln\left(\frac{z_u}{z_m}\right) ln\left(\frac{z_T}{z_h}\right)} \tag{5.27}$$

where k is the von Karman's constant 0.41 (–), z_u and z_T the height of wind and temperature observation above the snow surface (m), z_m the momentum roughness parameter, and z_h the heat roughness parameter. For a snow surface, the roughness parameters are given by Walter et al., (2005) as z_m ~ 0.001 m and z_h ~ 0.0002 m.

Eq. (5.27) is equivalent to the calculation of aerodynamic resistance in the Penman-Monteith equation (Allen et al., 1998) when applying a zero plane displacement for the snow surface and assumes neutral stability conditions, i.e. temperature, atmospheric pressure, and wind velocity distributions follow nearly adiabatic conditions. Otherwise, diabatic correction factors (see Campbell and Norman, 1998) have to be applied.

As can be seen from eq. (5.26), the sensible heat component is mainly dependent on wind speed and air temperature. During stable clear weather periods with typically light winds, the turbulent exchange is of less importance compared to the radiation components. For example, a wind speed of 1 m s^{-1} and an air temperature of 5 °C will result in a sensible heat flux of about 17 W m^{-2}. However, at warm rain events or at Föhn conditions with strong warm winds, turbulent exchange can significantly contribute to the melt process.

5.3.2.4 Latent Energy of Condensation or Vapourisation

The latent energy exchange reflects the phase change of water vapour at the snow surface, either by condensation of vapour contained in the air or by vapourisation of snow. Thus, it can either warm or cool the snowpack (Harpold and Brooks, 2018). The energy flux is dependent on the vapour gradient between air and snow surface and is, like the sensible heat exchange, a turbulent process that increases with the wind speed. Thus, the aerodynamic formulation is analogously to eq. (5.26)

$$Q_E = \rho_a \lambda_v C_E u(q_a - q_s) \tag{5.28}$$

where λ_v is the latent heat of vapourisation of water at 0°C (= 2.501×10^6 J kg^{-1}), C_E the exchange coefficient for latent heat (–) which is assumed to be equal to the exchange coefficient for sensible heat C_H, q_a the specific humidity of the air (–), and q_s the specific humidity at the snow surface (–).

The specific humidity q_a can be derived from measurements of relative humidity or dew point temperature. In cases where such data is not available, Walter et al., (2005) approximate the dew point

temperature by the minimum daily temperature. For any air temperature T (°C), the saturation vapour pressure p_0 (Pa) can be calculated by an empirical expression known as the Magnus-Tetens equation in the general form (Lawrence, 2005)

$$p_0 = C\, e^{\frac{A\,T}{B+T}} \tag{5.29}$$

where A, B, and C are coefficients e.g. after Allen et al., (1998) A = 17.2694, B = 237.3 °C, C = 610.78 Pa. At the snow surface, according to Lehning et al., (2002) the air temperature can be assumed equal to the snow surface temperature and eq. (5.29) is applied with coefficients for saturation vapour pressure over ice A = 21.8746, B = 265.5 °C, C = 610.78 Pa (Murray, 1967). At a temperature of 0°C, both coefficient sets yield the same saturation vapour pressure of p_0 = 611 Pa.

Knowing the vapour pressure p_v (Pa) at a given temperature, the respective specific humidity of the air or at the snow surface can be calculated by

$$q = \frac{e\ p_v}{p - (1-e)p_v} \approx \frac{e}{p} p_v \tag{5.30}$$

where p is the atmospheric pressure (Pa) and e the ratio of molar weights of water and dry air = 0.622. Thus, similar to the sensible heat flux Q_H, the latent energy exchange at the snow surface Q_E can be taken as a function of wind speed in combination with air and snow surface temperature, where the latter is assumed as 0°C at melting conditions.

While at positive air temperatures the sensible heat flux is always warming the snowpack, the latent heat flux can cool the snow by vapourisation if the relative humidity of the air is low. Even when assuming a relative humidity of 100% the latent heat flux into the snowpack will be comparatively small if wind speed is low, e.g. about 13 W m^{-2} at an air temperature of 5 °C and a wind speed of 1 m s^{-1}.

5.3.2.5 Ground Heat

Heat conduction from the ground into the snowpack is small and can be in general neglected except when first snow falls on warm ground (Anderson, 2006). If the snowpack is well established, due to the low thermal conductivity of snow the heat flux across the soil-snow interface becomes independent of air temperature fluctuations and depends only on the thermal conductivity of the soil and the temperature gradient in the upper soil layer. USACE, (1998) gives a range between 0 – 5 W m^{-2} for constant daily values. DeWalle and Rango, (2008) approximate a flux of 4 W m^{-2} assuming a soil temperature of 1 °C at a depth of 0.5 m, and a soil thermal conductivity of 2 W m^{-1} °C^{-1} that is at the higher end of the range of 0.2 – 2 W m^{-1} °C^{-1} given by Oke, (1987). It has to be noted, that the soil temperature gradually approaches the snowpack temperature during the winter (USACE, 1956; Marks et al., 1992), thus ground heat conduction will generally decrease. Own measurements of soil temperature show a similar behaviour. Soil temperature dropped from 1 – 3 °C shortly after

establishment of the snowpack to > 0 – 1 °C after about a month and then stayed constant until final melt.

5.3.2.6 Precipitation Heat

The heat transfer into the snowpack by lowering rain's temperature, that is usually assumed to be equal to the air temperature T_a (°C), down to the freezing point at 0°C can be estimated as

$$Q_P = c_w \, P \, T_a \tag{5.31}$$

where c_w is the specific heat capacity of water (4.2 kJ kg^{-1} °C^{-1}) and P is the daily rainfall depth (kg m^{-2} d^{-1}). The energy input from precipitation is usually quite small and even extreme weather situations, like heavy warm rain storms with temperatures of 15°C and a precipitation depth of 50 mm, that may occur e.g. during early winter in the alps, would result in a modest mean daily energy flux of 36.5 W m^{-2} where it has to be taken into account, that such events are only singular.

5.3.2.7 Change in Internal Energy

The rate of change in the energy stored in the snowpack ΔQ (W m^{-2}) represents the internal energy gains and losses due to the change of snow temperature and the melting of the ice portion or refreezing of liquid water in the snow. Until the snowpack temperature is isothermal at 0°C, any melt produced by surplus energy in the surface layer of the snowpack will percolate downward when the liquid water holding capacity of the porous snow matrix is exceeded and may be refrozen in colder lower layers. If a snowpack is isothermal at 0°C and is saturated, i.e. the residual volumetric water content of about 8% (Lehning et al., 2002) is filled with liquid water, the snowpack is called 'ripe'. In that state, any additional energy input will immediately produce snowmelt runoff according to eq. (5.3). If however a snowpack is still in the ripening phase, at least part of the incoming energy is absorbed to decrease the energy deficit and has to be subtracted from energy available for melt thus will reduce the respective *DDF*. The energy needed to bring the snowpack temperature isothermal at 0°C, i.e. the snowpack's energy deficit, is usually expressed as 'cold content' (Marks et al., 1999; Schaefli and Huss, 2011; Jennings et al., 2018).

The present paper aims to demonstrate the contribution of each energy flux component towards a resulting *DDF*. In this respect, the energy deficit in the ripening phase plays no role, as each flux component is analysed individually. Only when it comes to a comparison with observed melt data (see Sec. 5.4.6) the ripening state of the snowpack has to be taken into account. In this context, the study focusses only on melt periods where the snowpack is ripe while melt periods where the cold content is increased e.g. by new snow events or significant cooling phases are excluded from the analysis.

Certainly it is of interest to estimate *DDFs* also in cases where an internal energy deficit exists, e.g. because of radiational cooling during clear cold nights. The cold content usually is either estimated as

a function of meteorological parameters or calculated by keeping track of the residuals of the snowpack energy balance (Jennings et al., 2018). The SNOWPACK model (Lehning et al., 2002), that is operationally employed on a day-to-day basis for avalanche warning, is an excellent tool for a detailed simulation of the vertical mass, energy, and besides other state variables the snow temperature distribution inside a snowpack, taking into account the complex processes of snow metamorphosis and heterogeneity of layers in the snowpack, and as a by-product, also simulates snowmelt runoff. However, SNOWPACK requires a considerable number of qualified input variables with preferably at least hourly observations, which both is usually not available in the context where degree-day factor models are employed.

On the other hand Walter et al., (2005) apply a lumped approach, that accounts for the cold content by changing the (isothermal) snowpack temperature depending on the daily net energy flux. When the incoming energy flux is sufficient to raise the snow temperature to 0°C or when it is already at 0°C the day before, all additional available energy produces melt. This appealing approach, which does not need any additional data, however seems to significantly over-estimate the snowpack temperature in particular in situations with negative energy fluxes at night but a positive daily net balance, as a comparison with SNOWPACK results and with observations at Brunnenkopfhütte shows. Thus a suitable parametrisation of the cold content, that would enable satisfactory estimates of *DDFs* in situations when the snowpack is not completely ripe, remains subject to further research.

5.4 Results

In this section, the contribution of each energy flux component Q_i to the lumped daily *DDF* is presented. For this purpose, the respective melt depth M_i is calculated according to eq. (5.3) and further converted into the corresponding degree-day factor component DDF_i using eq. (5.2). Degree-days T_{DD} (°C d) in eq. (5.2) are estimated by the average daily air temperature, thus having the same numerical value as the air temperature T_a (°C) used in the calculation of several energy flux components.

Besides demonstrating the dependency of the *DDF* components on decisive parameters of the energy flux components, the presented tables and graphs, which are based on the approximate relationships given in section 3, can be used to estimate the *DDF* component values in case either observed data is not available or not sufficient for more sophisticated approaches. It should be noted that parameters are normalised where applicable, i.e. set to hypothetical values like clearness index $K_T = 1$ or wind speed $u = 1.0$ m s^{-1}, thus final *DDF* values can be obtained by multiplying the given figures by the actual values of those parameters. Furthermore, all results are based on the assumption that the snowpack is isothermal at 0°C and in fully ripe state.

5.4.1 Shortwave radiation component – DDF_S

Shortwave radiation induced melt is usually considered the most important *DDF* component especially at higher altitudes. The net energy flux Q_S is calculated using eq. (5.5), which consists of three factors (a) latitude, (b) albedo, and (c) clearness index K_T. The dependency of DDF_S on these factors is demonstrated in Figure 5.3 for the period between winter solstice (21st December) and summer solstice (21st June). As shortwave radiation is independent of air temperature and hence of degree-days, the corresponding melt is divided by a hypothetical degree-day value of 1 °C d to arrive at DDF_S values as presented. In case of actually higher degree-days, the given DDF_S values have to be divided accordingly.

Figure 5.3 (a) shows the variation of DDF_S depending on latitude for the range 30° – 60° North, while albedo ($A = 0$) and clearness index ($K_T = 1$) are set constant. Obviously, there is a significant difference in DDF_S for different latitudes around the winter solstice due to solar inclination, making latitude the predominant factor for DDF_S at this time of the year. However, around the summer solstice, DDF_S has nearly the same value at different latitudes because the lower solar angle at higher latitudes is counterweighted by a larger hour angle, i.e. longer sunlight hours. Thus, with the progress of the melting season the factors albedo and clearness index become more important than latitude.

Figure 5.3 (b) shows the influence of albedo on the DDF_S at a given latitude (Brunnenkopfhütte station latitude 47.58°) and normalised constant clearness index ($K_T = 1$). Snow albedo is varied between 0.9 – 0.4 covering the range between fresh and well-aged snow. As to be expected, the influence of albedo increases with increasing incoming solar radiation towards the summer solstice. A good estimate of albedo is therefore much more important when the snowmelt season progresses than in early spring. If for example the same degree-day value of 10 °C d is assumed on 21st March and on 21st May, the difference in DDF_S between fresh ($A = 0.9$) and aged ($A = 0.4$) snow would be 0.8 and 4.6 mm $°C^{-1}$ d^{-1} in March compared to 1.2 and 7.1 mm $°C^{-1}$ d^{-1} in May respectively.

The dependency of DDF_S on the clearness index K_T is shown in Figure 5.3 (c). As also evident from eq. (5.6), DDF_S under clear sky ($K_T = 0.75$) is always higher than under overcast conditions ($K_T = 0.25$). Similar to albedo, the influence of the clearness index becomes more pronounced, and thus the assessment of clearness conditions more important, with increasing solar angle when the snowmelt season progresses.

The influence of altitude on DDF_S in terms of increasing K_T values can be considered separately by multiplying K_{T_0} (at $z = 0$ m a.s.l.) calculated by any of the numerous solar radiation models with a clearness altitude factor as given in eq. (5.18). Figure 5.4 shows the range of clearness altitude factors for latitude 45° derived from four solar radiation models, which were calibrated including high altitude data (see Sec. 5.3.2.1). The dark grey area indicates the common overlap of the four models. All of these models show the same tendency of linear increase by altitude, with the altitude factor being comparatively smaller under clear sky compared to overcast conditions. When averaging models as

well as sky conditions, the clearness altitude factor and thus the resulting DDF_S increases by about 6% for each 1000 m altitude.

(a)

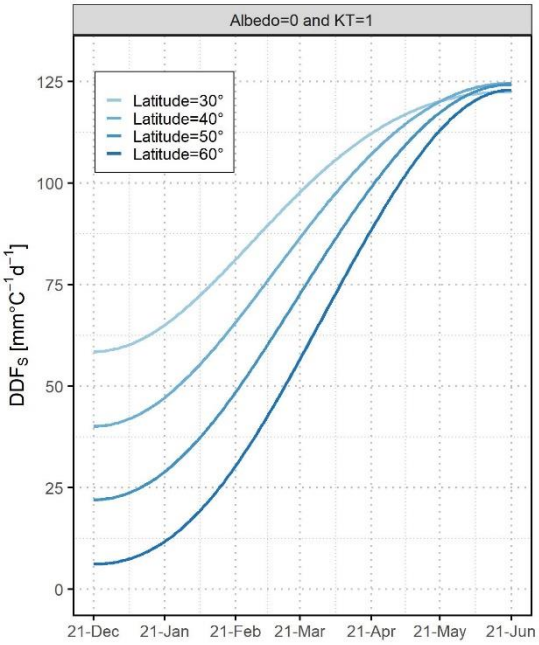

(b)

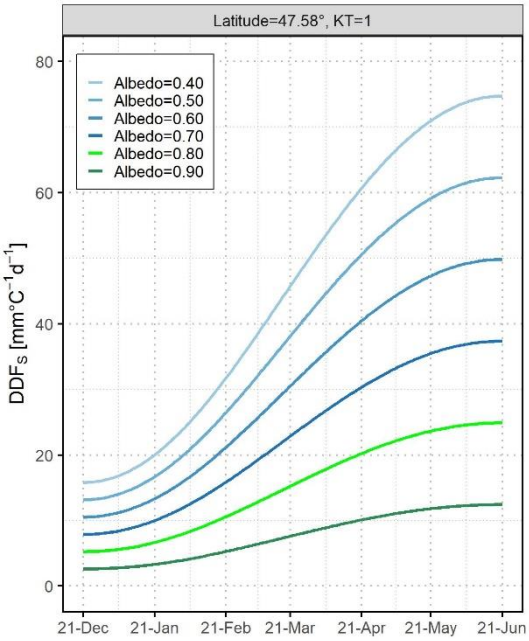

(c)

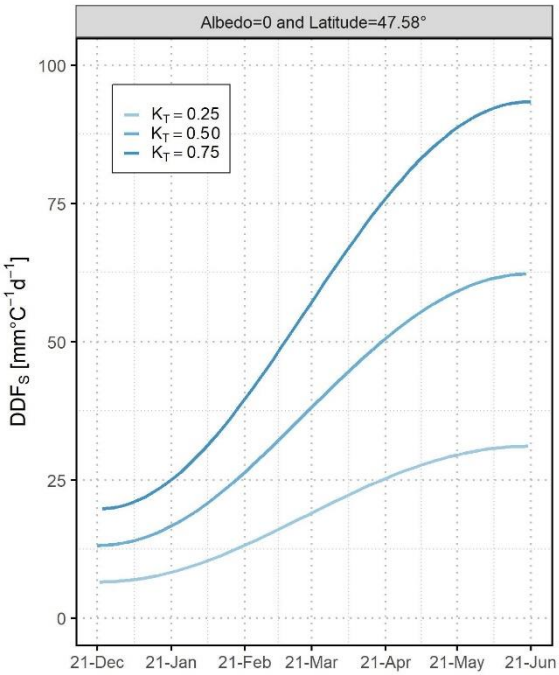

Figure 5.3 Variation of solar radiation based DDF_S for a degree-day value of 1°C d (a) for different latitudes under constant snow albedo and clearness index (b) for different snow albedo under constant latitude and clearness index (c) for different clearness index under constant latitude and snow albedo – Latitude 47.58° corresponds to the location of Brunnenkopfhütte snow station

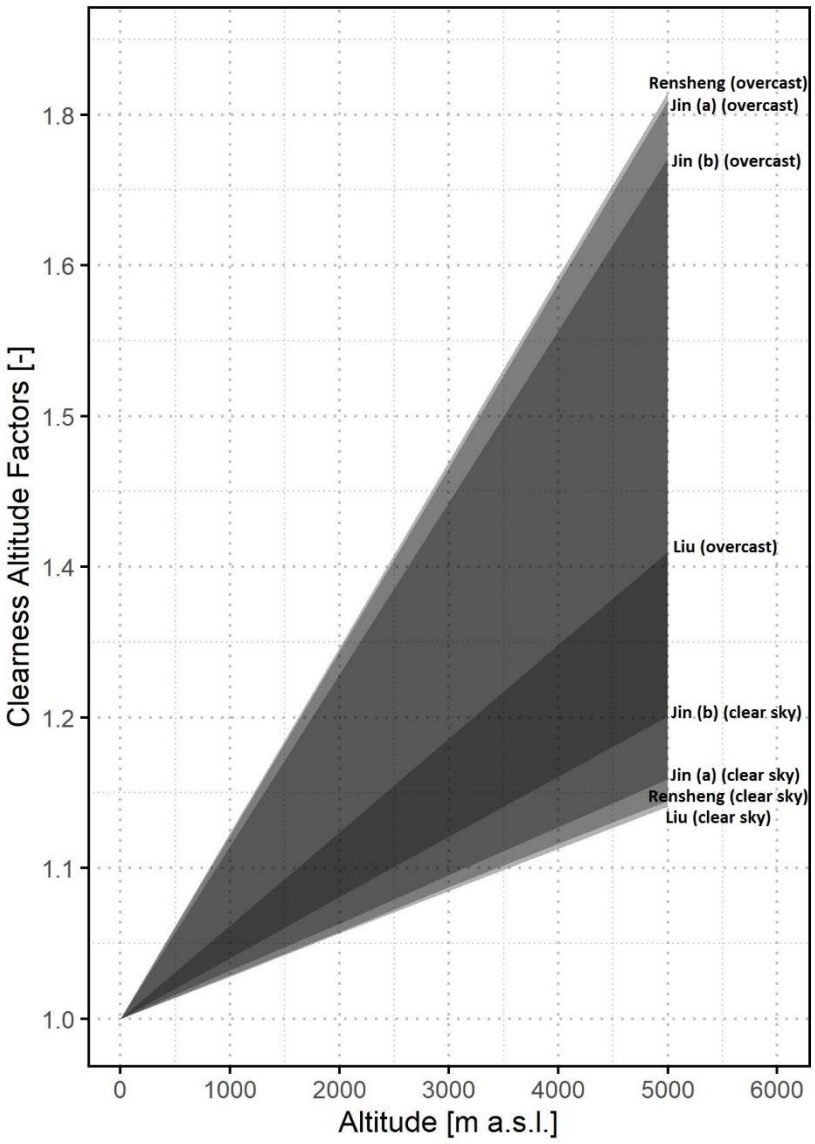

Figure 5.4 Clearness altitude factor for different altitudes ranges, based on different models presented in equations (5.14 – 5.17, i.e. Jin (a), Jin (b), Rensheng, and Liu) for latitude 45° where applicable

5.4.2 Longwave radiation component – DDF_L

The net longwave energy flux Q_L is calculated using eq. (5.20), in which the outgoing radiation from the snowpack can be assumed as constant. Thus, the contribution of longwave radiation component

DDF_L is mainly dependent on air temperature and the emissivity of the atmosphere, in particular cloudiness conditions. Figure 5.5 and Table 5.2 present the DDF_L as a function of degree-days T_{DD}, which are equivalent to the average daily air temperature, and cloudiness. For a wide range of degree-days especially in conjunction with low cloudiness, the outgoing longwave energy flux is higher than the incoming, resulting in a theoretically negative degree-day factor that will reduce the total *DDF*. This means that the DDF_L component under clear sky conditions usually is rather contributing to a cooling of the snowpack than to melting. Under overcast conditions, the DDF_L is relatively constant around 1 mm $°C^{-1}$ d^{-1} with a maximum value of 1.3 mm $°C^{-1}$ d^{-1} at T_{DD} = 20 °C d. Although this contribution to the total *DDF* is small compared to the shortwave radiation component DDF_S, it can be of importance at the onset of snowmelt in early spring, when the solar radiation is still low and the albedo of fresh snow is high.

Table 5.2 Longwave radiation component (DDF_L) [mm $°C^{-1}$ d^{-1}] for selected cloudiness [%]

	DDF_L										
	Cloudiness										
T_{DD} [°C d]	0%	10%	20%	30%	40%	50%	60%	70%	80%	90%	100%
1	-19.08	-17.17	-15.26	-13.35	-11.45	-9.54	-7.63	-5.72	-3.81	-1.90	0.01
2	-8.89	-7.94	-6.99	-6.04	-5.09	-4.14	-3.19	-2.24	-1.29	-0.33	0.62
3	-5.49	-4.86	-4.23	-3.59	-2.96	-2.33	-1.70	-1.07	-0.44	0.19	0.82
4	-3.78	-3.31	-2.84	-2.37	-1.90	-1.42	-0.95	-0.48	-0.01	0.46	0.93
5	-2.75	-2.38	-2.00	-1.63	-1.25	-0.88	-0.50	-0.13	0.25	0.62	1.00
6	-2.06	-1.75	-1.44	-1.13	-0.82	-0.51	-0.20	0.11	0.43	0.74	1.05
7	-1.57	-1.30	-1.04	-0.77	-0.51	-0.24	0.02	0.29	0.55	0.82	1.08
8	-1.19	-0.96	-0.73	-0.50	-0.27	-0.04	0.19	0.42	0.65	0.88	1.11
9	-0.90	-0.69	-0.49	-0.29	-0.08	0.12	0.32	0.53	0.73	0.93	1.14
10	-0.66	-0.48	-0.30	-0.11	0.07	0.25	0.43	0.61	0.79	0.98	1.16
15	0.08	0.19	0.31	0.43	0.54	0.66	0.77	0.89	1.01	1.12	1.24
20	0.48	0.56	0.64	0.72	0.81	0.89	0.97	1.05	1.13	1.21	1.30

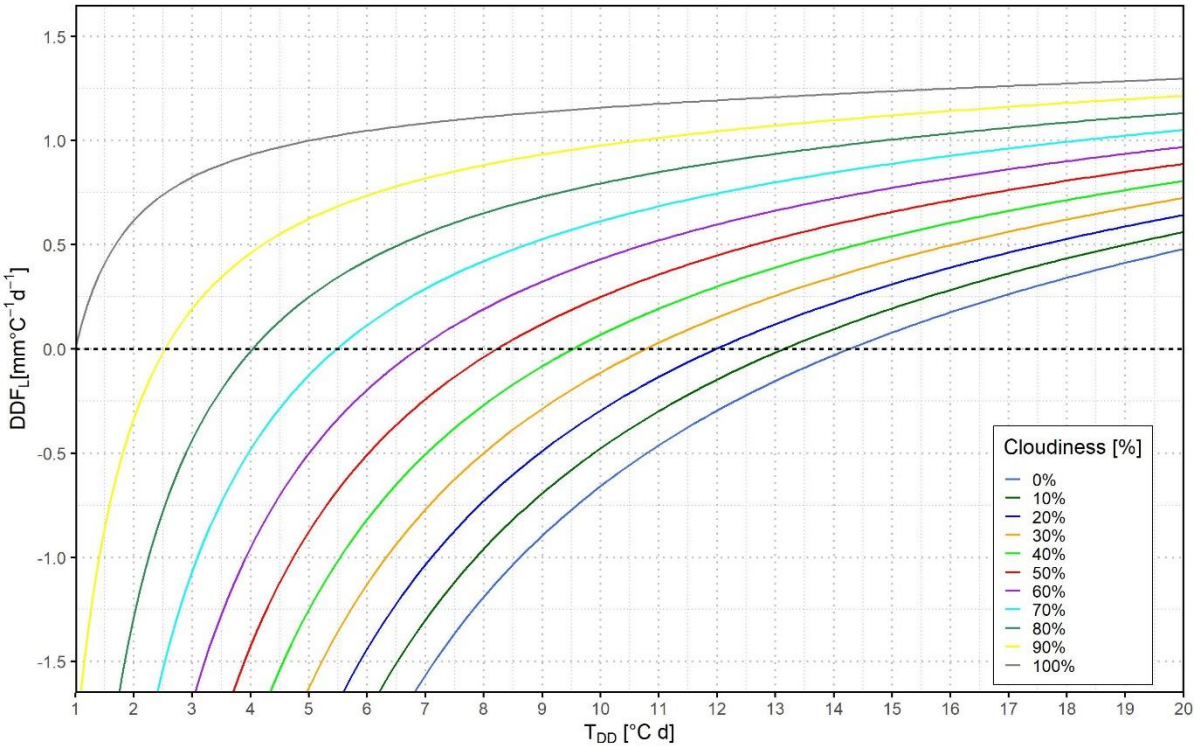

Figure 5.5 Longwave Radiation component (DDF_L) for selected cloudiness [%]

5.4.3 Sensible heat component – DDF_H

The sensible heat flux Q_H as given by eq. (5.26) is linear dependent on the temperature difference between air and snow surface. If the snowpack temperature is assumed to be constant at T_s = 0 °C, the division by degree-days according to eq. (5.2) makes DDF_H independent of temperature and proportional to the wind speed, resulting in a value of 0.86 mm $°C^{-1}$ d^{-1} for an average daily wind speed of u = 1.0 m s^{-1}. DDF_H for any other wind speed can easily be obtained by multiplication with the actual average daily value. Table 5.3 presents some examples for different values of u. It should be noted that Table 5.3 refers to melt conditions with positive air temperature, whereas negative air temperature would lead to respective negative DDF_H resulting in a cooling of the snowpack and a decrease of total *DDF*.

If wind speed observations are not available, DDF_H may be approximated using typical values. Stigter et al., (2021) for example give a range of wind speed at two different sites in the central Himalayas. At Ganja La the wind speed is generally low i.e. < 2 m s^{-1} and has no distinct diurnal cycle, whereas at Yala the wind speed exhibit a strong diurnal cycle with wind speeds ≥ 5 m s^{-1} occurring in the afternoon during the entire snow season. Dadic et al., (2013) found values around 3 – 5 m s^{-1} for a glaciered catchment in Switzerland. However, typical average values may not represent the actual wind

conditions and thus DDF_H on a certain day. While for example the geometric mean of observed daily wind speed at the Brunnenkopfhütte station is about 0.8 m s^{-1} resulting in a DDF_H of approx. 0.7 mm °C^{-1} d^{-1}, the maximum daily average wind speed is about 4.5 m s^{-1} which increases DDF_H to approx. 3.9 mm °C^{-1} d^{-1}.

Table 5.3 Sensible heat component (DDF_H) [mm °C^{-1} d^{-1}] for selected wind speed (u) [m s^{-1}]

Wind Speed (u)	0.1	0.5	1.0	2.0	3.0	4.0	5.0	10.0
DDF_H	0.09	0.43	0.86	1.73	2.59	3.46	4.32	8.64

5.4.4 Latent heat component – DDF_E

The latent heat flux Q_E approximated by an aerodynamic model as in eq. (5.28) shows, that the latent heat component DDF_E is dependent on the humidity gradient near the snow surface and proportional to the wind speed. Table 5.4 and Figure 5.6 give the resulting DDF_E as a function of degree-days for different values of relative humidity and an average daily wind speed of u = 1.0 m s^{-1}. As with the sensible heat component DDF_H, DDF_E for any other wind speed can be obtained by multiplication with the actual value. For relative humidity < 30% the DDF_E is negative over the whole range of degree-days, hence the latent heat component will reduce the total *DDF* under these conditions. Even if the air is humid and warm, contribution of latent heat is moderate, e.g. DDF_E =1.05 mm °C^{-1} d^{-1} at a relative humidity of 100% and T_{DD} = 20 °C d.

In general, humid air will promote condensation at a cooler snow surface, which releases latent energy and contributes to a positive *DDF*, while dry air will promote evaporation and sublimation from the snow surface, which abstracts energy from the snowpack. Especially in spring, when relative humidity is comparatively low in middle and northern latitudes, large parts of the incoming solar radiation can be consumed by evaporation from the snow surface reducing significantly the energy available for melt and thus reducing the corresponding *DDFs* (Lang and Braun, 1990; Zhang et al., 2006).

Table 5.4 Latent heat component (DDF_E) [mm °C^{-1} d^{-1}] for selected relative humidity [%]

	DDF_E									
	Relative Humidity									
T_{DD} [°C d]	10%	20%	30%	40%	50%	60%	70%	80%	90%	100%
1	-7.28	-6.40	-5.53	-4.66	-3.78	-2.91	-2.04	-1.16	-0.29	0.58
2	-3.61	-3.14	-2.67	-2.21	-1.74	-1.27	-0.80	-0.33	0.13	0.60
3	-2.38	-2.05	-1.72	-1.38	-1.05	-0.72	-0.38	-0.05	0.29	0.62
4	-1.77	-1.50	-1.23	-0.97	-0.70	-0.43	-0.16	0.10	0.37	0.64
5	-1.40	-1.17	-0.94	-0.71	-0.49	-0.26	-0.03	0.20	0.43	0.66
6	-1.15	-0.95	-0.75	-0.54	-0.34	-0.14	0.07	0.27	0.47	0.68
7	-0.98	-0.79	-0.61	-0.42	-0.23	-0.05	0.14	0.33	0.51	0.70
8	-0.84	-0.67	-0.50	-0.32	-0.15	0.03	0.20	0.37	0.55	0.72
9	-0.74	-0.58	-0.41	-0.25	-0.08	0.08	0.25	0.41	0.58	0.74
10	-0.66	-0.50	-0.34	-0.18	-0.02	0.13	0.29	0.45	0.61	0.77

15	-0.40	-0.26	-0.11	0.03	0.18	0.32	0.47	0.61	0.75	0.90
20	-0.26	-0.12	0.03	0.18	0.32	0.47	0.61	0.76	0.90	1.05

Note: These values are for u=1 m s^{-1}, for a different wind speed these values can be multiplied for desired wind speed.

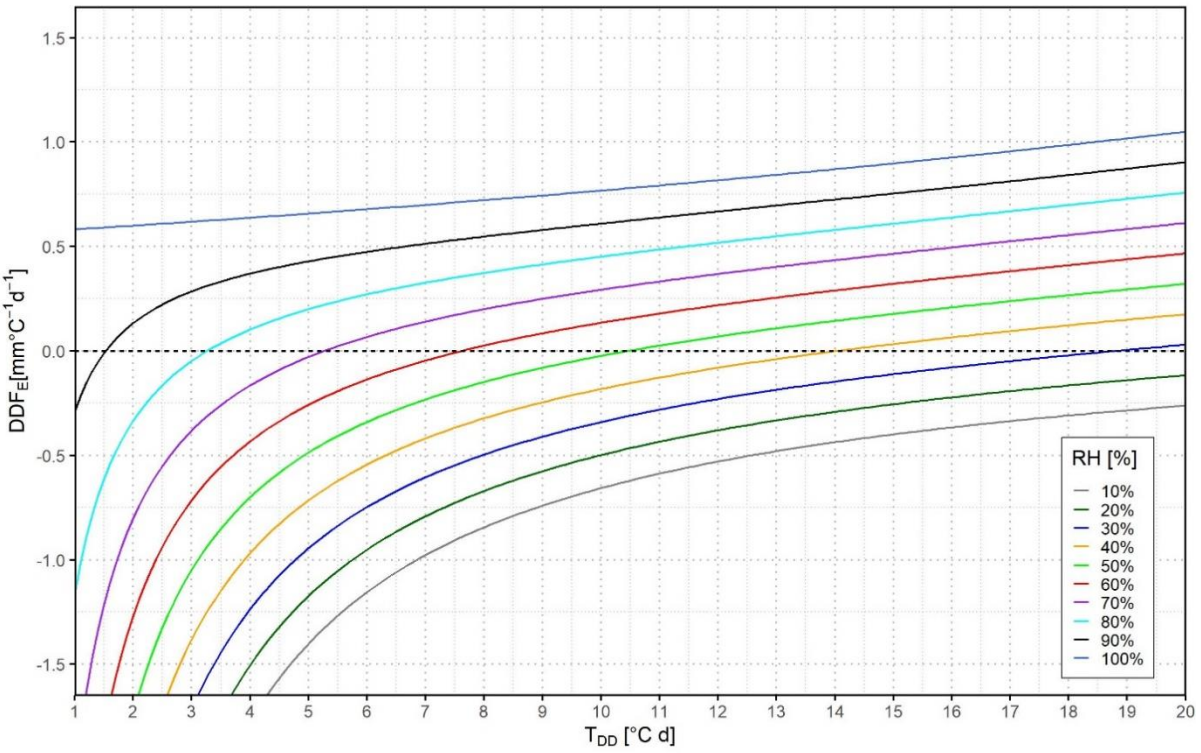

Figure 5.6 Latent Heat component (DDF_E) for selected relative humidity [%] and wind speed u = 1 m s^{-1}

5.4.5 Precipitation heat component – DDF_P

Rainfall can affect the snowpack energy budget by adding sensible heat due to warm rain and by release of latent heat if the rain is frozen in the snowpack (DeWalle and Rango, 2008). The latter effect is not considered in this study, as the snowpack is assumed at 0 °C melting condition. Because according to eq. (5.31) the precipitation heat Q_P is linearly dependent on air temperature, division by respective degree-days makes DDF_P independent of temperature and proportional to rainfall, resulting in a DDF_P = 0.0125 mm °C^{-1} d^{-1} for a precipitation depth of 1 mm per day. DDF_P for any other precipitation can be obtained by respective multiplication. The exemplary values in Table 5.5 show however, that the contribution of precipitation heat component DDF_P is modest compared to other DDF components. Even high rainfall of 50 mm in a day would release only a small amount of sensible heat, resulting in a DDF_P of 0.6 mm °C^{-1} d^{-1}.

Table 5.5 Precipitation heat component (DDF_P) [mm °C^{-1} d^{-1}] for selected precipitation [mm d^{-1}]

Precipitation (*P*)	1	2	5	10	25	50
DDF_P	0.0125	0.025	0.0625	0.125	0.313	0.625

5.4.6 DDF results comparison

In addition to the discussion on individual DDF components in previous sections, resulting total *DDFs* estimated from energy flux approaches are compared with observed *DDFs* at the Brunnenkopfhütte snow station. For this purpose, observed melt was estimated from the daily difference of observed snow water equivalent during melt periods (see Figure 5.7). Energy flux based melt was calculated by the formulas given in Sec. 5.3.2 using observed daily data from the Brunnenkopfhütte snow station (e.g. air temperature, wind speed, etc.) where applicable. Monthly averages of observed data (November 2016 – May 2021) can be found in Table 5.1.

As in operational degree-day models typically at least 10-daily constant degree-day factors are used, both, energy flux based and observed daily melt values were accumulated on 10-daily basis and divided by the degree-days of the respective period. This averaging procedure also smooths daily noise in the observed data, in particular inaccuracies in the determination of observed daily melt and unrealistic *DDF* values because of daily temperature averages just above 0 °C.

The comparison between observed and simulated (energy flux based) *DDFs* (see Figure 5.8) yields a fair agreement with BIAS = 0.2 mm °C^{-1} d^{-1} and RMSE = 1.1 mm °C^{-1} d^{-1}. Snowmelt periods in which a new snow event occurred (marked by hollow circles in Figure 5.8) were excluded from the calculation of the error metrics, since new snow events contradict the condition that the snowpack is ripe and isothermal at 0 °C. Fresh snow increases the cold content of the snowpack and a certain amount of the incoming energy is needed to bring it back to ‘ripe’ conditions, thus is not available for melt. This effect can be clearly seen in Figure 5.8, since all simulated *DDFs* belonging to periods with new snow events considerably overestimate the observed *DDFs*. Taking into account such changes in the internal energy of the snowpack under limited data availability would require a suitable parametrisation as discussed in Sec. 5.3.2.7, which is beyond the scope of the present study but may be subject to further research.

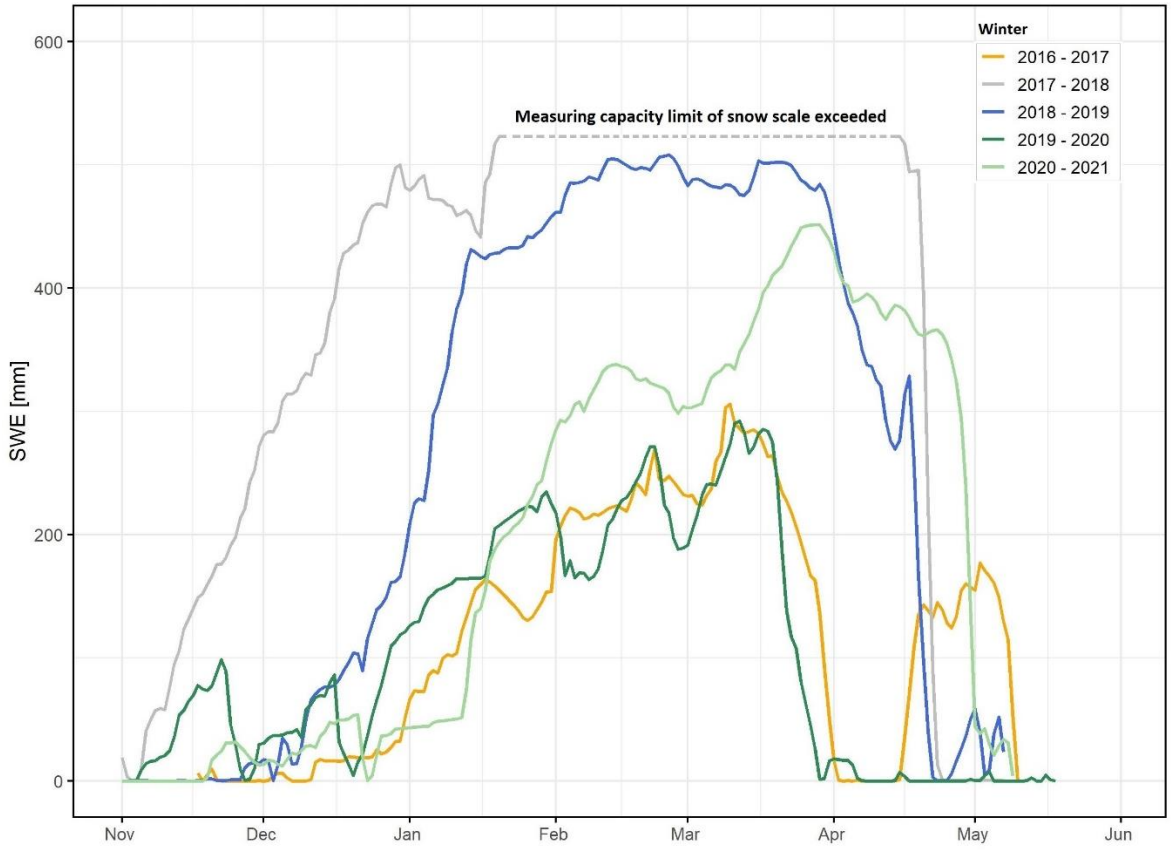

Figure 5.7 Observed snow water equivalent (SWE) at the Brunnenkopfhütte snow station (period: Winter 2016/2017 – 2020/2021)

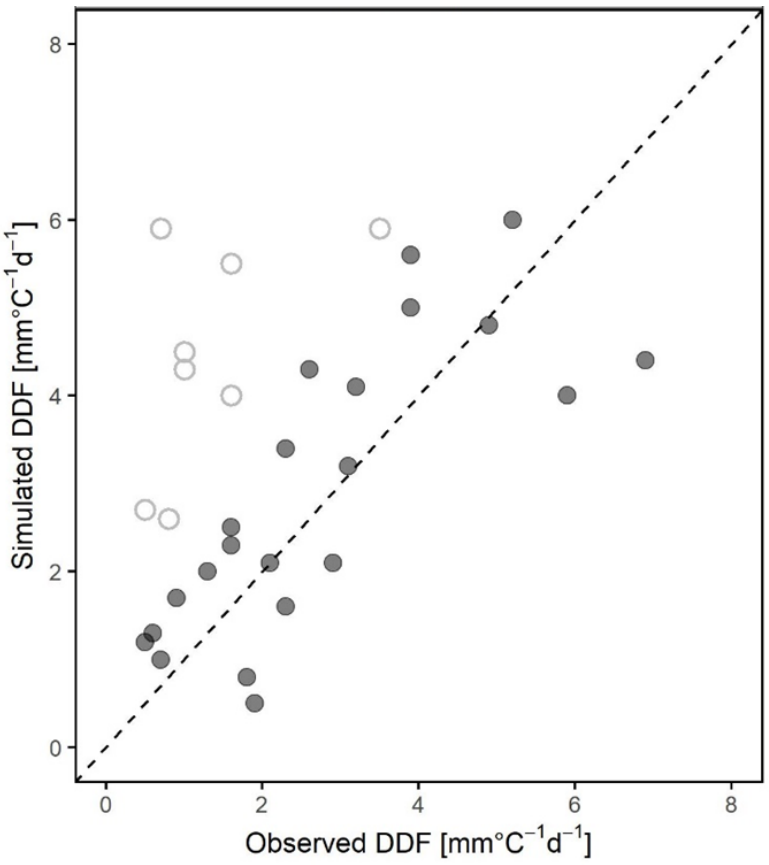

Figure 5.8 Comparison of observed vs simulated (energy flux based) 10-daily DDF for the Brunnenkopfhütte snow station (period: November 2016 – May 2021) – Hollow points represent DDFs during periods with new snow events

5.5 Discussion

While in the previous section the characteristic of each energy flux based DDF component is presented individually, in this section the influence of spatial, seasonal or meteorological conditions on the overall *DDF* is discussed. As before, all conclusions are under the assumption that the snowpack to isothermal at T_s = 0 °C and in ripe condition, hence all net incoming energy is available for melt and contributes to the total *DDF*. Other than the discussed variables are assumed constant with standard values u =1 m s^{-1}, RH = 70%, A = 0.5, P = 0 mm, latitude = 48° North (Brunnenkopfhütte snow station), and typical melt conditions of T_{DD} = 5 °C d if not stated otherwise.

5.5.1 Influence of latitude

Whereas local spatial variability in mountainous regions heavily affects melt by topographic effects, such as slope, aspect and shading, regional patterns of *DDFs* could not be detected in the data review by Hock, (2003). This observation is supported by a brief analysis of the effect of latitude where the *DDF* is compared not on the same date but at comparable melt conditions. The example compares

typical melt conditions of T_{DD} = 5 °C d at latitude 35° North (Naran station, Upper Jhelum catchment) (Bogacki and Ismail, 2016), which usually occur around mid-February, with similar conditions at a higher latitude of 48° (Brunnenkopfhütte) that arrive about one month later in mid-March. Figure 5.9 shows that the decisive solar radiation component is very similar in both situations, thus the total *DDF* is virtually identical at both locations. Therefore, at least in moderate latitudes, there is no significant effect of latitude on *DDF* when compared under similar melt conditions.

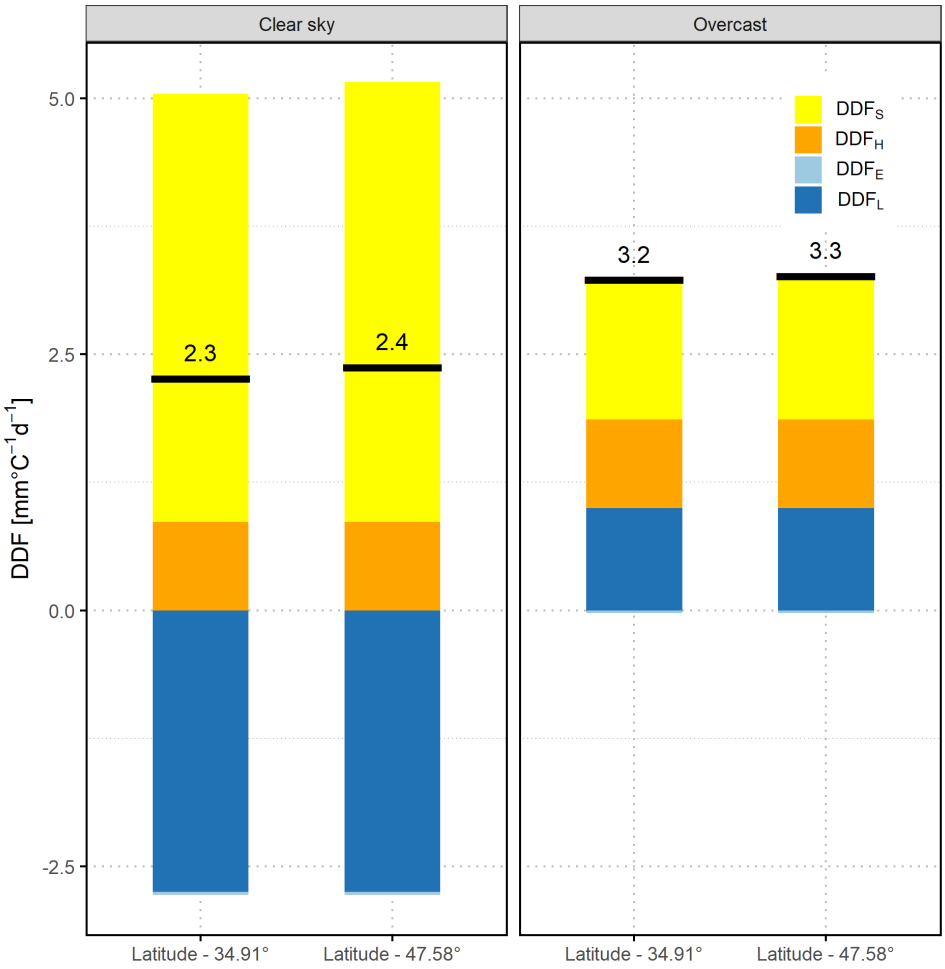

Figure 5.9 Influence of different latitudes on the *DDF* under clear sky and overcast conditions

5.5.2 Influence of altitude

Contrary to the compensating effect in the case of latitude, the delayed onset of snowmelt due to altitude influences the *DDF* noticeably, which becomes important in temperature-index models where calculation is usually based on elevation bands. In order to demonstrate the influence of altitude on the *DDF*, two elevation zones with an altitude of 2000 and 4000 m a.s.l. respectively are compared near Naran station in the Upper Jhelum catchment. As already mentioned, typical melt conditions of T_{DD} =

5 °C d occur at Naran usually around mid-February, while at 4000 m a.s.l. similar degree-days arrive about mid-May. The resulting *DDFs* (Figure 5.10) show a significant difference, both under clear sky as under overcast conditions, because of the different input in solar radiation caused by the alteration in solar angle.

Figure 5.10 shows an additional term DDF_A on top of the solar radiation component that represents the increase in incoming solar radiation due to the clearness altitude factor, which takes into account the increase of the clearness index with altitude. Averaging the factors proposed by different solar radiation models (see Figure 5.4) results in an additional component DDF_A of 0.4 and 1.4 mm °C^{-1} d^{-1} under clear sky and of 0.5 and 1.6 mm °C^{-1} d^{-1} und overcast conditions at 2000 and 4000 m a.s.l. respectively.
While for exemplification, snow albedo is assumed constant at 0.5 in Figure 5.10, taking into consideration the decrease of albedo as the snow ages e.g. A = 0.74 in February and A = 0.42 in May results in a more pronounced difference with altitude, i.e. a total *DDF* of 0.3 compared to 10.5 mm °C^{-1} d^{-1} under clear sky and of 2.7 versus 7.3 mm °C^{-1} d^{-1} under overcast conditions for the two altitudes respectively.

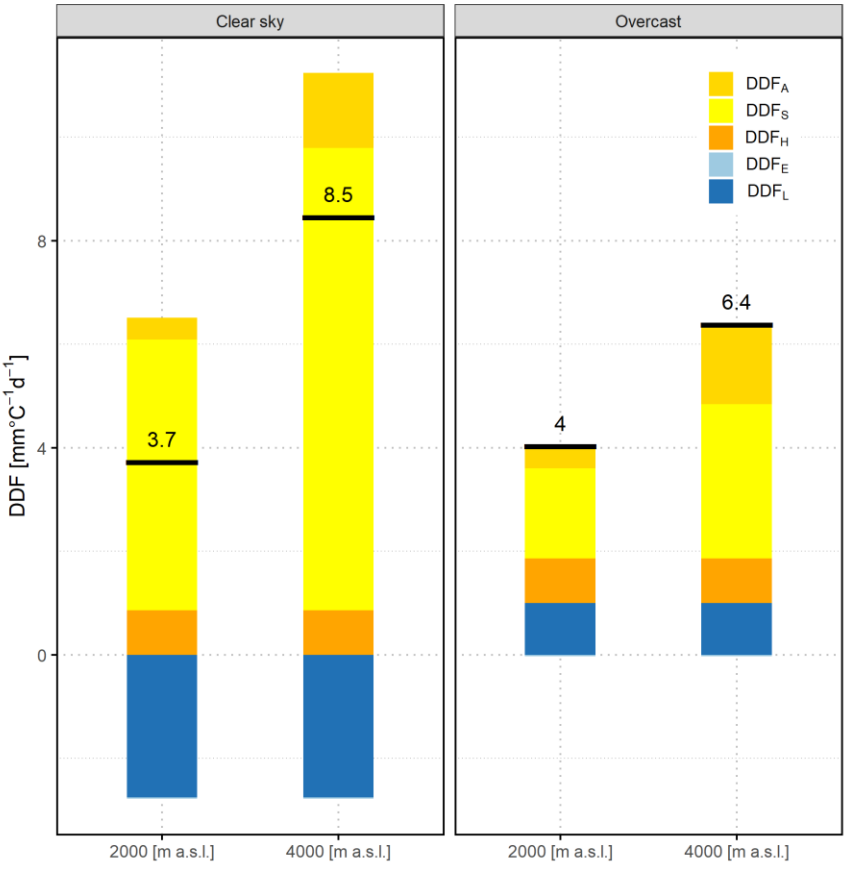

Figure 5.10 Influence of different altitudes on the *DDF* under clear sky and overcast conditions, DDF_A represents the increase in incoming solar radiation due to the clearness altitude factor

5.5.3 Influence of albedo

As already discussed in the sections before, snow albedo is a critical parameter for the *DDF* since according eq. (5.5) albedo directly controls the net solar radiation flux into the snowpack. While albedo of fresh snow is well above 0.9 hence reflecting most of the incoming shortwave radiation, it drops rapidly when larger grains form due to snow metamorphism. Figure 5.11 demonstrates the effect of aging snow after a new snow event, when a simple exponential decay model as given in eq. (5.19) is used and typical melting conditions T_{DD} = 5 °C d are assumed. Since directly after a new snow event (Day = 0) the fresh snow albedo is high (A = 0.95), the overall *DDF* is generally small. Under clear sky conditions, in case longwave radiation cooling is larger than net shortwave radiation flux, even a negative *DDF* value, i.e. no melt, may occur. If there is no new snow event in-between, albedo will decrease following the exponential decay model to 0.52 after 10 days resulting in a *DDF* of 5.8 mm °C^{-1} d^{-1} under clear sky and 4.4 mm °C^{-1} d^{-1} under overcast conditions. As described qualitatively in the literature e.g. (Hock, 2003), under all sky conditions the *DDF* is continuously increasing with decreasing albedo, with the increase however being more pronounced under clear sky than under overcast conditions.

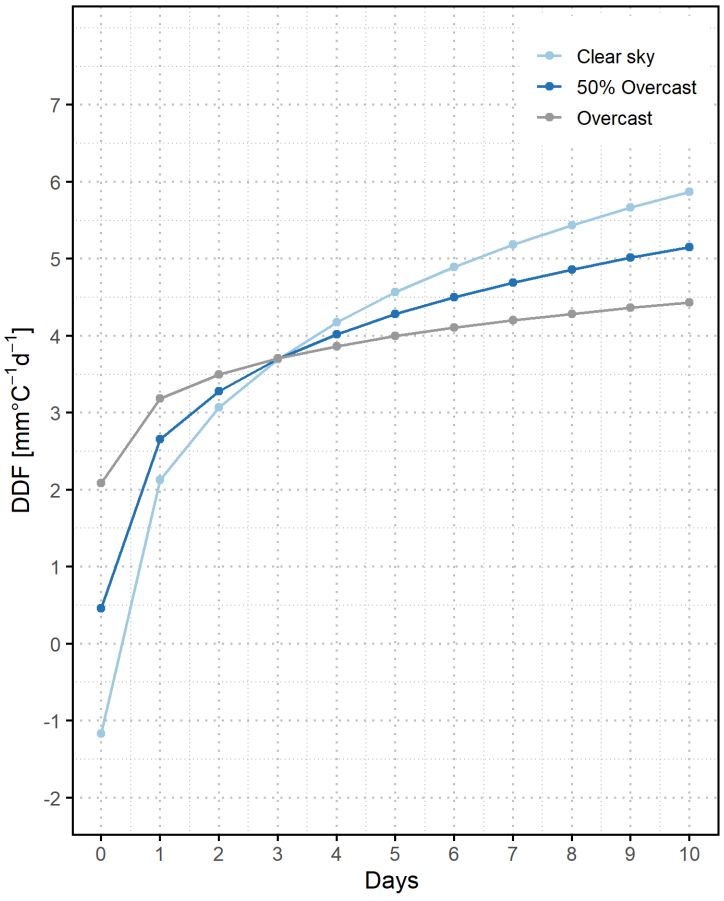

Figure 5.11 Influence of albedo over time on the *DDF* under different sky conditions

5.5.4 Influence of season

Since the solar angle is rising from its minimum at winter solstice in December to its maximum on 21th June, the solar radiation component DDF_S is increasing during the snowmelt season and thus the *DDF* is expected to increase respectively. Figure 5.12 shows the influence of season on the *DDF* at Brunnenkopfhütte snow station during the melt period, assuming average degree-days of 1, 4, and 7 °C d in March, April, and May respectively (see Table 5.1). Under clear sky conditions, as expected total *DDF* increases from a negative value of -3.6 mm °C^{-1} d^{-1} in March to 6.6 mm °C^{-1} d^{-1} in May. Under overcast conditions however, the *DDF* is virtually stable ranging from 4.4 to 4.5 mm °C^{-1} d^{-1} in the same period.

An evaluation of the individual DDF components shows, that under clear sky conditions the high impact of solar radiation in combination with low degree-days at the onset of the snowmelt season is counterweighted by a strong negative longwave radiation component that decreases as the season progresses. Under overcast conditions, DDF_L is neutral or slightly positive while the DDF_S component decreases because degree-days are rising faster than solar radiation input, which implies that sky conditions are more decisive for an estimate of the *DDF* than the date.

The effect of cloud cover is further amplified by the decrease in albedo while the melt season progresses, which becomes more significant under clear sky conditions. In the present example, that uses the average monthly albedo as specified in Table 5.1, only 30% of incoming solar radiation is contributing to melt in March, while it is about 60% in May, enhancing the marked increase of *DDF* under clear sky conditions.

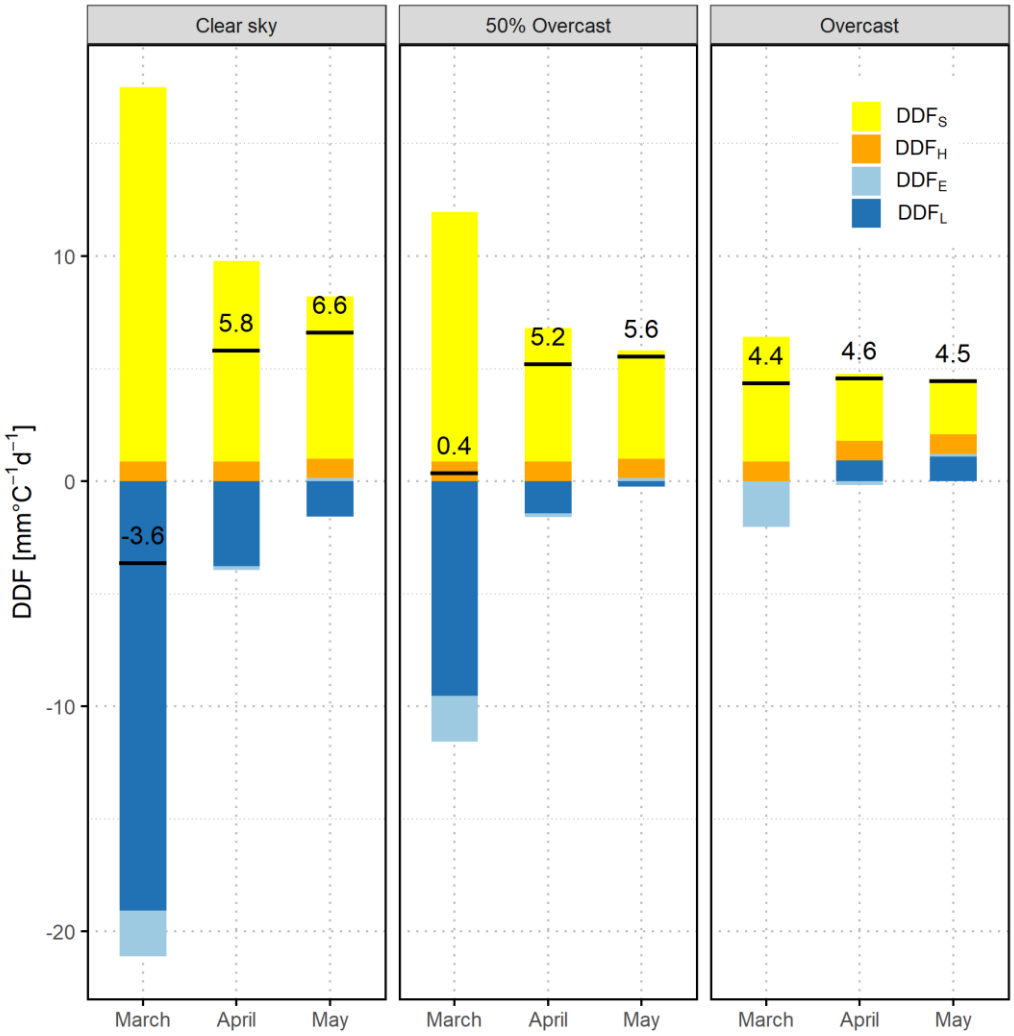

Figure 5.12 Influence of season on the *DDF* under different sky conditions

5.5.5 Rain on snow events

In general, precipitation heat component alone has only a minor effect on the *DDF*. However, in conjunction with certain weather conditions like braking in of warm and moist air, rain over snow events may lead to sudden melt and severe flooding. In a well-documented event in the Alps in October 2011 (Rössler et al., 2014) intensive rainfall (on average 100 mm d^{-1}) was accompanied by an increase in temperature by 9 °C, which shifted the 0 °C line from 1500 to 3200 m a.s.l. during one day. Similar conditions occurred e.g. end-December 2021 in Switzerland, when after the establishment of a solid snow cover, an Atlantic cyclone caused a sudden temperature rise up to 19 °C, wind gusts of 35 – 40 m s^{-1} and locally more than 70 mm precipitation (MeteoSchweiz, 2022), which e.g. at Adelboden (1325 m a.s.l.) caused the complete melt of an approx. 40 cm snow cover.

Figure 5.13 shows the different DDF components resulting from a hypothetical rain over snow event assuming an air temperature of 15 °C, a precipitation of 70 mm d^{-1}, an average daily wind speed of 10 m s^{-1}, a relative humidity of 100%, and overcast conditions. Although the amount of precipitation is substantial and rain's temperature is comparatively high, the contribution of DDF_P is still modest. However, air temperature, relative humidity, and in particular wind speed associated with such events increase the sensible and latent heat components significantly. Thus, the resulting overall *DDF* is much higher than under usual melt conditions, which may lead to a considerable melt that adds to the runoff already caused by the heavy rain.

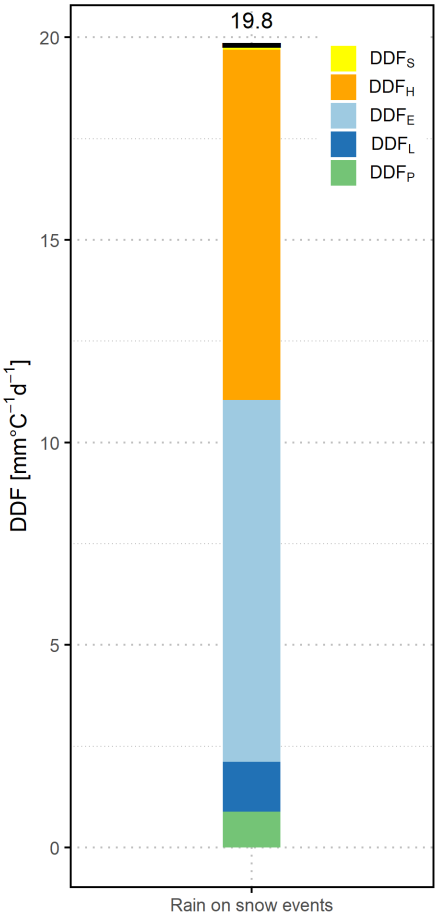

Figure 5.13 Influence of rain on snow events on the *DDF*, DDF_P is representing the contribution due to rainfall

5.5.6 DDF estimation for temperature-index modelling

Snowmelt runoff models using the temperature-index approach have proven useful tools for simulation and forecasting in large snow or glacier dominated catchments, in particular in remote mountainous regions where data is usually scarce. A good estimate of the degree-day factor as the decisive model

parameter is important either to stay in a realistic range when calibrating this parameter or in case of forecasting when estimating its changes while the season progresses. In order to demonstrate the alteration of *DDFs* over time and altitude, energy flux based *DDFs* are estimated using 10-daily average temperature (i.e. period 2000 – 2015) for the key elevation zones in the Upper Jhelum catchment (Bogacki and Ismail, 2016). Because of the lack of other than temperature and precipitation data, prevailing conditions during the melt season are crudely approximated by the standard conditions used in this section, assuming persistent clear sky conditions and albedo declining according eq. (5.19) after last fresh snow just before the beginning of the melting period.

Figure 5.14 (a) shows the development of *DDFs* in the elevation zones over time. As expected, melt starts earlier in lower elevation zones and successively progresses to higher altitudes. Interestingly, the *DDF* in the first 10-daily period of melting in each elevation zone increases with altitude. Obviously this is a combined effect of higher solar radiation input and decreasing albedo while the season progresses and the circumstance that the onset of melt in higher elevation zones starts at a lower degree-day threshold than in lower zones. In contrast to Figure 5.12, the *DDF* decreases continuously in all elevation zones in the subsequent melting periods since air temperature and thus degree-days rise faster than melt increases.

5.5.7 Influence of climate change

Climate change will ultimately influence snowmelt patterns depending on the projected changes in temperature and precipitation. In recent studies, usually model parameters including *DDFs* are considered as constant when assessing the climate change impact on future water availability from snow and glacier fed catchments (Lutz et al., 2016; Hasson et al., 2019; Ismail et al., 2020). However, due to the physical processes on which they depend these parameters are subject to climate change. In this section, an attempt is made to estimate the influence of climate change on the *DDFs* in different elevation zones. For this analysis, projected temperature changes for the period 2071 – 2100 that according to data for the Upper Indus Basin (Ismail et al., 2020) amount to ΔT = 2.3 °C under RCP2.6 and to ΔT = 6.5 °C under RCP8.5 are added to the temperatures in present climate for each elevation zone.

The first effect to be observed in Figure 5.14 (b) and (c) is the common finding that snowmelt will start earlier under climate change as temperatures rise earlier above freezing. In addition, since being earlier in the year, the *DDFs* in corresponding elevation zones are generally smaller compared to the current climate, though there are some outliers at the start of melting, due to division by low degree-day values. In case of the pessimistic scenario RCP8.5 (Figure 5.14 (c)), a seasonal snow cover will not establish any more in the lowest elevation zone (i.e. 2500 – 3000 m a.s.l.) as air temperature at this altitude is projected to stay well above freezing throughout the winter. In general, the results of this brief analysis

indicate, that the *DDFs* are expected to decrease under the influence of climate change, as melt will occur earlier in the year when solar radiation is smaller.

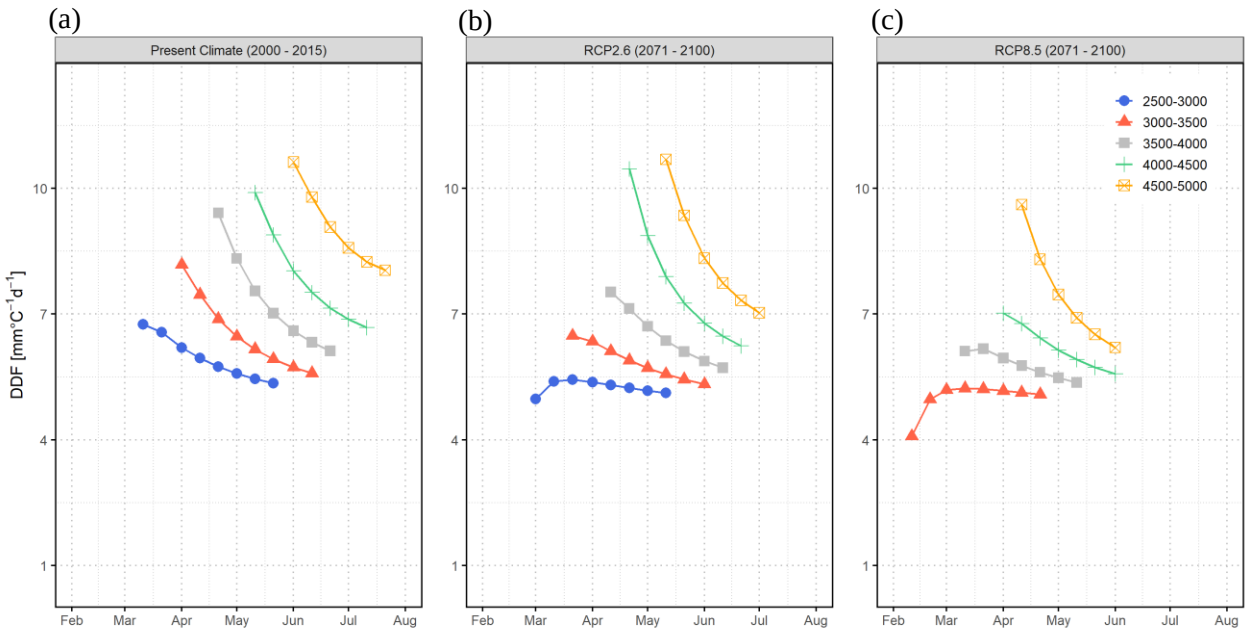

Figure 5.14 (a) *DDF* estimation for a temperature-index modelling (b) Influence of climate change – 2071 – 2100 under RCP2.6 (c) Influence of climate change – 2071 – 2100 under RCP8.5

5.6 Conclusions

Degree-day models are common and valuable tools for assessing present and future water availability in large snow or glacier melt dominated basins, in particular when data is scarce like e.g. in the Hindukush-Karakoram-Himalayas mountain ranges. The present study attempts to quantify the effects of spatial, temporal, and climatic conditions on the degree-day factor (*DDF*), in order to gain a better understanding which influencing factors are decisive under which conditions. While this analysis is physically based on the energy balance, approximate formulas for estimating the *DDFs* are used to account for situations where observed data is limited. In addition, resulting tables and graphs for typical melt conditions are provided for a quick assessment.

A comparison between observed and estimated *DDFs* at the Brunnenkopfhütte snow station shows a fair agreement with BIAS = 0.2 mm $°C^{-1}$ d^{-1} and RMSE = 1.1 mm $°C^{-1}$ d^{-1} that however only takes into account periods without new snow events, since fresh snow increases the cold content of the snowpack and contradicts the condition of the snowpack being ripe and isothermal at 0 °C. If, under the constraint of limited data availability, also changes in the cold content of the snowpack shall be considered, further research is needed on an approach that sufficiently parameterizes the diurnal dynamic of vertical temperature distribution in the snowpack.

Furthermore, it is neither intended to use these *DDF* estimates directly as a model parameter nor to incorporate an energy balance based *DDF* approach into a degree-day model. One important aspect of temperature-index models is, that the *DDF* is a lumped parameter, which is usually subject to calibration and accounts for uncertainties in different variables and parameters, e.g. temperature estimates, runoff coefficients, etc. Thus, the *DDF* estimated by the energy balance approach are rather aimed to validate the results of parameter calibration or to indicate necessary adjustments due to climate change.

The analysis of the energy balance processes controlling snowmelt indicates that cloud cover is the most decisive factor for the dynamics of the *DDF*. Under overcast conditions, the contribution of shortwave radiation is comparatively low whereas the other components are in general small. Therefore, total *DDF* is moderate and variations due to other factors are usually limited, apart from exceptional rainstorm events, for which however energy balance models are the more suitable approach.

Under clear sky conditions on the other hand, shortwave radiation is the most prominent component contributing to melt. The increase of solar angle while the melt season progresses in combination with declining albedo and a decreasing cooling effect by the longwave radiation component along with increasing air temperature leads to a pronounced temporal dynamic in the *DDF*. Whereas incoming solar radiation and net longwave radiation can be determined fairly accurate under clear sky conditions, albedo becomes the crucial parameter for estimating the *DDF*, especially when new snow events occur during the melt period.

Clear sky conditions promote the effect of increasing *DDF* with altitude if similar melting conditions are compared, since melting temperatures arrive later in the season at higher altitudes. The opposite effect can be observed with regard to climate change. It is well known and because of higher temperature evident, that at a certain altitude climate change will shift the snowmelt season earlier in the year. Consequently, when comparing periods of similar degree-days, as results from this study indicate the *DDFs* are expected to decrease, since solar radiation is lower and albedo is likely to be higher.

Therefore, and as pointed out by many researchers, the *DDF* cannot be considered a constant model parameter. Rather, its spatial and temporal variability must be taken into account especially when using temperature-index models for forecasting present or predicting future water availability.

Author contributions

MFI: Conceptualization, Methodology, Software, Formal analysis, Investigation, Data curation, Writing – original draft, editing, Visualization. **WB:** Conceptualization, Methodology, Software, Formal analysis, Investigation, Data curation, Writing – reviewing & editing. **MD:** Supervision, review & editing. **MS:** Data curation, review & editing, **LK:** Supervision, Data curation.

Competing Interest

The contact author has declared that neither they nor their co-authors have any competing interests.

Acknowledgements

We thank Koblenz University of Applied Sciences that we could use the data of the snow station for this study.

Chapter 6

Conclusions and outlook

This research focuses on assessing and forecasting the seasonal as well as future water availability in a data limited region (e.g. Upper Indus Basin – UIB) by employing an enhanced hydrological modelling as well as scenario-based forecasting approach. In order to fulfil the objectives of this research the main research topic was divided into three sub-topics. These topics focused on three important aspects listed as follows.

(i) Snow and ice melt runoff modelling and forecasting
(ii) Enhanced model evaluation for assessing the future water availability under current and climate change scenarios
(iii) Analysis of the degree-day factor

In this dissertation, a degree-day model with separate snow and ice melt component in conjunction with seasonal scenario forecast approach is used to forecast the seasonal water availability. Secondly, a comparison between conventional and enhanced hydrological model calibration/validation approach is performed in order to increase the confidence in the modelling outcome (i.e. simulated flows). Furthermore, assessment of future water availability especially major changes in snow and glacial water availability as well as changes in uncertainty contribution from different sources of uncertainty under the influence of climate change are carried out. Lastly, energy flux based degree-day factor (*DDF*) estimation is done to quantify the influence of different spatio-temporal and climatic conditions on the degree-day factors. The aim of this part of the study is to better understand the dependencies of the *DDF* and to help in selecting realistic values of the *DDF* during model calibration as well as specify necessary adjustments due to climate change.

6.1 Summary

Seasonal melting of snow and glaciers from the headwater catchments (i.e. Upper Indus, Kabul, Upper Jhelum and Upper Chenab) deliver a steady streamflow to the irrigated areas of Pakistan. However, there is a dire need to assess and evaluate seasonal melt water contributions from the Indus region in a

broader spectrum. Because in this region climate change has now started to influence, for example in the form of increasing intensities of natural disasters. With these climatic changes across this region, it is better to prepare the water managers and decision makers for different scenarios beforehand so that they might be able to take informed decisions regarding seasonal shift in the future water availability. There are several problems in this complex mountainous region for example, lack of sufficient ground based data, presence of large uncertainties in the hydrological budget due to complex snow and ice hydrology. This dissertation is an effort to help in tackling these challenges. Conclusions from all the work packages are discussed one by one as follows.

Firstly, the main challenge of simulating the snow and glacier ice runoff for the UIB was handled by employing a phenomenon based hydrological model with the aim of better understanding the snow and ice melt processes (Ismail and Bogacki, 2018). It is critical to develop an understanding about the snow and ice melt processes because their contributions as well as the response to the flows are different. Secondly, a scenario based seasonal water availability forecasting method was devised (Ismail and Bogacki, 2018), which has many commonalities with traditional Ensemble Streamflow Prediction (ESP) method (Day, 1985). The reason for using the scenario-based approach is its simplicity and the unavailability of reliable meteorological forecast of temperature and precipitation for a lead-time of 6 months.

Furthermore, numerous improvements have been introduced to the snowmelt runoff model in order to handle the specific needs of the UIB. One major modification in the model was the introduction of separate degree-day factor for considering the glacial ice melt contribution. Without glacial melt component, there exist a lack of water in simulations compared to observed hydrograph especially in the late Kharif season (i.e. July – September) when the snow line reaches to the higher elevations (i.e. permanent glacier areas). Besides, the eastern part of the UIB (i.e. Tibetan Plateau) which receives less precipitation behave quite differently compared to the western UIB even though the altitudinal ranges are similar for both the eastern and western portions of the basin. The reason for receiving less precipitation in the eastern part of UIB could be related to the westerlies (i.e. western disturbances). The MODIS snow data also confirmed that the snow cover was disappearing much faster in the Tibetan Plateau compared to the Karakoram region. This problem of unstable snow coverage led to the division of the UIB into two homogeneous units (i.e. upper and lower portions) in order to tackle this issue more reasonably. Application of the degree-day factor (*DDF*) in the forecast mode was handled by using a unique 'time-dependent' variation approach, where the *DDF* starts increasing by the time when melting has started in a particular elevation zone. This time dependent *DDF* approach is based on linear regression between the calibrated *DDFs* and time (i.e. 10-daily period). The increase in the *DDF* during the melt season is reasonable because of changing snow properties over time (i.e. snowmelt metamorphism). However, the weakness of this time dependent approach is that the *DDF* will not go

down if for example, there is a change in the meteorological conditions (i.e. decrease in temperatures or there is new snow event). In this case, simulated flows will be overestimated by this approach because of using high values of the *DDFs*, whereas in reality there is less or not snowmelt.

Furthermore, the seasonal scenario-based forecast approach is a step towards a hybrid forecasting approach, which uses a combination of process-based hydrological models as well as probabilistic forecasting approaches. On one hand, availability of reliable temperature and precipitation forecast on seasonal basis are still a major challenge. On the other hand, modelling results are primarily based on these (i.e. temperature and precipitation) input variables. One possible improvement in the seasonal water availability forecast could be the incorporation of teleconnection signals e.g. Southern Oscillation (ENSO: El Nino, La Nina) and North Atlantic Oscillation (NAO[1]). That could be a source of predictability of seasonal anomaly variation. If teleconnections can be found for this region, they can improve the seasonal forecasting of flows from the Indus River and its tributaries that will also help in addressing the current water crisis situation in Pakistan by allowing improved water management.

The summary of main conclusions from this study is as follows:

- The Snowmelt Runoff Model + Glaciers (SRM+G) model has the ability to simulate the snow and ice melt runoff for a complex rugged mountainous catchment.
- MODIS snow cover data presumed to be one of the best information sources to monitor the snow cover situation in the data scare regions and it represented well the variability of snow cover extent in the Upper Indus Basin.
- The seasonal scenario-based approach for forecasting the seasonal water availability is a reasonable approach in the absence of actual long-term forecasted data.
- The time dependent *DDF* approach shows the development of the *DDF* over time. However, this approach can be further improved by taking into account for the energy available for melt.

The second work package focuses on the enhanced calibration/validation approach and future water availability under climate change scenarios (Ismail et al., 2020). In climate impact studies there are two possible approaches to distinguish (i) using a multi-model ensemble disregarding model performance (ii) using models only after proper evaluation and considering their performance. In this work package, for climate impact assessment hydrological models were used after following a proper evaluation procedure. The main hypothesis was that a good performance of a hydrological model in the historical time period will increase confidence in projected impacts under climate change as well as decrease uncertainty of projections related to hydrological models. To do this, two hydrological models calibration/validation strategies were analysed and their influences on future water availability were

[1] El Niño-Southern Oscillation (ENSO); North Atlantic Oscillation (NAO)

quantified. The results of this analysis shows that the projections based on enhanced calibration/validation approach are more credible compared to conventional approach. In the enhanced method the hydrological model calibration parameters were not only tested for the sub-catchments but also contrasting climatic conditions were considered. Furthermore in order to ensure internal consistency of the simulated processes as well as comparatively addressing the challenge related to equifinality, proper attention was given by validating for additional variables in the form of considering glacier mass balance, evapotranspiration (or model losses) and snow cover dynamics. It has to be noted that the results for the intermediate gauges were not up to the mark in some cases because of the use of harmonized parameterization throughout the whole catchment. On the other hand, the outcome produced by this method to some extent can pave a way to address the climate non-stationarity by assuring that the model with these parameters is more appropriate to variable climate conditions.

Regarding the uncertainty quantification an analysis of variance (ANOVA) assessment was applied which showed that the results based on the enhanced model evaluation are more credible in terms that the uncertainty contribution is getting smaller for projections based on enhanced method. Even though, the results based on the conventional method are also quite reasonable. It was noted that different hydrological models give different signals for projected hydrological changes especially when the flow components are based on different sources like snow and ice melt. Moreover, the type of melt modelling approach (i.e. energy balance or temperature-index) also influences the results. This is the reason, it is important to use a multi-model ensemble for impact assessment in order to some extent minimize the model-related uncertainties.

It is admitted that the assessment of future water availability in terms of hydrological regime changes in the Upper Indus Basin is a vast and complex subject because there are a lot of interconnected phenomenon involved (e.g. melt-dominated dynamics) which ultimately cause uncertainties in estimating the hydrological budget. There are some assumptions (e.g. unavailability of simulated evapotranspiration in SRM+G model, estimated future snow cover area, absence of dynamic representation of glaciers) in the modelling approaches, which have certain shortcoming. In addition, these assumptions were made due to lack of data availability and data quality problems in such mountainous region. It is acknowledged that the results in this study would have been different if different assumptions were made. For example, a fixed glacier area reduction scenario had been assumed with an interval of 25% reduction under both Representative Concentration Pathways (i.e. RCP2.6 and RCP8.5). It would has made a lot more sense if glacier reduction scenario was considered separately for both RCPs depending upon how these climate forcing are developing for the future. Thus, a precise assessment of existing glaciers ‘tipping point’ is mandatory for assessing the future water availability and this can be done by dynamic representation of glaciers in a hydrological model. Moreover, depletion of Snow Cover Area (SCA) in the future was estimated by using a novel

'temperature similarity' approach with the assumption that snow cover conditions in an elevation zone are best defined by temperature. Of course, temperature is only one of the critical variable. Incorporation of precipitation (i.e. snow accumulation) in this approach might help in improving the results. The procedural gap like the absence of simulated actual evapotranspiration (ET_a) in the Snowmelt Runoff Model (SRM) model was handled by using model losses as a proxy to actual evapotranspiration. It can be said that the models used in this study can be further improved for a more accurate assessment of future water availability.

The key conclusions from this study can be summarized as follows:

- The model parameterization achieved in the enhanced calibration/validation method is better suited for climate change impact assessment because these parameters were tested at different gauges under different climate conditions and glacier mass balance (GMB) was also given due consideration.
- Calibration/validation for multiple variables (i.e. discharge, GMB, ET_a) lead to more accurate simulation of hydrological processes with little sacrifice of model performance in terms of goodness of fit statistics.
- Two different parameterizations of the hydrological models lead to different impact assessment results at the mean monthly and annual scales reaching up to 19% and 10%, respectively.
- According to the analysis of variance, the contribution of hydrological model parameter uncertainty to the overall uncertainty becomes very small by the end of the century using the enhanced calibration/validation approach.

The third work package is primarily focusing on the estimation of the *DDF* based on energy flux components (Ismail et al., 2022). Degree-day models are considered to be important tools for assessing water availability in snow or ice fed catchments, in particular when data is limited. Energy flux based estimation of the *DDF* is a value addition to time-dependent variation of the *DDF* (Ismail and Bogacki, 2018). The objective of this work package is to provide a simple solution for estimating the *DDF* with minimum possible available information. The advantage of this study is that it can rely exclusively on energy balance equations and climatic classification in the absence of ancillary ground observations. It is important to identify the actual variations of the *DDF* in order to accurately compute the snow and ice melt runoff. Under the influence of climate change, realistic computation of snowmelt will be beneficial for the water managers as well as policy makers in order to devise a better water management plan. Moreover, this *DDF* estimation method can act as a baseline for further validating the already calibrated *DDF* for the HKH region (Ismail and Bogacki, 2018).

A comparison between observed and estimated degree-day factors at the Brunnenkopfhütte snow station shows a fair agreement with BIAS = 0.2 mm $°C^{-1}$ d^{-1} and RMSE = 1.1 mm $°C^{-1}$ d^{-1}. But these results

are without consideration of new snow events, since fresh snow increases the cold content of the snowpack and contradicts the condition of the snowpack being ripe and isothermal at 0 °C. If cold content of the snowpack needs to be considered then further research is needed on an approach that appropriately parameterizes the dynamics of vertical temperature distribution within the snowpack.

The results from this study also supports the findings of other researchers that the *DDF* cannot be taken as a constant parameter and its spatio-temporal variability should be taken into consideration. Especially when using degree-day models for forecasting present or predicting future water availability.

The main conclusions from this study are summarized as follows.

- Snow albedo and sky conditions (i.e. clear sky and overcast) are crucial factors in deciding the final value of the *DDF*.
- If similar melting conditions are assumed then *DDFs* at higher altitude are expected to increase. However, *DDFs* are fairly stable at two different latitudes (but at the same altitude) as the melting conditions arrive early in the year at lower latitudes compared to the higher latitudes.
- *DDFs* are expected to decrease under the influence of climate change as snowmelt will shift earlier in the year due to projected increase in temperatures when radiation input will be lower and snow albedo will then likely to be higher.
- This study supports the findings of other researchers that the *DDF* is not constant but variable, even within a snowmelt season it varies from one event to another depending on changes in physical properties of snow in conjunction with the prevailing meteorological conditions.

To sum up, this dissertation consists of three main research objectives i.e. *developing a method for seasonal water availability forecast for a snow and glacier fed catchment*, *assessing future water availability while considering the model performance for climate impact studies,* and finally *estimating degree-day factor* with minimum available information. These three objectives are considered to be the building blocks of a water availability predictions. It shows that a temperature-index approach based hydrological model in conjunction with satellite based remote sensing snow and glacier data could be used for simulating the snow and ice melt runoff. In addition, for climate impact studies a comprehensive model evaluation has been implemented so that it could help minimize the uncertainties related to the hydrological models especially for a catchment that primarily has a snow and ice melt regime. All the results presented here are based on the temperature-index approach, therefore estimation of *DDFs* through energy flux-components is justified in order to know which influencing factors are decisive under which conditions and how to adjust the *DDFs* under different circumstances.

6.2 Future outlook

In this section of the dissertation a possible outlook for future research activities are given. Hence, a specific outlook is given in context of improvement in the existing SRM approaches as well as developing a snow and glacier assessment tool for a water availability dashboard.

6.2.1 Improvement in existing SRM+G approaches

The process-based snow and glacier melt runoff-modelling approach of existing SRM+G model can be improved by incorporating the evapotranspiration component in the existing model. In present state, the model is not directly dealing with evapotranspiration losses. Additionally, estimation of future depletion of the snow cover area in a catchment using the temperature similarity approach can be improved by taking into account not only the temperatures but also seasonal snow accumulation.

6.2.2 Hybrid forecasting approach

Process-based models can be more skilful in producing the forecasts compared to statistical models because these models have the capability of modelling the non-linear process of snow and ice melt. However, statistical models can quantify the uncertainties related to predictions more robustly in comparison to these process-based models. In order to better handle the uncertainties related to forecasts, hybrid forecasting models can be established which make use of the strengths of the statistical and process-based models. Scenario-based seasonal forecast in this dissertation is a step in this direction, which can be further improved by taking into account of different available statistical models and approaches.

6.2.3 Water availability dashboard

One future perspective of this research is the development of a water availability dashboard for Pakistan. Presently, there is no such tool/dashboard available in public domain. The core idea is to develop a water dashboard with freely available datasets that would provide an overview of the existing and future water availability. A special focus area will be the situation of fresh water resources (i.e. snow and glacier) under changing climate.

This Ph.D. project has opened new research paths and one possible future research activity relates to better utilization of freely available satellite-based snow and glacier information. In this respect, a Snow and Glacier situation Assessment Tool (SGAT) is in development. This tool will be helpful for water managers as well as policy makers for taking decisions related to future water availability in the Upper Indus Basin (UIB).

A complete software based on R-programing language has been prepared, which will provide the final product in the form of a map as shown in the Figure 6.1 and Figure 6.2. All the data as well as related information used to prepare these maps are freely available and is in public domain. Figure 6.1 is representing the snow and glacier situation in the upper basins (i.e. UIB, Upper Jhelum, Upper Chenab and Kabul River Basin) at the start of Kharif cropping season when most of the catchment area is covered with snow. In this map, locations and related information for all the hydro-meteorological stations operated by different departments and authorities have been provided. Furthermore, historic as well as current statistics of snow and glacier cover areas are also given.

Figure 6.2 is an example, showing end of Kharif cropping season when most of the seasonal snow has been disappeared and the glacier area has been exposed. This sort of visualization is providing a real time spatial coverage of snow and glaciers which will help in judging the snow and glacier situation in the upper catchments. Of course, this is just an initial idea to better utilize freely available remote sensing data. In the future, this tool will be further improved.

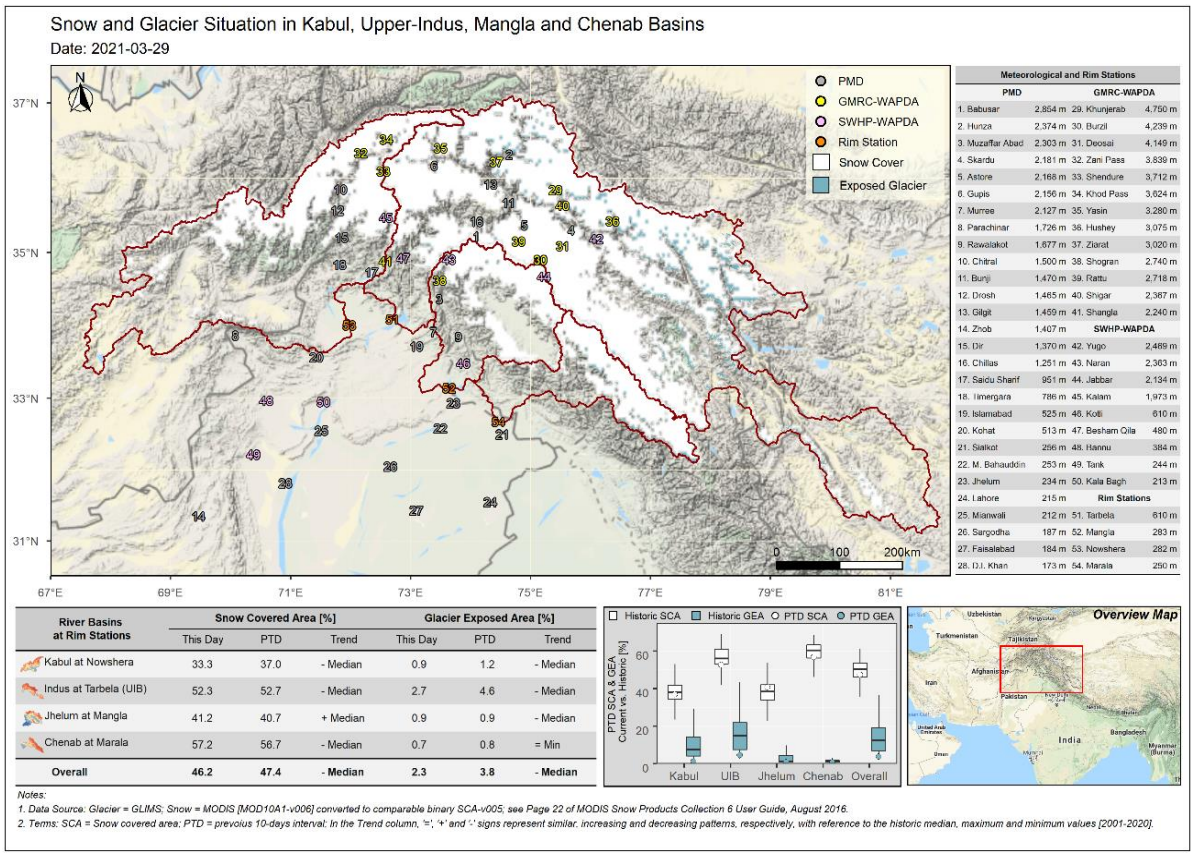

River Basins at Rim Stations	Snow Covered Area [%]			Glacier Exposed Area [%]		
	This Day	PTD	Trend	This Day	PTD	Trend
Kabul at Nowshera	33.3	37.0	- Median	0.9	1.2	- Median
Indus at Tarbela (UIB)	52.3	52.7	- Median	2.7	4.6	- Median
Jhelum at Mangla	41.2	40.7	+ Median	0.9	0.9	- Median
Chenab at Marala	57.2	56.7	- Median	0.7	0.8	= Min
Overall	**46.2**	**47.4**	**- Median**	**2.3**	**3.8**	**- Median**

Figure 6.1 Outcome of SGAT – providing snow and glacier situation in the broader study area at the start of Kharif season – i.e. snow covered

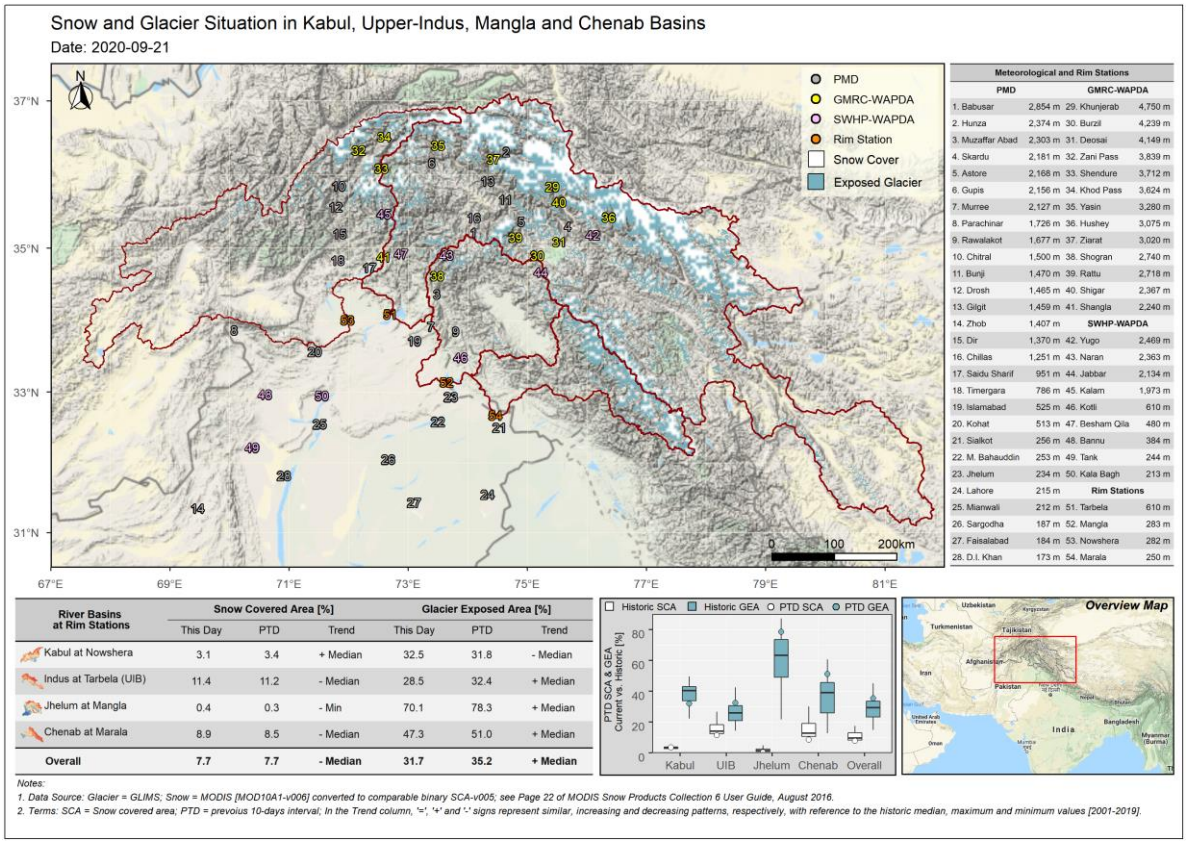

Figure 6.2 Outcome of SGAT – providing snow and glacier situation in the broader study area at the end of Kharif season – i.e. glacier covered

Figure 6.3 shows a flowchart of different processes being implemented in SGAT. As mentioned earlier, the complete software has been coded in the R-programming language. The major steps include downloading and processing of (i) MODIS snow data, (ii) preparation of glacier data i.e. Global Land Ice Measurements from Space (GLIMS) (Raup et al., 2007) and (iii) catchment shape files for extracting the area of interest as well as preparing maps. Production of cloud free MODIS snow cover data has been done by applying the similar methodologies presented in literature (Dong and Menzel, 2016; Gafurov et al., 2016). An application based on Shiny platform of R-programming language is under development. It will provide more freedom to the end users in terms of data interpretation as well as data visualization.

Additionally, in future it is intended to share automatically generated reports on the snow and glacier situation in the upper basins with the concerned departments in Pakistan. Figure 6.4 shows a draft of an overview of automatically generated report.

Present Snow and Glacier situation Assessment Tool (SGAT) will also be integrated in the anticipated water availability dashboard. Additionally, different key categories of information which are crucial for the understanding of water availability will be included in this dashboard.

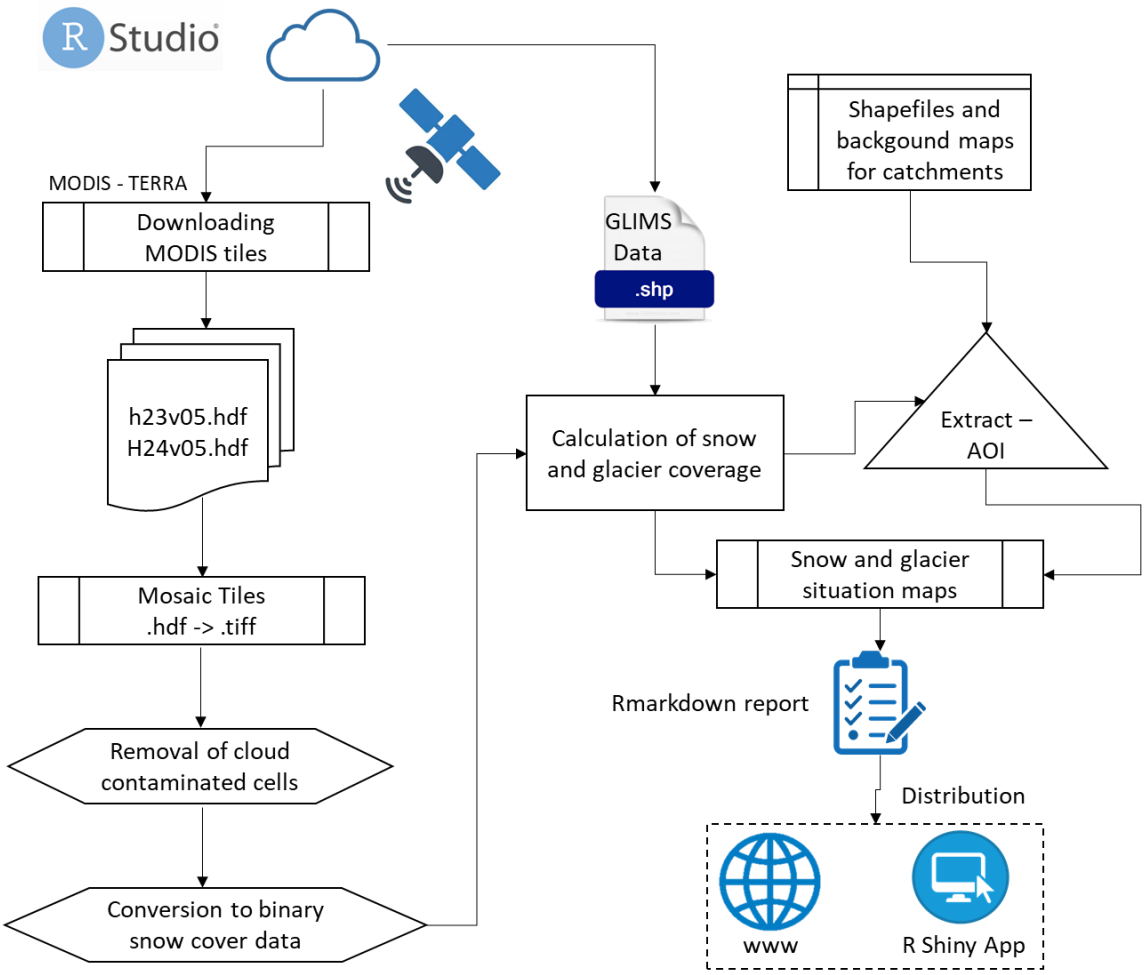

Figure 6.3 Flowchart of Snow and Glacier situation Assessment Tool (SGAT)

Snow and Glacier Assessment

A product of SGAT Team
Visit us at Rethinkingindus.com

Reference No.SGAT-01/20-11-2020

Snow and glacier situation in the upper catchments

Snow and glaciers are vital fresh water resources. Monitoring of snow and glacier situation through the available satellite data in the upper catchments (i.e.**Indus@Tarbela**, **Jhelum@Manla**, **Chenab@Marala** and **Kabul@Nowshera**) will be extremely helpful for the water managers and policy makers for making an *informed decision* for water policy.

Summary of snow and glacier cover situation in the Upper catchments

Rim Stations	**Tarbela [%]**	**Mangla [%]**	**Marala [%]**	**Nowshera [%]**
Last 10-day snowcover	11.4	0.4	8.9	3.1
Historic 10-day snowcover	11.2	0.1	8.5	3.4

Note: This forecast is updated on 10-daily basis.

Snowcover percentage of last 10 days is **10%** higher than normal overall in upper indus catchments.

Further details and latest glacier and snow situation maps can be downloaded from the following link:

- SGAT-PK

Figure 6.4 Automatically generated report format of SGAT

Bibliography

Adnan, M., Nabi, G., Saleem Poomee, M., and Ashraf, A.: Snowmelt runoff prediction under changing climate in the Himalayan cryosphere: A case of Gilgit River Basin, Geoscience Frontiers, 8, 941–949, https://doi.org/10.1016/j.gsf.2016.08.008, 2017.

Ahmad, M. J. and Tiwari, G. N.: Solar radiation models-A review, Int. J. Energy Res., 35, 271–290, https://doi.org/10.1002/er.1690, 2011.

Akram, A. A.: Indus Basin water resources, Tiempo Climate Cyberlibrary, 8, 2009.

Allen, R. G., Pereira, L. S., Raes, D., and Smith, M.: Crop evapotranspiration —guidelines for computing crop water requirements, FAO, 56, 1998.

Ambach, W.: Characteristics of the Heat Balance of the Greenland Ice sheet for Modelling, J. Glaciol., 31, 3–12, https://doi.org/10.3189/S0022143000004925, 1985.

Anderson, E. A.: National Weather Service river forecast system: snow accumulation and ablation model, 1973.

Anderson, E. A.: Snow Accumulation and Ablation Model - SNOW-17, NOAA's National Weather Service, Office of Hydrologic Development, Silver Spring, 2006.

Andreadis, K. M., Storck, P., and Lettenmaier, D. P.: Modeling snow accumulation and ablation processes in forested environments: VIC SNOW MODEL, Water Resour. Res., 45, https://doi.org/10.1029/2008WR007042, 2009.

Annandale, J., Jovanovic, N., Benadé, N., and Allen, R.: Software for missing data error analysis of Penman-Monteith reference evapotranspiration, Irrigation Science, 21, 57–67, https://doi.org/10.1007/s002710100047, 2002.

Archer, D.: Contrasting hydrological regimes in the upper Indus Basin, Journal of Hydrology, 274, 198–210, https://doi.org/10.1016/S0022-1694(02)00414-6, 2003.

Archer, D. R. and Fowler, H. J.: Spatial and temporal variations in precipitation in the Upper Indus Basin, global teleconnections and hydrological implications, Hydrol. Earth Syst. Sci., 8, 47–61, https://doi.org/10.5194/hess-8-47-2004, 2004.

Arendt, A. A. and Sharp, M. J.: Energy balance measurements on a Canadian high Arctic glacier and their implications for mass balance modelling, IAHS-AISH publication, 165–172, 1999.

Armstrong, R. L., Rittger, K., Brodzik, M. J., Racoviteanu, A., Barrett, A. P., Khalsa, S.-J. S., Raup, B., Hill, A. F., Khan, A. L., Wilson, A. M., Kayastha, R. B., Fetterer, F., and Armstrong, B.: Runoff from glacier ice and seasonal snow in High Asia: separating melt water sources in river flow, Reg Environ Change, 19, 1249–1261, https://doi.org/10.1007/s10113-018-1429-0, 2019.

Asaoka, Y. and Kominami, Y.: Incorporation of satellite-derived snow-cover area in spatial snowmelt modeling for a large area: determination of a gridded degree-day factor, Ann. Glaciol., 54, 205–213, https://doi.org/10.3189/2013AoG62A218, 2013.

Badescu, V. and Paulescu, M.: Statistical properties of the sunshine number illustrated with measurements from Timisoara (Romania), Atmospheric Research, 101, 194–204, https://doi.org/10.1016/j.atmosres.2011.02.009, 2011.

Bagchi, A. K.: Areal value of degree-day factor / Valeur spatiale du facteur degré-jour, Hydrological Sciences Journal, 28, 499–511, https://doi.org/10.1080/02626668309491991, 1983.

Barnard, P. L., Erikson, L. H., Foxgrover, A. C., Hart, J. A. F., Limber, P., O'Neill, A. C., van Ormondt, M., Vitousek, S., Wood, N., Hayden, M. K., and Jones, J. M.: Dynamic flood modeling essential to assess the coastal impacts of climate change, Sci Rep, 9, 4309, https://doi.org/10.1038/s41598-019-40742-z, 2019.

Beniston, M.: Climatic Change in Mountain Regions: A Review of Possible Impacts, 59, 5–31, https://doi.org/10.1023/A:1024458411589, 2003.

Bergström, S.: Development and application conceptual runoff model for scandinavian catchments, SMHI, Research Department, Hydrology, 162, 1976.

Bhatti, A. M., Suttinon, P., and Nasu, S.: Agriculture water deman management in Pakistan: A review and perspective, 2009.

Bogacki, W. and Hashmi, D.: Impact of Climate Change on the Flow Regime of the Mangla Basin, https://doi.org/10.13140/RG.2.1.1934.6167, 2013.

Bogacki, W. and Ismail, M. F.: Seasonal forecast of Kharif flows from Upper Jhelum catchment, Proc. IAHS, 374, 137–142, https://doi.org/10.5194/piahs-374-137-2016, 2016.

Bolch, T., Pieczonka, T., Mukherjee, K., and Shea, J.: Brief communication: Glaciers in the Hunza catchment (Karakoram) have been nearly in balance since the 1970s, The Cryosphere, 11, 531–539, https://doi.org/10.5194/tc-11-531-2017, 2017.

Bookhagen, B. and Burbank, D. W.: Toward a complete Himalayan hydrological budget: Spatiotemporal distribution of snowmelt and rainfall and their impact on river discharge, J. Geophys. Res., 115, F03019, https://doi.org/10.1029/2009JF001426, 2010.

Bormann, K. J., Evans, J. P., and McCabe, M. F.: Constraining snowmelt in a temperature-index model using simulated snow densities, Journal of Hydrology, 517, 652–667, https://doi.org/10.1016/j.jhydrol.2014.05.073, 2014.

Braithwaite, R. J.: Positive degree-day factors for ablation on the Greenland ice sheet studied by energy-balance modelling, J. Glaciol., 41, 153–160, https://doi.org/10.3189/S0022143000017846, 1995.

Braithwaite, R. J.: Temperature and precipitation climate at the equilibrium-line altitude of glaciers expressed by the degree-day factor for melting snow, J. Glaciol., 54, 437–444, https://doi.org/10.3189/002214308785836968, 2008.

Braithwaite, R. J., Konzelmann, T., Marty, C., and Olesen, O. B.: Reconnaissance Study of glacier energy balance in North Greenland, 1993–94, J. Glaciol., 44, 239–247, https://doi.org/10.3189/S0022143000002586, 1998.

Braun, L. N.: Simulation of snowmelt-runoff in lowland and lower alpine regions of Switzerland, Ph.D. Thesis, ETH Zurich, https://doi.org/10.3929/ETHZ-A-000334295, 1984.

Braun, Ludwig., Grabs, W., and Rana, B.: Application of a Conceptual Precipitation Runoff Model in the Langtang Kfaola Basin, Nepal Himalaya, Snow and Glacier Hydrology, 1993.

Bristow, K. L. and Campbell, G. S.: On the relationship between incoming solar radiation and daily maximum and minimum temperature, Agricultural and Forest Meteorology, 31, 159–166, https://doi.org/10.1016/0168-1923(84)90017-0, 1984.

Brutsaert, W.: On a derivable formula for long-wave radiation from clear skies, Water Resour. Res., 11, 742–744, https://doi.org/10.1029/WR011i005p00742, 1975.

Brutsaert, W.: Evaporation into the Atmosphere, Springer Netherlands, Dordrecht, https://doi.org/10.1007/978-94-017-1497-6, 1982.

Butt, M. J. and Bilal, M.: Application of snowmelt runoff model for water resource management, Hydrol. Process., 25, 3735–3747, https://doi.org/10.1002/hyp.8099, 2011.

Campbell, G. S. and Norman, J. M.: Introduction to environmental biophysics, 2nd ed., Springer, New York, 286 pp., 1998.

Charles, S.: Hydroclimate of the Indus: Synthesis of the literature relevant to Indus basin hydroclimate processes, trends, seasonal forecasting and climate change, https://doi.org/10.4225/08/58518B81BA769, 2016.

Cherkauer, K. A., Bowling, L. C., and Lettenmaier, D. P.: Variable infiltration capacity cold land process model updates, Global and Planetary Change, 38, 151–159, https://doi.org/10.1016/S0921-8181(03)00025-0, 2003.

Chinarro, D.: System Engineering Applied to Fuenmayor Karst Aquifer (San Julián de Banzo, Huesca) and Collins Glacier (King George Island, Antarctica), Springer International Publishing, Cham, https://doi.org/10.1007/978-3-319-08858-7, 2014.

Clarke, M.: Climate Change Considerations for Hydropower Projects in the Indus River Basin, Pakistan, 35th Annual Conference of the International Association for Impact Assessment, 2015.

Coron, L., Andréassian, V., Perrin, C., Lerat, J., Vaze, J., Bourqui, M., and Hendrickx, F.: Crash testing hydrological models in contrasted climate conditions: An experiment on 216 Australian catchments: TESTING HYDROLOGICAL MODELS IN CONTRASTED CLIMATE, Water Resour. Res., 48, https://doi.org/10.1029/2011WR011721, 2012.

Dadic, R., Mott, R., Lehning, M., Carenzo, M., Anderson, B., and Mackintosh, A.: Sensitivity of turbulent fluxes to wind speed over snow surfaces in different climatic settings, Advances in Water Resources, 55, 178–189, https://doi.org/10.1016/j.advwatres.2012.06.010, 2013.

Day, G. N.: Extended Streamflow Forecasting Using NWSRFS, Journal of Water Resources Planning and Management, 111, 157–170, https://doi.org/10.1061/(ASCE)0733-9496(1985)111:2(157), 1985.

De Souza, K., Kituyi, E., Harvey, B., Leone, M., Murali, K. S., and Ford, J. D.: Vulnerability to climate change in three hot spots in Africa and Asia: key issues for policy-relevant adaptation and resilience-building research, Reg Environ Change, 15, 747–753, https://doi.org/10.1007/s10113-015-0755-8, 2015.

Debele, B., Srinivasan, R., and Gosain, A. K.: Comparison of Process-Based and Temperature-Index Snowmelt Modeling in SWAT, Water Resour Manage, 24, 1065–1088, https://doi.org/10.1007/s11269-009-9486-2, 2010.

DeWalle, D. R. and Rango, A.: Principles of Snow Hydrology, Cambridge University Press, Cambridge, https://doi.org/10.1017/CBO9780511535673, 2008.

Dong, C. and Menzel, L.: Improving the accuracy of MODIS 8-day snow products with in situ temperature and precipitation data, Journal of Hydrology, 534, 466–477, https://doi.org/10.1016/j.jhydrol.2015.12.065, 2016.

Doorenbos, J. and Pruitt, W. O.: Guidelines for predicting crop water requirements, Rev., Food and Agriculture Organization of the United Nations, Rome, 144 pp., 1977.

Ekici, C.: Total Global Solar Radiation Estimation Models and Applications: A review, IJITIS, 2, 212-228 Pages, https://doi.org/10.15157/IJITIS.2019.2.2.212-228, 2019.

Evrendilek, F. and Ertekin, C.: Assessing solar radiation models using multiple variables over Turkey, Clim Dyn, 31, 131–149, https://doi.org/10.1007/s00382-007-0338-6, 2008.

Finger, D., Vis, M., Huss, M., and Seibert, J.: The value of multiple data set calibration versus model complexity for improving the performance of hydrological models in mountain catchments, Water Resour. Res., 51, 1939–1958, https://doi.org/10.1002/2014WR015712, 2015.

Forsythe, N., Fowler, H. J., Kilsby, C. G., and Archer, D. R.: Opportunities from Remote Sensing for Supporting Water Resources Management in Village/Valley Scale Catchments in the Upper Indus Basin, Water Resour Manage, 26, 845–871, https://doi.org/10.1007/s11269-011-9933-8, 2012.

Franz, K. J., Hartmann, H. C., Sorooshian, S., and Bales, R.: Verification of National Weather Service Ensemble Streamflow Predictions for Water Supply Forecasting in the Colorado River Basin, J. Hydrometeor, 4, 1105–1118, https://doi.org/10.1175/1525-7541(2003)004<1105:VONWSE>2.0.CO;2, 2003.

Franz, K. J., Hogue, T. S., and Sorooshian, S.: Snow Model Verification Using Ensemble Prediction and Operational Benchmarks, 9, 1402–1415, https://doi.org/10.1175/2008JHM995.1, 2008.

Frieler, K., Lange, S., Piontek, F., Reyer, C. P. O., Schewe, J., Warszawski, L., Zhao, F., Chini, L., Denvil, S., Emanuel, K., Geiger, T., Halladay, K., Hurtt, G., Mengel, M., Murakami, D., Ostberg, S., Popp, A., Riva, R., Stevanovic, M., Suzuki, T., Volkholz, J., Burke, E., Ciais, P., Ebi, K., Eddy, T. D., Elliott, J., Galbraith, E., Gosling, S. N., Hattermann, F., Hickler, T., Hinkel, J., Hof, C., Huber, V., Jägermeyr, J., Krysanova, V., Marcé, R., Müller Schmied, H., Mouratiadou, I., Pierson, D., Tittensor, D. P., Vautard, R., van Vliet, M., Biber, M. F., Betts, R. A., Bodirsky, B. L., Deryng, D., Frolking, S., Jones, C. D., Lotze, H. K., Lotze-Campen, H., Sahajpal, R., Thonicke, K., Tian, H., and Yamagata, Y.: Assessing the impacts of 1.5 °C global warming – simulation protocol of the Inter-Sectoral Impact Model Intercomparison Project (ISIMIP2b), Geosci. Model Dev., 10, 4321–4345, https://doi.org/10.5194/gmd-10-4321-2017, 2017.

Gafurov, A.: Water balance modeling using remote sensing information: focus on Central Asia, Ph.D. Thesis, Inst. f. Wasserbau, Stuttgart, 116 pp., 2010.

Gafurov, A., Lüdtke, S., Unger-Shayesteh, K., Vorogushyn, S., Schöne, T., Schmidt, S., Kalashnikova, O., and Merz, B.: MODSNOW-Tool: an operational tool for daily snow cover monitoring using MODIS data, Environ Earth Sci, 75, 1078, https://doi.org/10.1007/s12665-016-5869-x, 2016.

Gottschalk, L.: Methods of Analyzing Variability, in: Encyclopedia of Hydrological Sciences, edited by: Anderson, M. G. and McDonnell, J. J., John Wiley & Sons, Ltd, Chichester, UK, hsa006, https://doi.org/10.1002/0470848944.hsa006, 2005.

Greene, A. M., Goddard, L., and Lall, U.: Probabilistic Multimodel Regional Temperature Change Projections, 19, 4326–4343, https://doi.org/10.1175/JCLI3864.1, 2006.

Guo, D., Johnson, F., and Marshall, L.: Assessing the Potential Robustness of Conceptual Rainfall-Runoff Models Under a Changing Climate, Water Resour. Res., 54, 5030–5049, https://doi.org/10.1029/2018WR022636, 2018.

Hagg, W., Braun, L. N., Weber, M., and Becht, M.: Runoff modelling in glacierized Central Asian catchments for present-day and future climate, https://doi.org/10.5282/UBM/EPUB.13563, 2006.

Hall, D., Salomonson, Vincent V., and George, K.: MODIS/Terra Snow Cover Daily L3 Global 500m Grid, Version 5, https://doi.org/10.5067/63NQASRDPDB0, 2006.

Hargreaves, G. H. and Samani, Z. A.: Estimating Potential Evapotranspiration, J. Irrig. and Drain. Div., 108, 225–230, https://doi.org/10.1061/JRCEA4.0001390, 1982.

Harpold, A. A. and Brooks, P. D.: Humidity determines snowpack ablation under a warming climate, Proc Natl Acad Sci USA, 115, 1215–1220, https://doi.org/10.1073/pnas.1716789115, 2018.

Hasson, S. ul: Future Water Availability from Hindukush-Karakoram-Himalaya upper Indus Basin under Conflicting Climate Change Scenarios, Climate, 4, 40, https://doi.org/10.3390/cli4030040, 2016.

Hasson, S. ul, Saeed, F., Böhner, J., and Schleussner, C.-F.: Water availability in Pakistan from Hindukush–Karakoram–Himalayan watersheds at 1.5 °C and 2 °C Paris Agreement targets, Advances in Water Resources, 131, 103365, https://doi.org/10.1016/j.advwatres.2019.06.010, 2019.

Hayat, H., Akbar, T. A., Tahir, A. A., Hassan, Q. K., Dewan, A., and Irshad, M.: Simulating Current and Future River-Flows in the Karakoram and Himalayan Regions of Pakistan Using Snowmelt-Runoff Model and RCP Scenarios, Water, 11, 761, https://doi.org/10.3390/w11040761, 2019.

He, Z., Vorogushyn, S., Unger-Shayesteh, K., Gafurov, A., Kalashnikova, O., Omorova, E., and Merz, B.: The Value of Hydrograph Partitioning Curves for Calibrating Hydrological Models in Glacierized Basins, Water Resour. Res., 54, 2336–2361, https://doi.org/10.1002/2017WR021966, 2018.

He, Z. H., Parajka, J., Tian, F. Q., and Blöschl, G.: Estimating degree-day factors from MODIS for snowmelt runoff modeling, Hydrol. Earth Syst. Sci., 18, 4773–4789, https://doi.org/10.5194/hess-18-4773-2014, 2014.

Hempel, S., Frieler, K., Warszawski, L., Schewe, J., and Piontek, F.: A trend-preserving bias correction – the ISI-MIP approach, Earth Syst. Dynam., 4, 219–236, https://doi.org/10.5194/esd-4-219-2013, 2013.

Henning, W. R., Richling, A., Meredith, E., Fischer, M., Vagenas, C., Kadow, C., and Ulbrich, U.: A plugin for data extraction and conversion developed within and for BINGO, 2015.

Hijmans, R. J., Cameron, S. E., Parra, J. L., Jones, P. G., and Jarvis, A.: Very high resolution interpolated climate surfaces for global land areas, Int. J. Climatol., 25, 1965–1978, https://doi.org/10.1002/joc.1276, 2005.

Hinzman, L. D. and Kane, D. L.: Snow hydrology of a headwater Arctic basin: 2. Conceptual analysis and computer modeling, Water Resour. Res., 27, 1111–1121, https://doi.org/10.1029/91WR00261, 1991.

Hock, R.: A distributed temperature-index ice- and snowmelt model including potential direct solar radiation, J. Glaciol., 45, 101–111, https://doi.org/10.3189/S0022143000003087, 1999.

Hock, R.: Temperature index melt modelling in mountain areas, Journal of Hydrology, 282, 104–115, https://doi.org/10.1016/S0022-1694(03)00257-9, 2003.

Hock, R.: Glacier melt: a review of processes and their modelling, Progress in Physical Geography: Earth and Environment, 29, 362–391, https://doi.org/10.1191/0309133305pp453ra, 2005.

Hock, R. and Noetzli, C.: Areal melt and discharge modelling of Storglaciären, Sweden, Ann. Glaciol., 24, 211–216, https://doi.org/10.3189/S0260305500012192, 1997.

Huang, S., Kumar, R., Rakovec, O., Aich, V., Wang, X., Samaniego, L., Liersch, S., and Krysanova, V.: Multimodel assessment of flood characteristics in four large river basins at global warming of 1.5, 2.0 and 3.0 K above the pre-industrial level, Environ. Res. Lett., 13, 124005, https://doi.org/10.1088/1748-9326/aae94b, 2018.

Huss, M.: Present and future contribution of glacier storage change to runoff from macroscale drainage basins in Europe: GLACIER CONTRIBUTION TO CONTINENTAL-SCALE RUNOFF, Water Resour. Res., 47, https://doi.org/10.1029/2010WR010299, 2011.

Huss, M., Farinotti, D., Bauder, A., and Funk, M.: Modelling runoff from highly glacierized alpine drainage basins in a changing climate, Hydrol. Process., 22, 3888–3902, https://doi.org/10.1002/hyp.7055, 2008.

Immerzeel, W. W., Droogers, P., de Jong, S. M., and Bierkens, M. F. P.: Large-scale monitoring of snow cover and runoff simulation in Himalayan river basins using remote sensing, Remote Sensing of Environment, 113, 40–49, https://doi.org/10.1016/j.rse.2008.08.010, 2009.

Immerzeel, W. W., van Beek, L. P. H., and Bierkens, M. F. P.: Climate Change Will Affect the Asian Water Towers, Science, 328, 1382–1385, https://doi.org/10.1126/science.1183188, 2010a.

Immerzeel, W. W., Droogers, P., de Jong, S. M., and Bierkens, M. F. P.: Satellite Derived Snow and Runoff Dynamics in the Upper Indus River Basin, 303–312, 2010b.

Immerzeel, W. W., Wanders, N., Lutz, A. F., Shea, J. M., and Bierkens, M. F. P.: Reconciling high-altitude precipitation in the upper Indus basin with glacier mass balances and runoff, Hydrol. Earth Syst. Sci., 19, 4673–4687, https://doi.org/10.5194/hess-19-4673-2015, 2015.

Islam, S. U. and Déry, S. J.: Evaluating uncertainties in modelling the snow hydrology of the Fraser River Basin, British Columbia, Canada, Hydrol. Earth Syst. Sci., 21, 1827–1847, https://doi.org/10.5194/hess-21-1827-2017, 2017.

Ismail, M. F. and Bogacki, W.: Scenario approach for the seasonal forecast of Kharif flows from the Upper Indus Basin, Hydrol. Earth Syst. Sci., 22, 1391–1409, https://doi.org/10.5194/hess-22-1391-2018, 2018.

Ismail, M. F., Bogacki, W., and Muhammad, N.: Degree-day factor models for forecasting the snowmelt runoff for Naran watershed, SI, 27, 1951–1960, 2015.

Ismail, M. F., Naz, B. S., Wortmann, M., Disse, M., Bowling, L. C., and Bogacki, W.: Comparison of two model calibration approaches and their influence on future projections under climate change in the Upper Indus Basin, Climatic Change, 163, 1227–1246, https://doi.org/10.1007/s10584-020-02902-3, 2020.

Ismail, M. F., Bogacki, W., Disse, M., Schäfer, M., and Kirschbauer, L.: Estimating degree-day factors based on energy flux components, Snow/Energy Balance Obs/Modelling, https://doi.org/10.5194/tc-2022-64, 2022.

IUCAN: Pakistan Water Apportionment Accord for Resolving Inter-provincial Water Conflicts – Policy Issues and Options, 11, 2010.

Jansson, P., Hock, R., and Schneider, T.: The concept of glacier storage: a review, Journal of Hydrology, 282, 116–129, https://doi.org/10.1016/S0022-1694(03)00258-0, 2003.

Jennings, K. S., Kittel, T. G. F., and Molotch, N. P.: Observations and simulations of the seasonal evolution of snowpack cold content and its relation to snowmelt and the snowpack energy budget, The Cryosphere, 12, 1595–1614, https://doi.org/10.5194/tc-12-1595-2018, 2018.

Jin, Z., Yezheng, W., and Gang, Y.: General formula for estimation of monthly average daily global solar radiation in China, Energy Conversion and Management, 46, 257–268, https://doi.org/10.1016/j.enconman.2004.02.020, 2005.

Kane, D. L., Gieck, R. E., and Hinzman, L. D.: Snowmelt Modeling at Small Alaskan Arctic Watershed, Journal of Hydrologic Engineering, 2, 204–210, https://doi.org/10.1061/(ASCE)1084-0699(1997)2:4(204), 1997.

Kaufmann, J. and Schering, A.: Analysis of Variance ANOVA, in: Wiley StatsRef: Statistics Reference Online, edited by: Balakrishnan, N., Colton, T., Everitt, B., Piegorsch, W., Ruggeri, F., and Teugels, J. L., Wiley, https://doi.org/10.1002/9781118445112.stat06938, 2014.

Kayastha, R. B., Yutaka, A., Masayoshi, N., Koji, F., Akiko, S., and Yoshihiro, M.: Positive degree-day factors for ice ablation on four glaciers in the Nepalese Himalayas and Qinghai-Tibetan Plateau, Bulletin of glaciological research, 7–14, 2003.

Kendall, M. G.: Rank correlation methods, 4th ed., Charles Griffin, London, 1975.

Khan, A. and Koch, M.: Correction and Informed Regionalization of Precipitation Data in a High Mountainous Region (Upper Indus Basin) and Its Effect on SWAT-Modelled Discharge, Water, 10, 1557, https://doi.org/10.3390/w10111557, 2018.

Khan, A., Naz, B. S., and Bowling, L. C.: Separating snow, clean and debris covered ice in the Upper Indus Basin, Hindukush-Karakoram-Himalayas, using Landsat images between 1998 and 2002, Journal of Hydrology, 521, 46–64, https://doi.org/10.1016/j.jhydrol.2014.11.048, 2015.

Kirpich, Z. P.: Time of concentration in small agricultural watersheds, 10, 362–368, 1940.

Kling, H., Fuchs, M., and Paulin, M.: Runoff conditions in the upper Danube basin under an ensemble of climate change scenarios, Journal of Hydrology, 424–425, 264–277, https://doi.org/10.1016/j.jhydrol.2012.01.011, 2012.

Klok, E. J., Jasper, K., Roelofsma, K. P., Gurtz, J., and Badoux, A.: Distributed hydrological modelling of a heavily glaciated Alpine river basin, Hydrological Sciences Journal, 46, 553–570, https://doi.org/10.1080/02626660109492850, 2001.

Kopp, G. and Lean, J. L.: A new, lower value of total solar irradiance: Evidence and climate significance: FRONTIER, Geophys. Res. Lett., 38, n/a-n/a, https://doi.org/10.1029/2010GL045777, 2011.

Kopp, M., Tuo, Y., and Disse, M.: Fully automated snow depth measurements from time-lapse images applying a convolutional neural network, Science of The Total Environment, 697, 134213, https://doi.org/10.1016/j.scitotenv.2019.134213, 2019.

Krysanova, V. and Hattermann, F. F.: Intercomparison of climate change impacts in 12 large river basins: overview of methods and summary of results, Climatic Change, 141, 363–379, https://doi.org/10.1007/s10584-017-1919-y, 2017.

Krysanova, V., Vetter, T., Eisner, S., Huang, S., Pechlivanidis, I., Strauch, M., Gelfan, A., Kumar, R., Aich, V., Arheimer, B., Chamorro, A., van Griensven, A., Kundu, D., Lobanova, A., Mishra, V., Plötner, S., Reinhardt, J., Seidou, O., Wang, X., Wortmann, M., Zeng, X., and Hattermann, F. F.: Intercomparison of regional-scale hydrological models and climate change impacts projected for 12 large river basins worldwide—a synthesis, Environ. Res. Lett., 12, 105002, https://doi.org/10.1088/1748-9326/aa8359, 2017.

Krysanova, V., Donnelly, C., Gelfan, A., Gerten, D., Arheimer, B., Hattermann, F., and Kundzewicz, Z. W.: How the performance of hydrological models relates to credibility of projections under climate change, Hydrological Sciences Journal, 63, 696–720, https://doi.org/10.1080/02626667.2018.1446214, 2018.

Kustas, W. P., Rango, A., and Uijlenhoet, R.: A simple energy budget algorithm for the snowmelt runoff model, Water Resour. Res., 30, 1515–1527, https://doi.org/10.1029/94WR00152, 1994.

Laghari, A. N., Vanham, D., and Rauch, W.: The Indus basin in the framework of current and future water resources management, Hydrol. Earth Syst. Sci., 16, 1063–1083, https://doi.org/10.5194/hess-16-1063-2012, 2012.

Lang, H.: Forecasting Meltwater Runoff from Snow-Covered Areas and from Glacier Basins, in: River Flow Modelling and Forecasting, vol. 3, edited by: Kraijenhoff, D. A. and Moll, J. R., Springer Netherlands, Dordrecht, 99–127, https://doi.org/10.1007/978-94-009-4536-4_5, 1986.

Lang, H. and Braun, L.: On the information content of air temperature in the context of snow melt estimation, IAHS, 190, 347–354, 1990.

Lange, S.: EartH2Observe, WFDEI and ERA-Interim data Merged and Bias-corrected for ISIMIP (EWEMBI), https://doi.org/10.5880/PIK.2016.004, 2016.

Lange, S.: Bias correction of surface downwelling longwave and shortwave radiation for the EWEMBI dataset, Earth Syst. Dynam., 9, 627–645, https://doi.org/10.5194/esd-9-627-2018, 2018.

Lawrence, M. G.: The Relationship between Relative Humidity and the Dewpoint Temperature in Moist Air: A Simple Conversion and Applications, Bull. Amer. Meteor. Soc., 86, 225–234, https://doi.org/10.1175/BAMS-86-2-225, 2005.

Leavesley, G. H.: Problems in snowmelt runoff modelling for a variety of physiographic and climatic conditions, 34, 617–634, 1989.

Lehning, M., Bartelt, P., Brown, B., and Fierz, C.: A physical SNOWPACK model for the Swiss avalanche warning, Cold Regions Science and Technology, 35, 169–184, https://doi.org/10.1016/S0165-232X(02)00072-1, 2002.

Lemon, J.: a package in the red light district of R, 8–12, 2006.

Liang, X., Lettenmaier, D. P., Wood, E. F., and Burges, S. J.: A simple hydrologically based model of land surface water and energy fluxes for general circulation models, J. Geophys. Res., 99, 14415, https://doi.org/10.1029/94JD00483, 1994.

Liu, Y., Tan, Q., and Pan, T.: Determining the Parameters of the Ångström-Prescott Model for Estimating Solar Radiation in Different Regions of China: Calibration and Modeling, Earth and Space Science, 6, 1976–1986, https://doi.org/10.1029/2019EA000635, 2019.

Lohmann, D., Raschke, E., Nijssen, B., and Lettenmaier, D. P.: Regional scale hydrology: I. Formulation of the VIC-2L model coupled to a routing model, Hydrological Sciences Journal, 43, 131–141, https://doi.org/10.1080/02626669809492107, 1998.

Luo, Y., Arnold, J., Liu, S., Wang, X., and Chen, X.: Inclusion of glacier processes for distributed hydrological modeling at basin scale with application to a watershed in Tianshan Mountains, northwest China, Journal of Hydrology, 477, 72–85, https://doi.org/10.1016/j.jhydrol.2012.11.005, 2013.

Lutz, A. F., Immerzeel, W. W., Shrestha, A. B., and Bierkens, M. F. P.: Consistent increase in High Asia's runoff due to increasing glacier melt and precipitation, Nature Clim Change, 4, 587–592, https://doi.org/10.1038/nclimate2237, 2014.

Lutz, A. F., Immerzeel, W. W., Kraaijenbrink, P. D. A., Shrestha, A. B., and Bierkens, M. F. P.: Climate Change Impacts on the Upper Indus Hydrology: Sources, Shifts and Extremes, PLoS ONE, 11, e0165630, https://doi.org/10.1371/journal.pone.0165630, 2016.

Mann, H. B.: Non-parametric tests against trend, Econometrica, 13, 245–259, 1945.

Marks, D., Dozier, J., and Davis, R. E.: Climate and energy exchange at the snow surface in the Alpine Region of the Sierra Nevada: 1. Meteorological measurements and monitoring, Water Resour. Res., 28, 3029–3042, https://doi.org/10.1029/92WR01482, 1992.

Marks, D., Domingo, J., Susong, D., Link, T., and Garen, D.: A spatially distributed energy balance snowmelt model for application in mountain basins, Hydrol. Process., 13, 1935–1959, https://doi.org/10.1002/(SICI)1099-1085(199909)13:12/13<1935::AID-HYP868>3.0.CO;2-C, 1999.

Marsh, C. B., Pomeroy, J. W., and Spiteri, R. J.: Implications of mountain shading on calculating energy for snowmelt using unstructured triangular meshes: Implication of Mountains shading for snowmelt, Hydrol. Process., 26, 1767–1778, https://doi.org/10.1002/hyp.9329, 2012.

Martens, B., Miralles, D. G., Lievens, H., van der Schalie, R., de Jeu, R. A. M., Fernández-Prieto, D., Beck, H. E., Dorigo, W. A., and Verhoest, N. E. C.: GLEAM v3: satellite-based land evaporation and root-zone soil moisture, Geosci. Model Dev., 10, 1903–1925, https://doi.org/10.5194/gmd-10-1903-2017, 2017.

Martinec, J.: The degree-day factor for snowmelt-runoff forecasting, 51, 468–477, 1960.

Martinec, J.: Snowmelt - runoff model for stream flow forecasts, 145–154, 1975.

Martinec, J. and de Quervain, M. R.: The effect of snow displacement by avalanches on snowmelt and runoff, 104, 364–377, 1975.

Martinec, J., Rango, A., and Roberts, R.: Snowmelt Runoff Model (SRM) User's Manual, 180, 2008.

Masters, G. M.: Renewable and efficient electric power systems, John Wiley & Sons, Hoboken, NJ, 654 pp., 2004.

Matthews, T. and Hodgkins, R.: Interdecadal variability of degree-day factors on Vestari Hagafellsjökull (Langjökull, Iceland) and the importance of threshold air temperatures, J. Glaciol., 62, 310–322, https://doi.org/10.1017/jog.2016.21, 2016.

Mayr, E., Hagg, W., Mayer, C., and Braun, L.: Calibrating a spatially distributed conceptual hydrological model using runoff, annual mass balance and winter mass balance, Journal of Hydrology, 478, 40–49, https://doi.org/10.1016/j.jhydrol.2012.11.035, 2013.

McGinn, R. A.: Degree-day snowmelt runoff experiments; Clear Lake Watershed, Riding Mountain National Park, Geographical Essays, 15, 16, 2012.

Meeus, J.: Astronomical algorithms, 1st English ed., Willmann-Bell, Richmond, Va, 429 pp., 1991.

Ménégoz, M., Gallée, H., and Jacobi, H. W.: Precipitation and snow cover in the Himalaya: from reanalysis to regional climate simulations, Hydrol. Earth Syst. Sci., 17, 3921–3936, https://doi.org/10.5194/hess-17-3921-2013, 2013.

Merz, R., Parajka, J., and Blöschl, G.: Time stability of catchment model parameters: Implications for climate impact analyses: TIME STABILITY OF CATCHMENT MODEL PARAMETERS, Water Resour. Res., 47, https://doi.org/10.1029/2010WR009505, 2011.

MeteoSchweiz: MeteoSchweiz - Klimabulletin Dezember 2021, 2022.

Miralles, D. G., Holmes, T. R. H., De Jeu, R. A. M., Gash, J. H., Meesters, A. G. C. A., and Dolman, A. J.: Global land-surface evaporation estimated from satellite-based observations, Hydrol. Earth Syst. Sci., 15, 453–469, https://doi.org/10.5194/hess-15-453-2011, 2011.

Monteith, J. L. and Unsworth, M. H.: Principles of environmental physics: plants, animals, and the atmosphere, 4th ed., Elsevier/Academic Press, Amsterdam ; Boston, 401 pp., 2013.

Muhammad, S., Tian, L., and Khan, A.: Early twenty-first century glacier mass losses in the Indus Basin constrained by density assumptions, Journal of Hydrology, 574, 467–475, https://doi.org/10.1016/j.jhydrol.2019.04.057, 2019.

Mukhopadhyay, B.: Detection of dual effects of degradation of perennial snow and ice covers on the hydrologic regime of a Himalayan river basin by stream water availability modeling, Journal of Hydrology, 412–413, 14–33, https://doi.org/10.1016/j.jhydrol.2011.06.005, 2012.

Mukhopadhyay, B. and Khan, A.: A reevaluation of the snowmelt and glacial melt in river flows within Upper Indus Basin and its significance in a changing climate, Journal of Hydrology, 527, 119–132, https://doi.org/10.1016/j.jhydrol.2015.04.045, 2015.

Murphy, A. H.: Scalar and vector partitions of the probability score: Part II. N-state situation, 11, 1183–1192, 1972.

Murphy, A. H.: A new vector partition of the probability score, J. Appl. Meteor., 12, 595–600, 1973.

Murphy, A. H. and Winkler, R. L.: A general framework for forecast verification, Weather Rev, 1330–1338, 1987.

Murray, F. W.: On the Computation of Saturation Vapor Pressure, J. Appl. Meteor., 6, 203–204, https://doi.org/10.1175/1520-0450(1967)006<0203:OTCOSV>2.0.CO;2, 1967.

Murray, S. J., Foster, P. N., and Prentice, I. C.: Evaluation of global continental hydrology as simulated by the Land-surface Processes and eXchanges Dynamic Global Vegetation Model, Hydrol. Earth Syst. Sci., 15, 91–105, https://doi.org/10.5194/hess-15-91-2011, 2011.

Naz, B. S., Frans, C. D., Clarke, G. K. C., Burns, P., and Lettenmaier, D. P.: Modeling the effect of glacier recession on streamflow response using a coupled glacio-hydrological model, Hydrol. Earth Syst. Sci., 18, 787–802, https://doi.org/10.5194/hess-18-787-2014, 2014.

Naz, B. S., Kao, S.-C., Ashfaq, M., Rastogi, D., Mei, R., and Bowling, L. C.: Regional hydrologic response to climate change in the conterminous United States using high-resolution hydroclimate simulations, Global and Planetary Change, 143, 100–117, https://doi.org/10.1016/j.gloplacha.2016.06.003, 2016.

Nijssen, B., O'Donnell, G. M., Lettenmaier, D. P., Lohmann, D., and Wood, E. F.: Predicting the Discharge of Global Rivers, J. Climate, 14, 3307–3323, https://doi.org/10.1175/1520-0442(2001)014<3307:PTDOGR>2.0.CO;2, 2001.

Oke, T. R.: Boundary Layer Climates, 0 ed., Routledge, https://doi.org/10.4324/9780203407219, 1987.

Orth, R., Staudinger, M., Seneviratne, S. I., Seibert, J., and Zappa, M.: Does model performance improve with complexity? A case study with three hydrological models, Journal of Hydrology, 523, 147–159, https://doi.org/10.1016/j.jhydrol.2015.01.044, 2015.

Palazzi, E., von Hardenberg, J., and Provenzale, A.: Precipitation in the Hindu-Kush Karakoram Himalaya: Observations and future scenarios: PRECIPITATION IN HINDU-KUSH KARAKORAM HIMALAYA, J. Geophys. Res. Atmos., 118, 85–100, https://doi.org/10.1029/2012JD018697, 2013.

Paterson, W. S. B.: The physics of glaciers, 3rd ed., Oxford: Pergamon, 2002.

Pelkowski, J.: A physical rationale for generalized Ångström–Prescott regression, Solar Energy, 83, 955–963, https://doi.org/10.1016/j.solener.2008.12.011, 2009.

Pellicciotti, F., Brock, B., Strasser, U., Burlando, P., Funk, M., and Corripio, J.: An enhanced temperature-index glacier melt model including the shortwave radiation balance: development and testing for Haut Glacier d'Arolla, Switzerland, J. Glaciol., 51, 573–587, https://doi.org/10.3189/172756505781829124, 2005.

Pellicciotti, F., Buergi, C., Immerzeel, W. W., Konz, M., and Shrestha, A. B.: Challenges and Uncertainties in Hydrological Modeling of Remote Hindu Kush–Karakoram–Himalayan (HKH) Basins: Suggestions for Calibration Strategies, Mountain Research and Development, 32, 39–50, https://doi.org/10.1659/MRD-JOURNAL-D-11-00092.1, 2012.

Piani, C., Haerter, J. O., and Coppola, E.: Statistical bias correction for daily precipitation in regional climate models over Europe, Theor Appl Climatol, 99, 187–192, https://doi.org/10.1007/s00704-009-0134-9, 2010a.

Piani, C., Weedon, G. P., Best, M., Gomes, S. M., Viterbo, P., Hagemann, S., and Haerter, J. O.: Statistical bias correction of global simulated daily precipitation and temperature for the application of hydrological models, Journal of Hydrology, 395, 199–215, https://doi.org/10.1016/j.jhydrol.2010.10.024, 2010b.

Prasad, V. H. and Roy, P. S.: Estimation of Snowmelt Runoff in Beas Basin, India, Geocarto International, 20, 41–47, https://doi.org/10.1080/10106040508542344, 2005.

Pritchard, H. D.: Asia's shrinking glaciers protect large populations from drought stress, Nature, 569, 649–654, https://doi.org/10.1038/s41586-019-1240-1, 2019.

Quick, M. C. and Pipes, A.: U.B.C. Watershed model / Le modèle du bassin versant U.C.B, Hydrological Sciences Bulletin, 22, 153–161, https://doi.org/10.1080/02626667709491701, 1977.

Qureshi, A. S.: Water Management in the Indus Basin in Pakistan: Challenges and Opportunities, Mountain Research and Development, 31, 252–260, https://doi.org/10.1659/MRD-JOURNAL-D-11-00019.1, 2011.

Ragettli, S., Pellicciotti, F., Bordoy, R., and Immerzeel, W. W.: Sources of uncertainty in modeling the glaciohydrological response of a Karakoram watershed to climate change: Sources of uncertainty in glaciohydrological modeling, Water Resour. Res., 49, 6048–6066, https://doi.org/10.1002/wrcr.20450, 2013.

Rango, A. and Martinec, J.: Application of a Snowmelt-Runoff Model Using Landsat Data, 10, 225–238, https://doi.org/10.2166/nh.1979.0006, 1979.

Rango, A. and Martinec, J.: Revisiting the degree-day method for snowmelt computations, J Am Water Resources Assoc, 31, 657–669, https://doi.org/10.1111/j.1752-1688.1995.tb03392.x, 1995.

Raup, B., Racoviteanu, A., Khalsa, S. J. S., Helm, C., Armstrong, R., and Arnaud, Y.: The GLIMS geospatial glacier database: A new tool for studying glacier change, Global and Planetary Change, 56, 101–110, https://doi.org/10.1016/j.gloplacha.2006.07.018, 2007.

Reda, I. and Andreas, A.: Solar position algorithm for solar radiation applications, Solar Energy, 76, 577–589, https://doi.org/10.1016/j.solener.2003.12.003, 2004.

Reed, S., Koren, V., Smith, M., Zhang, Z., Moreda, F., Seo, D.-J., and DMIP Participants, and: Overall distributed model intercomparison project results, Journal of Hydrology, 298, 27–60, https://doi.org/10.1016/j.jhydrol.2004.03.031, 2004.

Reggiani, P. and Rientjes, T. H. M.: A reflection on the long-term water balance of the Upper Indus Basin, 46, 446–462, https://doi.org/10.2166/nh.2014.060, 2015.

Rensheng, C., Shihua, L., Ersi, K., Jianping, Y., and Xibin, J.: Estimating daily global radiation using two types of revised models in China, Energy Conversion and Management, 47, 865–878, https://doi.org/10.1016/j.enconman.2005.06.015, 2006.

Rössler, O., Froidevaux, P., Börst, U., Rickli, R., Martius, O., and Weingartner, R.: Retrospective analysis of a nonforecasted rain-on-snow flood in the Alps – a matter of model limitations or unpredictable nature?, Hydrol. Earth Syst. Sci., 18, 2265–2285, https://doi.org/10.5194/hess-18-2265-2014, 2014.

Schaefli, B. and Huss, M.: Integrating point glacier mass balance observations into hydrologic model identification, Hydrol. Earth Syst. Sci., 15, 1227–1241, https://doi.org/10.5194/hess-15-1227-2011, 2011.

Schaper, J. and Seidel, K.: Modelling daily runoff from snow and glacier melt using remote sensing data, Special Interest Group Land Ice and Snow, 2000.

Schaper, J., Martinec, J., and Seidel, K.: Distributed mapping of snow and glaciers for improved runoff modelling, Hydrol. Process., 13, 2023–2031, https://doi.org/10.1002/(SICI)1099-1085(199909)13:12/13<2023::AID-HYP877>3.0.CO;2-A, 1999.

Schaper, J., Seidel, K., and Martinec, J.: Precision snow cover and glacier mapping for runoff modelling in a high alpine basin, 267, 105–111, 2000.

Schmid, M.-O., Gubler, S., Fiddes, J., and Gruber, S.: Inferring snowpack ripening and melt-out from distributed measurements of near-surface ground temperatures, The Cryosphere, 6, 1127–1139, https://doi.org/10.5194/tc-6-1127-2012, 2012.

Schreider, S. Yu., Whetton, P. H., Jakeman, A. J., and Pittock, A. B.: Runoff modelling for snow-affected catchments in the Australian alpine region, eastern Victoria, Journal of Hydrology, 200, 1–23, https://doi.org/10.1016/S0022-1694(97)00006-1, 1997.

Sen, P. K.: Estimates of the Regression Coefficient Based on Kendall's Tau, Journal of the American Statistical Association, 63, 1379–1389, https://doi.org/10.1080/01621459.1968.10480934, 1968.

Shafeeque, M., Luo, Y., Wang, X., and Sun, L.: Revealing Vertical Distribution of Precipitation in the Glacierized Upper Indus Basin Based on Multiple Datasets, 20, 2291–2314, https://doi.org/10.1175/JHM-D-19-0081.1, 2019.

Shea, J. M., Dan Moore, R., and Stahl, K.: Derivation of melt factors from glacier mass-balance records in western Canada, J. Glaciol., 55, 123–130, https://doi.org/10.3189/002214309788608886, 2009.

Smith, P. J., Beven, K. J., and Tawn, J. A.: Detection of structural inadequacy in process-based hydrological models: A particle-filtering approach: DETECTION OF MODEL INADEQUACY, Water Resour. Res., 44, https://doi.org/10.1029/2006WR005205, 2008.

Stigter, E. E., Steiner, J. F., Koch, I., Saloranta, T. M., Kirkham, J. D., and Immerzeel, W. W.: Energy and mass balance dynamics of the seasonal snowpack at two high-altitude sites in the Himalaya, Cold Regions Science and Technology, 183, 103233, https://doi.org/10.1016/j.coldregions.2021.103233, 2021.

Tahir, A. A., Chevallier, P., Arnaud, Y., and Ahmad, B.: Snow cover dynamics and hydrological regime of the Hunza River basin, Karakoram Range, Northern Pakistan, Hydrol. Earth Syst. Sci., 15, 2275–2290, https://doi.org/10.5194/hess-15-2275-2011, 2011.

Tahir, A. A., Adamowski, J. F., Chevallier, P., Haq, A. U., and Terzago, S.: Comparative assessment of spatiotemporal snow cover changes and hydrological behavior of the Gilgit, Astore and Hunza River basins (Hindukush–Karakoram–Himalaya region, Pakistan), Meteorol Atmos Phys, 128, 793–811, https://doi.org/10.1007/s00703-016-0440-6, 2016.

Tarasova, L., Knoche, M., Dietrich, J., and Merz, R.: Effects of input discretization, model complexity, and calibration strategy on model performance in a data-scarce glacierized catchment in Central Asia: MODEL PERFORMANCE IN A GLACIERIZED BASIN, Water Resour. Res., 52, 4674–4699, https://doi.org/10.1002/2015WR018551, 2016.

Taylor, K. E.: Summarizing multiple aspects of model performance in a single diagram, J. Geophys. Res., 106, 7183–7192, https://doi.org/10.1029/2000JD900719, 2001.

Troin, M., Poulin, A., Baraer, M., and Brissette, F.: Comparing snow models under current and future climates: Uncertainties and implications for hydrological impact studies, Journal of Hydrology, 540, 588–602, https://doi.org/10.1016/j.jhydrol.2016.06.055, 2016.

USACE: Snow hydrology: Summary report of the snow investigations, 1956.

USACE: Runoff from Snowmelt, https://www.publications.usace.army.mil/Portals/76/Publications/EngineerManuals/EM_1110-2-1406.pdf, 31 March 1998.

USDA: National Engineering Handbook, Section 4, Part 630 Hydrology Chapters, Department of Agriculture, Natural Resources Conservation Service, 2010.

Vanham, D., Fleischhacker, E., and Rauch, W.: Technical Note: Seasonality in alpine water resources management – a regional assessment, Hydrol. Earth Syst. Sci., 12, 91–100, https://doi.org/10.5194/hess-12-91-2008, 2008.

Vaughan, D. G., Comiso, J. C., Allison, I., Carrasco, J., Kaser, G., Kwok, R., Mote, P., Murray, T., Paul, F., Ren, J., Rignot, E., Solomina, O., Steffen, K., and Zhang, T.: Observations: Cryosphere. In: Climate Change 2013: The Physical Science Basis. Contribution of Working Group I to the Fifth Assessment Report of the Intergovernmental Panel on Climate Change, 2013.

Vaze, J., Post, D. A., Chiew, F. H. S., Perraud, J.-M., Viney, N. R., and Teng, J.: Climate non-stationarity – Validity of calibrated rainfall–runoff models for use in climate change studies, Journal of Hydrology, 394, 447–457, https://doi.org/10.1016/j.jhydrol.2010.09.018, 2010.

Vetter, T., Huang, S., Aich, V., Yang, T., Wang, X., Krysanova, V., and Hattermann, F.: Multi-model climate impact assessment and intercomparison for three large-scale river basins on three continents, Earth Syst. Dynam., 6, 17–43, https://doi.org/10.5194/esd-6-17-2015, 2015.

Viviroli, D., Dürr, H. H., Messerli, B., Meybeck, M., and Weingartner, R.: Mountains of the world, water towers for humanity: Typology, mapping, and global significance: MOUNTAINS AS WATER TOWERS FOR HUMANITY, Water Resour. Res., 43, https://doi.org/10.1029/2006WR005653, 2007.

Walter, M. T., Brooks, E. S., McCool, D. K., King, L. G., Molnau, M., and Boll, J.: Process-based snowmelt modeling: does it require more input data than temperature-index modeling, Journal of hydrology, v. 300, 65–75, 2005.

Ward, E., Buytaert, W., Peaver, L., and Wheater, H.: Evaluation of precipitation products over complex mountainous terrain: A water resources perspective, Advances in Water Resources, 34, 1222–1231, https://doi.org/10.1016/j.advwatres.2011.05.007, 2011.

Warren, S. G.: Optical properties of snow, Rev. Geophys., 20, 67, https://doi.org/10.1029/RG020i001p00067, 1982.

Warren, S. G. and Wiscombe, W. J.: A Model for the Spectral Albedo of Snow. II: Snow Containing Atmospheric Aerosols, J. Atmos. Sci., 37, 2734–2745, https://doi.org/10.1175/1520-0469(1980)037<2734:AMFTSA>2.0.CO;2, 1980.

Wilks, D. S.: Statistical methods in the atmospheric sciences, 2nd ed., Elsevier, Amsterdam Paris, 2006.

Wiscombe, W. J. and Warren, S. G.: A Model for the Spectral Albedo of Snow. I: Pure Snow, J. Atmos. Sci., 37, 2712–2733, https://doi.org/10.1175/1520-0469(1980)037<2712:AMFTSA>2.0.CO;2, 1980.

Wood, A. W. and Lettenmaier, D. P.: An ensemble approach for attribution of hydrologic prediction uncertainty, Geophys. Res. Lett., 35, L14401, https://doi.org/10.1029/2008GL034648, 2008.

Wortmann, M., Bolch, T., Su, B., and Krysanova, V.: An efficient representation of glacier dynamics in a semi-distributed hydrological model to bridge glacier and river catchment scales, Journal of Hydrology, 573, 136–152, https://doi.org/10.1016/j.jhydrol.2019.03.006, 2019.

Xie, P., Yarosh, Y., Love, T., Jonowiak, J. E., and Arkin, P. A.: A real-time daily precipitation analysis over south asia, Preprint of the 16th Conference on Hydrology, 2002.

Yatagai, A., Kamiguchi, K., Arakawa, O., Hamada, A., Yasutomi, N., and Kitoh, A.: APHRODITE: Constructing a Long-Term Daily Gridded Precipitation Dataset for Asia Based on a Dense Network of Rain Gauges, 93, 1401–1415, https://doi.org/10.1175/BAMS-D-11-00122.1, 2012.

Zhang, Y., Liu, S., Xie, C., and Ding, Y.: Application of a degree-day model for the determination of contributions to glacier meltwater and runoff near Keqicar Baqi glacier, southwestern Tien Shan, Ann. Glaciol., 43, 280–284, https://doi.org/10.3189/172756406781812320, 2006.

Zhu, J., Forsee, W., Schumer, R., and Gautam, M.: Future projections and uncertainty assessment of extreme rainfall intensity in the United States from an ensemble of climate models, Climatic Change, 118, 469–485, https://doi.org/10.1007/s10584-012-0639-6, 2013.

Zuzel, J. F. and Cox, L. M.: Relative importance of meteorological variables in snowmelt, Water Resour. Res., 11, 174–176, https://doi.org/10.1029/WR011i001p00174, 1975.

A Appendix

Snow measurement station – fieldwork impressions

Figure A.1 Snow station relocation - work in progress [May-2019] – (image credit: Oliver Koch)

Figure A.2 Snow situation at the Brunnenkopfhütte station – (March – 2019)

Figure A.3 Snow core sampling in the Dreisäulerbach catchment – (image credit: Michael Schäfer)

B Article supplementary materials

Supplementary materials to chapter 4

B.1 Climate and sub-catchments of the Upper Indus Basin

The climate of UIB is under the influence of two different climatic systems. The South West Indian Monsoon is the source of monsoonal rainfall in the summer season, mainly affecting the most eastern and the southern slopes of the basin. The Westerlies control the north and west of the basin. In winter, the snow line reaches down to about 2200m a.s.l accumulating more than 60% of annual water input, later discharged as snowmelt into the Upper Indus River (Bookhagen and Burbank, 2010).

The UIB is comprised of several snow and glacier fed sub-basins (e.g. Astore (3,980 km^2) and Hunza (13,740 km^2)), where Astore is dominated by snowmelt and Hunza is driven by glacier melt (Archer, 2003; Mukhopadhyay and Khan, 2015). Astore basin contributes about 2.3% and 6.4% in area and discharge of the total UIB, respectively. Whereas, Hunza contributes 7.9% in area and 13.2% in discharge of the total UIB. The distribution of monthly inflows to Tarbela (capacity: 13.7 km^3) (see Figure B.1) shows that flows tend to rise progressively (e.g. April) as melting temperatures advance into areas of densified snowpack at the higher elevations until they reach their maximum in July. Peak flow events usually occur during the intersection of meltwater and monsoonal peaks in July–September. As the snow cover recedes in summer, the glacier melt contribution increases. The calculated mean annual flow volume from the available time series (i.e. 2000 – 2016) at Tarbela is about ~70 km^3. A major portion of meltwater is contributing to irrigation requirements of the Kharif cropping season from April to September throughout Pakistan (Ismail and Bogacki, 2018). The hypsometric mean elevation characteristics for the UIB is give in Figure B.2.

B.2 Hydrological Models

B.2.1 SRM+G

SRM+G has already been applied with high accuracy to several European basins, such as Rhine-Felsberg (3241 km^2, 1.9% glacier area, 575 – 3614 m a.s.l.), Rhone-Sion (3371 km^2, 17% glacier area, 488 – 4634 m a.s.l.), Ticino-Bellinzona (1515 km^2, 0.5% glacier area, 192 – 3402 m a.s.l.) and Massa-

Blatten (196 km^2, 67% glacier area, 1447±4191 m a.s.l.) under different topographic, physiographic and climatic conditions (Schaper et al., 1999; Schaper and Seidel, 2000).

B.2.2 VIC

In contrast to lumped models, the semi-distributed VIC model represents the spatial variability of soil and vegetation in a watershed by grid cell. A routing algorithm external to the VIC model is used to simulate the streamflow at a specified location by routing runoff and base flow from each grid cell (Lohmann et al., 1998). Each VIC model grid cell can be subdivided into snow elevation bands to represent the effect of sub-grid topography on snow accumulation and melt. As implemented here, the VIC model represents the areal extent of the snow cover based on the assumption that snow fully covers the fractional area of each snow elevation band. The elevation bands where the glaciers do not exist, were only covered with seasonal snow. The snow and ice melt within each elevation band directly contribute to surface runoff at each time step. To explicitly simulate glacier melt in each grid cell, a novel approach as a third bottom ice layer is introduced to the two-layer VIC snow model (Sup., Fig. S3). During the model run, the ice thickness is updated at each model time step for each elevation band as a function of net mass balance changes using a similar approach to (Naz et al., 2014).

In case of VIC-Glacier, a one-at-a-time sensitivity analysis was done for a single grid cell to analyse the influence of subsurface flow parameters on total runoff, base flow and snow roughness on peak discharge. The sensitivity analysis showed that peak discharge and timing was highly sensitive to the snow roughness length parameter, while less sensitive to the subsurface flow parameters of the VIC-Glacier model, which might be because of the limited water holding capacity in this area due to shallow soil depth and sandy soil texture.

B.3 Ice ablation in the VIC model

The required input to the ice accumulation and ablation routine in the VIC model is the initial ice thickness (IWQ_{init}) for ice layer introduced in the VIC snow model. The IWQ_{init} for each individual elevation band (the elevation bands where glacier ice exists) for glacier grid cells was estimated using the surface slope information from the high resolution digital elevation data and assuming the gravitational driving stress $\tau_b = \rho g h \sin(\alpha)$ equals 1 at the glacier base (Paterson, 2002), as:

$$IWE_{init} = \left(\frac{1}{\rho_{ice} g \sin(\alpha)}\right) \times \frac{\rho_{ice}}{\rho_w} \qquad \text{Eq. (1)}$$

Where, g is acceleration due to gravity (910 kg/m^3), ρ_{ice} is the mean ice density, ρ_w is the water density and α is the DEM-derived surface slope.

As shown in Figure S3, for each elevation band the upper two snow layers overlie a bottom layer of glacier ice. When the snow has completely melted, the ice layer becomes exposed and continues to thin by melting at a rate determined using the energy balance approach in the VIC model. The ice water equivalent (IWE) (m w.e.) of the ice layer is therefore updated at sub-daily time steps only through ice melt and snow densification to ice as follows:

$$IWE(i, t + dt) = IWE(i, t) + SWE_{dens} \quad \text{Eq. (2)}$$

Where, IWE is updated through the amount of ice melt out of the elevation band i which is calculated using a similar energy balance approach as used for snowmelt (Andreadis et al., 2009). SWE_{dens} refers to the amount of SWE from the overlying snow pack which compacted to ice through the densification process. The transformation of snow to ice during the snow metamorphism process is implemented based on snow ice density changes within the snow pack. Snow densification in the VIC model is represented using a variation of the SNTHRM algorithm as described by (Andreadis et al., 2009), which predicts a mean pack density in each time step. The snow to ice transformation process only takes place when snow density increases to a threshold density of 850kg/m^3 at any time step. Assuming a linear distribution of snow density within the pack from the density of fresh snow at the top, the amount of SWE that can be added to IWE and subtracted from the SWE is calculated by estimating the maximum snow density at the bottom of the pack. The temperatures of the snow layers are explicitly simulated, while the temperature of the ice layer is considered isothermal (0°C).

The net annual glacier mass balance is determined from the change in storage states of SWE and IWE at the end of each hydrological year as follows:

$$GMB_i = \Delta SWE_i + \Delta \mathrm{IWE}_i \quad \text{Eq. (3)}$$

where $\Delta IWE\ (m.w.e)$ is the annual change in the ice layer as a result of ice melt and snow densification and $\Delta SWE\ (m.w.e)$ is the annual change in SWE through snow accumulation, melt, and densification to ice in a given year.

B.4 Future course of snow covered area

Due to unavailability of the future snow cover area which is a major input variable to the SRM+G model, different tests were done in order to get the approximate future snow cover area for the UIB. The approach is named as 'Temperature Similarity' approach. All of these tests have an assumption that at an elevation zone the snow cover condition is best defined by the temperature patterns in that elevation zone. Figure B.4 is showing a typical snow depletion curve and Figure B.5 is showing the exposed glacier area for different elevation zones for the UIB.

B.5 Temperature Similarity Approach

In the selected methodology, mean monthly historic and future temperature data for each zone were compared and then based on the best KGE value the relevant zonal snow covered area was selected from the historic dataset [i.e. 2000 – 2016 obtained from the MODIS snow cover data MOD10A1-Collection 5]. Following is a description of the three different methods evaluated to get the future time series of snow covered area.

In the first method, the mean monthly temperature from the GCMs was compared to the mean monthly historical temperatures for each elevation zone and each month. Based on this comparison a best matched value of temperature (i.e. minimum difference) is obtained from the historical data. Corresponding to that temperature data the historical snow covered area for that month was selected.

Example: Monthly mean temperature from GCM (rcp8.5) in January 2071 from elevation zone 5 was compared to all the observed January mean values for elevation zone 5, in all the historic years (i.e. 2000 – 2016) and the month which has the least difference was identified (e.g. January 2005). The snow covered area from January 2005, zone 5 was selected as an input to the model for January 2071 zone 5.

In the second method, a set of 12 monthly (i.e. January–December) values from the GCMs were compared to the historical data for the same elevation zone in order to find the best matched year, on average. The snow covered area from all 12 months was selected as an input to the model.

Example: The monthly average temperature from GCM (rcp8.5) in year 2071 and elevation zone 5 was compared to the mean monthly temperature in zone 5 for each historic year (i.e. 2000–2016) and the Kling-Gupta Efficiency (KGE) was calculated. The year with the highest KGE was selected. For example, if year 2012 has the maximum KGE value from the given matrix. Then, the snow covered area of year 2012, zone 5 was picked up as an input to the model for the year 2071 zone 5.

In the third method instead of remaining in the relevant zone, more flexibility was given in which the temperature comparison was not restricted to the same elevation zone but the set of 12 monthly (i.e. January – December) values from the GCMs were compared to all 11 elevation zones, as well as all the years from the historical time series (i.e. 2000–2016). The best KGE value was used to locate the year and zone to be selected as an input snow covered area in the future.

Example: Temperature data from GCM (rcp8.5) in year 2071 is compared with the data from all historic years as well as 11 elevation zones. Then, the data was filtered for the different elevation zones from different years. e.g.:

1. For the elevation zone-1 year 2071 best KGE was found in year 2007 in zone-2.
2. For the elevation zone-2 year 2071 best KGE was found in year 2011 in zone-3.
3. For the elevation zone-3 year 2071 best KGE was found in year 2006 in zone-4.
4. For the elevation zone-4 year 2071 best KGE was found in year 2002 in zone-5.
5. For the elevation zone-5 year 2071 best KGE was found in year 2005 in zone-7.

Finally we have selected the 3rd method for this study which is more flexible in a way that it encompass both the earlier applied methods.

Figure B.**6** presents the monthly variation of snow covered area for the historic time period while the RCP2.6 and RCP8.5 data represents the overall picture of snow covered area obtained using the third method for three different climate change scenarios (i.e. near future: 2011 – 2040, mid future: 2041 – 2070 and far future: 2071 – 2099).

B.6 Kling-Gupta Efficiency (KGE)

The Kling-Gupta Efficiency (Kling et al., 2012) addresses several shortcomings in Nash-Sutcliffe Efficiency (NSE) and is increasingly used for model calibration and evaluation:

$$KGE = 1 - \sqrt{(r-1)^2 + (\alpha-1)^2 + (\beta-1)^2} \quad \text{Eq. (4)}$$

Where r is the linear correlation between observations and simulations, α is a measure of relative variability in the simulated and observed values, and β is the ratio between the mean simulated and mean observed flows i.e. β represents the bias (see Eq. below)

$$KGE = 1 - \sqrt{(r-1)^2 + \left(\frac{\sigma_s}{\sigma_o} - 1\right)^2 + \left(\frac{\mu_s}{\mu_o} - 1\right)^2} \quad \text{Eq. (5)}$$

Where, σ_o is the standard deviation in observations, σ_s is the standard deviation in simulations, μ_s is the simulation mean, and μ_o is the observation mean. KGE = 1, indicates perfect agreement between simulations and observations. The range for KGE is -∞ to 1.0. Negative KGE values are viewed as bad model performance, and only positive values are seen as good model performance.

B.7 EWEMBI Temperatures Evaluation

This issue came into notice while calibrating the hydrological model for the Upper Indus Basin (UIB). It was found that EWEMBI[1] temperatures (T_{avg}[2]) within the UIB do not go along with the observed temperatures specifically at higher elevations (e.g. >3000 m a.s.l.). This behaviour is consistent throughout the time period i.e. 2000 − 2012 for which the data has been analysed. Table B.6 shows the list of stations and providing agency/organization.

The following steps were adopted to perform the evaluations for the EWEMBI temperatures:

1. A 30 m DEM aggregated to 0.5° in order to have the same spatial resolution as EWEMBI grid. Three methods for aggregation (Min., Max. and Median) were adopted in order to see the elevation variation within a pixel size of 50 km. Figure B.17 shows the pixels variations in the

[1] (Lange, 2016): EartH2Observe, WFDEI and ERA-Interim data Merged and Bias-corrected for ISIMIP (EWEMBI). GFZ Data Services. http://doi.org/10.5880/pik.2016.004

[2] T_{avg} was used for this analysis because SRM+G ultimately uses the average temperatures

western portion of the UIB, while Figure B.18 Shows the portion of the UIB (western-UIB) where all of the observation stations are located. It can be seen that there is more than 4000 m of elevation variation within a pixel, which ultimately has an impact on the temperature gradient.

2. A comparison of the SRTM 30 m aggregated to 0.5° grid vs the EWEMBI elevation grid is shown in Figure B.19. It is evident that there are certain difference between these two datasets. The EWEMBI elevation grid data has been utilized for the temperature bias correction, because this grid has been used in developing the EWMEBI temperature.
3. A daily regression analysis between the EWEMBI data for each pixel vs elevation of each pixel for 13 years (i.e. 2000 − 2012) has been performed (see Figure B.20). There are 308 EWEMBI grid cells covering the UIB extent (x_{min}=71.5, x_{max}=82.5, y_{min}=30.5, y_{max}=37.5). The observed data was plotted versus their station elevation to observe the differences between the EWEMBI temperatures and the observed station data. It seems that at higher elevations the EWEMBI temperatures are very high (sometimes difference is more than 10 °C) thus producing more snow and glacier melt than actually anticipated.
4. Figure B.21 presents a typical example for stations >3000 m a.s.l. Where the observed temperatures at the Khunjerab station (4730 m a.s.l.) were compared with the adjusted EWEMBI temperatures calculated by a linear model (i.e. EWEMBI Temperature vs EWEMBI Elevation).
5. SRM+G works with elevation zones (bands). The recommended elevation interval (Martinec et al., 2008) is 500 m a.s.l. The hypsometric characteristics for the UIB can be seen in Figure B.22, including the 11 elevation zones identified for the whole UIB.
6. A long term mean annual temperature lapse rate for the whole UIB was also calculated using the available observed data having Skardu as a base station (Figure B.23). This gives an idea about the generalized temperature lapse rate for the UIB. The estimated lapse rate with Skardu as base station is about 6.57 °C km^{-1}.

B.8 EWEMBI Temperatures Bias Correction

There were two methods adopted to correct the EWEMBI temperatures. Both the methods are explained below.

B.8.1 Method 01: Direct Difference

1. First of all, a daily regression analysis of observed (station) temperatures vs elevation was performed to get the daily lapse rate from the observed data (Figure B.24).
2. Based on this daily temperature lapse rate from the observed data the temperatures were predicted according to the hypsometric mean elevation of each elevation zone.

3. A daily lapse rate analysis for western portion (where all the observation stations are located) of the UIB as well as for the whole UIB against their corresponding elevations was also performed in order to check the differences between the lapse rate obtained from the western (Figure B.25) as well as whole UIB (Figure B.26).
4. In Figure B.27, it seems that there is no major difference between the lapse rate of the whole UIB and UIB-west so the whole UIB was selected for further analysis.
5. A raster brick consisting of 11 layers (i.e. 11 elevation zones) was prepared for the whole UIB with reference to the hypsometric mean elevation of each elevation zone as well as using a daily variable temperature lapse rate obtained from the regression analysis between the EWEMBI grid elevations vs EWEMBI temperatures as explained in the previous step.
6. In this step, the lapsed temperature for each elevation zone was extracted from this raster brick.
7. Station based zonal temperatures as obtained in step 2 as well as EWEMBI based zonal temperatures as obtained in step 6 are then aggregated on monthly basis for each elevation zone in order to get the difference of mean monthly temperatures between these two data sets.
8. The monthly difference of these two temperature datasets (see Table B.7 were then subtracted from the daily EWEMBI zonal temperatures to get the daily bias corrected EWEMBI temperatures.

B.8.1.2 Method 02: Quantile Mapping

1. In this method, a quantile (probability) mapping (Piani et al., 2010a, b)was performed to bias correct the EWEMBI temperatures.
2. First of all, the quantiles were calculated against each temperature for each elevation zone using the EWEMBI as well as the station based zonal temperatures (see Method 1).
3. The probability of daily zonal EWEMBI temperatures was calculated using the curve as shown in Figure B.28. These probabilities were then mapped to the station based curve and then temperatures were interpolated with the help of linear interpolation against each probability to get the temperature time series for each elevation zone. The Table B.8 and Table B.9 summarize the details for zonal temperatures based on EWEMBI and station based observed data.
4. The final comparison between the results of these two methods as well as station and EWEMBI based temperatures for an elevation zone can be seen in Figure B.29. There is not much difference between the results of these two methods so finally the method 2 was selected to bias correct the temperatures because it not only provide the differences but also the same distribution.

B.9 Bias correction for the GCMs Temperature data

The available GCMs dataset is bias corrected to the EWEMBI data set. Therefore, it is indeed necessary to bias corrected the GCMs temperatures as well because of the bias correction of EWEMBI temperatures data with the observed temperature data. It was assumed that the transformation T (and thus the correction) between observed and EWEMBI is the same as between observed (station based) and the GCMs.

In bias correcting the GCMs, the difference of EWEMBI temperature data to the observed data has been subtracted from the GCMs using the quantile (probability) mapping method as discussed earlier.

Concerning the tackling of future higher temperatures of the GCMs, the difference between EWEMBI and observed data for the highest EWEMBI temperatures has been used as a constant offset for the GCMs temperatures outside the present range (Henning et al., 2015).

B.10 Bias correction for the EWEMBI precipitation

EWEMBI data strongly underestimate precipitation for the UIB. Average annual precipitation by these gridded products for the period (2000 – 2016) has been summarized in Table B.10, In order to see the range provided by these gridded products. Therefore, precipitation was bias corrected using the altitude correction formula proposed by (Immerzeel et al., 2015). Following method has been applied for correcting the EWEMBI precipitation.

The precipitation fields are corrected using Precipitation Gradient PG (%m^{-1}). Precipitation is positively lapsed using a PG between a reference elevations (HREF) to an elevation of maximum precipitation (HMAX). At elevations above HMAX, the precipitation is negatively lapsed from its maximum at HMAX with the same PG according to equation (6 and 7).

$$P_{corr} = P_{APHRODITE} \times \left(1 + (H - HREF)\right) \times PG \times 0.01) \qquad for\ HREF < H \leq HMAX \qquad Eq.(6)$$

$$P_{corr} = P_{APHRODITE} \times (1 + (((HMAX - HREF) + (HMAX - H)) \times PG \times 0.01) \qquad for\ H > HMAX \qquad Eq.(7)$$

Where, HREF=2500 m, HMAX=4500 m for Himalayan and 5500 m for Hindu Kush and Karakoam regions.

Based on the elevation of each grid cell, (Immerzeel et al., 2015) have calculated a correction factor using different Median PG values for each of the mountain regions. Median precipitation gradients in the Hindu Kush and Karakoram ranges (0.260 and 0.119%m^{-1}) respectively, are significantly larger than those observed in the Himalayan range, e.g. 0.044%m^{-1}.

In the first step, we applied these equations to the APHRODITE (Yatagai et al., 2012) data for the UIB upstream of Tarbela in order to calculate the correction factor for our catchment. The reclassified (0.5°) original EWEMBI grid (download: ftp://rfdata:forceDATA@ftp.iiasa.ac.at/) file was used to extract the elevation information for each grid cell.

The corrected APHRODITE precipitation for the UIB using this method is about 578.5 mm/yr for a period of 2003 – 2007, while it is 913±323 mm/yr for the same period (Immerzeel et al., 2015). The difference in results is because of the consideration of different catchment area.

Based on this correction of APHRODITE data a bias correction factor of 1.65 (Corrected APHRODITE = 578.5 mm/a divided by Uncorrected EWEMBI = 350.9 mm/a) has been estimated for EWEMBI precipitation data for the concurrent period (i.e. 2003 – 2007). Finally, bias corrected EWEMBI precipitation for the UIB upstream of Tarbela is about 604 mm/a (i.e. Period: 2000 – 2016). This bias corrected precipitation is in range comparable to the values found in literature i.e. 675±100 mm/a (Reggiani and Rientjes, 2015), 608 mm/a (Khan and Koch, 2018) and 593 mm/a (Shafeeque et al., 2019) who considered a similar catchment area to the present study. Lastly, the same bias correction factor has been applied to the GCMs based precipitation data.

B.11 Inclusion of Glacier Mass Balance (GMB) in model calibration/validation

In the UIB, the most important discharge component is melt water generation through snow and glacial melt. Hence, it is essential to take into account the GMB while simulating discharges in order to prevent internal process compensation (Hagg et al., 2006; Finger et al., 2015; He et al., 2018). In case of SRM+G model, we have manually adjusted the Degree-Day Factors for glaciers (a_g) in order to tune the mass balance for the enhanced calibration method. The a_g values ranges from 2.5–6.0 mm $°C^{-1}$ day^{-1} (see Table S3). These values are well within the range as suggested by (Lutz et al., 2016) for the Upper Indus Basin (See Table S11).

In case of VIC-Glacier model, the model parameters related to snow accumulation/ablation such as maximum and minimum snow temperature and snow/glacier albedo parameters were set to default parameters (hard coded in the code) (see (Cherkauer et al., 2003) for more details). The snow roughness length parameter (range of 0.005–10mm) and temperature lapse rate parameter (i.e. temperature lapse rate to lapse the mean pixel temperature from the meteorological forcings to each elevation band) were manually calibrated which have higher impact on the timings/magnitude of the snowmelt. A higher value of the snow roughness length will force the snowmelt to come earlier in the snowmelt season. After calibration a final value for the snow roughness length of 5 mm and lapse rate of -6.5°C/km were selected based on the higher weighted KGE values for both dry/cold and wet/warm periods (2000–2004 and 2008–2010, respectively), and comparison of the mean annual glacier mass balance value over the UIB for the period of 2000–2016 with observations was done.

In addition, bias correction of precipitation and number of elevation bands within a grid cell also has a greater impact on the snow accumulation and melt processes in the case of VIC-Glacier model, particularly smaller elevation band intervals allow to determine glacier area more accurately within a grid cell. With these changes the model predicted lower mass loss (-130 mm/year) compared to -200 mm/year for the model run without bias-correction of precipitation.

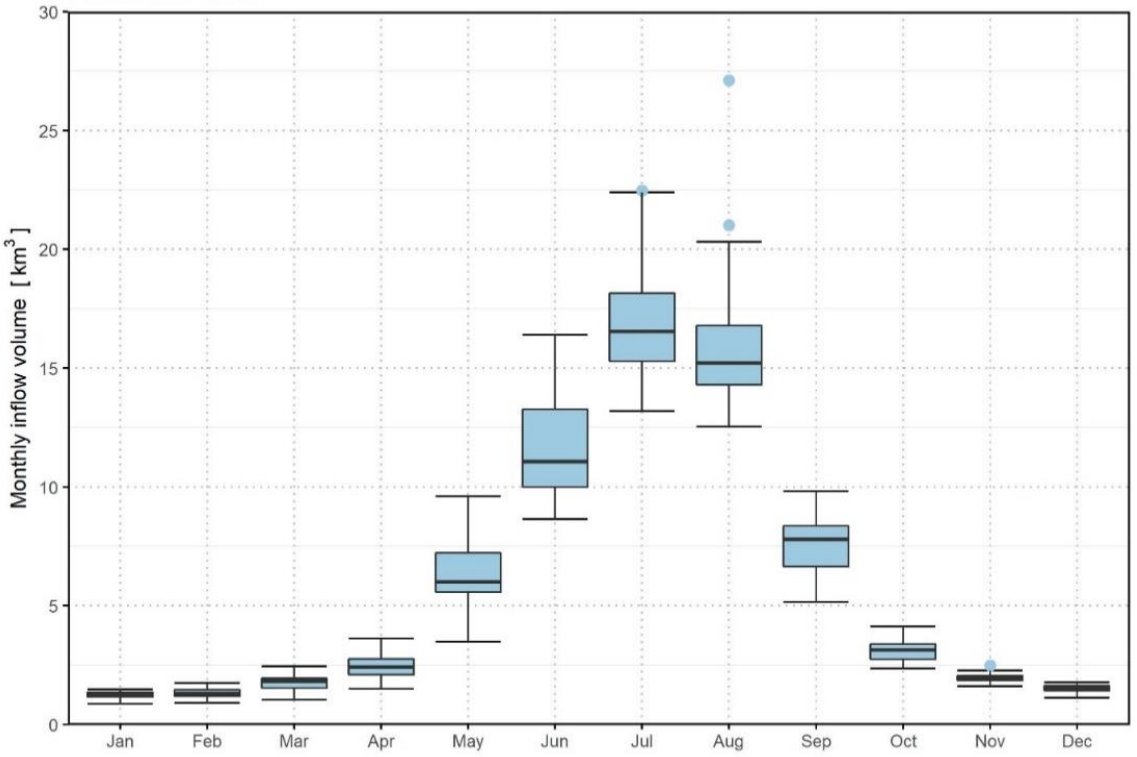

Figure B.1 Monthly distribution of discharge volumes at Tarbela [Period: 2000 – 2016]

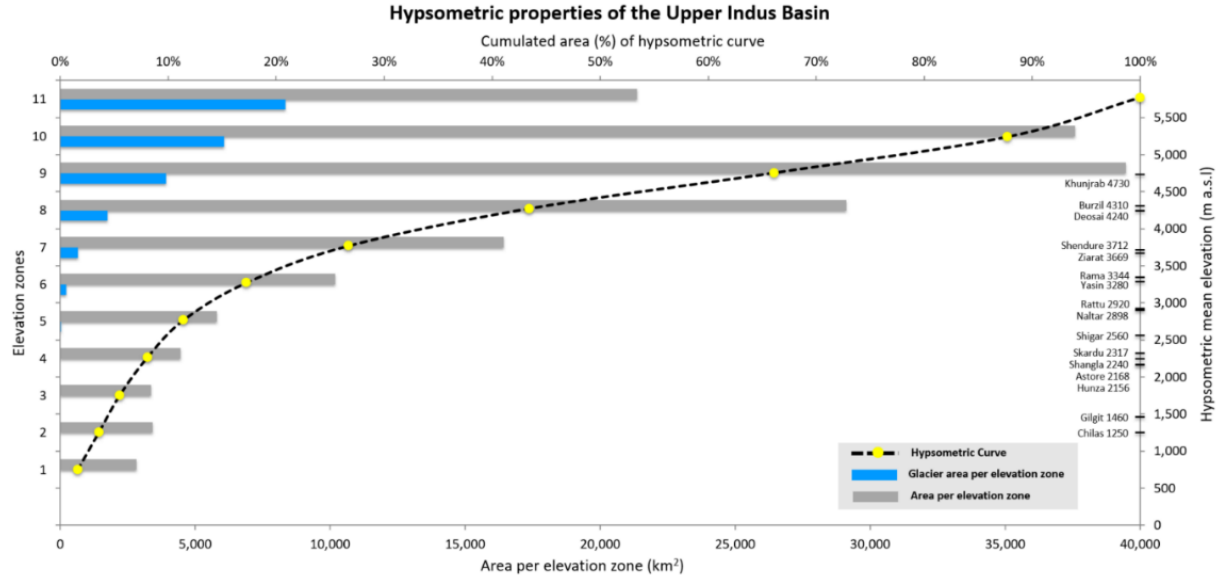

Figure B.2 Hypsometric curve of the UIB. The primary y-axis is showing the glacier and zonal area per elevation zone while the secondary y-axis is showing the elevation of different meteorological stations within the UIB [GLIMS dataset was used for the glaciers area representation]

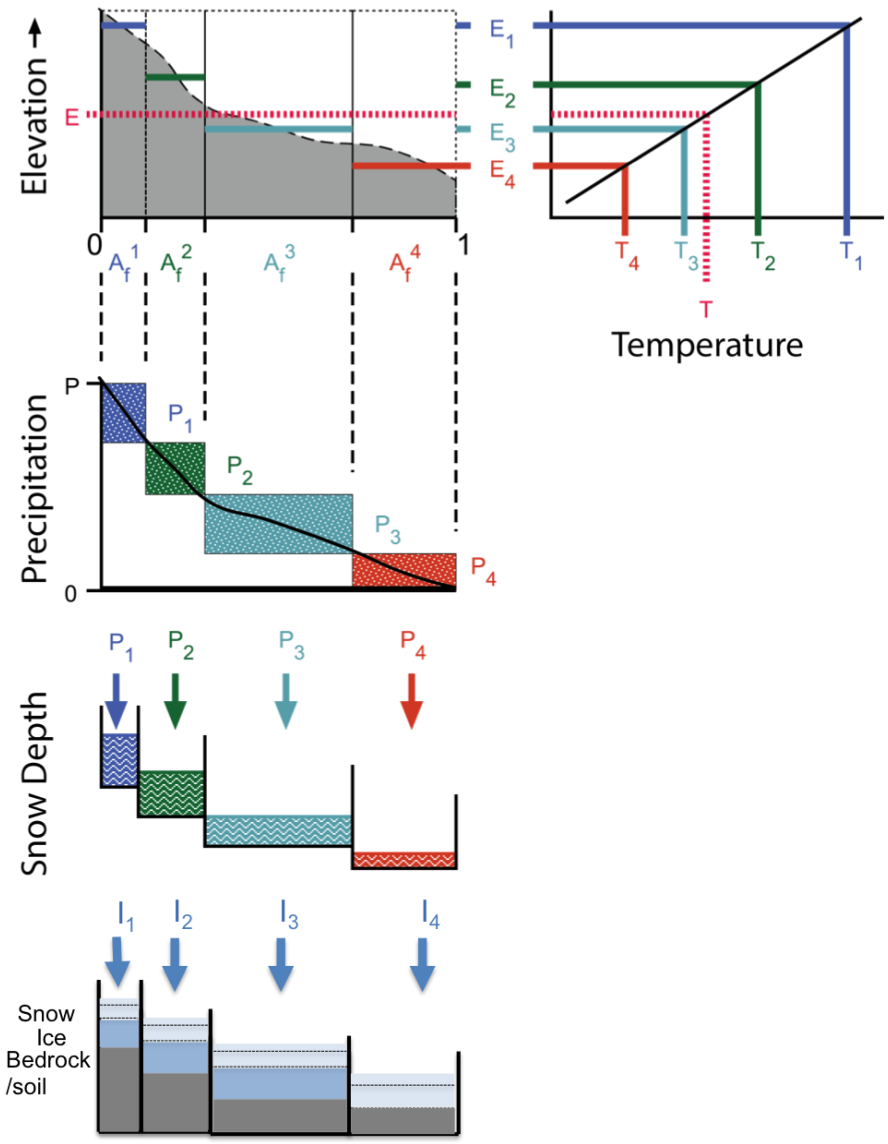

Figure B.3 Implementation of the snow elevation bands and glacier representation in the VIC snow model.

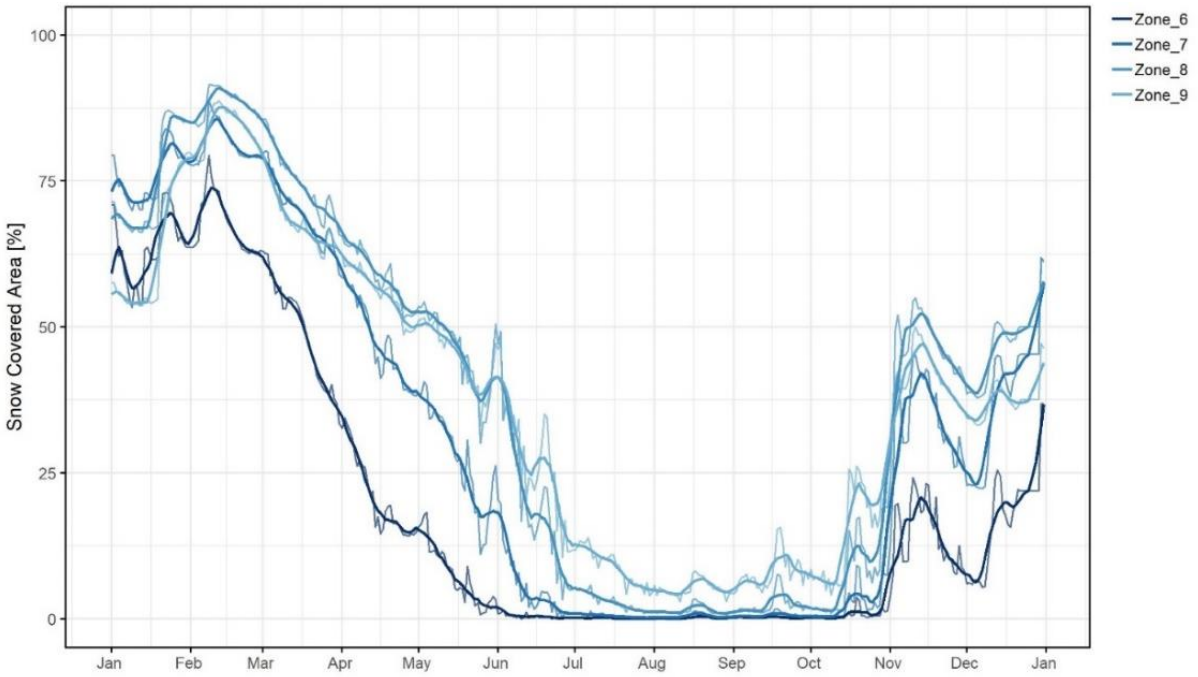

Figure B.4 Daily snow cover depletion curves for the Upper Indus Basin [Year-2013] – thick lines are representing the 9-day moving averages while the thin lines are the original data [Data source: MODIS MOD10A1 - C5]

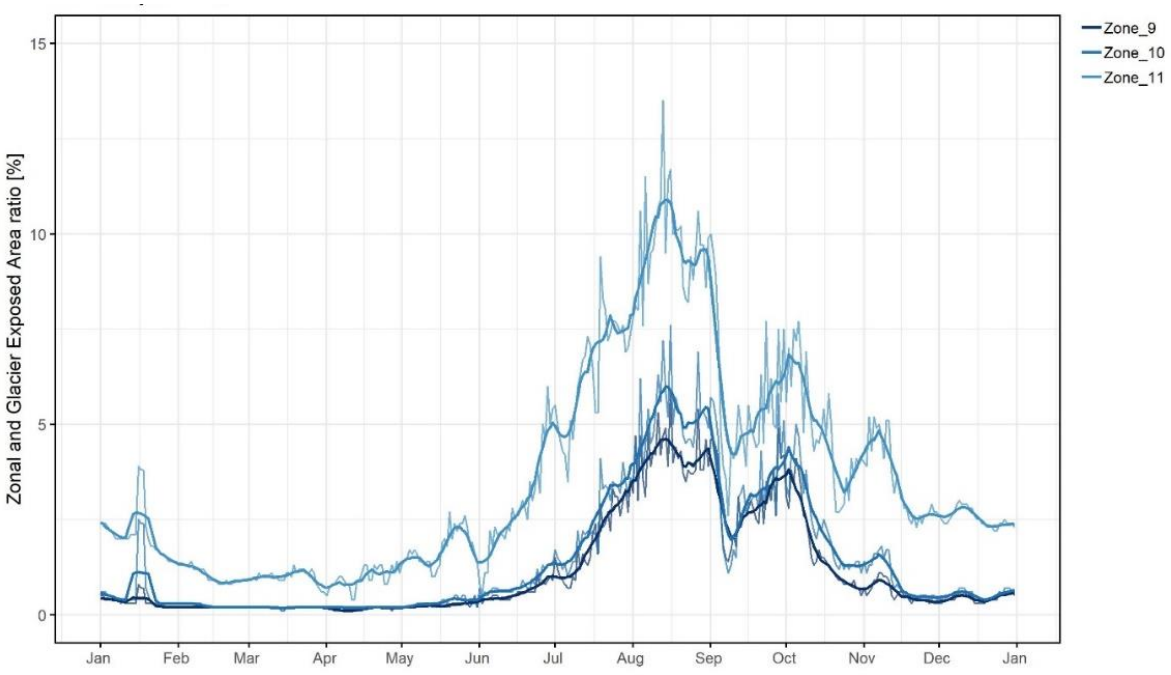

Figure B.5 Daily ratio of zonal area to exposed glacier area in the UIB [Year-2009] thick lines are representing the 9-day moving averages while the thin lines are the original data [Source: GLIMS dataset]

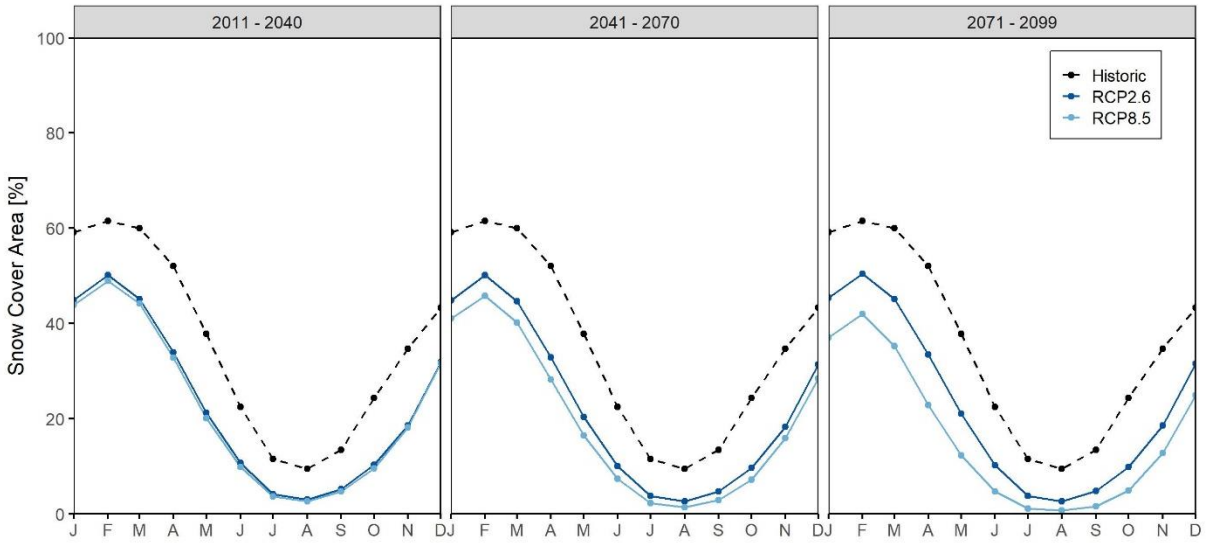

Figure B.6 Comparison of the historic [2000–2016] and future [Near: 2011–2040, Mid: 2041–2070 and Far: 2071–2099] distribution of monthly snow cover area in the UIB

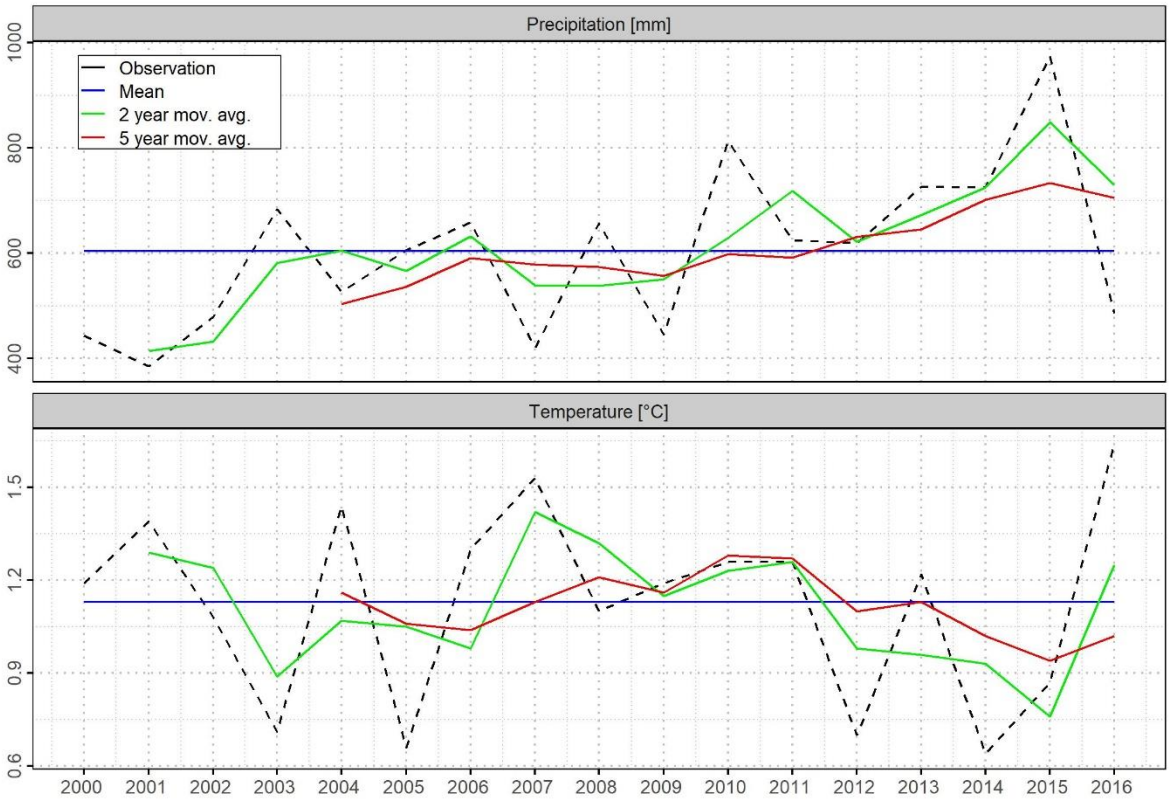

Figure B.7 Subdivision of available data into different climatic periods (dry/cold: 2000–2004, wet/warm: 2008–2010) based on the bias corrected EWEMBI temperature and precipitation

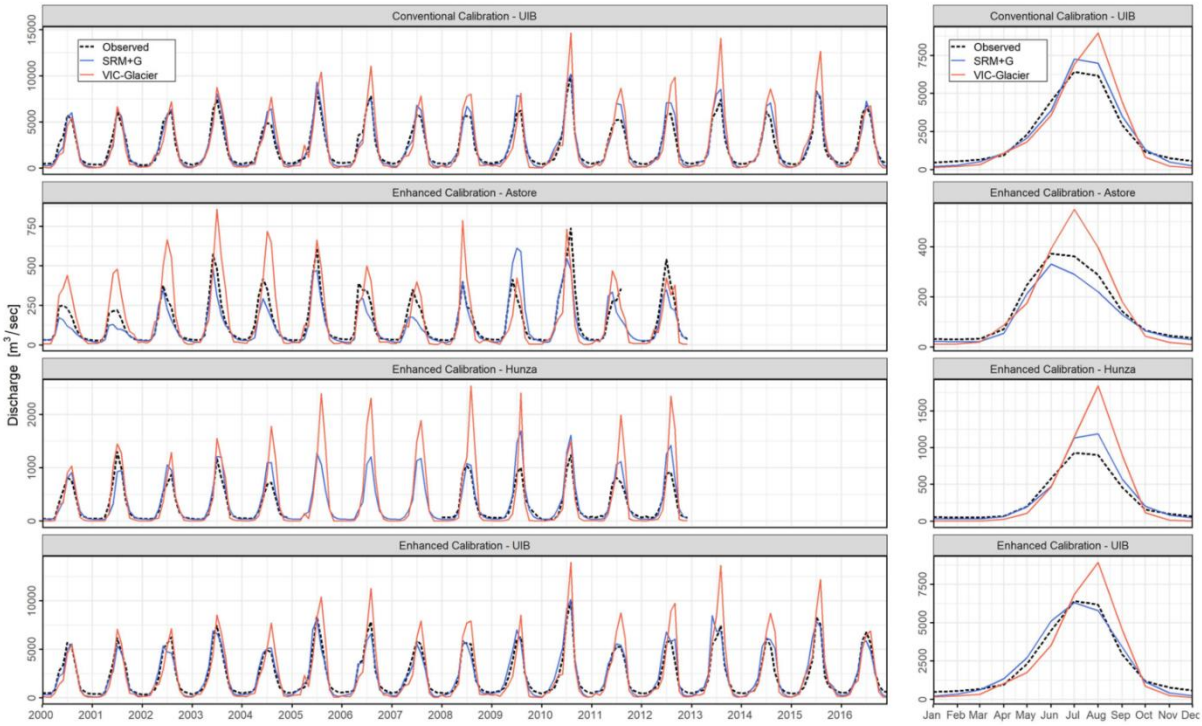

Figure B.8 Results of calibration and validation using SRM+G and VIC-Glacier model for the UIB – [conventional calibration 1st facet], [enhanced calibration 2nd to 4th facet] including the intermediate gauges (Hunza and Astore) modelled from 2000–2012 while the UIB was simulated for 2000–2016. The right side panel is showing the long-term mean monthly dynamics

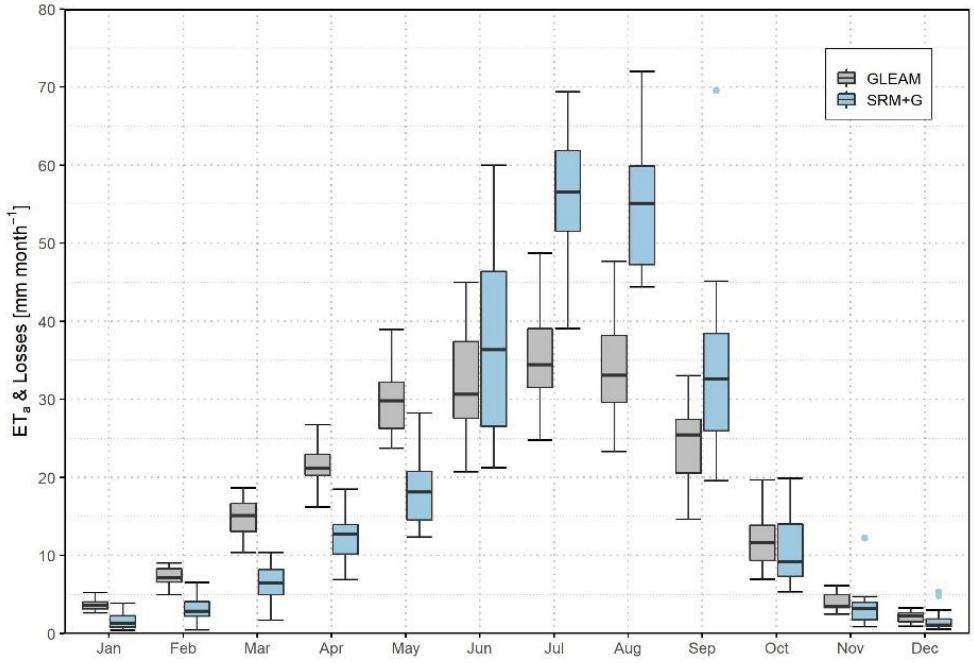

Figure B.9 Long term mean monthly comparison of actual evapotranspiration modelled by GLEAM vs losses (SRM+G uses runoff coefficients for snow, glacier and rain in order to account for the losses) from the SRM+G model [period: 2000–2016]

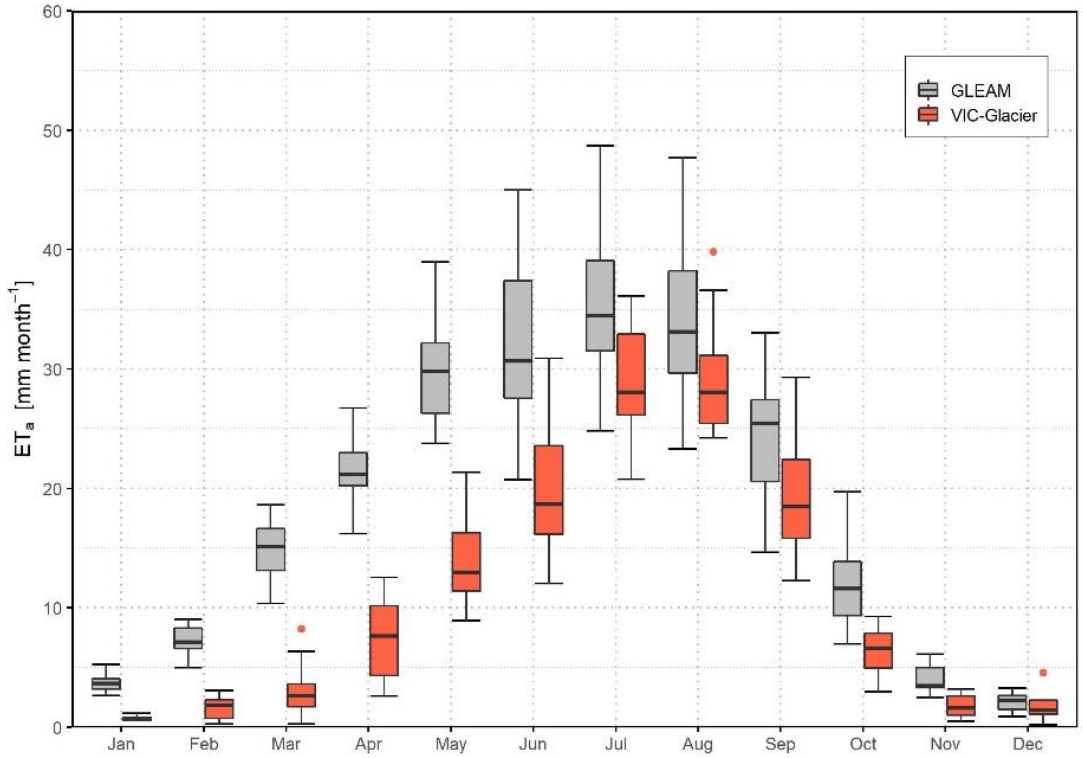

Figure B.10 Long term mean monthly comparison of actual evapotranspiration modelled by GLEAM vs VIC-Glacier model [period: 2000–2016]

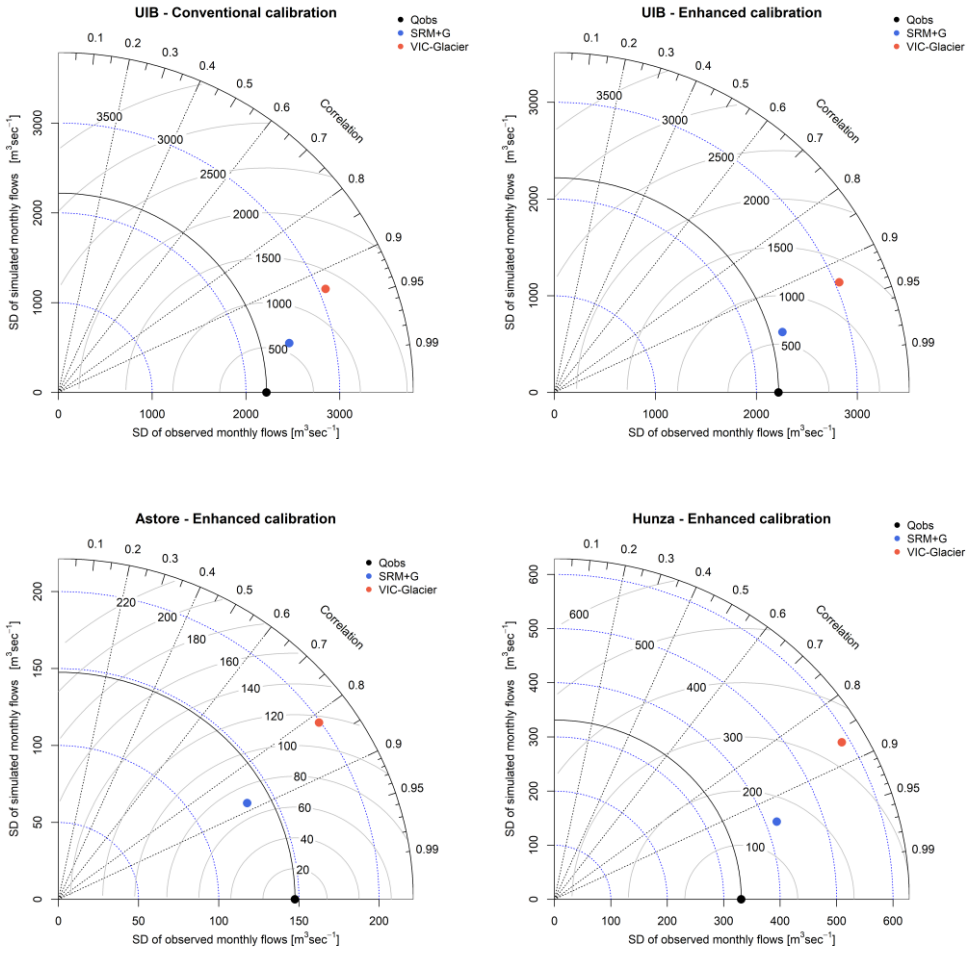

Figure B.11 Taylor diagram for model performance evaluation in the conventional and enhanced calibrations [circles around the observed flow are the centred Root Mean Squared Error [m^3sec^{-1}] the smaller the better]. Blue dotted circles around the origin show the standard deviation SD of observed and modelled flows [m^3sec^{-1}]. The nearer the model SD to the observed flow's SD the better. The strait dotted lines represent the anomaly correlation between observed and simulated flows.

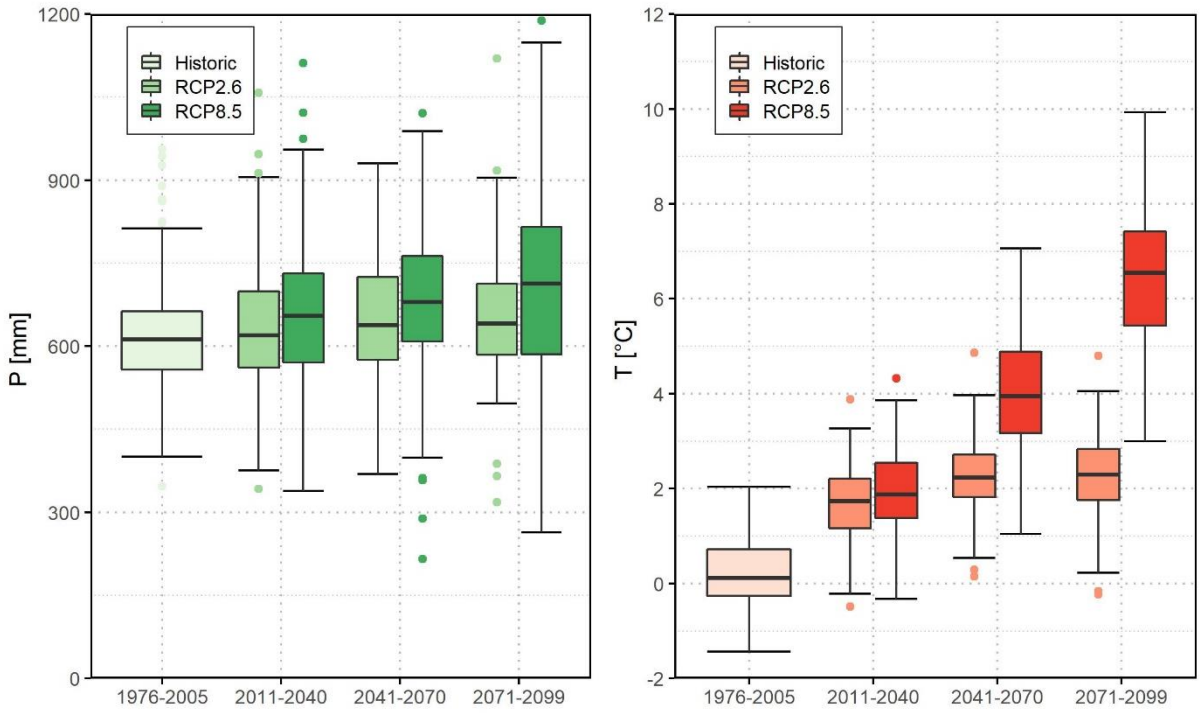

Figure B.12 Evaluation of ensemble mean long-term basin averaged bias corrected precipitation (left) and temperature (right) simulated by four GCMs in the UIB for the historical [1976 – 2005] as well as three future periods near: 2011 – 2040, mid: 2041 – 2070 and far: 2070 – 2099 including two RCPs scenarios: 2.6 and 8.5

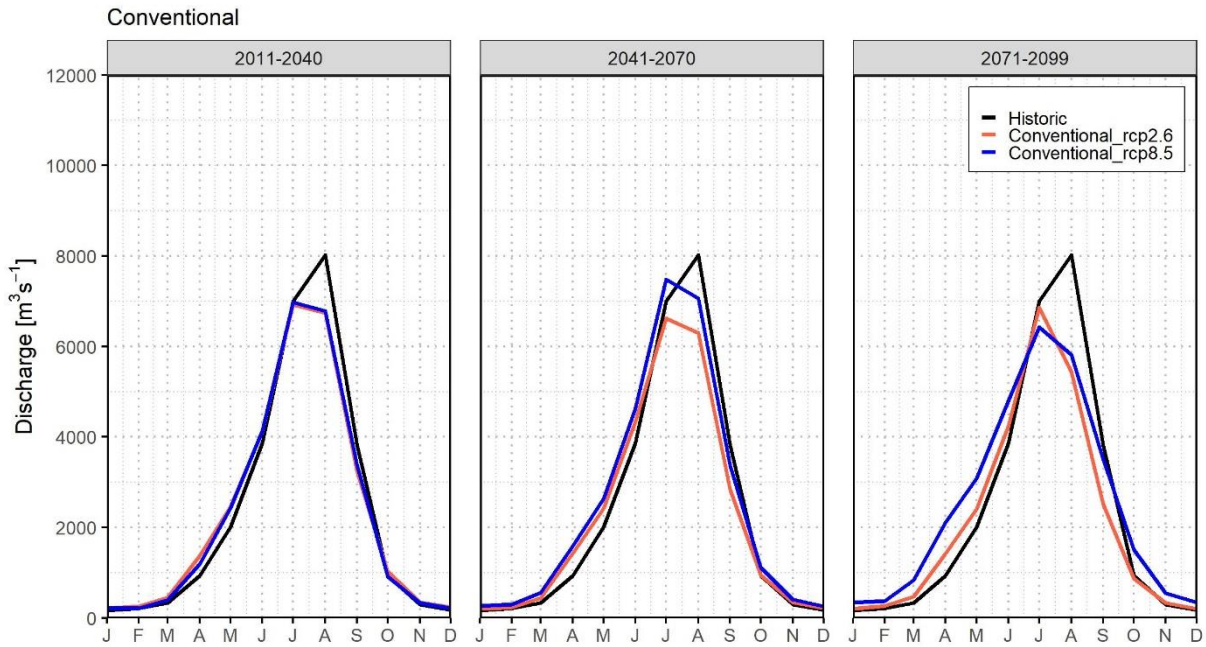

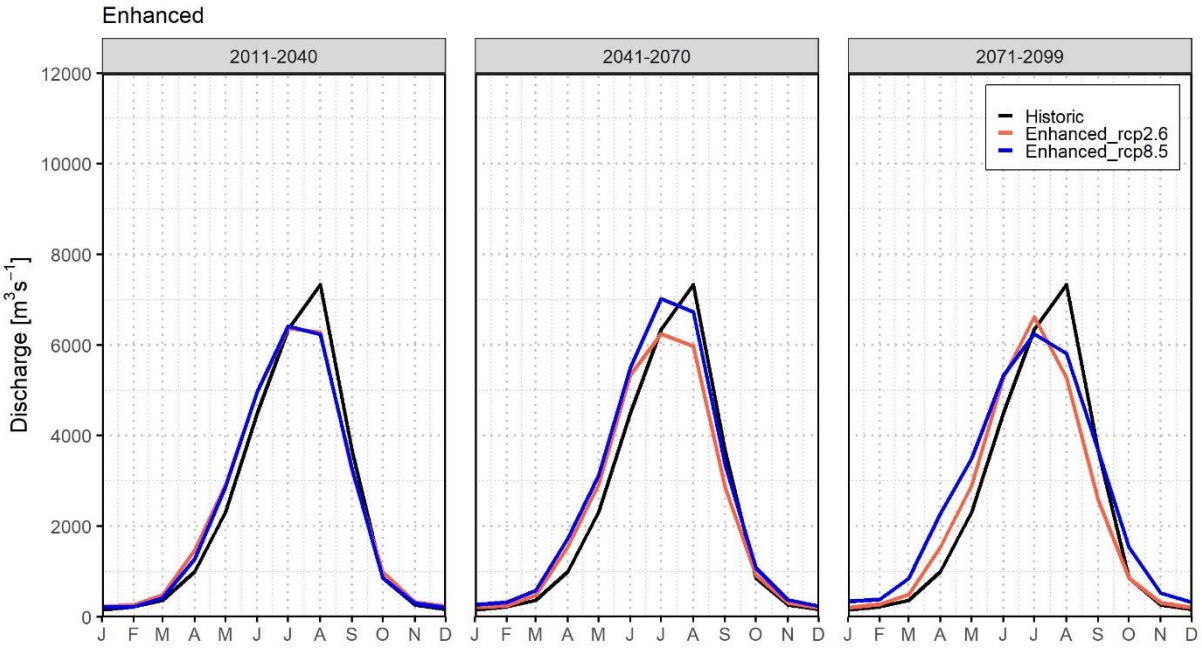

Figure B.13 Long-term mean monthly simulated discharges for RCPs 2.6 and 8.5 in three future periods based on both calibration methods using both HMs (SRM+G has assumed the glacier area reduction scenarios with 75% remaining glacier area in the near, 50% in the mid and 25% in the far future periods, while VIC-Glacier explicitly model the glacier area as a result of glacier ablation within a given elevation zone)

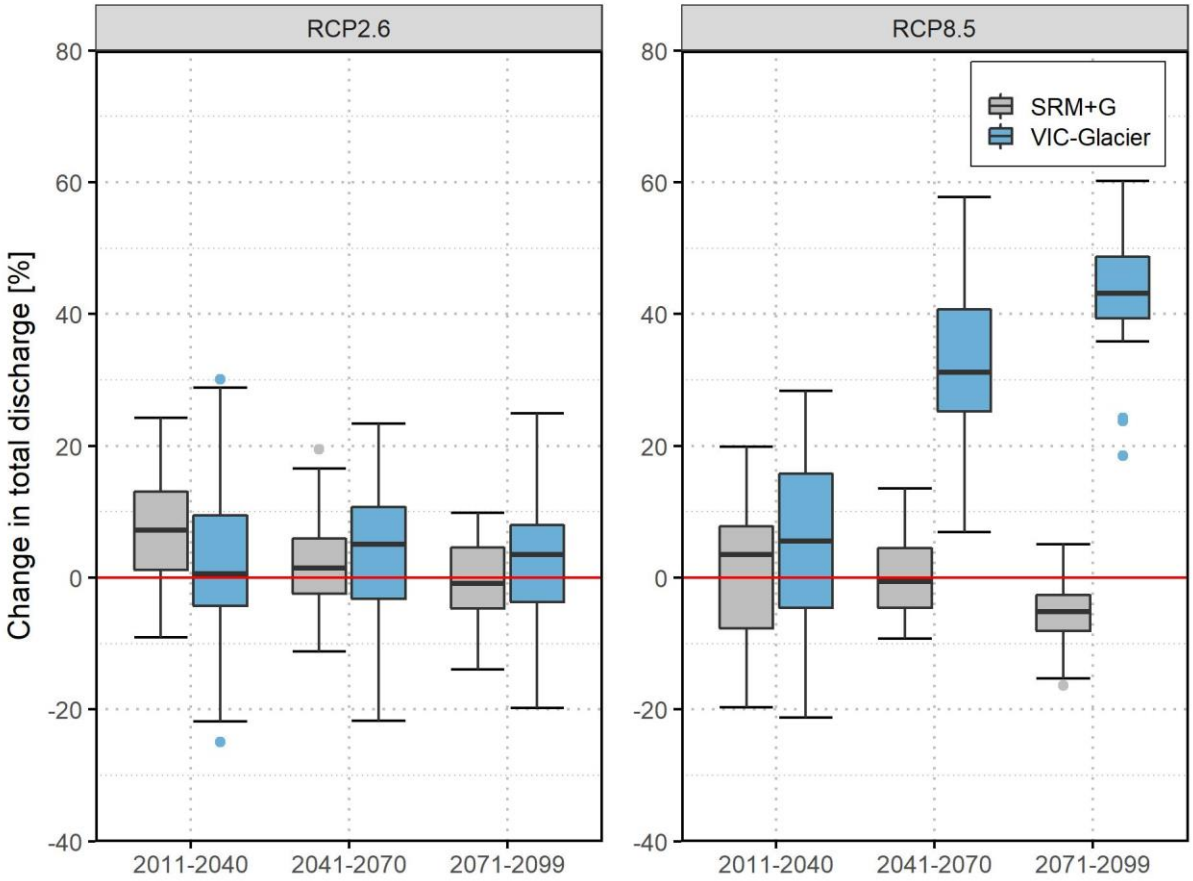

Figure B.14 Comparison of SRM+G and VIC-Glacier model for projected long-term hydrological changes in the total discharge using the enhanced calibration/validation approach (SRM+G, has assumed the glacier area reduction scenarios with 75% remaining glacier area in the near, 50% in the mid and 25% in the far future periods, while VIC-Glacier explicitly modelled the glacier area as a result of glacier ablation within a given elevation zone).

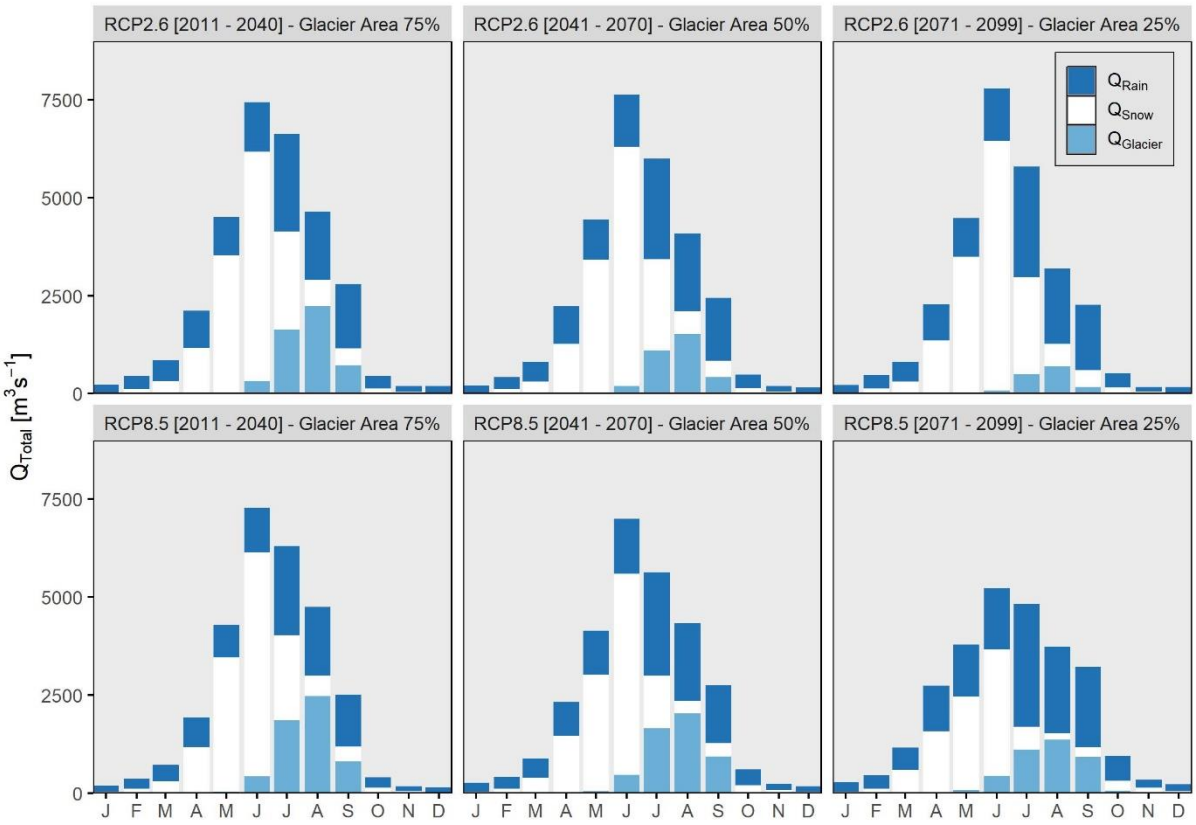

Figure B.15 Ensemble mean monthly flows and separation of runoff components for the near, mid and far future periods also highlighting glacier area loss scenario [75%, 50% and 25%] under both the RCPs using only SRM+G model

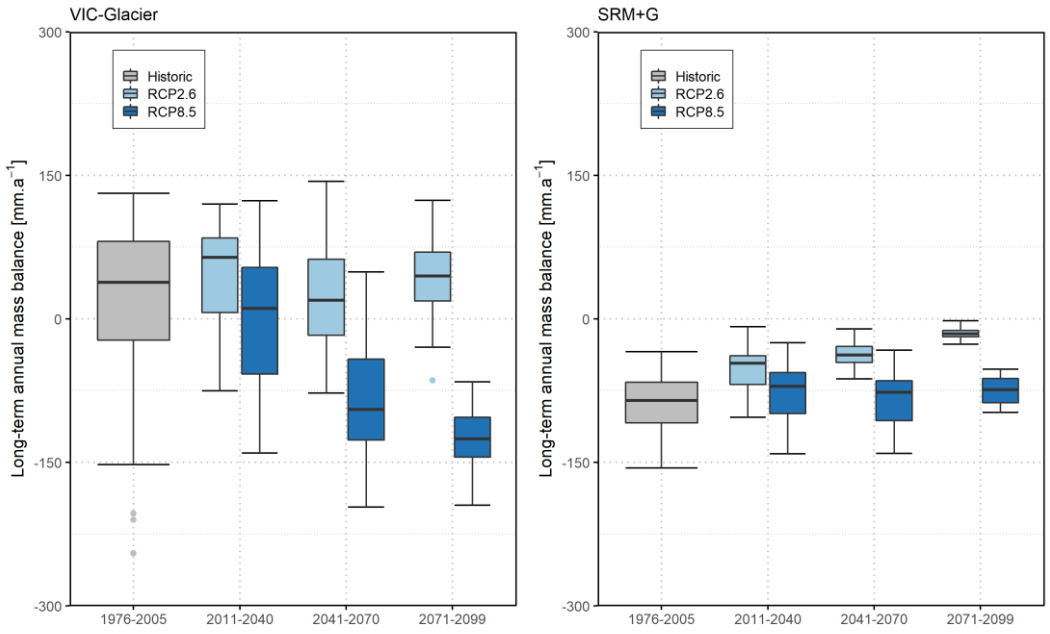

Figure B.16 Estimation of glacier mass balance for historical (i.e. 1976 – 2005) and future periods (2011 – 2099) based on 4 GCMs using VIC-Glacier and SRM+G hydrological model

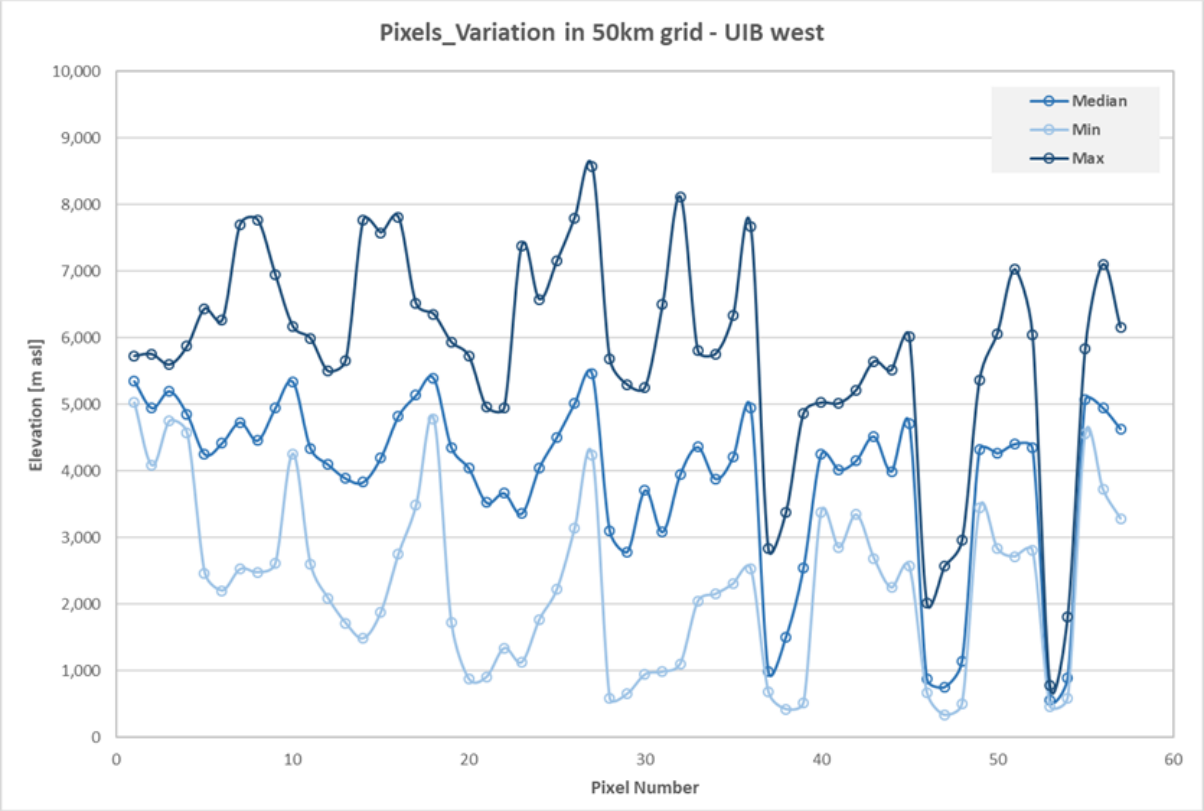

Figure B.17 Elevation variation within a pixel aggregated to 50km for the western UIB

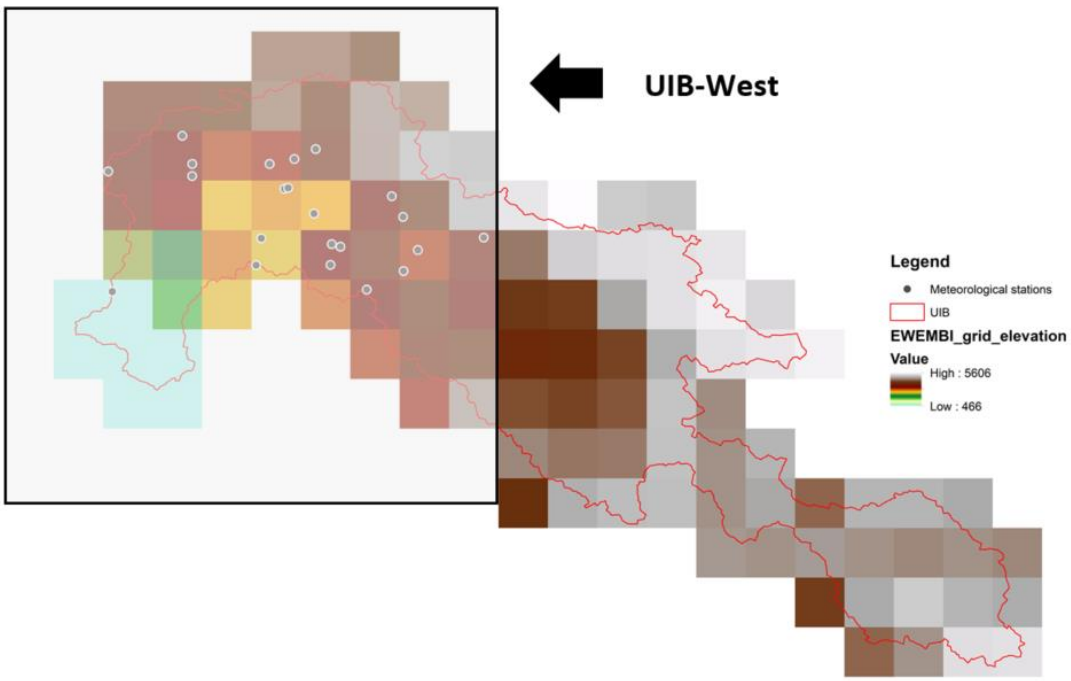

Figure B.18 EWEMBI elevation pixels covering the Upper Indus Basin

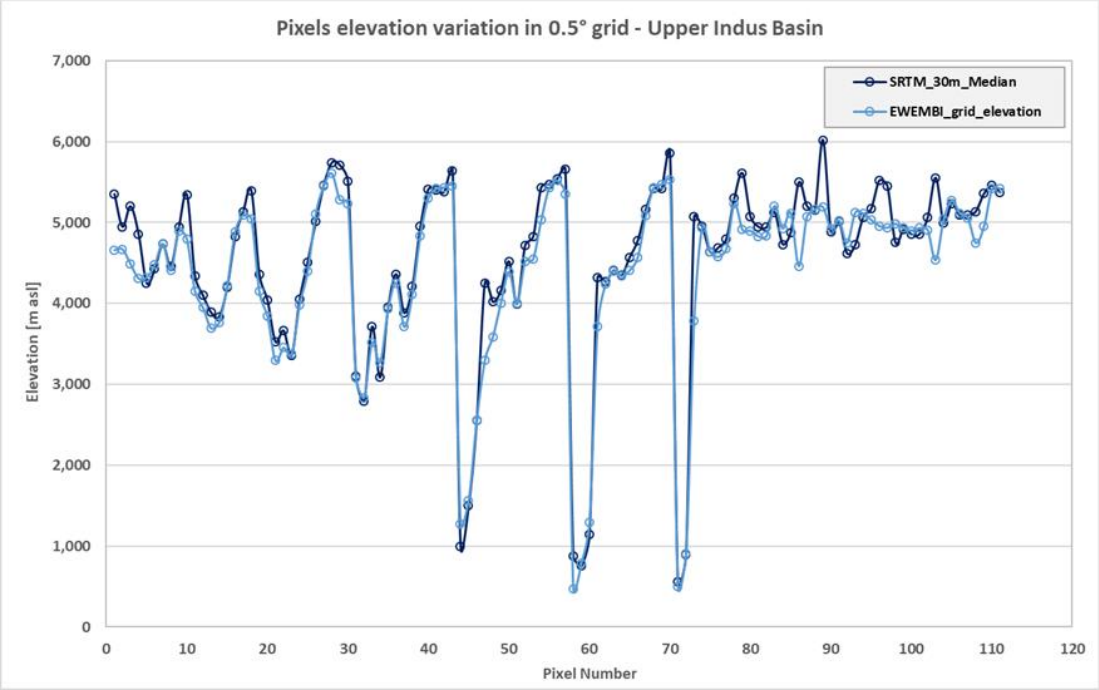

Figure B.19 Comparison of pixels elevation between aggregated 30m SRTM (Median) and original EWEMBI grid

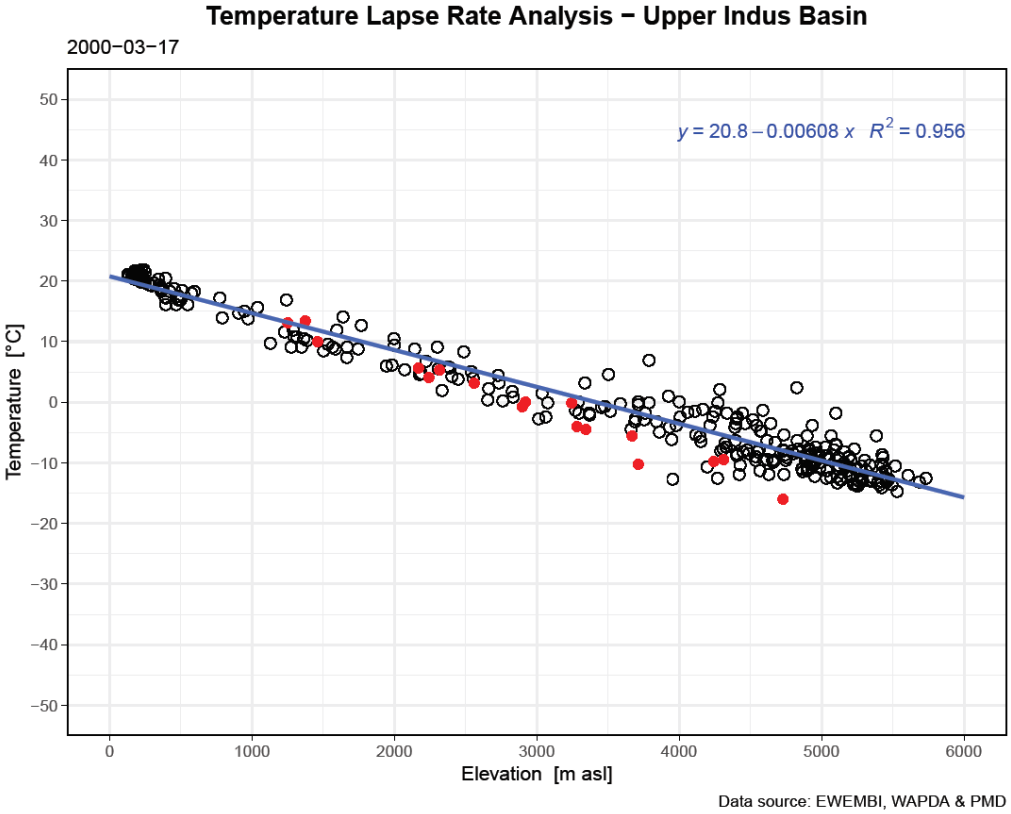

Figure B.20 Regression analysis between the EWEMBI elevation grid vs EWEMBI temperatures (T_{avg}) (hollow circles = EWEMBI data and Red points = observed data (T_{avg}))

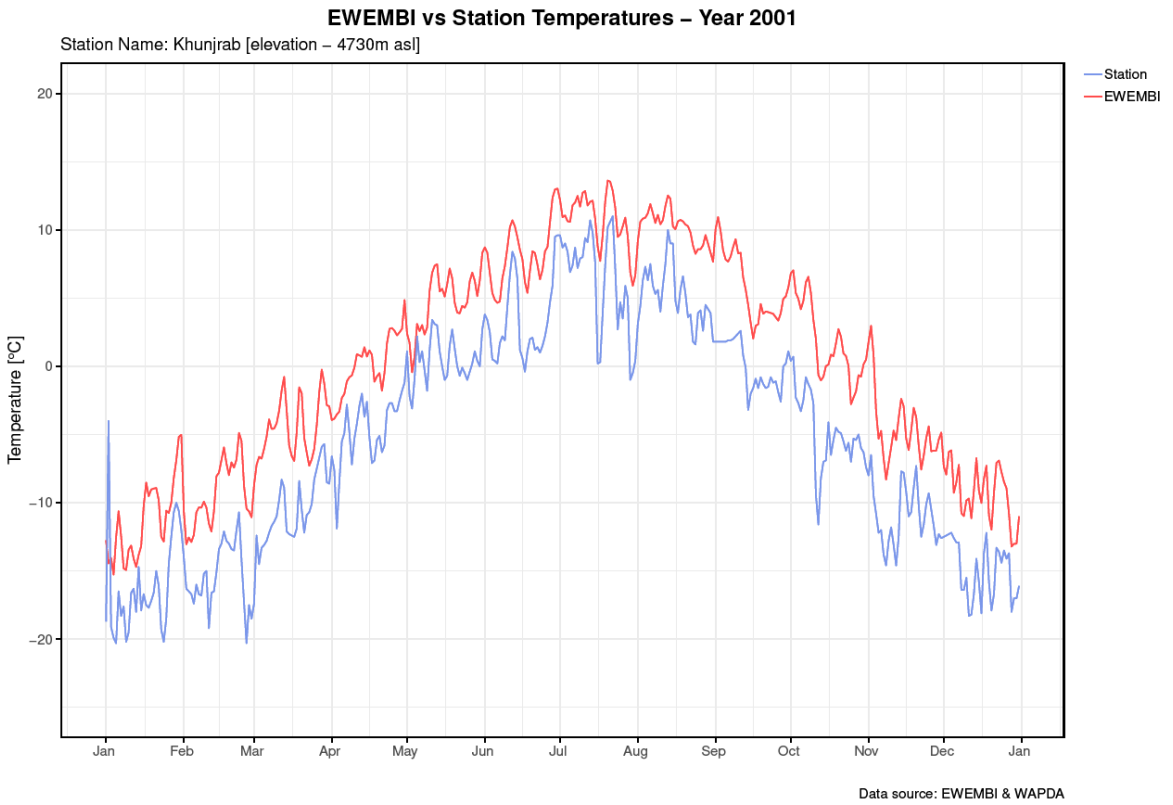

Figure B.21 Comparison of observed data (T_{avg} at Khunjerab 4730m a.s.l.) vs EWEMBI temperature (using the daily lapse rate which was obtained from the regression analysis between the EWEMBI elevation grid vs EWEMBI temperatures)

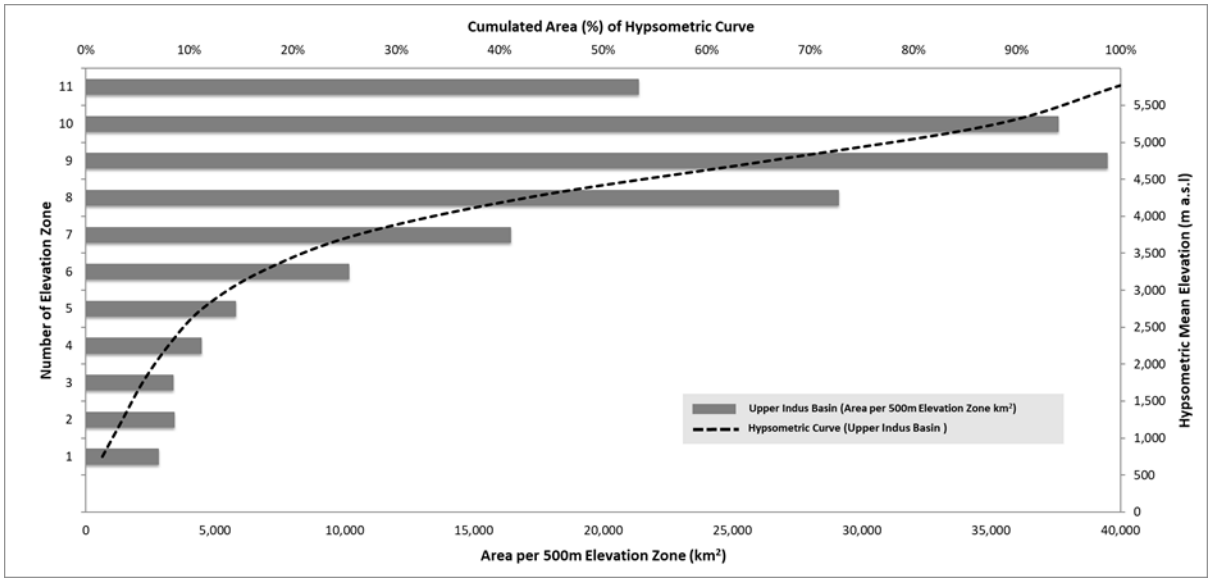

Figure B.22 Hypsometric curve and area per elevation zone for the Upper Indus Basin

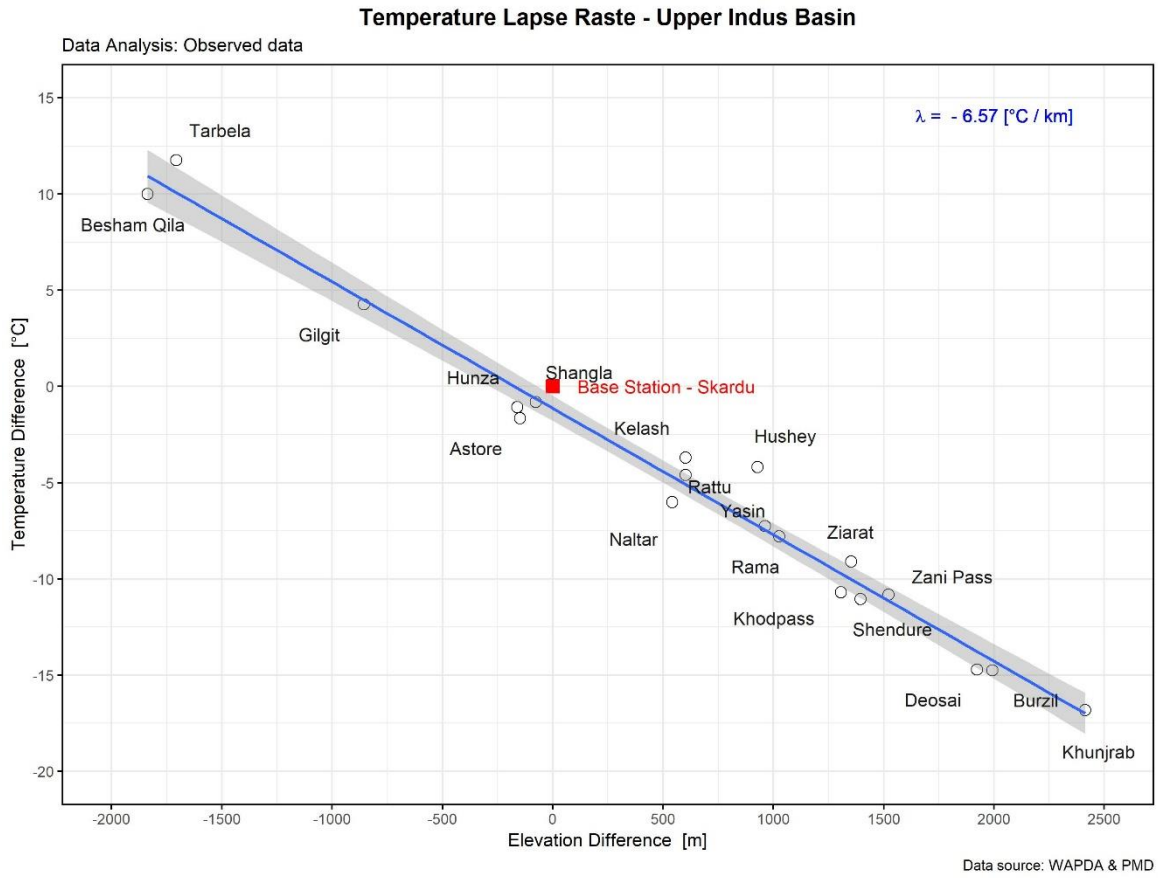

Figure B.23 Long-term mean annual temperature lapse rate [Base station: Skardu]

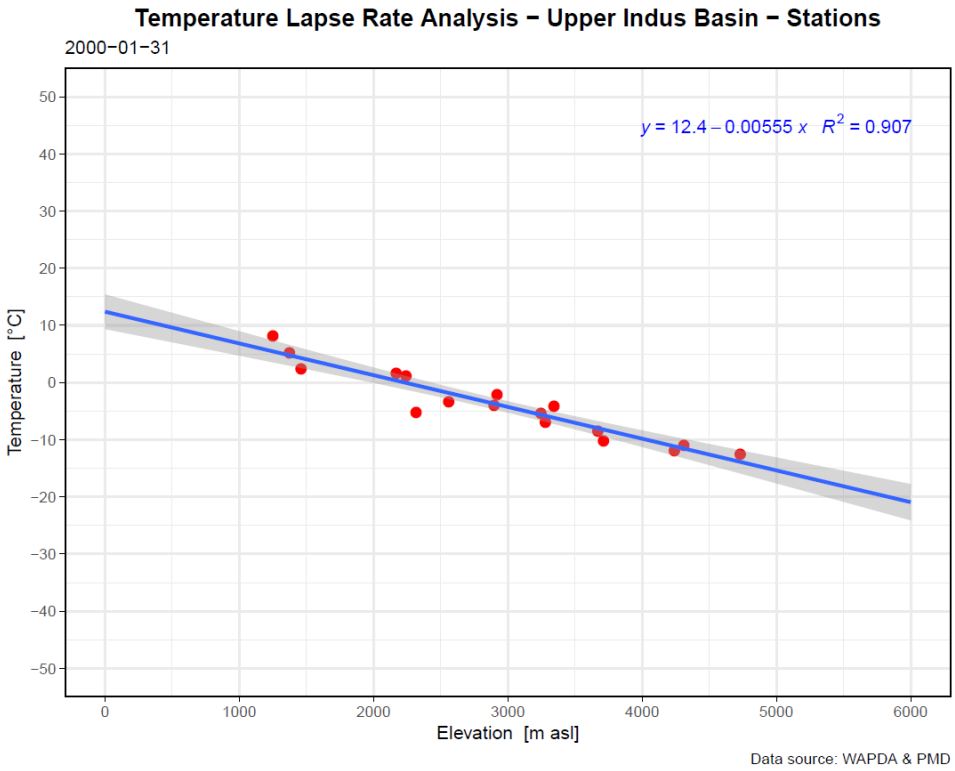

Figure B.24 Daily regression analysis between the station elevations and average temperatures

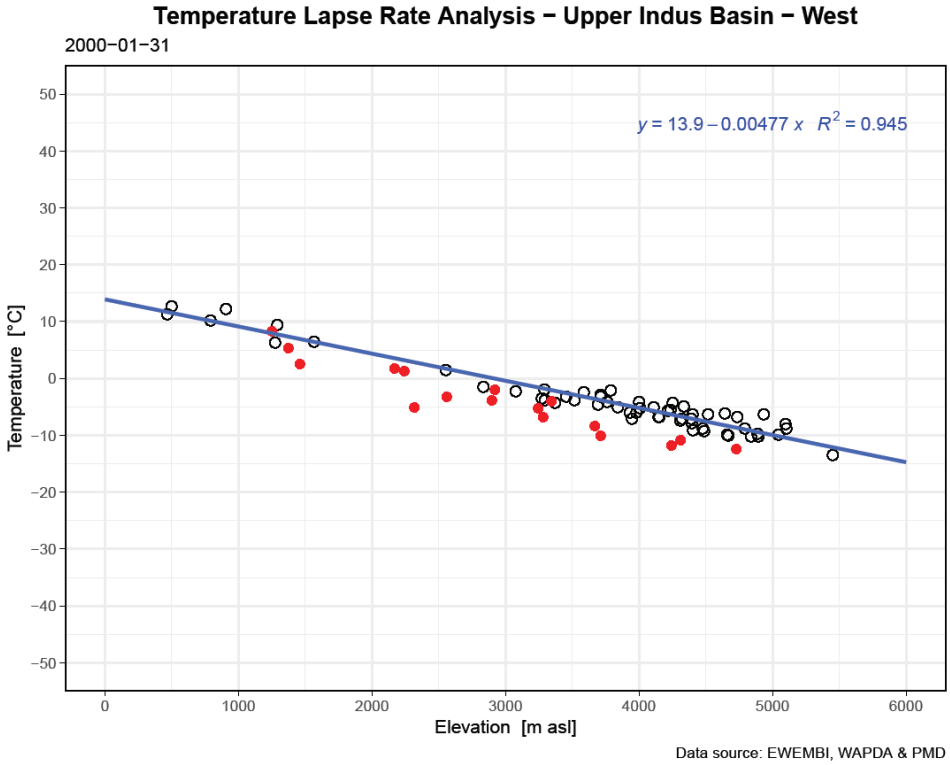

Figure B.25 Daily regression analysis between the EWEMBI elevation grid vs EWEMBI temperatures – UIB west [Red dots are representing the stations]

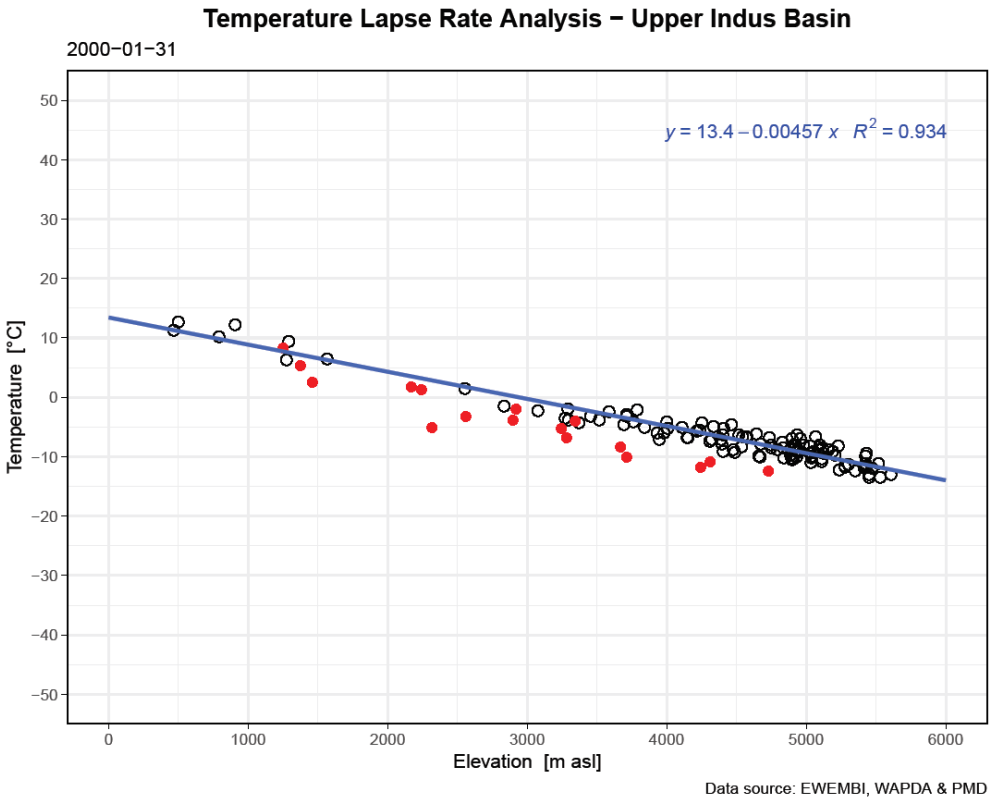

Figure B.26 Daily regression analysis between the EWEMBI elevation grid vs EWEMBI temperatures – whole UIB [Red dots are representing the stations]

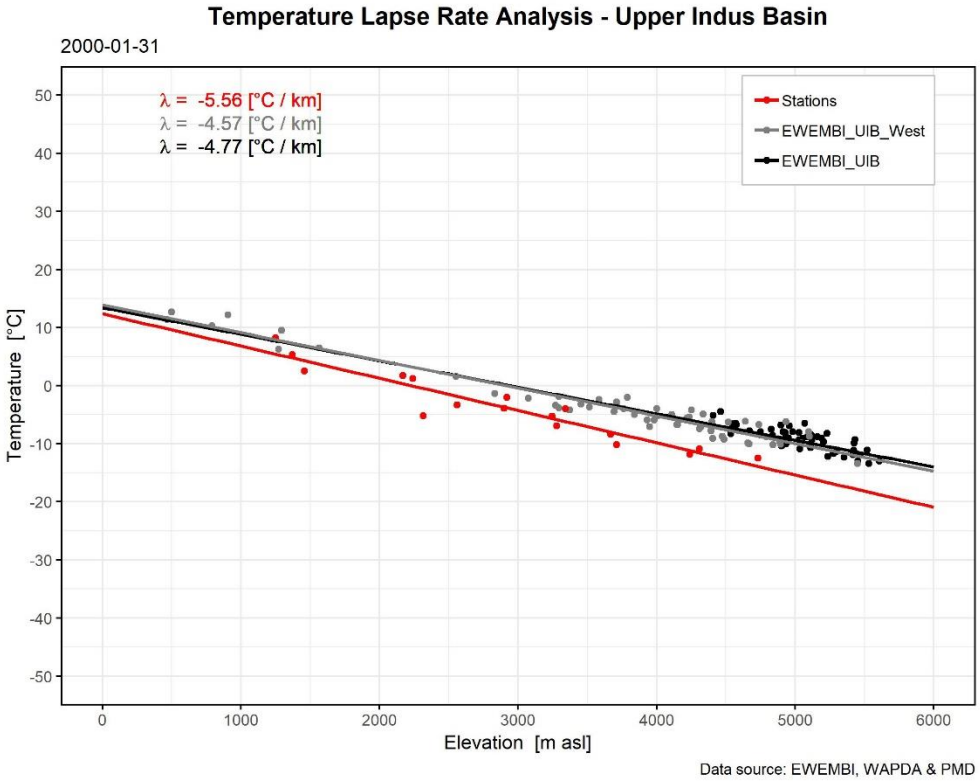

Figure B.27 Comparison of daily temperature lapse rate for western UIB, whole UIB and stations

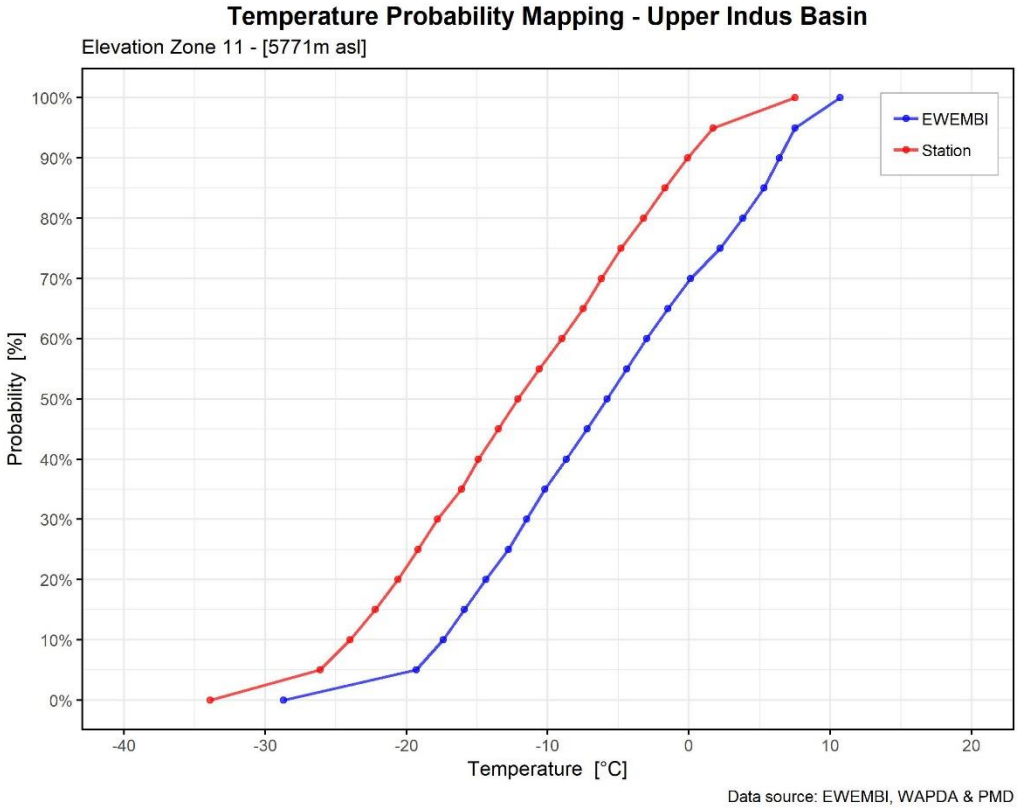

Figure B.28 Probability mapping for the EWEMBI and station based zonal temperature

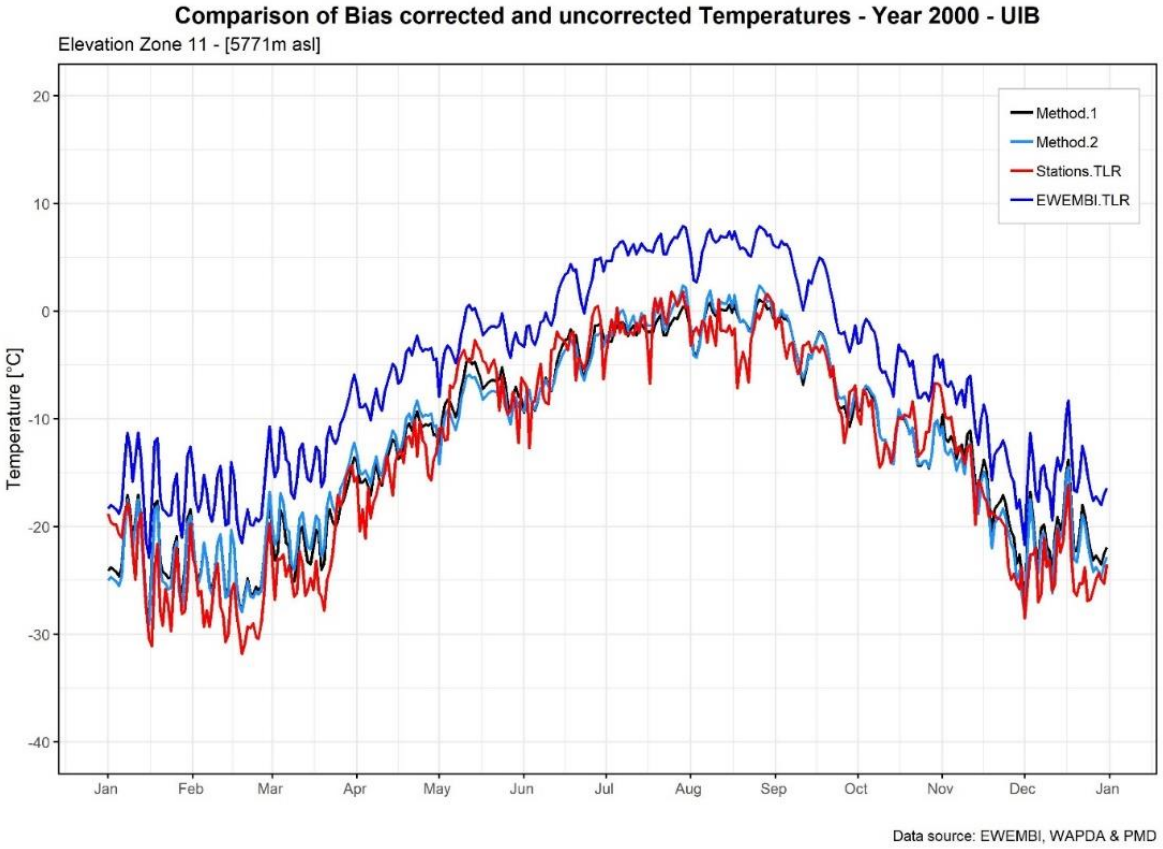

Figure B.29 Comparison of zonal bias corrected (Method-1 & Method-2) temperature with the EWEMBI and stations based temperature

Table B.1 Main components and methods used by the two hydrological models used in the study

Hydrological Models		
Model Features	SRM+G	VIC-Glacier
Spatial type	Lumped elevation zones, 11 elevation zones of 500m each	Grid cells (0.25°), sub-grid heterogeneity (8 elevation bands and land cover classes and initial glacier thickness)
Input climate data	Temperature, Precipitation, Snow cover area and Glacier exposed area	Temperature, Precipitation, Humidity, Wind speed, Shortwave and Longwave Radiation
Soil representations	NA	3 soil layers and 19 parameters
Calculation of potential evapotranspiration	Represented in runoff coefficients	Penman-Monteith
Snowmelt calculation method	Degree-day	Two snow layer energy balance
Glacier melt calculation method	Degree-day	One layer energy balance
Runoff routing method	Non-constant recession approach	Linearized St. Venant equations
Calibration/validation approaches	1. Conventional 2. Enhanced	1. Conventional 2. Enhanced
Parameters	1. Temperature Lapse Rate 2. Recession Coefficients 3. Critical Precipitation 4. Lag Time 5. Critical Temperature 6. Rainfall Contributing Area 7. Runoff coefficient – snow, rain, glacier 8. Degree-Day Factor – snow, glacier	1. Ds (base flow parameter) 2. DSmax (maximum base flow that occur from the lowest soil layer) 3. Snow roughness length 4. Ws (the fraction of the maximum soil moisture of the lowest soil layer) 5. bi (Variable infiltration parameter
Gauging stations	1. Indus @ Tarbela 2. Hunza@ Daniyor 3. Astore @ Doyian	

Table B.2 Area and percentage of glaciers by elevation zone [GLIMS dataset was used for the glaciers area representation]

Elevation Zone	Altitude [m a.s.l.]	Zonal Area [km^2]	Glacier Area [km^2]	Glacier Area [%]
1 - 3	≤ 2000	9554	–	–
4	2500	4395	1.0	0.01
5	3000	5690	39.9	0.19
6	3500	9998	213.0	1.01
7	4000	16183	659.1	3.14
8	4500	28845	1750.1	8.33
9	5000	39473	3928.4	18.70
10	5500	37819	6065.6	28.88
11	≥ 5500	21388	8346.9	39.74
	Total	173345	21004.0	100%

Table B.3 SRM+G model parameters used for the calibration and validation

Parameters	Symbol	Value	Units	Remarks
Temperature Lapse-Rate	γ	6.0	°C km^{-1}	
Recession Coefficient	k_x	1.050		constant
	k_y	0.015		January – March
		0.019	–	April – May
		0.020		June - July
		0.100		August – September
		0.017		October - December
Critical Precipitation	P_{crit}	1	cm	constant
Lag Time	L	45	h	UIB @ Tarbela
		18		Hunza @ Daniyor
		18		Astore @ Doyian
Critical Temperature	T_{crit}	0.5–3.0	°C	variable
Rainfall Contributing Area	RCA	0	–	November – March
		1		April – October
Runoff Coefficient - Snow	c_S	0.80	–	constant
Runoff Coefficient - Glacier	c_G	0.70	–	constant
Runoff Coefficient - Rain	c_R	0.40–0.60	–	variable
Degree-Day Factor - Snow	α_S	1.0–7.0	mm °C^{-1}d^{-1}	variable
Degree-Day Factor - Glacier	a_G	2.5–6.0	mm °C^{-1}d^{-1}	variable

Note: Degree-day factors (snow and glaciers) and critical temperature (which bifurcates the falling precipitation between snow and rain) are not constant parameters but they are varied on monthly basis depending upon prevailing temperature in the catchment. These ranges are also available in the literature (e.g. Tahir et al. 2011, Ismail and Bogacki 2018, Hayat et al. 2019) for the UIB and its sub-catchments.

Table B.4 Comparison of results for Glacier Mass Balance (GMB) for the calibration/validation period (i.e. 2000–2016) in present study to other studies

	Glacier Mass Balance [mm w.e. yr^{-1}]	
Reference	Period	Karakoram
Kääb et al. (2015)	2003–2009	-100 ± 60
Braun et al. (2017)	2000–2016	-30 ± 70
Bolch et al. (2017)	1999–2009	-80 ± 210
Lin et al. (2017)	2000–2014	-101 ± 58
Muhammad et al. (2019)	2000–2016	-30 ± 170
Present Study	2000–2016	
SRM+G		-98
VIC-Glacier		-83

Table B.5 Differences between mean monthly and mean annual impacts (as presented in Figures. 4.2a and 4.2b) based on two model parameterizations after the conventional and enhanced calibration/validation methods

Monthly	Enhanced - Conventional [RCP2.6]			Enhanced - Conventional [RCP8.5]		
	2011−2040	2041−2070	2071−2099	2011−2040	2041−2070	2071−2099
Jan	2.9%	2.3%	2.2%	1.5%	2.4%	3.0%
Feb	0.9%	0.4%	0.9%	-0.7%	-1.0%	-2.7%
Mar	-2.8%	-2.9%	-3.5%	-3.0%	-8.2%	-17.2%
Apr	0.9%	1.6%	1.5%	0.6%	3.6%	3.3%
May	3.5%	5.6%	5.9%	3.5%	3.9%	-2.1%
Jun	3.8%	6.2%	7.4%	3.6%	2.4%	-5.7%
Jul	1.6%	3.6%	6.3%	1.4%	3.7%	6.5%
Aug	1.5%	3.0%	4.2%	0.5%	3.8%	6.9%
Sep	2.6%	3.4%	4.6%	0.7%	3.2%	8.1%
Oct	6.3%	6.9%	7.5%	2.6%	8.0%	18.9%
Nov	6.3%	7.3%	8.6%	4.3%	9.3%	17.6%
Dec	5.6%	3.3%	4.1%	2.6%	3.7%	5.7%
	Enhanced - Conventional [RCP2.6]			Enhanced - Conventional [RCP8.5]		
Annual	2011−2040	2041−2070	2071−2099	2011−2040	2041−2070	2071−2099
	6.3%	8.1%	9.4%	5.5%	8.2%	10.0%

Table B.6 List of the hydro-meteorological data sets, providing agencies as well as location and altitude of the stations

Sr. No.	Station Name	Station Type	Period	Data Agency	Latitude [degrees]	Longitude [degrees]	Altitude [m a.s.l.]
1	Skardu	Meteorological	2000 - 2012	PMD	35.30	75.68	2317
2	Astore	Meteorological	2000 - 2012	PMD	35.37	74.90	2168
3	Hunza	Meteorological	2000 - 2012	PMD	35.32	74.65	2156
4	Gilgit	Meteorological	2000 - 2012	PMD	35.92	74.33	1460
5	Chilas	Meteorological	2000 - 2012	PMD	35.42	74.10	1250
6	Khunjrab	Meteorological	2000 - 2012	WAPDA	36.84	75.42	4730
7	Burzil	Meteorological	2000 - 2012	WAPDA	34.90	75.16	4310
8	Deosai	Meteorological	2000 - 2012	WAPDA	35.09	75.54	4240

9	Ziarat	Meteorological	2000 - 2012	WAPDA	36.77	74.46	3669
10	Shendure	Meteorological	2000 - 2012	WAPDA	36.09	72.55	3712
11	Rama	Meteorological	2000 - 2012	WAPDA	35.36	74.81	3344
12	Yasin	Meteorological	2000 - 2012	WAPDA	36.40	73.50	3280
13	Naltar	Meteorological	2000 - 2012	WAPDA	36.17	74.18	2898
14	Rattu	Meteorological	2000 - 2012	WAPDA	35.15	74.80	2920
15	Shigar	Meteorological	2000 - 2012	WAPDA	35.63	75.53	2560
16	Shangla	Meteorological	2000 - 2012	WAPDA	34.88	72.59	2240
17	Tarbela	Discharge	2000 - 2016	WAPDA	34.33	72.86	475
18	Daniyor	Discharge	2000 - 2012	WAPDA	74.38	35.93	1370
19	Doyian	Discharge	2000 - 2012	WAPDA	35.55	74.70	1583

PMD = Pakistan Meteorological Department.

WAPDA = Water and Power Development Authority Pakistan.

Table B.7 Monthly temperature bias correction for each elevation zone

Bias Correction - T_{avg}											
Elevation zones	z1	z2	z3	z4	z5	z6	z7	z8	z9	z10	z11
Mean elevation [m a.s.l]	749	1255	1755	2266	2767	3272	3769	4272	4754	5240	5771
Jan	0.26	0.61	0.73	0.81	1.26	2.08	2.90	3.75	4.46	5.22	5.75
Feb	-1.38	-1.02	-0.79	-0.41	0.28	1.37	2.40	3.52	4.51	5.53	6.37
Mar	-2.35	-1.75	-1.15	-0.30	0.71	2.10	3.31	4.47	5.43	6.59	7.72
Apr	-2.14	-1.78	-1.33	-0.56	0.35	1.66	2.76	3.88	4.81	5.91	7.00
May	-1.58	-1.66	-1.61	-1.29	-0.68	0.32	1.20	2.25	3.14	4.11	5.01
Jun	-2.23	-2.26	-2.11	-1.69	-0.95	0.22	1.25	2.62	3.81	4.97	6.10
Jul	-4.91	-4.46	-3.70	-2.65	-1.45	0.16	1.52	3.17	4.58	5.98	7.52
Aug	-5.44	-4.85	-3.99	-2.87	-1.67	-0.12	1.19	2.70	3.95	5.27	6.77
Sep	-2.90	-2.61	-2.12	-1.34	-0.38	1.00	2.13	3.43	4.52	5.68	6.92
Oct	-1.53	-0.97	-0.43	0.29	1.11	2.26	3.21	4.01	4.55	5.41	6.34
Nov	-1.07	-0.54	-0.18	0.20	0.78	1.70	2.51	3.22	3.71	4.44	5.11
Dec	0.53	0.93	1.06	1.18	1.62	2.43	3.19	3.89	4.42	5.07	5.53

Table B.8 Probability mapping for zonal temperature – EWEMBI based

Elevation zone	z1	z2	z3	z4	z5	z6	z7	z8	z9	z10	z11
Mean elevation [m asl]	749	1255	1755	2266	2767	3272	3769	4272	4754	5240	5771
Probability [%]											
0	4.2	0.8	-3.2	-7	-9.8	-12.7	-15.2	-17.2	-20.6	-24.3	-28.7
5	8.9	5.9	2.5	-0.9	-3.8	-6.3	-8.7	-11.2	-13.7	-16.2	-19.3
10	10.1	7.1	3.9	0.8	-2	-4.5	-7	-9.4	-11.9	-14.4	-17.4
15	11.1	8.2	5.2	2.1	-0.7	-3.1	-5.5	-8	-10.6	-13	-15.9
20	12.2	9.3	6.3	3.4	0.7	-1.7	-4.1	-6.6	-9.1	-11.5	-14.35
25	13.6	10.7	7.8	4.7	2	-0.4	-2.8	-5.2	-7.7	-10.1	-12.8
30	14.9	12	9	6	3.4	1.1	-1.3	-3.9	-6.4	-8.7	-11.5
35	16.1	13.2	10.3	7.4	4.8	2.4	0	-2.5	-5.1	-7.5	-10.2
40	18	14.9	11.9	9	6.4	4.2	1.7	-0.9	-3.5	-5.9	-8.7
45	19.6	16.5	13.5	10.6	7.9	5.6	3.1	0.6	-2	-4.4	-7.2
50	21.2	18	14.9	12	9.3	6.9	4.5	1.9	-0.7	-3.2	-5.8
55	22.6	19.4	16.2	13.3	10.6	8.2	5.7	3.2	0.7	-1.7	-4.4

60	23.9	20.7	17.5	14.55	11.8	9.4	7	4.6	2.2	-0.2	-3
65	24.8	21.8	18.8	15.8	13.1	10.8	8.3	6	3.7	1.2	-1.5
70	25.6	22.6	19.8	16.9	14.3	12.1	9.7	7.3	4.9	2.7	0.1
75	26.3	23.3	20.5	17.8	15.4	13.1	10.8	8.8	6.6	4.6	2.2
80	26.9	23.9	21.1	18.5	16.1	14.1	12	10	8.1	6.1	3.8
85	27.6	24.5	21.7	19.2	16.9	15	13	11.2	9.3	7.4	5.3
90	28.6	25.4	22.5	20	17.7	15.8	13.9	12.1	10.2	8.4	6.4
95	29.8	26.5	23.5	21	18.8	16.9	14.9	13.1	11.2	9.4	7.5
100	36.8	32.5	28.3	24.9	22.9	21	18.9	16.6	14.3	12.4	10.7

Table B.9 Probability mapping for zonal temperature – Station based

Elevation zone	z1	z2	z3	z4	z5	z6	z7	z8	z9	z10	z11
Mean elevation [m asl]	749	1255	1755	2266	2767	3272	3769	4272	4754	5240	5771
probability											
0	5.1	2.3	-1.6	-5.7	-9.7	-13.7	-17.7	-21.6	-25.5	-29.3	-33.9
5	8.6	5.5	2.4	-0.9	-4.4	-7.8	-11.4	-15.0	-18.5	-22.1	-26.1
10	9.9	6.6	3.4	0.1	-3.2	-6.5	-9.9	-13.4	-16.8	-20.1	-24.0
15	11.4	7.9	4.5	1.2	-2.0	-5.3	-8.6	-12.0	-15.3	-18.6	-22.2
20	13.1	9.7	6.2	2.7	-0.7	-4.1	-7.4	-10.7	-13.9	-17.0	-20.6
25	14.6	11.2	7.8	4.3	0.9	-2.6	-5.9	-9.1	-12.4	-15.6	-19.2
30	16.2	12.7	9.2	5.7	2.3	-1.0	-4.4	-7.8	-11.0	-14.2	-17.8
35	18.0	14.5	11.0	7.6	4.1	0.6	-2.8	-6.1	-9.4	-12.7	-16.1
40	19.7	16.3	12.8	9.2	5.7	2.3	-1.2	-4.6	-8.0	-11.3	-14.9
45	21.2	17.8	14.4	10.8	7.4	3.8	0.4	-3.0	-6.4	-9.8	-13.5
50	22.6	19.1	15.7	12.2	8.7	5.3	1.8	-1.7	-5.1	-8.4	-12.1
55	24.1	20.6	17.2	13.7	10.3	6.8	3.4	-0.1	-3.5	-6.9	-10.6
60	25.4	22.1	18.7	15.2	11.8	8.3	4.9	1.4	-1.9	-5.3	-9.0
65	26.8	23.4	20.0	16.6	13.1	9.7	6.2	2.8	-0.5	-3.8	-7.5
70	28.3	24.8	21.4	17.9	14.5	11.0	7.5	4.0	0.8	-2.6	-6.2
75	29.5	26.1	22.8	19.2	15.8	12.4	9.0	5.6	2.3	-1.1	-4.8
80	30.8	27.3	23.8	20.4	17.1	13.7	10.4	6.9	3.7	0.3	-3.2
85	32.0	28.5	25.1	21.6	18.2	14.9	11.5	8.2	5.0	1.8	-1.7
90	33.2	29.7	26.2	22.6	19.3	15.9	12.7	9.4	6.4	3.3	-0.1
95	35.0	31.4	27.8	24.3	20.8	17.4	14.1	10.9	7.9	4.8	1.7
100	40.0	36.0	32.2	28.4	24.6	21.4	18.4	15.6	13.0	10.3	7.5

Table B.10 Comparison of annual precipitation totals averaged for the UIB from Gridded precipitation products [period: 2000–2016]

Precipitation Product	Precipitation [mm yr^{-1}]
EWEMBI	366.2
RFE v2.0 Central Asia	789.5
MERRA-2	262.9
APHRO_MA_V1101*	253.3
APHRO_MA_V1901	408.5
TRMM_3B42_v7	344.0
CMORPH_bld	185.7
ERA-interim	751.2

* period: 2000 - 2007

Table B.11 Literature based ranges of the parameters used in the models calibration in the Upper Indus Basin

Model	Source	Parameter	Range
SRM+G	Lutz et al. (2016)	DDF (debris-covered glaciers)	5.0–8.0 mm $°C^{-1}$ day^{-1}
		DDF (debris-free glaciers)	2.0–4.5 mm $°C^{-1}$ day^{-1}
VIC-Glacier	Cherkauer et al. (2003)	Snow roughness length	0.005–10mm
	De Scally, F. A., (1997)	Temperature lapse rate	-9.0– -6.5 °C/km